Development and characterization of Fired Passivating Contacts for p-type silicon solar cells fabrication

Anatole Desthieux

INSTITUT POLYTECHNIQUE DE PARIS

NNT : 2021IPPAX091

Thèse de doctorat

ÉCOLE POLYTECHNIQUE

IP PARIS

Development and characterization of Fired Passivating Contacts for p-type silicon solar cells fabrication

Thèse de doctorat de l'Institut Polytechnique de Paris
préparée à l'Ecole Polytechnique

École doctorale n°626 Institut Polytechnique de Paris (ED IP Paris)
Spécialité de doctorat : Physique

Thèse présentée et soutenue à Palaiseau, le 15/11/2021, par

ANATOLE DESTHIEUX

Composition du Jury :

Olivier Palais Professeur, Aix-Marseille Université (Institut Matériaux Microélectronique Nanosciences de Provence)	Président
Marie-Estelle Gueunier-Farret Maître de Conférence - HDR, Université Paris-Saclay (Laboratoire Génie Electrique et Electronique de Paris)	Rapporteur
Lars Korte Senior Scientist, Helmoltz-Zentrum Berlin (Young Investigator Group Perovskite Tandem Solar Cells)	Rapporteur
Erwin Kessels Professeur, Eindhoven University of Technology (Department of Applied Physics)	Examinateur
Delfina Muñoz Ingénieur Chercheur, Commissariat à l'Energie Atomique et aux Energies Alternatives (Institut National de l'Energie Solaire)	Examinateur
Damien Aureau Chargé de Recherche, Université de Versaille - Saint Quentin (Laboratoire institut Lavoisier de Versailles)	Examinateur
Pere Roca i Cabarrocas Directeur de Recherche, Ecole Polytechnique (Laboratoire de Physique des Interfaces et Couches Minces)	Directeur de thèse
Jorge Posada Ingénieur Chercheur, EDF R&D	Encadrant de thèse
Barbara Bazer-Bachi Ingénieur Chercheur, Photowatt - EDF ENR PWT	Invité

"It is crucial that the difference principle includes an idea of reciprocity: the better endowed (who have a fortunate place in the distribution of native endowments they do not morally deserve) are encouraged to acquire still further benefits [...] on condition that they train their native endowments and use them in ways that contribute to the good of the less endowed (whose less fortunate place in the distribution they also do not morally deserve)."

Justice as Fairness, A Restatement
John Rawls

Acknowledgements

Ce manuscrit de thèse parachève trois années de travail que j'ai pu réaliser entre EDF R&D, l'Institut Photovoltaïque d'Ile-de-France (IPVF), et le Laboratoire de Physique des Interfaces et Couches Minces (LPICM) dans le cadre d'une Convention Industrielle de Formation par la Recherche en Entreprise (CIFRE). Je tiens donc tout d'abord à remercier *Mattieu Versavel* et *Marie Jubault* pour m'avoir permis de rentrer chez EDF initialement pour mon stage de master. Merci à *Cédric Guérard* et *Mireille Owona* pour m'avoir épaulé par la suite dans mes démarches administratives et pour leur aide et encadrement durant le reste de mon contrat de thèse.

Ensuite, du fond du cœur merci à *Jorge Posada* pour m'avoir fait confiance dans la réalisation de cette thèse, et merci pour ton encadrement toujours bienveillant, et les discussions (nombreuses) en salle chimie sur la grandeur de l'IRDEP et sur les contes et légendes autour des personnalités de feu ce laboratoire. A *Pere Roca i Cabarrocas*, un éternel remerciement, pour ta présence, ta passion, ton souci du détail, ton travail acharné et ta bonne humeur constante. À vous deux, je n'aurais pas pu rêver un meilleur binôme pour m'encadrer.

Par ailleurs, un immense merci aux membres de mon jury de thèse : *Olivier Palais* qui en aura été le président, mes deux rapporteurs *Marie-Estelle Gueunier-Farret* et *Lars Korte*, mais aussi *Erwin Kessels*, *Delfina Muñoz* et *Damien Aureau*.

J'ai réalisé une immense partie de mes travaux expérimentaux au LPICM, et rien n'aurait été possible sans les équipes du BEER qui étaient toujours présentes en soutien des expériences ou pour régler des problèmes de machines. En particulier, merci à *Cyril Jadaud*, *François Silva* et *Jonathan Meot* pour leur aide précieuse. Un immense merci à *Pavel Bulkin* pour les nombreux décapages HF et dépôts d'AlO_x, et les autres discussions autour de l'exodiffusion et des techniques de dépôt, merci à *Ileana Florea* pour les préparation FIB et les mesures TEM, ainsi qu'à *Mengkoing Sreng* pour avoir rendu les mesures de MPL *in situ* possibles. A *Dmitri Daineka*, merci pour les répétitions de musique, ainsi que pour les discussions scientifiques au sein du groupe PROM ou au coin d'un couloir avec également *Angelo Pirangelo*, *Denis Tondelier*, *Erik Johnson*,, *Jean-Charles Vanel*,*Jean-Eric Bourré* et *Karim Ouaras*. Et enfin un énorme big up à tous les amis du LPICM, toujours là quand il faut, et avec qui j'aurais aimé passer un peu plus de temps au quotidien. En particulier, merci à *Chloé*, *Ronan*, *Malinka* (ton bébé Octopus se porte toujours très bien), *Eric*, *Ghewa*, *Hindia*, *Minjin*, *Tinghui*, *Junha*, *Robert*, *Gookbin*, *Michel*, *Hae-yeon Lakshmann*, *Josef*, *Junkang*, *Antonio*, *Daniel*, *Monalisa* (do not worry, you will definitely end up mastering the beast) et toutes les autres personnes avec qui j'ai pu discuter au cours de ces trois dernières années. Good luck to *Mateusz* for the upcoming evolution of *in situ* passivation measurements, I am sure you will do great.

Je suis infiniment reconnaissant envers mes différents collaborateurs: ceux de l'Institut Lavoisier de Versailles (ILV) avec *Davina Messou*, *Solène Béchu* et *Muriel Bouttemy*, avec qui j'ai beaucoup apprécié échanger et qui ont toujours pris le temps de discuter

des résultats d'XPS, et ceux de l'Ecole Polytechnique Fédéral de Lausanne (EPFL) avec *Mario Lehmann*, *Franz-Josef Haug* et *Audrey Morisset* qui ont eu la gentillesse de me contacter à l'issue d'une conférence en ligne (pas toujours le plus simple pour initier des collaborations) et m'ont apporté beaucoup dans mes réflexions sur la compréhension des résultats de MPL !

Un immense merci à *Sophie Gaillard* pour les innombrables nettoyages RCA, pour ta gentillesse, ton énergie, et pour les sorties natation qui m'ont fait le plus grand bien, et merci à *Valérie Daniau* pour tous les efforts dans les labos, ton sourire toujours collé aux lèvres et la chouette randonnée à Fontainebleau ! Un grand merci à tous permanents EDF qui m'ont aidé de près ou de loin au cours de ma thèse, avec qui j'ai pu discuté autour d'un café ou d'un brunch (merci papa *Régis Tuyizere*).

Et puis l'IPVF c'est beaucoup, beaucoup d'échanges et de belles rencontres réalisées au fil de l'eau ! Une pensée attendrie pour tous les "anciens", collègues doctorants partis trop tôt: *Adrien*, *Cécile*, *Fabien*, *Harold*, , *Louis*, *Mishael*, *Rafaël*, *Romaric* et *Valentin* côté doctorants, mais aussi *Baljeet* et *Kathy* pour les discussions passionnantes et les super concerts qu'on a pu préparer ensemble. À *Caterine*, *Christian* et *Maria* un grand merci pour cet air hispanique que vous avez insufflé à notre openspace du 2B.B13. Je ne remercierai jamais assez ceux qui m'ont initié à l'escalade, et toutes les personnes de la team Arkose avec qui ce fut un plaisir de grimper ! Parmi eux *Olivier* (mon gars sûr), *Thomas* (Monsieur Conseil), *Alex Py* (le gecko), *Arpit* ("voiture"), mais aussi *Alexandre*, *Arthur*, *Géraud* et *Marie*. Merci et bon courage aux doctorants plus jeunes, et merci pour les bons moments de convivialités passés ensemble autour d'un verre ou d'une soirée : *Carlos*, *Célia*, *Claire*, *Elisa*, *Guillaume*, *Javid*, *Lise*, *Salim* et *Thomas*. Mentions spéciales pour *Bérengère* et les discussions infinies qu'on peut avoir, et pour *Capu* pour tout, et en particulier nos petits moments musicaux et gourmands. Enfin, ces trois années auraient été beaucoup plus fades s'il n'y avait pas eu mes petits Tuches dans l'affaire : *Margot*, *Minouche*, *Sophie* et *Yéyé* et leur enthousiasme débordant pour faire des soirées, s'endormir devant des films à la qualité douteuse, et discuter autour des cafés les mardredis et les vendredis philo.

Un coup de chapeau particulier à *Daniel Suchet* pour les discussions passionnantes, son aide précieuse pour la préparation de la semaine ATHENS, et merci de m'avoir fait découvrir Citoyens Pour Le Climat !

À mes amis fidèles et toujours présents, qui m'ont permis de sortir ma petite tête de ma bulle, un immense merci ! Parmi eux, merci à mes éternels amis d'enfance que je chéris du fond de mon cœur : ma *Juli*, et la clique avec *Anne So*, *Claire*, *Delf*, *Guigui* et *Salomé* ! Merci à ma *Coco* pour les innombrables jap et ses vocaux interminables, aux expats et derniers parisiens de la P2018 avec *Alexis*, *Gabi*, *Nathan*, *Louis* (on adore les semaines de télétravail posés au bord de la mer), *JB*, *Koen* et *Pham*, et aux anciens de l'OPA: *Ivan* pour les conseils de pro à l'escalade, *Jordan*, *Pierre* et *Lucas* pour nos petits Skype des familles et *Gautier* pour les soirées musique et magie dans lesquelles il met toujours une ambiance de feu ! Un bisou à *Sacha* et ses tracos rigolos. Enfin, à *Neil* et *Dinou*, vous êtes moches mais drôles (l'un des deux est faux), et je vous aime fort.

Et pour finir un immense merci à ma famille, pour l'amour qu'ils me donnent depuis ma plus tendre enfance, et sans qui je ne serais pas la personne que je suis devenue.

Acronyms

µc-Si:H	hydrogenated micro-crystalline silicon
µc-SiO$_x$:H	hydrogenated micro-crystalline silicon oxide
4PP	4-points probe
a-Si:H	hydrogenated amorphous silicon
a-SiN$_x$:H	hydrogenated amorphous silicon nitride
Al-BSF	aluminum back-surface field
ALD	atomic layer deposition
AlO$_x$	aluminum oxide
ARC	anti-reflection coating
AZO	aluminum-doped zinc oxide
c-Si	crystalline silicon
CCGT	combined cycle gas turbine
CCP	capacitively coupled plasma
COCOS	corona oxide characterisation on semiconductor
CVD	chemical vapor deposition
Cz	Czochralsky
DSP	double-side polished
EGS	electronic grade silicon
FGA	forming gas annealing
FIB	focused ion beam
FPC	fired passivated contact
FT	fire-through
FTIR	fourier transform infrared spectroscopy
FZ	float-zone
HIT	heterojunction with intrinsic thin layer
HWCVD	hot-wire chemical vapor deposition
IBC	interdigitated back contact
IPCC	International Panel on Climate Change
ITO	indium-doped tin oxide
LCOE	levelized cost of electricity
LPCVD	low pressure chemical vapor deposition
mc-Si	multi-crystalline silicon
MGS	metallurgical grade silicon
MPL	modulated photoluminescence
NAOS	nitric acid oxidation of silicon
PA-ALD	plasma-assisted atomic layer deposition
PANO	plasma-assisted nitrous oxide
PCE	power conversion efficiency
PECVD	plasma-enhanced chemical vapor deposition

PERC	passivated emitter and rear contact
PL	photoluminescence
POLO	poly-crystalline silicon on oxide
PSG	phospho-silicate glass
PV	photovoltaics
PVD	physical vapor deposition
QSSPC	quasi steady-state photoconductance
RCA	Radio Corporation of America
RF	radio-frequency
SC-1	standard cleaning 1
SC-2	standard cleaning 2
SDE	saw-damage etched
SDR	saw-damage removal
SE	spectroscopic ellipsometry
SGS	solar grade silicon
SiC_x	silicon carbide
SiH_4	silane
SiO_x	silicon oxide
SIPOS	semi-insulating poly-crystalline silicon
SRH	Shockley-Read-Hall
STEM-HAADF	scanning transmission electron microscopy-high angle annular dark field
TCO	transparent conductive oxide
TDS	thermal desorption spectrocsopy
TEM	transmission electron microscopy
TMA	trimethylaluminum $Al(CH_3)_3$
TMB	trimethylborane $B(CH_3)_3$
TMO	transparent metal oxide
TOPCon	tunnel oxide passivated contact
UV	ultraviolet
XPS	X-ray photoelectron spectroscopy
XRR	X-ray reflectometry

List of Symbols

$[X-H]$ Concentration in $X-H$ bonds

α Absorptivity

Δn Excess electron density

Δp Excess hole density

η Power conversion efficiency

η_n Electro-chemical potential of electrons

η_p Electro-chemical potential of holes

λ Wavelength

$\mathcal{V}$ Volume of the studied ensemble of particles

μ_n Electron mobility

μ_p Hole mobility

ω Angular frequency of the incident light

ϕ Phase shift between the laser excitation and the modulated photoluminescence signal

ϕ_n Chemical potential of electrons

ϕ_p Chemical potential of holes

ρ_c Specific contact resistivity

σ_n Electron conductivity

σ_p Hole conductivity

σ_{X-H} IR-scattering cross-section of $X-H$ bonds

τ_{Auger} Characteristic minority carrier lifetime related to Auger recombinations

$\tau_{eff,diff}$ Differential effective minority carrier lifetime

τ_{eff} Effective minority carrier lifetime

τ_m Minority carrier lifetime measured by modulated photoluminescence

τ_{rad} Characteristic minority carrier lifetime related to radiative recombinations

τ_{SRH}	Characteristic minority carrier lifetime related to SRH recombinations
τ_{surf}	Characteristic minority carrier lifetime related to surface recombinations
ε_{Fn}	Quasi-Fermi level of electrons
ε_{Fp}	Quasi-Fermi level of holes
φ	Electric potential
A	Area of the solar cell
A_{XH}	Area of the $X-H$ stretching mode peak
B_{rad}	Radiative recombination coefficient
c	Speed of light in vacuum
C_n	Trap capture coefficient of electrons
C_p	Trap capture coefficient of holes
$C_{A,n}$	Auger recombination coefficient for electrons
$C_{A,p}$	Auger recombination coefficient for holes
D_n	Diffusion coefficient of electrons
D_p	Diffusion coefficient of holes
D_H	Hydrogen diffusion coefficient
D_{it}	Surface defect density
E	Electric field
E_g	Energy band gap
E_i	Fermi level for an intrinsic semiconductor
E_t	Trap energy level in the band gap
F_a	Fraction of amorphous material in the ellipsometric model
F_c	Fraction of crystallised material in the ellipsometric model
FF	Fill Factor
G	Generation rate
h	Planck constant
I	Light intensity
I_0	Incident light intensity
iV_{oc}	Implied open-circuit voltage
J	Current density

J_0 Saturation current density

$J_{0,c}$ Recombination current density at the metallic contact

J_{gen} Photogenerated current density

$J_{n,diff}$ Diffusion current density of electrons

J_n Total current density of electrons

$J_{p,diff}$ Diffusion current density of holes

j_{PL} Luminescence photon flux

J_p Total current density of holes

J_{sc} Short circuit current density

k Boltzman's constant

n Density of free electrons

N_A Density of acceptor atoms

N_A^- Density of ionized acceptor atoms

N_C Effective density of states of electrons in the conduction band

N_D Density of donor atoms

N_D^+ Density of ionized donor atoms

n_e Free electron density in a plasma

n_i Intrinsic electron density at thermal equilibrium

N_t Trap density

N_V Effective density of states of holes in the valence band

N_{firing} Density of recombination centers created during a firing step

P Output power of a solar cell

p Density of free holes

P_{inc} Incident radiative power density

P_{mpp} Output power at maximum power point

q Elementary charge

Q_e Average number of electron-hole pair generated by one photon

Q_f Fixed charge density

R Dilution ratio of silane in hydrogen

R_f Front surface reflectivity

R_p	Parallel resistance
R_s	Series resistance
R_{Aug}	Auger recombination rate
R_{bulk}	Bulk recombination rate
R_{eff}	Effective recombination rate
R_{ms}	Surface roughness coefficient
R_{rad}	Radiative recombination rate
R_{SRH}	Shockley-Read-Hall recombination rate
R_{surf}	Surface recombination rate
S	Entropy
T	Temperature
T_e	Electron temperature in a plasma
T_g	Gas temperature of a plasma
U	Internal energy
V	Voltage
V_{oc}	Open circuit voltage

Table of contents

List of Figures

List of Tables

Introduction

Global energy context

The Human Development Index (HDI) is an indicator of life expectancy, education and per capita income. It is broadly considered as a gauge of progress and development of the countries. According to the United Nations Development program, there appears to be a correlation between HDI and the energy consumption per capita [1]. Access to affordable energy is thus of paramount importance for the development of countries and their ability to provide higher standards of living to their populations. The World Energy Council pointed out three main challenges that the energy sector needs to tackle: the energy Trilemma [2]. These three pillars are *energy equity*, *energy security* and *environmental sustainability*.

Energy inequality is very large worldwide, with energy consumption per capita varying a hundredfold between nations (0.25 toe/cap for Bangladesh versus 16.38 toe/cap for Qatar in 2017 [3]) mostly due to the differences in gross domestic product. Even within countries, households can be very unevenly provided with energy because of high prices or lack of grid connection. Energy systems should also be safe, flexible and resilient in order to avoid blackouts that can have dire effects on mortality (shutdown of hospitals) or on the economy. The International Panel on Climate Change (IPCC) additionally reports that the climate change that scientists have been reporting on for decades - related to global warming, ocean acidification and biodiversity collapse - is due to human activities and more specifically to the emission of CO_2 or other greenhouse gases [4]. Indeed, a strong economical activity is correlated with a high energy consumption, and the world energy mix of today is mostly based on fossil fuels that are carbon intensive when being used (combustion to transform chemical energy into mechanical, thermal or electrical energy) [3].

Solar photovoltaics (PV) is an energy source that could address at least two of the aforementioned issues. The sun shines in every country of the globe, thus nearly removing the problem of resource distribution and allowing energy independence of countries (*energy equity*). Most of all, its working principle does not rely on fossil fuels and emits significantly less greenhouse gas per kWh of generated energy compared with conventional energy sources (on average, 48 gCO_2eq/kWh for solar PV versus 469 gCO_2eq/kWh for natural gas in 2011 [5]), which is relevant to tackle the problem of *environmental sustainability*.

In order to make this energy generation system relevant, it needs to be able to provide energy at a competitive cost. The average sales price in USD_{2018}/kWp has tremendously decreased during the last decade, and its learning rate is of 23.2 % per doubling of the cumulative PV module shipments [6] as shown in Figure A3.1a. This decrease is due to different factors such as the relocation of activities, a dedicated silicon wafer manufacturing industry and an increase in module efficiency. These additionally went along with a boom in annual worldwide installed capacity (as shown in Figure A3.1b) thus significantly

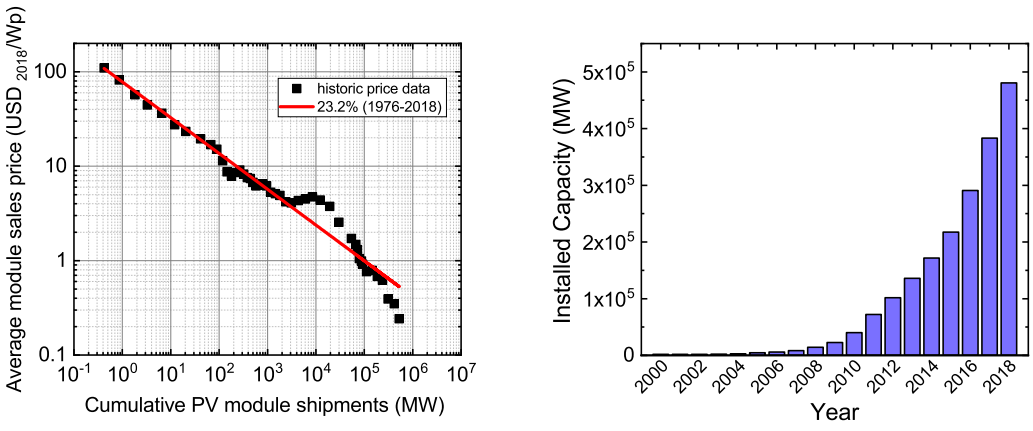

(a) (b)

Figure 1: (a) Learning curve of the module spot market prices as a function of the cumulative PV module shipments [6]. (b) Worldwide cumulative capacity of installed solar photovoltaic power in MWp from 2000 to 2018 [7].

decreasing marginal costs (economies of scale).

To assess the competitiveness of this technology, it is relevant to compare the levelized cost of electricity (LCOE) *i.e.* the production cost of one kWh of electricity, taking into account the investment cost, the lifetime of the system, the operating and maintenance costs, and the fuel. As of today, in Germany, PV production is soon to be or already cheaper than other conventional technologies like coal combustion power plants or combined cycle gas turbine (CCGT) (see Figure A3.2) [8].

Even though prices are low, the market penetration of solar energy remains marginal. Indeed, as can be seen in Figure A3.3a, the global energy production is still broadly dominated by fossil fuels (natural gas, coal and oil accounting for 81.3 % of the total), and the fraction of this energy produced by solar photovoltaics was around 0.27 % in 2018 (444 TWh or 38 Mtoe of production with respect to a total production of 13972 Mtoe) [3].

In order to foster this development, and particularly if the environmental policies stay unchanged (taxes on carbon emissions ...) it is necessary to keep decreasing prices. This would allow both (i) energy providers to invest more in PV, and (ii) governments to reduce the amount of subsidies, resulting in a lower pressure on taxpayers and a higher investment capacity in other important sectors (energy efficiency, electricity infrastructures, electrification, ...). As can be seen in Figure A3.3b, the cost of the module accounts for around 50 % of the final LCOE for utility scale PV, and even less than 10 % for residential PV, since soft costs and the balance of system are relatively high [9]. A solution for a significant decrease in LCOE is to make more efficient modules while keeping module fabrication and investment costs low. This allows to shrink all the contributions since more efficient devices mean more output power for the same soft costs (land acquisition, labor costs, etc.).

These arguments are also valid for the carbon intensity of the photovoltaic electricity: a higher efficiency of PV modules for the same amount of green-house gas emissions leads to less CO_2 emitted per kWh of electricity generated [10]. This feature will be of great importance in the future since, if a large amount of the global energy comes to be generated by PV plants, reducing the carbon intensity of this energy will be critical to reach the

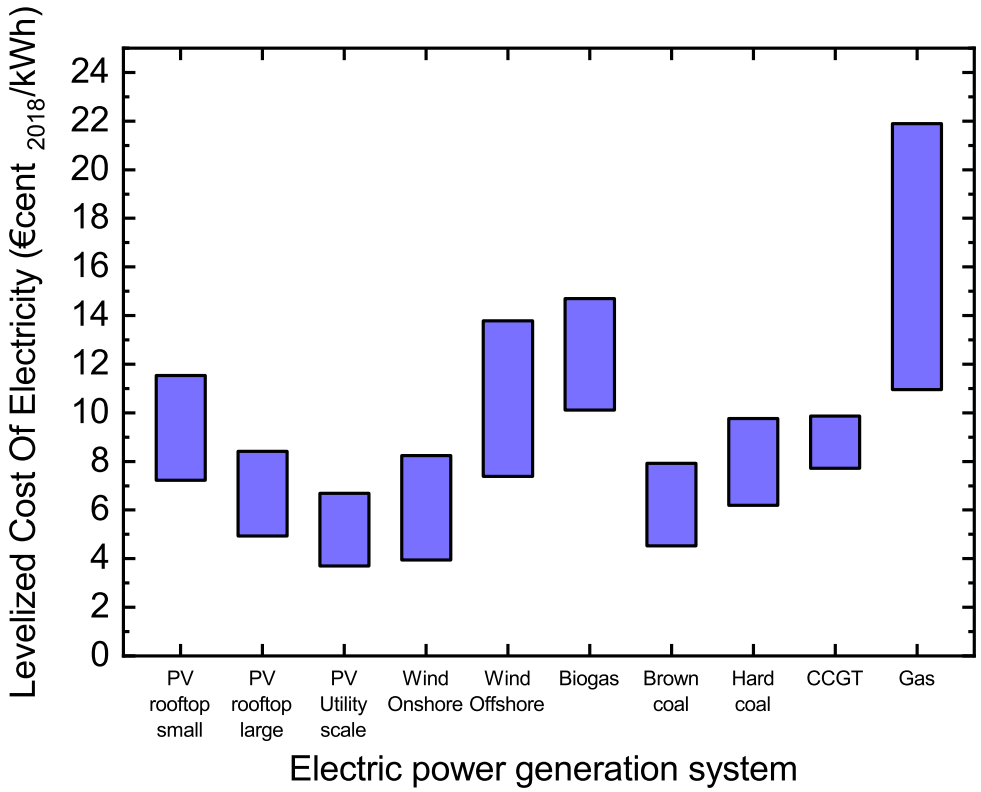

Figure 2: Levelized cost of electricity for different power generation technologies, in Germany in 2018 [8]. PV production is calculated with a Global Horizontal Irradiance between 950 and 1300 kWh.m^2.a^{-1}. The Full Load Hours ranges (in h/a) are taken as: 1800-3200 for Wind Onshore, 3200-4500 for Wind Offshore, 5000-7000 for Biogas, 6450-7450 for Brown coal, 5350-6350 for Hard coal, 3000-4000 for CCGT, and 500-2000 for Gas.

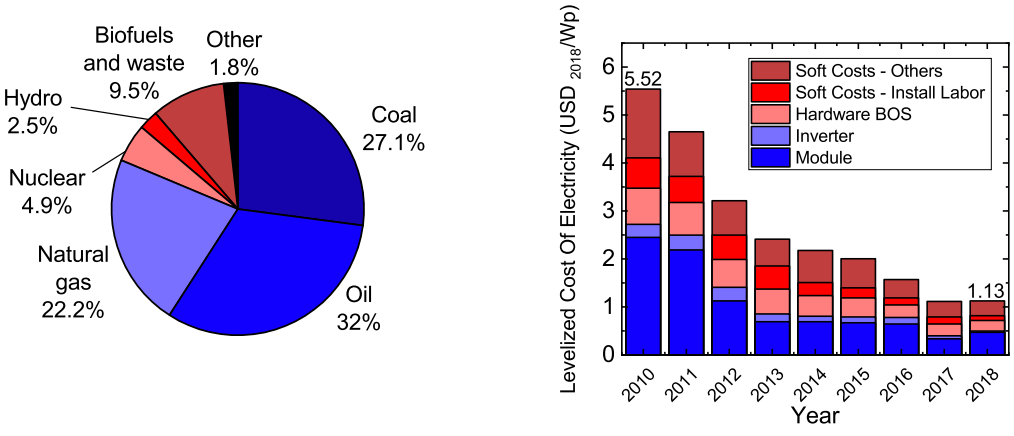

(a) (b)

Figure 3: (a) Share of energy resources in the global energy mix, 2017 [3]. (b) NREL LCOE (inflation adjusted) 2010-2018 for Utility-Scale PV with One-Axis Tracker (100 MW) [9].

carbon neutrality of the global economy.

Today, the photovoltaic industry is most widely based on the use of silicon as a semiconducting material. This kind of solar panel accounted for up to 95 % of the total photovoltaic market in 2018 [11] and is based on the use of slices of crystalline silicon, called wafers. The majority of the current solar cells are based on mono-crystalline silicon wafers which allow good device performances but are relatively expensive and rely on energy-intensive manufacturing processes. The device technology called PERC solar cells, which is the most widely manufactured solar cell architecture, relies on a simple fabrication process and has a high energy yield.

Reducing both the silicon wafer fabrication costs and CO_2 emissions is possible by using low-cost, high-quality *cast-mono silicon wafers* which fabrication process is less energy-intensive than the one of standard industrial mono-crystalline silicon wafers. Additionally, a very promising silicon solar cell technology to achieve the objectives of increasing the efficiency further while maintaining low manufacturing costs in the near future is the *passivated contact technology*. It allows to reach higher cell efficiencies by reducing electrical losses, and has the advantage of mostly using tools that are already present in the current industrial production lines. It is already being implemented in mass-production by some leading solar PV manufacturing companies [12]. Nonetheless, the standard fabrication process for this passivated contact solar cell architecture requires many steps, along with a high thermal budget due to long annealing processes at temperatures between 600 and 850 °C. That is why novel ways to manufacture this kind of solar cells need to be investigated, processes which would be less energy-intensive and require less manufacturing steps.

Purpose and structure of this work

This PhD thesis focuses on the investigation of a simplified passivating contact manufacturing process called fired passivated contact (FPC), which allows to have fewer processing steps and subject the solar cell to a low thermal budget. The major features studied are the passivation properties of the FPC stack, which account for the electrical losses in the device. *In situ* modulated photoluminescence characterizations are carried out, to achieve this goal: they allow to measure the evolution of the passivation properties in real time during a specific process step. Ultimately, these contacts are integrated on cast-mono wafers produced by Photowatt™, a French company which developed a technology called Crystal Advanced [13].

- Chapter 1 sets the background of this thesis, the working principle of a solar cell, and introduces the poly-Si passivating contact structure and its advantages along with a review of the paramount results from the literature. Further details on metallization and silicon wafer manufacturing are given in order to grant a more general understanding of the challenges of this work.

- Chapter 2 describes the development and optimization of the different layers of the FPC passivating stack. Advanced characterization techniques are used for a thorough understanding of the evolution of the materials properties during the fabrication process.

- Chapter 3 describes an *in situ* modulated photoluminescence acquisition setup, that allows to measure in real time the effective minority carrier lifetime of a sample.

A case study of the evolution of the passivation properties of an aluminum oxide passivated sample is performed using this tool.

- Chapter 4 focuses on the use of this *in situ* modulated photoluminescence technique to study FPC samples. The evolution of the passivation properties during different process steps (annealing, plasma processes, and layer deposition) of the passivating contacts fabrication is investigated.

- Chapter 5 studies the transfer of the optimized FPC process on industrial-size wafers. Both Czochralski and cast-mono silicon wafers are investigated in this section. The importance of the surface morphology for FPC samples is discussed. The electrical properties of a first device are finally presented.

A summary of these results and a general conclusion of the work performed during this PhD thesis are proposed. Ways of improvement of the solar cell architecture and of the fabrication process are discussed to put this work in perspective.

Chapter 1

Context, background and objectives

In order to know how to improve PV devices and its market penetration, it is worth understanding how a solar cell works, what are the current architectures that can be found on the market, and how to make them more efficient while keeping the fabrication costs low.

Contents

1.1 Basic concepts of solar cells

We first describe the theoretical framework to understand the physics behind the energy conversion in a solar cell. This allows us to introduce intrinsic limitations of standard solar cells, and the main features that we are interested in at the device level. A more thorough description of the physics of solar cells can be found in the book of Wurfel and Wurfel [14].

1.1.1 Working principle of a solar cell

A solar cell is an opto-electronic device, which purpose is to convert solar (electromagnetic) radiations into electricity. It is based on semiconductor materials that are characterized by energy bands corresponding to available states for electrons in the matter. These available states are linked to different electron energy values. The Pauli principle stipulates that two electrons cannot be in the same quantum state, meaning that each energy level can be occupied by at most two electrons (spin multiplicity). This principle implies that an electron cannot "move" to an already occupied state. The aforementioned energy bands are quasi-continua of quantum states, that are separated by energy *gaps*: ranges of energy in which no state is available. As a consequence, no electron can have energy values in the band-gaps of the material (see Figure 1.1 for illustration).

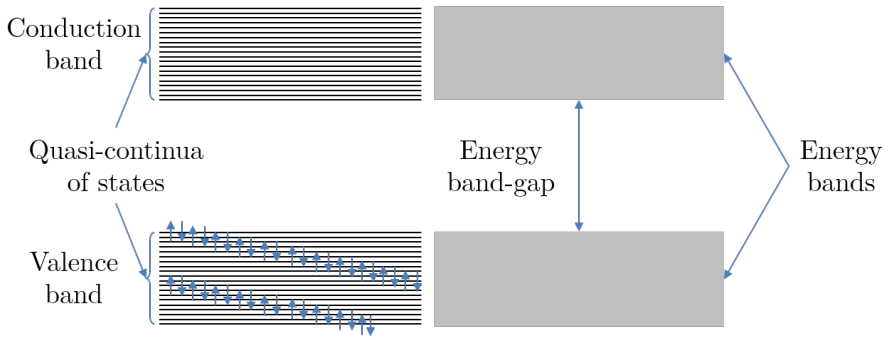

Figure 1.1: Scheme of the energy bands of a semi-conductor. Horizontal black lines are quantum states that can be filled by at most 2 electrons (arrows up and down accounting for 2 electron spin values). They form quasi-continua represented by energy bands, separated by a band-gap in which no available quantum state exists.

At a temperature of $T = 0$ K, a semiconductor material has a given number of energy bands completely filled with electrons, up to the highest occupied band called *valence band*. The next energy band, the unoccupied band of lowest energy, is called the *conduction band*. The energy difference between the bottom of the conduction band and the top of the valence band is called the *gap* of such a material and is a very important characteristic of the semiconductor as will be seen in the next sections.

Absorption

These materials have the ability to absorb light thanks to the interaction between a photon and an electron. During such a process, the photon is annihilated and the electron "gains" the energy of the photon. This interaction can only happen if there is an available state that can host the electron of higher energy (excited electron). For a given incident light

intensity I_0 at the surface, the absorption profile in the material is usually described by a Beer-Lambert law:

$$I(z,\lambda) = (1 - R_f) I_0 e^{-\alpha(\lambda) z} \tag{1.1}$$

where I is the light intensity (in W.m^{-2}) for a given wavelength λ at a given depth in the material z, R_f the reflectivity of the front surface and α the absorption coefficient which depends on the wavelength. Absorbed photons excite electrons that "jump" in the conduction band, each one leaving a *hole* in the valence band, which acts as a positive free charge. Both electrons and holes can contribute to the current and are called *charge carriers*. Electron-hole pairs are generated at a rate called *generation rate* G (in cm^{-3}.s^{-1}) that can be expressed as:

$$G(z,\lambda) = (1 - R_f) Q_e \alpha(\lambda) \frac{I_0 \lambda}{hc} e^{-\alpha(\lambda) z} \tag{1.2}$$

where Q_e is the average number of electron-hole pairs generated by one photon, h is Planck's constant and c the velocity of light in vacuum. As will be seen in the following section, photogenerated electron-hole pairs must be separated, and the charge carriers collected by different metallic contacts (see Figure 1.2) in order to extract energy.

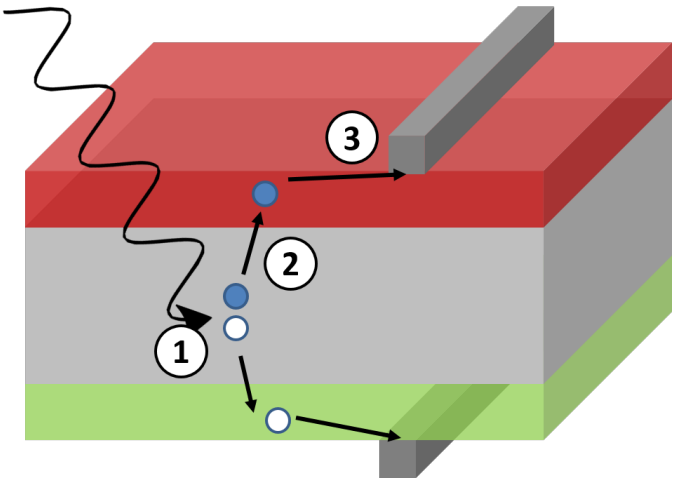

Figure 1.2: Scheme of the working principle of a solar cell. The blue circle represents an electron and the white circle a hole. ① A photon of energy greater than the band-gap is absorbed and creates an electron-hole pair. ② The charge carriers are separated (drift-diffusion). ③ They are extracted at the metallic contacts. The grey layer is the absorber layer, the red one the electron transport layer and the green one the hole transport layer.

Charge separation

We have seen that electron-hole pairs can be generated in a semiconductor material like bare silicon. But we cannot extract energy from a raw piece of semiconductor: both voltage and current are needed. Since an electron-hole pair is neutral, charges need to be separated in order for a non-null electrical current to be extracted. If the semiconductor is homogeneous (no gradient of band-gap and electron affinity), two main phenomena govern the motion of charges in the semi-conductor material: drift and diffusion.

Drift is the action of an electric field E (in V.cm^{-1}) on an electrically charged body. If such an electric field exists in some part of the solar cell and is the only driving force, then it induces a drift current density which can be expressed as:

$$J_{n,drift} = qn\mu_n E = \sigma_n E = -\frac{\sigma_n}{q}\nabla\left(q\varphi\right) \tag{1.3a}$$

$$J_{p,drift} = qp\mu_p E = \sigma_p E = \frac{\sigma_p}{q}\nabla\left(q\varphi\right) \tag{1.3b}$$

where $J_{n,drift}$ and $J_{p,drift}$ are drift current densities for respectively electrons and holes (in A.cm^{-2}), $q = 1.62\times10^{-19}$ C is the elementary charge, n and p the (free) electron and hole densities (in cm^{-3}) and μ_n and μ_p the electron and hole mobilities (in cm^2.V^{-1}.s^{-1}). $\sigma_n = nq\mu_n$ and $\sigma_p = pq\mu_p$ are the electron and hole conductivities and φ the electric potential. The electric force acting on the particles is thus $-\nabla\left(q\varphi\right)$ for electrons and $+\nabla\left(q\varphi\right)$ for holes.

Diffusion results from nonuniformities in the charge carrier concentration. According to Fick's law, charge carriers diffuse from regions of high concentration (or high chemical potential) towards regions of low concentration. Consequently, if no electric field exists in the material, the diffusion current densities are given by:

$$J_{n,diff} = qD_n\nabla n = -\frac{\sigma_n}{q}\nabla\phi_n \tag{1.4a}$$

$$J_{p,diff} = -qD_p\nabla p = -\frac{\sigma_p}{q}\nabla\phi_p \tag{1.4b}$$

Where $J_{n,diff}$ and $J_{p,diff}$ are diffusion current densities of respectively electrons and holes (in A.cm^{-2}) and D_n and D_p the diffusion coefficients of electrons and holes with $D_{n/p} = \mu_{n/p}kT/q$. Here $\phi_n = kT\ln\left(\frac{n}{N_C}\right)$ is the chemical potential of electrons with N_C the effective density of states of electrons in the conduction band. Equivalently, $\phi_p = kT\ln\left(\frac{p}{N_V}\right)$ is the chemical potential of holes, with N_V the effective density of states of holes in the valence band. The driving force is thus $-\nabla\phi$.

If both these phenomena apply, the resulting force is $-\nabla\left(\phi_{n/p} \mp q\varphi\right) = -\nabla\eta_{n/p}$ with $\nabla\eta_{n/p}$ the electro-chemical potential of electrons or holes. The probability of occupation of an energy state being described by a Fermi-Dirac distribution, the electro-chemical potential values can be identified as the quasi-Fermi levels of electron and holes: $\eta_n = \varepsilon_{Fn}$ and $\eta_p = -\varepsilon_{Fp}$. These are the energy values of virtual states that have a probability of 50 % to be occupied by an electron (for $\eta_n = \varepsilon_{Fn}$) or by a hole (for $\eta_p = -\varepsilon_{Fp}$). This leads to the expressions of the real charge current densities:

$$J_n = \frac{\sigma_n}{q}\nabla\varepsilon_{Fn} \tag{1.5a}$$

$$J_p = \frac{\sigma_p}{q}\nabla\varepsilon_{Fp} \tag{1.5b}$$

An asymmetry in the solar cell electro-chemical properties results in the separation of the charge carriers, and may allow their collection in electrical contacts. Under thermodynamic equilibrium, $\varepsilon_{Fn} = \varepsilon_{Fp}$. Under illumination, these quasi-Fermi levels split, and their difference corresponds to the chemical energy produced, which is the maximum

energy that can be extracted from an electron-hole pair. This value is called implied open-circuit voltage $iV_{oc} = \varepsilon_{Fn} - \varepsilon_{Fp}$. Creating an asymmetric gradient of quasi-Fermi levels is difficult under no bias-voltage. As a consequence, the easiest way to separate charge carriers is to tune their conductivity close to metallic contacts, in order to selectively direct electrons and holes towards separated electrodes. A thorough description of the physics of solar cells can be found in the book "Physics of Solar Cells: From Basic Principles to Advanced Concepts" by P. and U. Wurfel [14], [15].

At the device level, the output power will result from the flow of charge carriers collected (current) and the amount of usable energy that each one of them carries (voltage).

1.1.2 Characteristics of a solar cell

A solar cell in the dark acts electrically as a diode, and additionally generates current under illumination (electron-hole pair generation, separation and extraction). As shown in the equivalent electrical circuit of Figure 1.3, it also comes with parasitic resistances: series resistance R_s (contact resistance, finite conductivity of the layers, ...) and parallel resistance R_p (shunt currents, leaky layers, ...). In order for the device to be efficient, R_s needs to be minimized and R_p maximized.

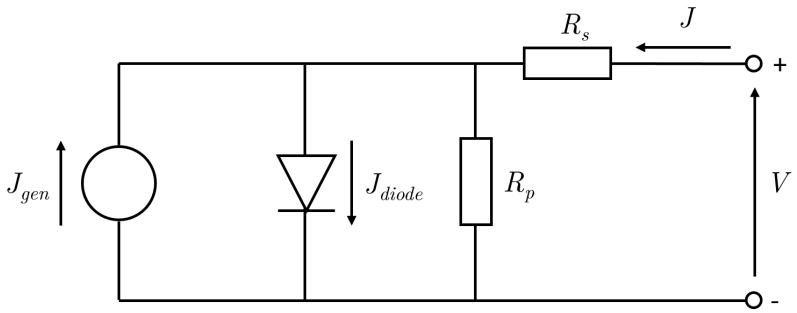

Figure 1.3: Equivalent electrical circuit of a solar cell, one-diode model.

The $J(V)$ characteristic follows the equation:

$$J(V) = J_0 \left[\exp\left(\frac{q\,(V - AJR_s)}{kT} \right) - 1 \right] + \frac{V - AJR_s}{AR_p} - J_{gen} \tag{1.6}$$

with J_0 the saturation current density, A the area of the solar cell, and J_{gen} the photo-generated current density. From Figure 1.4, which represents the $J(V)$ characteristic of such a device, we can identify three characteristic parameters: the open circuit voltage V_{oc} (at which $J = 0$), the short circuit current density J_{sc} (at $V = 0$) and the maximum power point (at which $\partial P/\partial V = 0$). We may introduce an additional feature called Fill-Factor FF defined as:

$$FF = \frac{P_{mpp}}{J_{sc}V_{oc}} \tag{1.7}$$

From FF, J_{sc} and V_{oc} can be extracted the power conversion efficiency (PCE) η at a given incident radiative power density P_{inc}:

$$\eta = \frac{FFJ_{sc}V_{oc}}{P_{inc}} \tag{1.8}$$

In the photovoltaic industry, these characteristics are measured under standard test conditions: 25 °C and an illumination of the AM1.5 solar spectrum (see Figure 1.6 further down) corresponding to a power density of 1000 W.m^{-2}.

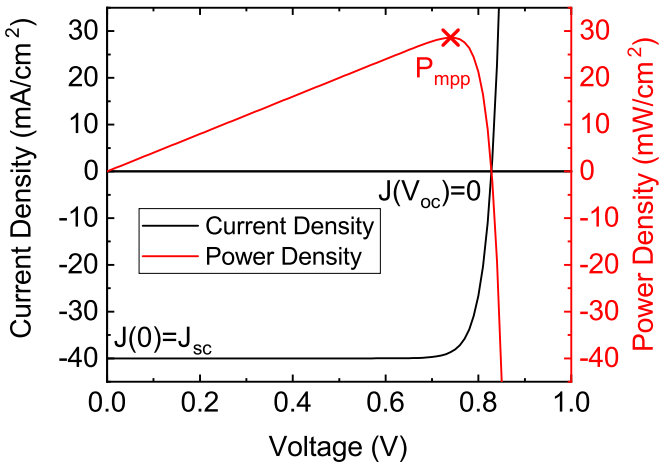

Figure 1.4: Example of evolution of the current density and output power density with applied voltage. J_{sc} is the short circuit current density, V_{oc} the open circuit voltage, and P_{mpp} the output power density at maximum power point.

1.1.3 Limits of conversion efficiency

All the radiative power incident on the solar cell cannot be converted to electricity. The study of an ideal solar cell allows to determine a maximum PCE for a standard device. Some additional limitations come from the device fabrication. We need to understand what these are, and how to reduce them.

Shockley-Queisser maximum efficiency limit

This thesis focuses on single junction solar cells, involving only one absorbing semiconductor material: crystalline silicon (c-Si). Single junction solar cells have a maximum theoretical efficiency of 33 % which is called the limit of Shockley-Queisser [16]. Ideality hypotheses have been made in order to determine this theoretical limit: (1) the incident light comes from the sun modeled as a black body of temperature 6000 K, (2) the incident light is fully absorbed and produces one electron-hole pair per photon, (3) the only recombination losses are due to radiative recombinations (see next section 1.1.3) which means that a perfect contact and an ideal transport of charge carriers in the solar cell are assumed. This limit of 33 % results from two main phenomena: incomplete absorption of the solar spectrum and thermalisation losses.

Incomplete absorption of the solar spectrum: as mentioned in section 1.1.1, photon-electron interactions can only occur if there is an unoccupied state that can host the excited electron. For photon energies higher than the band gap, photons can be absorbed and electrons excited because the electrons with energies close to the maximum of the valence band will find available states at the bottom of the conduction band. However, a photon with an energy lower than the energy band gap will not be absorbed, because there is no available state within the band gap: the low-energy range of the solar spectrum cannot be harnessed (see Figure 1.5a). Consequently, the smaller the band gap, the more electron-hole pairs can be generated and collected, so the larger the extracted current. This feature mainly impacts J_{sc}.

Thermalization losses: when a photon is absorbed, an electron is excited in the con-

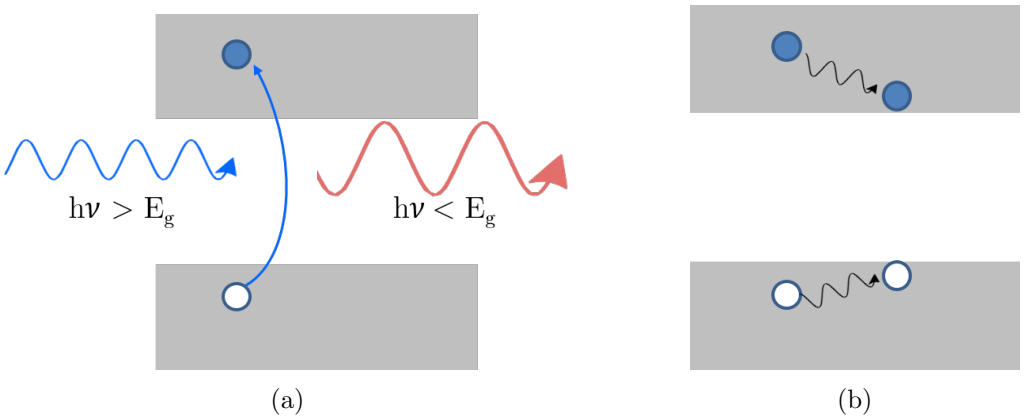

Figure 1.5: (a) Schematic of incomplete absorption of the solar spectrum: the red photon (energy lower than band-gap) is not absorbed, while the blue photon is (energy larger than the band-gap). (b) Thermalization loss of the excited electron and hole.

duction band and it may have an energy significantly higher than the bottom of the conduction band (excess energy brought by the photon). This means there is a large amount of available states of lower energy, from this excited state to the bottom of the conduction band. The excess energy is thus lost extremely rapidly (within a few picoseconds) through electron-optical phonons interaction, and then electron-phonon scattering [17]: this is called the "relaxation" process or "thermalization" because energy is lost under the form of heat. It is represented in Figure 1.5b. This implies that the larger the band gap, the lower the thermalization losses, and the larger the output voltage (and open circuit voltage V_{OC}).

Figure 1.6 shows the impact of these two main loss mechanisms with respect to the solar spectrum. There is a competition between the two aforementioned phenomena. Therefore an optimum value of energy band gap exists in order to maximize the output power. These losses - along with other thermodynamic limitations - lead to the well-known Shockley-Queisser maximum efficiency of 33 % for a semiconductor with a energy bandgap of 1.25 eV [16]. This theoretical limit is obtained for an ideal device.

However, other so-called "intrinsic" losses (such as Auger recombinations, see in the following section) cannot be avoided. A new calculation of the maximum theoretical efficiency of crystalline silicon solar cells was carried out in 2013 by Richter *et al.*, taking these into account along with bandgap narrowing phenomena and updating several parameters. This lead to an estimation of a maximum theoretical efficiency of 29.4 % [19]. Furthermore, it is not possible to effectively reach this theoretical limit because additional losses occur in the solar cell, due to some non-ideality of the device (resistive losses, incomplete absorption, losses inside the silicon wafer, ...). As of today, Yoshikawa *et al.* showed that the practical limit of silicon solar cell manufacturing is 27.1 % [20].

Other losses: focus on recombinations

There are three main origins of parasitic losses: optical, resistive and recombination losses. *Optical losses* may be due to the incomplete absorption of the solar spectrum because of reflection (surface reflectivity, or reflection by front metallic contacts), or to parasitic absorption within other layer than the main absorber (passivation, transport layers or metallic contacts). These may be reduced by adding anti-reflection layers, or putting all contacts at the rear side (interdigitated back contact (IBC)). *Resistive losses* result from

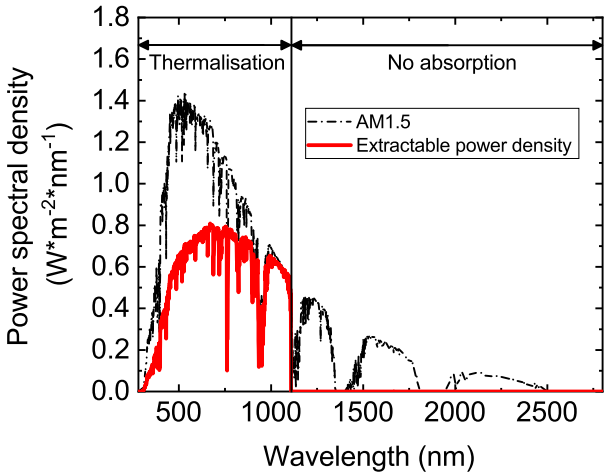

Figure 1.6: AM1.5 power spectral density (black line) compared with maximum power spectral density extractable from a single junction solar cell (1.12 eV semiconductor band gap) after thermalisation and partial absorption (red line). Adapted from [18].

Joule effect in metallic contacts or parasitic resistances within the cell structure. These may be reduced for example by using half-cells, that decrease the total current that must be extracted by metallic fingers. *Recombination losses* are the result of photo-generated electron-hole pairs not being successfully extracted: the charge carriers recombine. The recombination mechanisms may be of three different kinds: radiative, Auger, trap assisted (through bulk or surface defects). These three types of recombinations are schematically represented in Figure 1.7.

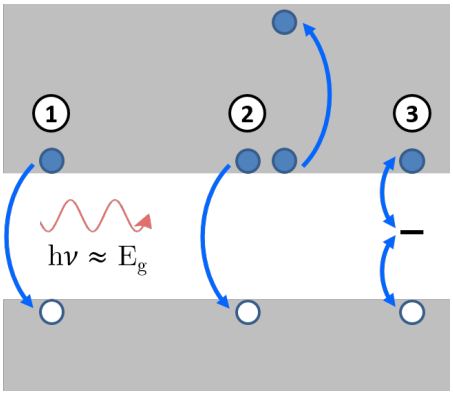

Figure 1.7: Schematic representation of recombination mechanisms: ① radiative, ② Auger, and ③ SRH recombinations.

Radiative recombination: the excited electron falls back in the valence band and recombines with a hole. This transition emits a photon with an energy approximately equal to the energy band gap. The recombination rate associated with this type of recombination R_{rad} can be put under the form of a simple two-body mechanism: a product of the electron density in the conduction band n and of the hole density in the valence band p [21]:

$$R_{rad} = B_{rad} np \tag{1.9}$$

where B_{rad} is the radiative recombination coefficient. This is an intrinsic phenomenon that may be exploited through photoluminescence measurements.

Auger recombination: as for the radiative recombination, an excited electron recombines with a hole of the valence band, but the energy is, this time, transferred to a third charge carrier (electron or hole). Since the mechanism requires an additional hole or electron compared with radiative recombination, the Auger recombination rate can be put under the form [14]:

$$R_{Aug} = np\left(C_{A,n}n + C_{A,p}p\right) \tag{1.10}$$

with $C_{A,n}$ and $C_{A,p}$ the Auger recombination coefficients. This is followed by the thermalization of the newly excited charge carrier. One way to reduce this kind of recombination is to avoid high doping concentrations (because R_{Aug} increases with doping concentration for a constant np product). It is worth noting that in crystalline silicon, this kind of recombination is favored compared with radiative recombination because of the indirect bandgap of this semiconductor which hinders radiative recombinations and conversely increases the concentration of charge carriers in the material.

Shockley-Read-Hall (SRH) recombination: this kind of recombination is a defect assisted recombination mechanism. A defect (either in the bulk of the semiconductor or at its surface) may create a state within the band gap of the semiconductor. Such a state can easily trap a charge carrier because of the reduced energy difference between the bands where lie the charge carriers and the energy level of the trap state. This leads to trapping and detrapping mechanisms. The recombination rate associated to a type of trap of density N_t and of energy level in the band gap E_t is given by [22]:

$$R_{SRH} = \frac{C_n C_p N_t \left(np - n_i^2\right)}{C_n\left(n + n_1\right) + C_p\left(p + p_1\right)} \tag{1.11}$$

with C_n and C_p the capture coefficients for electron and holes respectively, n_i the electron density in an intrinsic specimen, $n_1 = n_i \exp\left(\frac{E_t - E_i}{kT}\right)$ and $p_1 = n_i \exp\left(-\frac{E_t - E_i}{kT}\right)$ (here E_i is the Fermi level for an intrinsic specimen in the dark, T is the temperature and k Boltzmann's constant). This last type of recombination is called extrinsic loss: it is possible to improve the material quality and the architecture of the device in order to limit its detrimental effect.

Passivation

Shockley-Read-Hall recombinations mostly depend on N_t, the density of trap states, on the energy position of the defect within the band gap E_t, and on the charge carrier densities n and p. It is possible to inhibit this phenomenon by using passivation strategies, that prevent recombinations from happening.

Chemical passivation consists in reducing the density of defects in the semiconductor device. In silicon, defect states may be due to crystallographic defects or impurities. Metallic impurities can result from the fabrication process of the silicon ingot (Fe, Al, Cu, Sb, etc.) or from surface pollution (organic molecules, etc.). Their density can be decreased thanks to a higher purification during the wafer processing (see section 1.4) or by cleaning the surface right before the solar cell fabrication. In a silicon wafer, crystallographic defects may exist inside the bulk, through dislocations or grain boundaries. The surface of the silicon wafer also acts as a crystallographic defect. These chemically correspond to silicon atoms with at least one chemical bond being non satisfied: *dangling bonds*. These dangling bonds create a mid-gap defect state, that is a very efficient recombination

center. In order to decrease their density, it is necessary to fill these dangling bonds either in the bulk through a better crystallization (formation of Si-Si bonds) or through a *hydrogenation process* that allows to form Si-H bonds which energy level no longer lies in the band gap. Hydrogen atoms are very light and mobile, and are consequently very efficient to fill dangling bonds. This hydrogenation can be achieved by forming gas annealing (FGA), deposition of a hydrogen rich silicon layer and annealing to drive-in H atoms, or through hydrogen plasma processes. Passivation of the dangling bonds at the surface of the silicon wafer may be filled by depositing or growing dielectric layers such as hydrogenated amorphous silicon nitride (a-SiN_x:H), aluminum oxide (AlO_x), silicon oxide (SiO_x) or depositing hydrogenated amorphous silicon (a-Si:H). The hydrogen content of these layers can be increased in order to get a better surface passivation (formation of Si-H bonds).

Field-effect passivation can also reduce SRH recombinations by repelling one of the carriers from the recombination centers thanks to an electric field. This can be achieved thanks to fixed charges naturally existing inside some passivation layers (negative fixed charges in AlO_x or positive fixed charges in a-SiN_x:H), or by corona charge (depositing charges at an interface). By pushing one of the types of charge carriers away from the traps, a low recombination rate can be achieved despite a large density of interface defects. The reader is invited to consult the thorough review of Aberle [23] on passivation for silicon solar cells for a more detailed description.

Managing to passivate the defects in the bulk or at the surface allows to reduce electrical losses and is the central subject of this thesis. Different approaches can be used to do so in solar cells. The following section describes the evolution of the passivation strategies in the history of silicon solar cells manufacturing.

1.1.4 Homojunction solar cells

The most common kind of solar cells are called homojunction solar cells and rely on a p-n junction - which allows to separate charge carriers - and on a direct contact between the metal and the absorber layer.

Working principle: the p-n junction

Semiconductor materials can be tuned in order to increase the amount of one type of free charge carrier. This tuning is called *doping*. An n- respectively p-doped semiconductor is a material in which impurities have been introduced on purpose: these add available energy levels close to the energy bands. This can respectively add either electrons in the conduction band (introduction of donor atoms, often phosphorous in silicon), or holes in the valence band (acceptor atoms, often boron in silicon). For a p-type semiconductor, electrons are called "minority carriers" and holes "majority carriers" (and *vice versa* for n-type semiconductors). Because of the electrical neutrality of the bulk, this implies that:

$$N_A^- + n = N_D^+ + p \tag{1.12}$$

where N_A^- is the density of ionized acceptor atoms and N_D^+ the density of ionized donor atoms. At ambient temperature, all substitutional doping atoms are ionized, and $N_D^+ = N_D$ or $N_A^- = N_A$. Given that the product $np = n_i^2 = 1{\times}10^{20}$ cm^{-3} is constant under thermal equilibrium at ambient temperature, a typical doping level of $n = N_D = 1{\times}10^{16}$ cm^{-3} in n-type c-Si leads to a hole concentration of $3{\times}10^4$ cm^{-3}. This results in a strong difference of conductivity between electrons and holes due to the difference in carrier concentration.

Standard solar cells are based on the p-n junction. A homojunction p-n device is a junction between an electron rich and a hole rich layer of the same material. This creates a spatial asymmetry in electron and hole conductivity through a large difference in concentration ($\sigma_x = xq\mu_x$ for $x = n$ or p). Under such conditions, the separation of electron and holes is possible (see section 1.1.1). Then the metallic contacts remain to be made, in order to extract the current and fuel an electrical circuit. Standard homojunction solar cells form a direct contact between the metallic fingers - that extract the current - and the materials of the p-n junction.

Common architectures and limitations

One intrinsic limitation of p-n homojunctions is the following: in the dark the difference of conductivity is significant, however under illumination the increase of minority carrier conductivity is way larger than the one of majority carriers. This results in a small flow of holes towards the electron contact and vice versa, thus reducing J_{sc} and V_{oc} [15] because of recombinations at the contact. This must be avoided, and can be done by passivating the different contacts.

The historical architecture of industrial solar cells is the aluminum back-surface field (Al-BSF) structure (see Figure 1.8a), because of its simple fabrication process and low manufacturing cost. The process flow for Al-BSF manufacturing is shown in Figure 1.8b. The silicon wafer is first textured (KOH + additives) for anti-reflection purposes. Then it undergoes a phosphorous diffusion: a liquid precursor ($POCl_3$) forms a phosphorous rich oxide (phospho-silicate glass (PSG)) at the surface of the wafer, and a 30 min-long annealing around 900 °C allows phosphorous to diffuse inside the silicon wafer. The rear side is etched and the PSG removed. The passivation and anti-reflection coating (ARC) of the front side follows, by the deposition of a SiO_x/a-SiN_x:H stack by plasma-enhanced chemical vapor deposition (PECVD) (see section 2.1.1). Finally, a front side silver grid and a rear side full-area aluminum contact are screen printed, and undergo a co-firing step (a few seconds at 850 °C). The firing allows the alloying of the Al-Si rear side that provides a good contact and induces a field effect, along with the penetration of silver through the front a-SiN_x:H dielectric layer to establish the electrical contact. The phosphorous diffusion allows to form the p-n junction with the p-doped silicon wafer, and to achieve an ohmic contact between the phosphorous-doped c-Si emitter and the front silver grid. The SiO_x/a-SiN_x:H provides both chemical passivation (formation of Si-O and Si-H bonds) and field-effect passivation (high positive fixed charge density in a-SiN_x:H). Despite the simplicity of the process, this structure has a few drawbacks: it has a poor red response due to strong light absorption by free carriers at the Al-Si interface, and the large metallized area leads to high recombination losses and high J_0 values (corresponding to a recombination current). Maximum efficiencies of 20 % could be reached with such a structure [6].

A way to improve this architecture is to decrease the metallized area by passivating a large fraction of the rear side: this leads to the passivated emitter and rear contact (PERC) structure (on Figure 1.9a). The process flow for PERC solar cell fabrication is shown in Figure 1.9b. The front side is the same as the Al-BSF structure but, before screen printing, the rear side is passivated by an AlO_x/a-SiN_x:H stack. This is followed by Laser Contact Opening and screen printing of the metallic paste. Various adaptations of this architecture have been proposed in order to obtain further improvements (with and without local diffusion of Al at the Al-Si interface, grid metallization or point contacts etc.). This kind of structure is expected to reach maximum efficiencies of 23.5 % for p-type

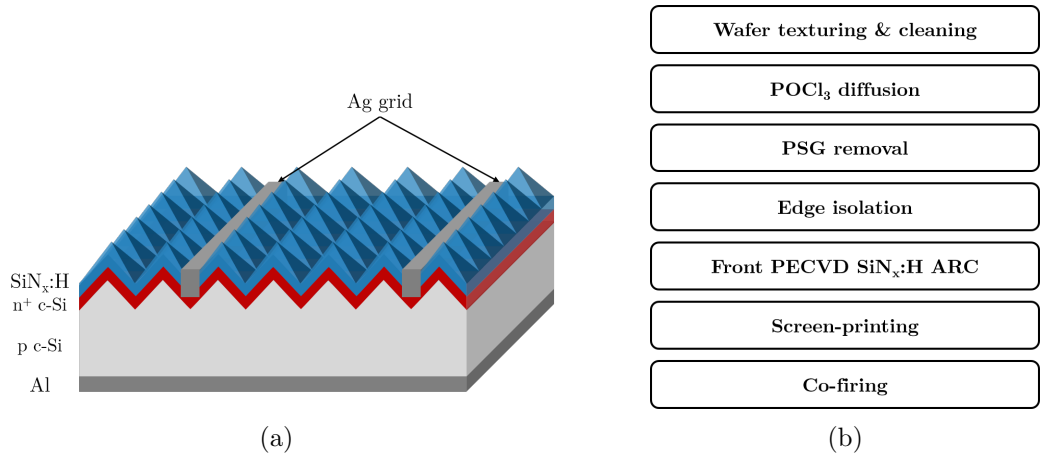

Figure 1.8: (a) Architecture and (b) process-flow for the fabrication of Al-BSF solar cells.

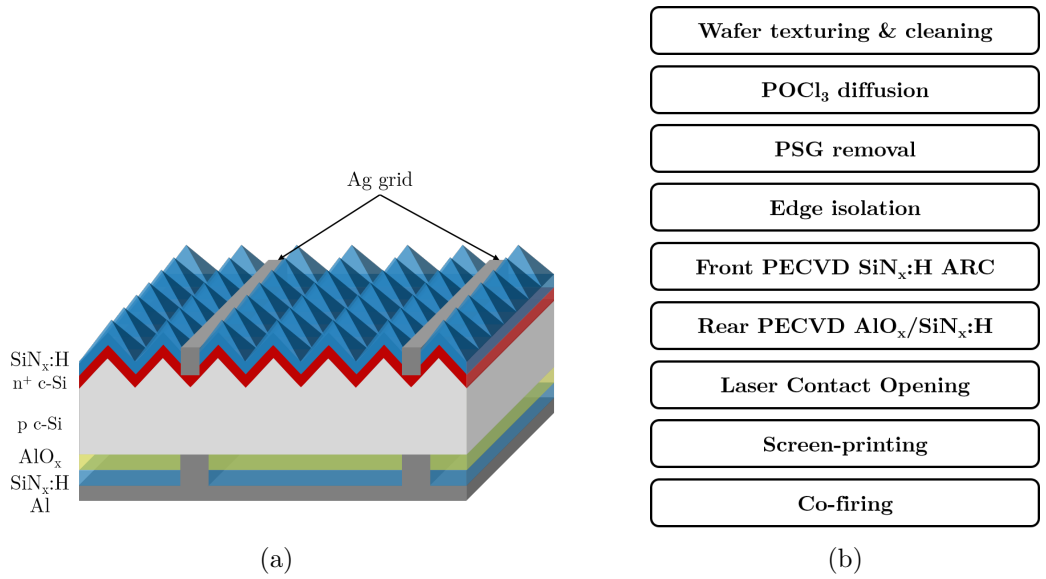

Figure 1.9: (a) Architecture and (b) process-flow for the fabrication of PERC solar cells.

c-Si substrates and 24.1 % for n-type c-Si [6].

In order to further improve the performances of c-Si based solar cells, the main source of losses may be completely removed: the metal-semiconductor interface.

1.2 Passivating contacts: toward higher efficiency

1.2.1 Working principle

It has been mentioned in section 1.1.4 that the direct metal/absorber interface is a source of significant recombination losses due to a high defect density at that interface (Metal-Induced Gap States, dangling bonds, impurities, etc.) [24]. Passivating contact architectures allow to remove this interface by adding a thin insulating layer (most often intrinsic a-Si:H or SiO_x) between the metallic contact and the c-Si absorber. This provides surface (chemical) passivation of the wafer, which limits recombination losses. It also acts as a potential barrier [25]. Then, an extraction layer is added in order to selectively transport

one of the two types of charge carriers to the metallic contact while blocking the other one, which is necessary in order to achieve the carrier selectivity (see section 1.1.1) and keep a low contact resistivity. This structure prevents Fermi level pinning and the formation of a Schottky-barrier at the metal/semi-conductor interface and allows to significantly reduce the total J_0 [26].

1.2.2 Heterojunction technology and limitations

The architecture that allowed to reach the highest power conversion efficiency is the heterojunction with intrinsic thin layer (HIT) solar cell [27]. It relies on junctions between two different materials: c-Si and a-Si:H. The passivated contact is a stack of thin (≈ 5-10 nm) (i) a-Si:H/doped a-Si:H (≈ 10-20 nm)/transparent conductive oxide (TCO) layer such as indium-doped tin oxide (ITO) and a low temperature screen printed silver grid (see Figure 1.10a). a high passivation is achieved thanks to the intrinsic a-Si:H layer which provides a lot of atomic hydrogen that binds to silicon dangling bonds. This hetero-structure also induces a strong inversion layer at the hetero-interface, which favors the tunneling of charge carriers through the potential barrier (see Figure 1.10b). Such a structure, along with an IBC architecture lead to the record high efficiency for a single junction solar cell: 26.7 % [20].

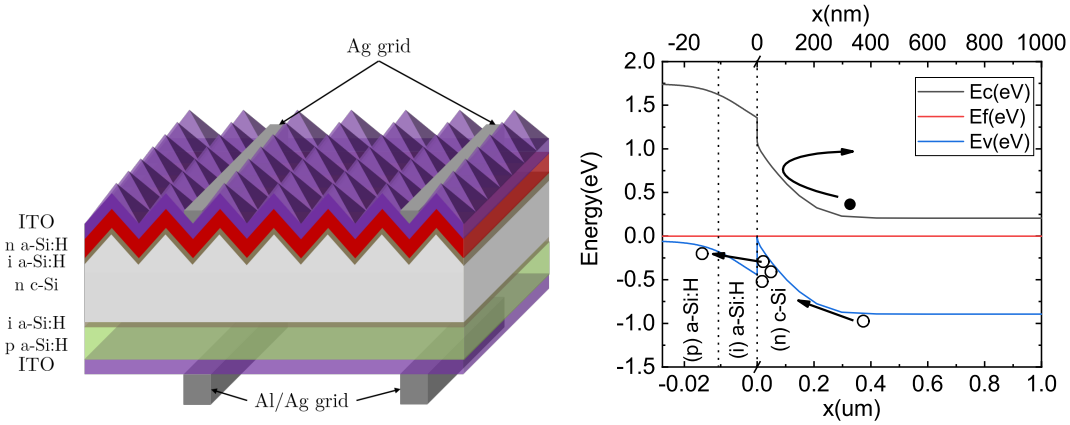

(a) (b)

Figure 1.10: (a) Architecture of a bifacial HIT solar cell and (b) its energy band diagram in the dark near the rear p-i-n hetero-interface - calculated with SCAPS software. White and black circles represent respectively holes and electrons, and the arrows the directions of the current densities.

However, HIT solar cells have a poor blue response due to the strong parasitic absorption in this spectral range of a-Si:H, and especially of (p) a-Si:H. This is why the emitter is placed at the rear side of the solar cell. However this inverted structure requires high-lifetime silicon wafers since most of the charge carriers are photogenerated at the front side of the solar cell (see equation 1.2) [28]: the minority carriers (holes) need to travel through the wafer all the way to the rear side of the solar cell to be collected. a-Si:H passivation also degrades at temperatures higher than 300 °C and its conductivity is rather low due to a poor doping efficiency. This results in the necessity of using a TCO that is expensive (and often contains indium, a scarce material) and low temperature screen printing metallic pastes (not yet an industrial standard).

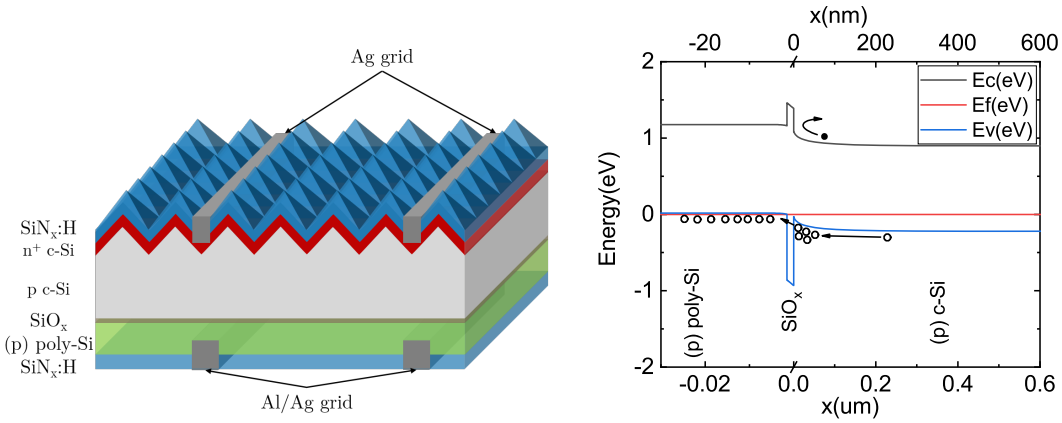

(a) (b)

Figure 1.11: (a) Architecture of p-type bifacial TOPCon solar cells and (b) its Energy Band Diagram in the dark near the hole-selective contact (adapted from [34], [39]) - calculated with SCAPS software. White and black circles represent respectively holes and electrons, and the arrows the directions of current densities.

1.2.3 Tunnel oxide passivating contacts

In order to maintain these good passivation properties while tackling the issues of high-temperature degradation and high parasitic absorption, a mainstream structure is currently being extensively studied: TOPCon solar cells.

Main architecture

tunnel oxide passivated contact (TOPCon) solar cells [29]–[31] use a stack of oxide and doped poly-Si on which the contact is taken (see Figure 1.11a). These structures are resistant to high temperature processes and the crystallization of the silicon layer allows to decrease the parasitic absorption losses due to a-Si:H [32]. The tunnel oxide layer reduces the interface defect density (chemical passivation) while allowing one type of carrier to reach the contact by quantum tunneling or diffusion through pinholes in the oxide [33]–[38]. The energy band diagram of such a contact is shown in Figure 1.11b.

Different structures and state of the art

The SiO_x/poly-Si passivated contacts were first implemented in bipolar junction transistors allowing a significant reduction of the recombination losses [40]. It was later adapted to solar cells for the first time in the 1980's under the semi-insulating poly-crystalline silicon (SIPOS) denomination [41], [42]. An open circuit voltage of 720 mV was achieved (for a 2.5 nm-thick oxide layer and 100 nm of n^+ poly-SiO_x) but lead to low efficiencies due to a high series resistance. Other studies progressively improved the structure without achieving a major breakthrough in efficiency, until the tunnel oxide passivated contact (TOPCon) concept proposed by Feldmann *et al.* in 2014 [43]. Since then, numerous structures and denominations have been proposed by different research groups (POLO by ISFH [44], PERPoly by ECN Solar energy research group [45], monoPoly™ and polyPoly™ by SERIS [31], FPC by EPFL [46], etc.) which are all gathered under the denomination TOPCon in this thesis.

Record efficiencies of 25.7% for TOPCon [47] and 26.1 % for POLO with IBC [48] were achieved on lab scale solar cells ($\approx 4\times4$ cm^2), while on industrial wafers (244 cm^2) SERIS achieved 22.8 % of PCE [49] and Trina Solar claimed a record efficiency of 24.58 % in mass production [50]. A thorough literature revue was carried out, and state of the art efficiencies along with process, main features and solar cell area are summarized in Table 1.1. The evolution of record efficiencies with time can also be found in Figure 1.12. The table was made in order to give some insight on the best efficiencies for TOPCon solar cells with different specific features: higher constraints from the wafer bulk quality (p-type vs. n-type and Cz vs FZ silicon wafers, see Section 1.4 for the difference in wafer types), from the size of the cell (lab scale vs. industrial size wafers), from the metallization process (high temperature fire-through pastes), or from mass production industrial pilot lines.

A similar work was carried out for the passivation properties of these passivating stacks. Table 1.2 displays some of the highest passivation properties for n-type and p-type TOPCon on different kinds of substrate (n-type or p-type, Cz or FZ) and surface preparation (textured, after saw-damage removal (SDR), saw-damage etched (SDE), or double-side polished (DSP)). The results are mainly categorized by the doping of the passivating contact (n-type for the top part of the Table, p-type for the bottom part), and subdivided by bulk wafer type. It can be noticed that boron-doped TOPCon generally provide a lower passivation quality. A few propositions have been made to explain this phenomenon: a larger diffusion of boron in silicon, boron-induced defects in the gate oxide [51], [52], as well as SiO_x being a larger potential barrier for holes than for electrons [35]. Another limitation to TOPCon integration on c-Si solar cells is the lower passivation it provides on textured surfaces. It was shown to be due to a lower passivation of surfaces with a <111> crystal orientation compared with <100> [53], [54]. In the context of this thesis, the most relevant results are the last 3 lines corresponding to the maximum passivation properties for p-type TOPCon on p-type silicon wafers. These reach up to 735 mV and 5 fA/cm^2 after a hydogenation step at the end of the process to boost the passivation properties [55].

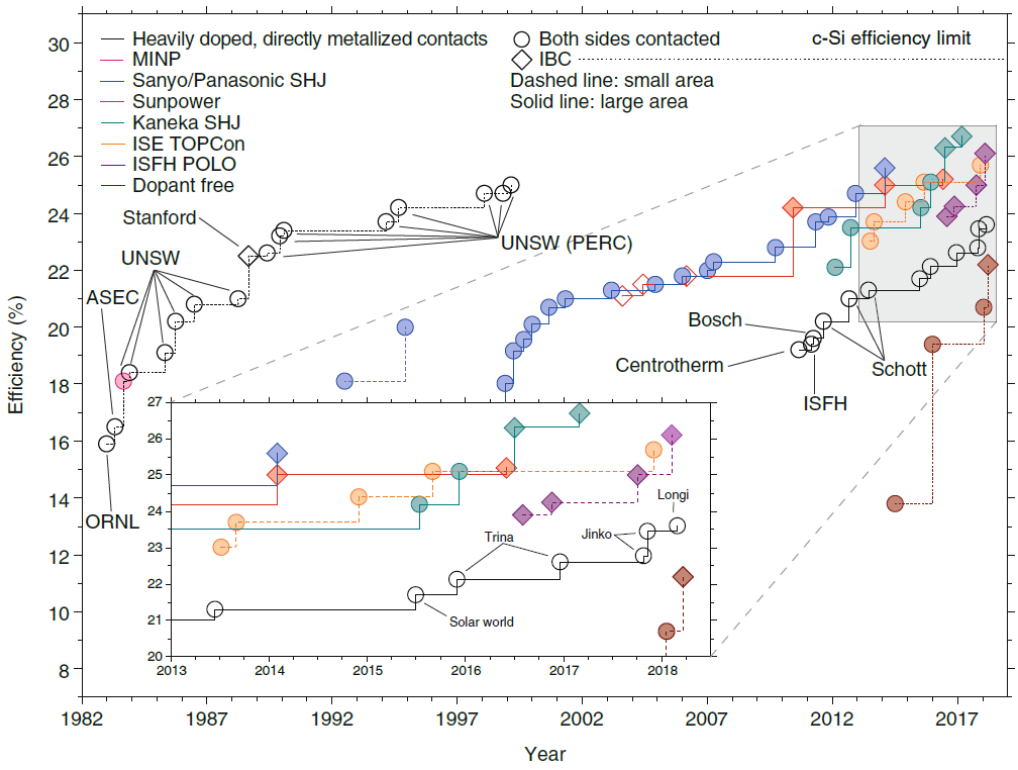

Figure 1.12: "Historical progression of notable c-Si solar cell efficiencies. The solid, colored data points represent passivating contact devices; open data points represent heavily doped, directly metallized contacts; circles indicate both sides contacted designs; and diamonds represent IBC designs. The red open diamonds represent Sunpower devices fabricated prior to their explicitly mentioning the use of passivating contacts in the device structure. Record efficiencies of large-area industrial PERC cells (open circles, solid line) are approaching the efficiency ceiling of this device design, foreshadowing a shift in production towards passivating contact cell architectures. The theoretical efficiency limit for c-Si solar cells (29.4 %) is represented by the dotted line. Inset: details of recent results, highlighting the progress in passivating contact cell structures."[26]

Table 1.1: Table of TOPCon solar cells efficiencies. This shows the variety of the type of substrate, fabrication processes and architectures that are studied in the literature, as well as the area of the solar cells. Strong efforts have been made on going from lab scale to industrial wafers and processes.

Institute	Substrate	Oxide	poly-Si	Area	Type of cell	Efficiency	Main features	Ref
ECN	n Cz	Chemical (NAOS)	LPCVD poly-Si n^+	239 cm^2	rear nTOPCon	20.7 %	large, FT metal, Bifacial	[45]
Fraunhofer-ISE	n FZ	Chemical (NAOS)	PECVD poly-Si n^+	4 cm^2	rear nTOPCon	25.7 %	Both-side contacted	[47]
ISFH	p FZ	Thermal	LPCVD poly-Si n^+ & p^+	4 cm^2	POLO-IBC	26.1 %	Record, IBC	[48]
SERIS	n Cz	PECVD	PECVD poly-Si n^+	4 cm^2	rear nTOPCon	22.8 %	Full PECVD	[49]
EPFL	n FZ	Chemical (NAOS)	PECVD poly-SiC n^+ & p^+	4.4 cm^2	Both-side TOPCon	22.6 %	SiC_x, 2 polarities	[55]
EPFL	p FZ	LPCVD	PECVD SiC_x p^+	4 cm^2	rear pTOPCon, front HIT	21.9 %	pTOPCon, SiC, FPC (no annealing)	[46]
CSEM	p Cz	LPCVD	PECVD SiC_x p^+	256 cm^2	rear pTOPCon, front HIT	21.7 %	large, pTOPCon, p Cz, SiC, FPC	[56]
Trina Solar	n Cz	LPCVD	LPCVD poly-Si n^+	256 cm^2	rear nTOPCon	24.6 %	Mass production	[50]
SERIS	n Cz	LPCVD	LPCVD poly-Si n^+	256 cm^2	rear nTOPCon	22.6 %	M2, FT metal	[57]
ISFH	p Cz	H_2O-O_3	PECVD poly-Si n^+	256 cm^2	rear nTOPCon	22.23 %	M2, p Cz wafers	[58]

Table 1.2: Table of passivation properties for TOPCon. This summarizes the best passivation properties achieved for different kinds of substrate, surface morphology, oxide growth and poly-Si fabrication technique. Outstanding J_0 values lower than 1 fA.cm^{-2} were reached.

1^{st} Author	Date	Substrate	Surface	Oxide	poly-Si	Doping	Annealing	Hydrogenation	iV_{oc} (mV)	J_0 (fA/cm^2)	Ref
Feldmann	2018	n FZ	DSP	Thermal	PECVD poly-Si n^+	in-situ PECVD	900°C, 10 min	RPHP	736	1.8	[59]
Polzin	2018	n FZ	textured	Thermal	PECVD poly-Si n^+	in-situ PECVD	900°C, 10 min	RPHP	732		[60]
Peibst	2016	n Cz	SDR	H_2O-O_3	LPCVD poly-Si n^+	ion implantation	900°C, 30 min	SiN_x	747	0.6	[35]
Peibst	2016	n Cz	textured	Thermal	LPCVD poly-Si n^+	ion implantation	900°C, 30 min	SiN_x	741	3.8	[35]
Chen	2020	n Cz	SDE	NAOS	PECVD poly-Si n^+	$POCl_3$ diff.	none	FGA	747	2	[61]
Yang	2020	n Cz	SDE	NAOS	PECVD poly-Si n^+	in-situ PECVD	820°C, 10 min	AlO_x + 450°C 10 min	730	4.2	[62]
Haase	2018	p FZ	DSP	Thermal	LPCVD poly-Si n^+	ion implantation	900°C, 30 min+1000°C 1h	SiN_x:H+425°C, 30 min	733	2	[48]
Ingenito	2018	p FZ	DSP	Thermal	PECVD poly-SiC n^+	in-situ PECVD	850°C 8 min	SiN_x:H+450°C, 30 min	746	4	[63]
Ingenito	2018	p FZ	textured	Thermal	PECVD poly-SiC n^+	in-situ PECVD	850°C 8 min	SiN_x+450°C, 30 min	737	7	[63]
Gao	2019	p Cz	SDR	PANO	PECVD poly-Si n^+	in-situ PECVD	880°C, 30 min	FGA+AlO_x+400°C	742	3	[64]
Limodio	2019	n FZ	textured	NAOS	LPCVD poly-Si p^+	ion implantation	950°C, 5 min	FGA 400°C, 2h	716	10	[65]
Polzin	2018	n FZ	textured	Thermal	PECVD poly-Si p^+	in-situ PECVD	900°C, 10 min	RPHP	732		[60]
Morisset	2019	n Cz	DSP	H_2O-O_3	PECVD poly-Si p^+	in-situ PECVD	800°C, 30 min	SiN_x+firing	734	7	[66]
Stodolny	2018	n Cz	SDR	LPCVD	LPCVD poly-Si p^+	BBr_3 diff.	none	AlO_x/SiN_x/AlO_x	741	3	[67]
Stodolny	2018	n Cz	textured	LPCVD	LPCVD poly-Si p^+	BBr_3 diff.	none	AlO_x/SiN_x/AlO_x	722	9	[67]
Haase	2018	p FZ	DSP	Thermal	LPCVD poly-Si p^+	ion implantation	900°C, 30 min+1000°C 1h	SiN_x:H+425°C, 30 min	717	6	[48]
Nogay	2018	p FZ	DSP	NAOS	PECVD poly-SiC p^+	in-situ PECVD	none	SiN_x:H+450°C, 30 min	735	5	[55]
Allebé	2018	p Cz	SDE	NAOS	PECVD poly-SiC p^+	in-situ PECVD	none	SiN_x:H+450°C, 30 min	735	5	[56]

Process for passivating contact integration

The large variety of solar cell architectures mentioned above also comes along with very different process flows. The doped semi-conductor layer can be made of poly-Si (most of the studies), silicon carbide (SiC_x) [46], [55], [56], [68] or SiO_x [49], with various deposition techniques such as plasma-enhanced chemical vapor deposition (PECVD) [29], [60], [69], [70], low pressure chemical vapor deposition (LPCVD) [45], [50], [57] or hot-wire chemical vapor deposition (HWCVD) [71], [72]. The doping of this layer can be achieved *in situ* in PECVD [60] and LPCVD deposition chambers, as well as *ex situ* by ion implantation [65], [73], [74], or diffusion [75]–[77]. The fabrication of the thin oxide layer may be done by nitric acid oxidation of silicon (NAOS) [43], [65], [74], [78], [79], chemical oxidation by Radio Corporation of America (RCA) Cleaning [33], [80]–[82], thermal oxidation in quartz furnace [37], [83] or LPCVD chamber [31], [67], plasma-assisted nitrous oxide (PANO) oxidation [64], [84], [85], PECVD deposition [49], [69], [86], UV-O_3 [87]–[89], H_2O-O_3 [66], [89], [90], atomic layer deposition (ALD) [91], [92]... or even replacing it by AlO_x [80] or a-SiN_x:H [93]. Many studies have been made on benchmarking the SiO_x deposition process [54], [87], [94]–[97]. Thermal oxides usually lead to better passivation properties, but require higher process temperatures.

In the most standard processes, the thermal budget of such structures is high, often requiring a 5-to-15-min long annealing step between 800 and 1000 °C for crystallization and dopant activation (sometimes much more). This is not desirable in industrial processing, and especially for the integration of such structures on multi-crystalline or cast-mono silicon wafers [23]. One way to tackle this issue was presented by Ingenito *et al.* from EPFL through the development of fired passivated contact (FPC) [46]. The aim of this approach is to remove the long-and-high-temperature annealing step, and to limit the high temperature processes to a single firing step ($>$ 700 °C for a few seconds) necessary for the front side metallization. However, one problem that emerges from annealing the silicon layer is the formation of blisters, that are highly detrimental for the electrical properties of the device [62], [98]–[100]. To prevent this from happening, the silicon layer in the FPC must be mechanically resistant to the firing step. Their research group uses SiC_x (with a low carbon content of approximately 2.5 at%), which has a larger mechanical resistance than a-Si:H, and a larger optical band gap, thus leading to less parasitic absorption. More details on this process will be given in section 1.5.

1.2.4 Transparent Metal Oxides

Another technology that is being investigated by the PV research community is based on the dopant-free passivating contacts, such as Transparent Metal Oxides (TMOs). The "dopant-free" denomination implies that highly-doped silicon layers are not used in such devices. The optical and electrical properties of TMOs can be tuned in order to meet specific needs in the silicon solar cells. Noticeably, these materials are wide band-gap semiconductors allowing to reduce parasitic absorption and are dopant-free therefore suppressing free-carrier absorption thus tacking the two main limiting factors in poly-Si and a-Si:H-based passivated contacts. TMOs were first explored in the 1970's as an alternative to homojunction solar cells [101]. There has recently been a regain of interest in these technologies due to improvements of the passivating layers, the current limitations of solar cell efficiencies by parasitic absorption, and improvements in the manufacturing of high/low work function materials [102] from organic electronics [103]. A thin passivating layer between the TMO and the c-Si bulk is usually required: an (i) a-Si:H layer is deposited or a thin SiO_x layer grows at the Si/TMO interface (either naturally [104] or

voluntarily), thus providing a good passivation of the silicon wafer surface.

MoO_x [30] [102], [105]–[107], WO_x [107] and VO_x [104] hole selective layers have high work functions that induce a bending of the silicon energy bands, which allows carrier selectivity (see Figure 1.13a). Efficiencies as high as 23.5 % were reached for MoO_x carrier selective contacts [108].

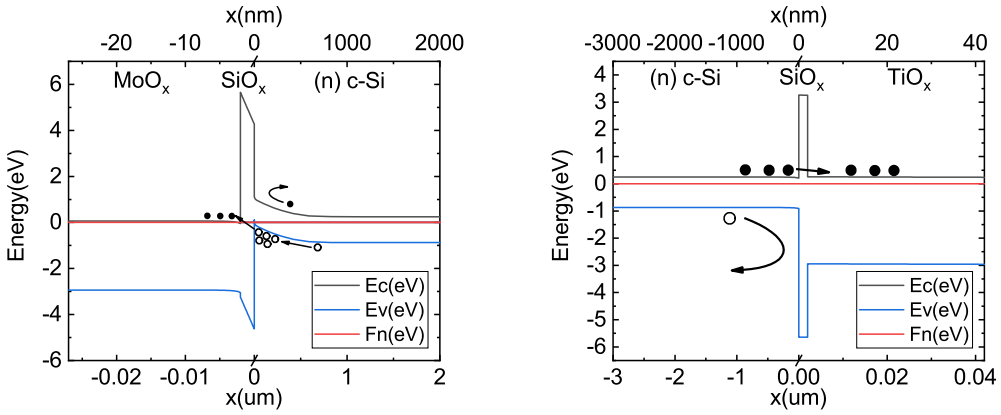

Figure 1.13: Energy band diagrams calculated with SCPAS for a stack of (a) n-type c-Si/SiO_x/MoO_x (band alignment extracted from [109]) and (b) n-type c-Si/SiO_x/TiO_x (band alignment extracted from [110]). White and black circles represent respectively holes and electrons, and the arrows the directions of current densities.

Electron-selective transparent metallic oxides such as TiO_x [110]–[112] or TiO_x:Al [113], NbO_x [114] and ZnO_x [115] are also being studied. They are based on low work-function materials, which allows an adequate band alignment of the conduction bands, and create a large potential barrier for holes (see Figure 1.13b).

This kind of material is deposited by sputtering or ALD, usually at low temperature (below 350 °C), thus resulting in a significantly lower thermal budget than TOPCon contacts processed at high temperatures.

1.3 Metallization of TOPCon solar cells

In order to extract the current from the solar cell and connect it to an electrical load, metallic contacts have to be added to the solar cell. A wide variety of such contacts exist at the laboratory scale - sometimes marginally in industry - and have been tested on TOPCon: photolithography, Ni/Cu plating [116], [117], evaporation [32], [98]. But in the industry, the most widely used metallization technique is screen-printing (97 % of production [6]), and will thus be described hereafter.

1.3.1 Screen printing

Screen printing metallization consists in printing a pre-defined shape with a metallic paste, by using a stencil. To achieve this, a photostencil with a given pattern (an H-pattern for example) is put on top of a synthetic or metallic mesh, just above the substrate to be printed. The mesh is filled with metallic paste thanks to a flushbar, and is brought in contact with the substrate thanks to a squeegee, which allows both (i) to bring the

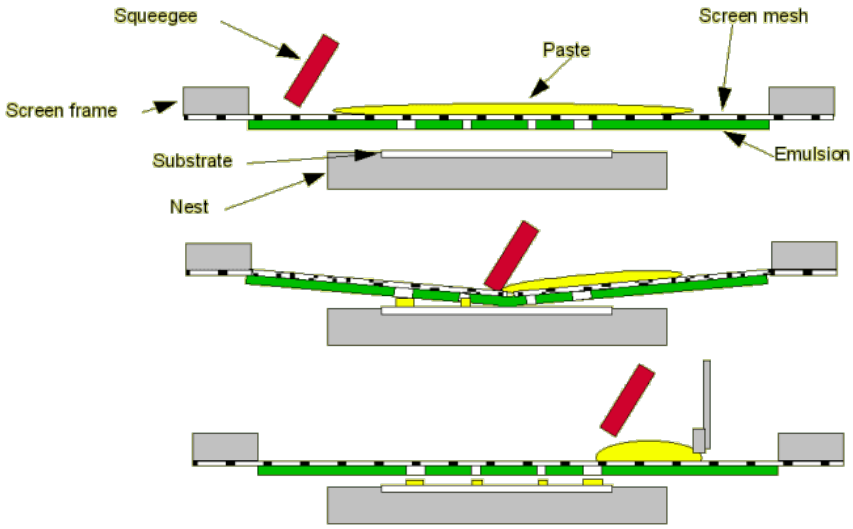

Figure 1.14: The basic screen print process [118].

metallic paste to the substrate, and (ii) to remove the excess paste. A scheme of the working principle of screen printing can be seen in Figure 1.14 [118].

The viscosity and concentration of the metallic paste, as well as the deposition parameters (distance mesh/substrate, angle and velocity of squeegee, ...) need to be finely tuned in order to provide a high-conductivity, conformal and homogeneous contact, with the adequate aspect ratio (height/width). Different kinds of metallic pastes can be used, depending on the architecture of the solar cell and on the process it is able to withstand.

1.3.2 Low-temperature metallization

In TOPCon solar cells, if the silicon-based layer is very thin or not highly doped, the sheet resistance of the extraction layer can be too high, thus leading to high a series resistance. In order to reduce this loss, it is possible to add a TCO layer on top of the poly-Si layer, such as ITO [46], [88] or aluminum-doped zinc oxide (AZO) [119]. However, these layers degrade under high temperature process steps. That is why dedicated low-temperature metallic pastes based on polymer materials with metallic inclusions have been developed. They are simply screen printed, and the cell is subsequently cured at a temperature around 300 °C. Because of their low metal content, they provide a rather low conductivity, thus requiring the use of a higher amount of metallic paste in order to limit electrical losses (resistive losses).

This kind of paste has been historically developed for HIT solar cells [120]. The combined use of a TCO and the low-temperature metallic paste when adequately optimized usually provides high efficiencies with low parasitic resistances, since it does not strongly damage the underlying layers (the main degradation may come from bombardment during the sputtering step of the TCO layer). However, this method remains relatively expensive for now compared to high-temperature, fire-through metallic pastes.

1.3.3 Fire-through metallic paste

High-temperature fire-through (FT) metallic contacting uses a special metallic paste that allows to go through the capping dielectric layer of the solar cell, in order to reach the underlying carrier transport layer, and make the electrical contact without needing a

dedicated step to remove the dielectric layer with spacial selectivity (mask, Laser Contact Opening, etc.). The paste is composed of metallic particles (for conductivity), glass frit (for contact resistance) and an organic binder (width and height of the contact). The glass frit is an oxide that usually contains Pb, or other metals such as Te or V [121]. After the screen printing and drying of the metallic paste on the solar cell precursor (bare silicon or a dielectric layer such as a-SiN_x:H), it undergoes a firing step (750-900 °C) for a few seconds. A standard temperature profile of a firing step can be found in Figure 1.15.

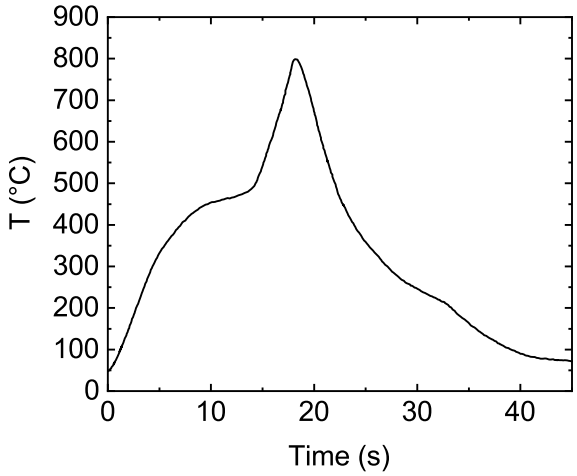

Figure 1.15: Recommended firing temperature profile [122].

During this firing step, the contacting mechanism is believed to involve the following steps: (i) the organic binders burns out, (ii) the glass frit starts melting, etches the dielectric layer and is reduced to Pb (fire-through step), (iii) the silver particles melt into Pb, and Si melts into the Pb/Ag mix, (iv) after the peak temperature Ag precipitates and Si regrows epitaxial [123].

This FT method is the most widely used, and allows the simultaneous metallization of both sides through a *co-firing* when using adapted metallic pastes (usually Ag for the n-type and Ag/Al for the p-type contact). However, due to the high temperature of the firing, some layers may be damaged during the process.

For TOPCon applications, FT screen printing is being more and more studied in order to improve the readiness of this technology to go industrial [12], [31], [49], [57], [67], [124]. Specific contact resistivities and recombination current densities underneath the contact as low as $\rho_c = 1.3$ mΩ.cm^2 and $J_{0,c} = 40$ fA/cm^2 have been reached [57], to be compared with $J_{0,c} \approx 1000$ fA/cm^2 for FT screen printing metallization on diffused emitters.

1.3.4 n-type and p-type TOPCon FT metallisation

Because of the higher passivation quality achieved on n-type TOPCon, most of the first solar cells using FT metallization used a diffused p-type front side and a rear n-type passivating contact. Very little work has been done on FT metallization of p-type TOPCon. We thus gather information mainly from two studies [124], [125]. These studies show that the FT metallization pastes etch a significant amount of the poly-Si layer, and even more dramatically for Ag-Al metallization for (p) poly-Si [125]. As a result, a relatively thick poly-Si layer ($\approx$ 150 nm) is necessary in order to get low $J_{0,c}$ values. The record low recombination current value for p-type poly-Si is 200 fA/cm^2 for fire-through contacts.

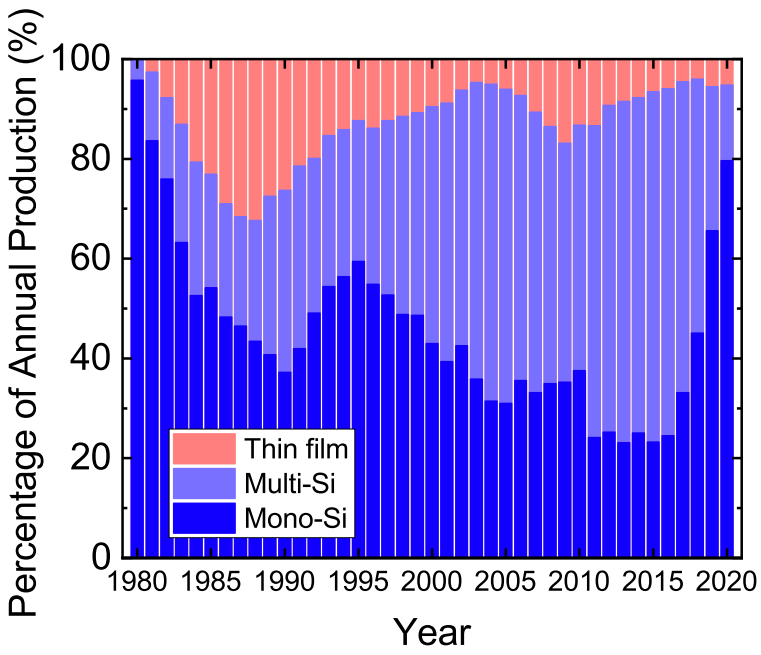

Figure 1.16: Evolution of the percentage of global annual PV production held by the different technologies of solar cell [11].

These results strongly depend on the composition of the metallic paste, which is why researchers usually collaborate directly with metallic paste manufacturers to develop these new products.

The previous sections allowed to understand the working principle of solar cells, what structures exist in order to make them more efficient, and how to metallize poly-Si based passivating contacts. This efficiency increase allows to shrink the total carbon intensity of 1 kWh of photovoltaic energy produced. However, a large part of the carbon footprint of the module comes from the silicon wafer manufacturing process. In the following section we will thus make a brief overview of some fabrication processes of silicon wafers.

1.4 Silicon Wafer manufacturing

Today, 95 % of PV modules market shares are held by the silicon-based solar cell technologies described previously (see Figure 1.16) [11]. They all rely on silicon wafers a few hundred microns thick (typically 180 µm). In order to get highly efficient devices, this fundamental building block needs to be extremely pure. Various methods exist to achieve a low level of impurity.

1.4.1 From quartzite to polycrystalline silicon rods

Silicon is a very common element and is the second most abundant one in Earth's crust after oxygen. For silicon wafer fabrication in the solar industry, blocks of quartzite (SiO_2) are used as the base material.

These blocks first undergo a *carbothermic reduction* in an electric arc furnace [126]. It takes place in a crucible filled with quartzite and carbon based material (coal, coke and wood chips), in which are immersed electrodes (see Figure 1.17a). The temperature

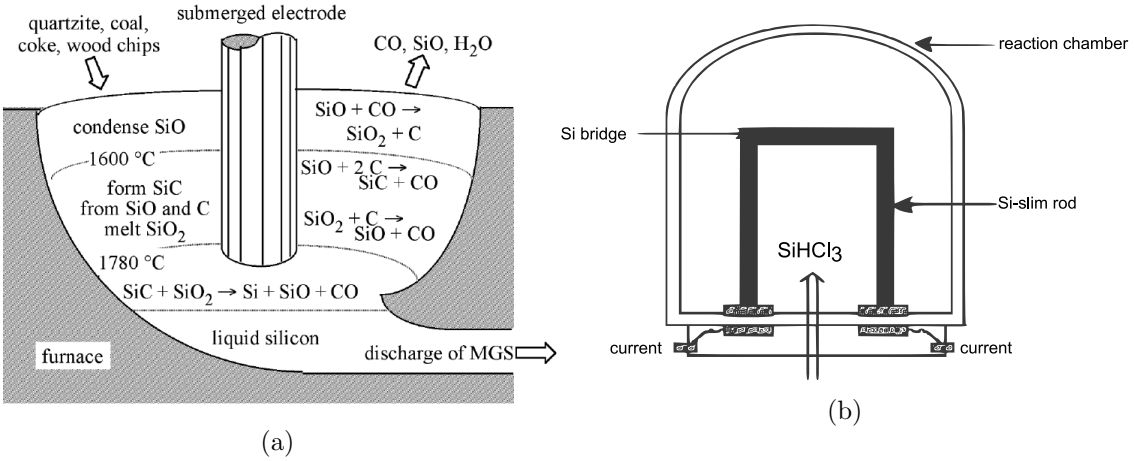

Figure 1.17: (a) Schematic of submerged-electrode arc furnace for the production of metallurgic-grade silicon (MGS) [127]. (b) Schematic representation of Siemens deposition reactor [127].

reached is around 1800 °C and allows the formation of pure silicon, with effusion of gases like CO and H_2O. This leads to the formation of metallurgical grade silicon (MGS) of purity between 98 and 99 wt.%. The impurities are mostly aluminum and iron atoms.

The MGS formed is then further purified to get electronic grade silicon (EGS) or solar grade silicon (SGS). The most common way to get EGS is to go through the *Siemens Process*. It consists in heating MGS powder with anhydrous hydrogen chloride (HCl) at around 300 °C to get trichlorosilane ($SiHCl_3$) in vapor phase. This gas is further distilled and is subsequently used as a precursor for the formation of a poly-crystalline silicon rod (later written polysilicon) by chemical vapor deposition (CVD) (see Figure 1.17b). This leads to very high purity EGS, up to 9N, or 99.9999999 %. Other techniques, such as fluidized bed reactors, allow to get SGS with lower purity (4-6 N) but with a lower energy consumption.

A final step for further purification and crystallization is carried out, followed by the ingot sawing process, in order to get standard silicon wafers. Different crystallization routes of the polysilicon rods are presented in the following sections.

1.4.2 Multi-crystalline silicon

Until recently, multi-crystalline silicon (mc-Si) wafers were the most common silicon wafers because of their low manufacturing cost compared to fully mono-crystalline silicon wafers. They still held half the world market shares in 2018 [6] (see Figure 1.16). Their cost-effectiveness is due to the casting method. Polysilicon is molten in a crucible, and a controlled cooling process results in a slow recrystallization from the bottom to the top of the crucible. This method allows large scale production and high throughput, but induces a relatively high impurity level (such as a high Fe concentrations) due to diffusion from the crucible and its Si_3N_4 coating, and a large amount of crystal defects may appear (dislocations).

1.4.3 Mono-crystalline silicon

A way to achieve higher wafer quality is to grow a single crystal in order to get rid of grain boundaries. There are two major ways to achieve this mono-crystal of silicon (that

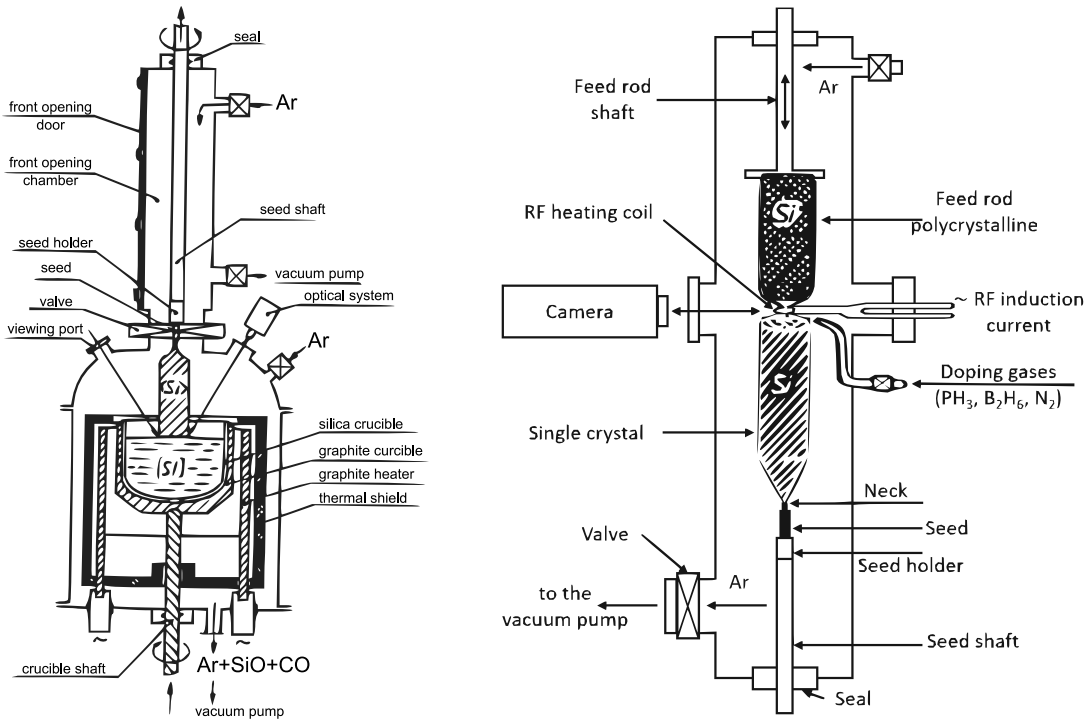

Figure 1.18: (a) Schematic of a modern Cz-Si single-crystal puller for the growth of large crystals [128]. (b) Schematic of a modern FZ-Si single-crystal puller for the growth of large crystals [128].

needs to be larger than the desired size of a silicon wafer): Czochralski process and the Float-Zone technology.

Czochralski method

In the Czochralsky (Cz) growth process, the polysilicon is first molten in a quartz crucible. It is then recrystallized thanks to a crystalline silicon seed, that comes in contact with the surface of the molten silicon. By fine tuning the temperature, the pulling speed and the rotational velocity, it is possible to grow a pencil-like shaped mono-crystal of silicon with a typical size of 20-30 cm of diameter and 2 meters of height. Figure 1.18a shows a schematic of the Cz growth setup. This can lead to a single crystal free of dislocation if the process is done adequately. One disadvantage of this technique is that, due to the silica crucible, oxygen is incorporated in the silicon matrix (up to a concentration of 1×10^{18} cm^{-3}), which can lead to light induced degradation later in the life cycle of the solar cell.

Float-zone technology

An alternative method for the growth of large mono-crystal silicon ingots is the float-zone (FZ) method. A rotating mono-crystalline seed is placed in contact with a polysilicon rod in an inert environment (Ar). A heating coil is then slowly moved from the bottom (the seed) to the top, and locally melts and crystallizes the polysilicon rod (see Figure 1.18b). This provides a high quality single-crystal of silicon, because impurities are more soluble in melted silicon, and consequently migrate with the molten zone, thus leaving the single

crystal extremely pure. However, the temperature gradient also induces the formation of extended defects that can be passivated by doping the wafer with nitrogen [129].

1.4.4 Cast-mono wafers

The aim of cast-mono wafers is to ally the high throughput, simple process of mc-Si casting with the high crystalline quality of single-crystal silicon wafers. It consists in casting polysilicon chunks like in the case of mc-Si, that is to say melting the polysilicon in a crucible and vertically controlling the cooling step (Directional Solidification System). The major change is that mono crystal seeds are put at the bottom of the crucible, which allows an epitaxial growth, with the same orientation as the seed [130]. This produces a chessboard patterned ingot, with large grains that have the size of the desired wafers and with the height of the ingot. This has the advantage of getting rid of most grain-boundary-related defects, keeping the oxygen content lower than in Cz ingots, and allowing easy mass production. However, a relatively high level of metallic impurities (mostly Fe) can still be found due to diffusion from the crucible, and dislocations may still appear due to high stress points during the crystallization process.

One growth technology is the SMART technology developed by Takahashi *et al.* from Fraunhofer ISE [131]. The crystal orientation of the seed is chosen to create artificial grain boundaries. This allows to grow controlled sections of dislocation-rich silicon, preventing dislocations to expand in the silicon-wafers over a quality-controlled area. An environmental analysis shows that using SMART cast-mono wafers instead of Cz wafers for manufacturing PERC solar cells allows to reduce the global warming potential from 42.0 to 37.9 gCO_2eq/kWh [132]. This highlights the interest of investigating the use of cast-mono wafers for a more environmental-friendly PV industry.

1.5 Objectives of the study

Ingenito *et al.* [46] proposed a process flow shown in Figure A3.4a for the formation of a passivating contact without a long (5 to 15 min) and high-temperature (800 to 1000 °C) annealing step. It consists in depositing a silicon-based layer resistant to the firing step such as amorphous or nano-crystalline silicon carbide (a-SiC_x or nc-SiC_x) in their case, on top of a thin tunnel oxide layer. Then the sample is subject to a firing step for further crystallization of the (p) a-SiC_x:H layer and front side metallization. In order to reach a high quality of passivation, an additional hydrogenation process was shown to be necessary [87]. A hydrogenated amorphous silicon nitride layer is deposited by PECVD, and annealed at 450 °C for 30 minutes. It is subsequently removed thanks to a dip in hydrofluoric acid, and the cell is completed by depositing a TCO layer and screen printing a silver grid at low temperature.

As shown in the previous sections, long hydrogenation steps are not desirable for industrial integration and high-temperature is preferred to low-temperature metallization for an easy compatibility with preexisting industrial tools and processes. For simplification purposes, we investigate another process-flow for the fabrication of FPC, shown in figure A3.4b. It starts with a Radio Corporation of America (RCA) standard cleaning step followed by the deposition of a tunnel oxide layer. We then deposit a boron doped silicon layer by PECVD at 13.56 MHz, which needs to be resistant to the firing step. This is followed by the deposition of a-SiN_x:H by PECVD on top of it, the screen printing of the metallic contacts, and finishing with a high temperature firing step in order to contact the cell. This process flow, which reduces the number of process steps from 9 to 6, is

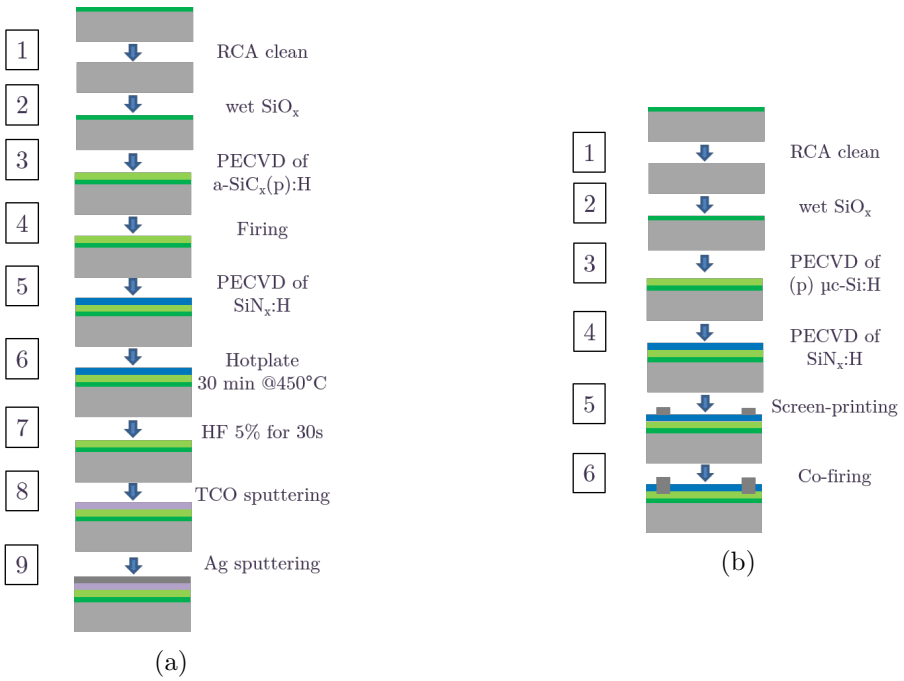

Figure 1.19: (a) Initial process flow for a Fired Passivating Contact (FPC), EPFL [46]. (b) Simplified process flow for a FPC without a post-firing hydrogenation step.

schematically shown in Figure A3.4b.

The purpose of this thesis is to investigate this simplified process flow for the integration of passivating contacts. The objective is to use p-type cast-mono Si wafers for their low energy consumption and cost compared to standard Cz wafers, combined with the aforementioned process to remove time-consuming and high-temperature processes in order to limit the thermal budget of the solar cell.

The study of this process consists first in the standard optimization of the deposition of the various layers of the stack, with comprehensive characterizations of the materials deposited. It is then investigated further by *in situ* modulated photoluminescence (MPL), a technique that allows to measure in real time the evolution of the minority carrier lifetime in a sample during a given fabrication process step. We first focus on better understanding this new characterization technique through a case study of silicon wafers coated with aluminum oxide, and then use it on FPC samples. Finally, the transfer of this passivating contact fabrication process on large area industrial wafers (Cz and cast-mono) is presented.

Chapter 2

Materials development and optimization

This section presents the optimization of the deposition processes of the passivating stack. We start by describing two types of silicon oxide layers (wet-chemically grown and PECVD deposited) and the deposition of a p-type (boron-doped) silicon layer that is mechanically resistant to a high-temperature firing step (absence of blisters). The impact of this deposition on the chemical composition of the underlying silicon oxide layer is further analyzed. We then detail the optimization of a phosphorous-doped layer for the development of n-type passivated contact cells. Finally, the influence of the capping layer and more specifically of the silicon nitride layer on the passivation properties and thermal stability is studied.

Contents

2.1 Deposition tools and methods

In this section, we introduce the plasma-enhanced chemical vapor deposition (PECVD) technique and the deposition tools operated in this thesis, the cleaning procedure followed in order to remove impurities from the surface of the silicon wafers, and finally the different types of wafer used and their preparation.

2.1.1 Plasma-enhanced chemical vapor deposition

A plasma is an "ionized gas" in which a significant fraction of free charges are created by collision or photoionization. The thermodynamic temperature $T = (\partial U/\partial S)_{\mathcal{V}}$ translates the agitation of particles, with U the internal energy, S the entropy and $\mathcal{V}$ the volume of the studied ensemble of particles. In such media, two different thermodynamic temperatures may be defined: one for electrons T_e, and one for the rest of the gas T_g (ions, molecules, radicals, particles, ...). Plasmas represent 99 % of the mass of ordinary matter of the universe and refer to extremely diverse media with great variations of physical properties. Generally speaking, the different plasma regimes can be categorized by their electron density n_e and electron temperature T_e. The different regimes and the corresponding ranges of these two properties are shown in Figure 2.1. Most strikingly, the variety of the kinds of plasma can be assessed by the fact that T_e and n_e are varying over several tens of orders of magnitude.

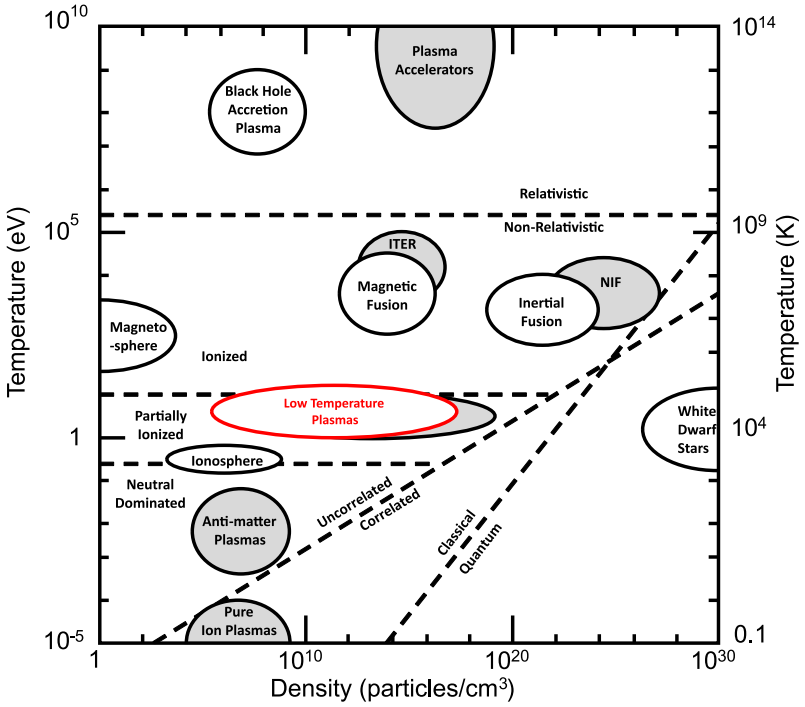

Figure 2.1: Different plasma regimes as a function of the electron temperature and density [133].

As introduced in section 1.5, many of the layers of the passivated contacts will be deposited by PECVD in this thesis. Contrary to standard LPCVD that allows the deposition of a thin film by heating the substrate at high temperature (more than 500 °C) in order to thermally activate chemical reactions at the surface of the substrate, PECVD uses a

plasma to facilitate the deposition. It consists in putting a substrate in a high vacuum chamber (pressure lower than 1×10^{-6} mbar), and subsequently igniting a plasma out of a mixture of reactive gases through the application of an electromagnetic excitation. In this thesis, we use parallel-plate radio-frequency (RF) capacitively coupled plasmas (CCPs) in which a generator excites one of two parallel electrodes with an RF voltage at 13.56 MHz. This is a standard frequency used in industrial applications, and it sits between the plasma frequency of electrons and of heavy particles. Consequently, electrons are mobile enough to follow the electric field variations, whereas heavy particles only respond to the average electric field due to their higher inertia. This creates a glow-discharge plasma, included in the category of low-temperature plasmas, in red in Figure 2.1. In these also called "non-thermal plasmas", T_e and T_g values may be greatly different from one another: T_g may be close to ambient temperature while T_e can reach a few 10000 °C. The high energy electrons can inelastically collide with the low-temperature gas particles, giving them enough energy to be excited (under the form of radicals, ions, atoms ...) and become highly reactive species. Once these reach the surface of the substrate, they may chemically react at temperatures significantly lower than what would be needed for neutral species (typically 175 °C instead of 600 °C for the deposition of silicon layers in this thesis).

The main tunable parameters that can change the plasma characteristics, and thus govern the thin film properties are the:

- nature of the gases and their flow rates,
- RF power,
- inter-electrode distance,
- gas pressure,
- gas temperature T_g.

Different regimes of deposition can be achieved depending on (i) the gases used (surface oxidation with an O_2 or CO_2 plasma, versus a-Si:H deposition from a soft, low RF power SiH_4 plasma), (ii) the RF power (chemical vapor deposition (CVD) regime for lower self-bias voltages, versus physical vapor deposition (PVD) for higher self-bias voltages), and (iii) the gas pressure (high pressure can lead to gas-phase reactions, leading to the formation of particles, nano-crystals or agglomerates in the plasma [134]). The energy provided ends up as chemical bonding energy (through chemical reactions involving radicals, ions, electrons and photons) but most of it is thermally dissipated (through bombardment, recombination, radiative excitation, ...) as more thoroughly described in [135].

During this doctoral work, the depositions were done in two different reactors. One is Octopus II by INDEOtec, a fully automated and semi-industrial RF CCP PECVD cluster tool. A scheme of it can be seen in Figure 2.2a. The reactor is hosted at LPICM (Laboratoire de Physique des Interfaces et Couches Minces, Ecole Polytechnique) where the experiments were carried out. It is currently equipped with two separate PECVD chambers, one dedicated to high-temperature processes (up to 450 °C) and made out of stainless steel, the other one for lower deposition temperatures (max 250 °C) and made out of aluminum. These are composed of a closed plasma-box including a showerhead electrode - through which the gases are flowing - and the substrate holder. This plasma box is surrounded by the rest of the chamber that is itself under vacuum ("double-box" design) as shown in Figure 2.2b. The large dimensions of the substrate holder (350×450 mm^2) allow depositions on up to 4 M2 industrial wafers (156×156 mm^2) in one single run. In

this reactor, the a-SiO_x:H, p-type and n-type µc-Si:H and µc-SiO_x:H as well as a-Si:H layers were deposited.

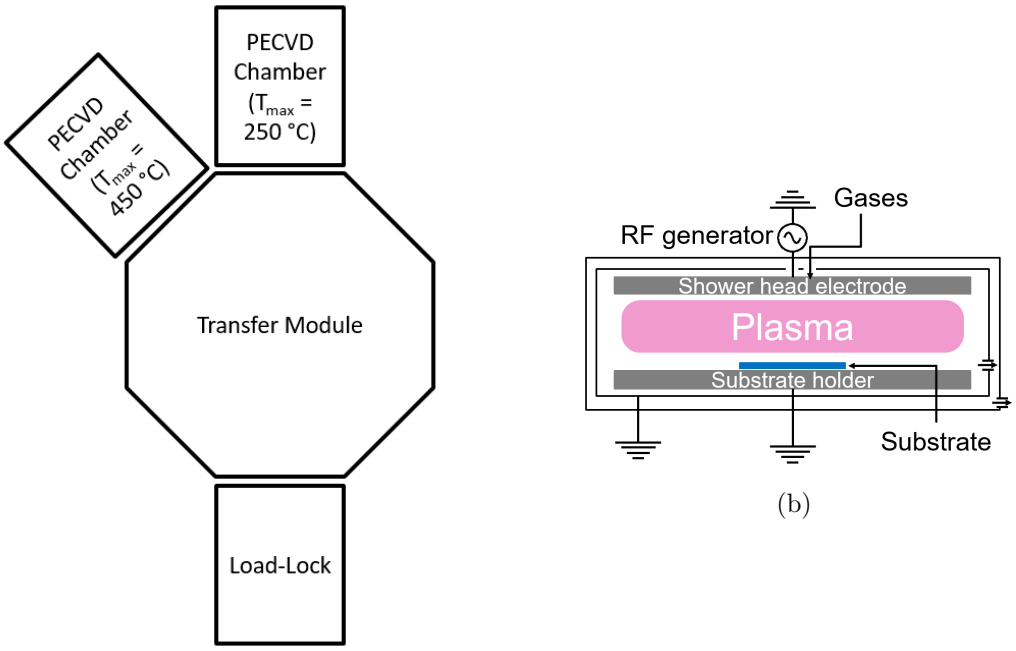

(a) (b)

Figure 2.2: (a) Schematic representation of the Octopus II cluster by INDEOtec [136] and (b) simplified scheme of the double-box design.

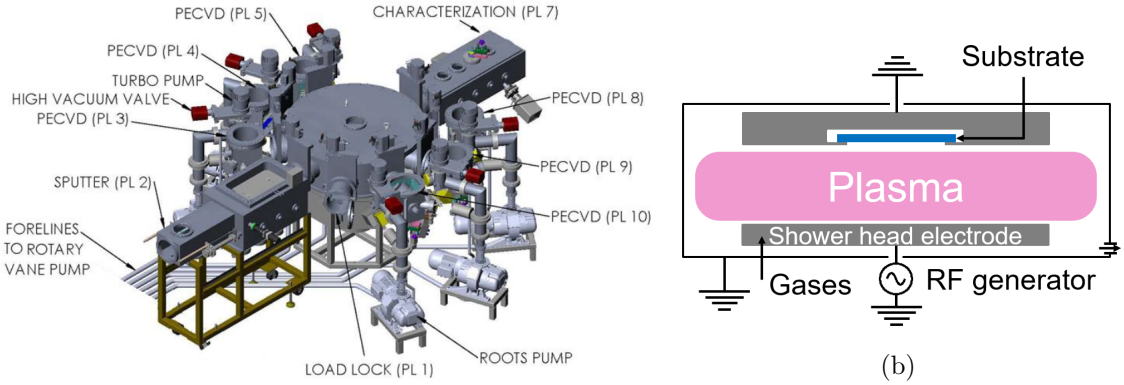

(a) (b)

Figure 2.3: (a) Schematic representation of the cluster tool by MVS (extracted from [137]). (b) Simplified scheme of the PL3 plasma chamber.

The second PECVD reactor used is a cluster tool by MVSystems, which 3D schematic representation is shown in Figure 2.3a. It is composed of a load lock, one sputtering chamber, and 7 PECVD chambers. Contrary to the Octopus cluster tool, the plasma is ignited below the substrate as represented in Figure 2.3b. In this work we only use PECVD chambers "PL3" and "PL8" to deposit silicon nitride a-SiN_x:H. PL3 is a standard PECVD chamber, whereas PL8 is additionally equipped with an *in situ* modulated

photoluminescence acquisition setup that will be further described in chapter 4.

The optimization of the PECVD deposition conditions of the various layers will be the object of this chapter.

2.1.2 Radio Corporation of America (RCA) cleaning

Silicon crystal surfaces are very reactive to ambient air, and naturally get oxidized very rapidly. This forms a thin layer at the surface of a raw silicon wafer, called *native oxide*. However, this layer is very defective, which leads to relatively poor passivation properties whatever the kind of materials deposited on top of this oxide. Consequently, chemical cleaning of the wafers is necessary before any deposition step in order to get a high quality final device. A standard chemical used in order to remove the native oxide layer is hydrofluoric acid (HF). The chemical reaction describing the etching of the surface silicon oxide layer may be written as [138]

$$SiO_{2(s)} + 6HF_{(aq)} \longrightarrow H_2\left[SiF_6\right]_{(aq)} + 2H_2O_{(l)}$$

This results in a silicon wafer with hydrogen terminated bonds at its surface. However, organic, ionic (alkali), and metallic contaminations may remain at the surface of the wafer and deteriorate the final device performances. A more thorough cleaning procedure was developed by W. Kern and D.A. Puotinen while working at Radio Corporation of America [139], which gave the name RCA cleaning. It is mostly based on the use of hydrogen peroxide H_2O_2 that can easily oxidize silicon. The full standard procedure consists in 4 steps:

- standard cleaning 1 (SC-1) - Organic contaminants removal: removal of contaminants from the wafer surface and formation of complexes with group I and II metals
  Process: De-Ionized $H_2O_{(l)}$:$H_2O_{2(aq)}$:$NH_{3(aq)}$ with a 5:1:1 ratio at 75 °C for 5 min
  Rinsing 3 min in De-Ionized $H_2O_{(l)}$

- Oxide layer removal
  Process: HF 5% in De-Ionized $H_2O_{(l)}$ for 15 s
  Rinsing 30 s in De-Ionized $H_2O_{(l)}$

- standard cleaning 2 (SC-2) - Ionic contamination removal: dissolution of the metal and ionic complexes
  Process: De-Ionized $H_2O_{(l)}$:$H_2O_{2(aq)}$:$HCl_{(aq)}$ with a 6:1:1 ratio at 75 °C for 10 min
  Rinsing 5 min in De-Ionized $H_2O_{(l)}$

- Oxide layer removal
  Process: HF 5% in De-Ionized $H_2O_{(l)}$ for 15 s
  Rinsing 30 s in De-Ionized $H_2O_{(l)}$

This provides a contamination-free surface and a clean silicon wafer, with hydrogen-terminated silicon bonds. Depositions can subsequently be carried out on the clean samples. It is worth noting that the high viscosity of the SC-2 solution can lead to difficulties during the subsequent rinsing step. All the cleaning steps were done by permanent EDF R&D staff for safety reasons.

2.1.3 Substrates and characterizations

In this work, different kinds of substrates are used in order to characterize the various physical properties of the deposited layers.

- double-side polished (DSP) n-type Cz 1/4 wafers (100 mm of diameter, 280 µm-thick, 1-5 Ω.cm) are used as substrates for spectroscopic ellipsometry (SE), X-ray photoelectron spectroscopy (XPS), confocal microscope images, transmission electron microscopy (TEM), thermal desorption spectrocsopy (TDS), and corona oxide characterisation on semiconductor (COCOS).

- DSP p-type float-zone (FZ) 1/4 wafers (100 mm of diameter, 280 µm-thick, 2-4 Ω.cm) are needed in order to assess the passivation properties of the layers or stacks deposited. quasi steady-state photoconductance (QSSPC) and fourier transform infrared spectroscopy (FTIR) spectroscopy were done on these samples.

- Corning glass slides (2 mm-thick, 1"×1") are used as substrates for the samples characterized by Raman spectroscopy and 4-points probe (4PP) conductivity measurements.

The p-type FZ wafers were RCA cleaned before the deposition of the passivation layers. For the optical and chemical characterization of the n-type Cz wafers, a simple HF dip for 30 s was made in order to remove the native oxide. No specific pre-treatment was done on the glass substrates.

Some characterizations result from collaborations with researchers from various research units.

- The XPS experiments shown in the following sections were carried out at Institut Lavoisier de Versailles (ILV) - Université de Versailles Saint-Quentin. A Thermo Fischer K-Alpha$^+$ spectrometer was used with a monochromatic Al-Kα source at 1486.6 eV. The in-depth composition and chemical environments were obtained by sequential Ar^+ sputtering (1000 eV, 10 mA, static mode, raster size 2 mm, 10 s to 30 s sputtering steps depending on the depth probed). The XPS spot size was 400 µm with a probed depth of the order of 10 nm. High resolution spectra were acquired using a 20 eV pass energy. Data were processed using the Thermo Advantage© software. Si_{2p} spectra were deconvoluted using two contributions corresponding to the c-Si matrix (at 98.8 eV) and the Si oxide (around 103.0 eV) environments [140]–[142]. The respective proportion of each environment was determined by comparing the corresponding areas of the contributions after a Shirley background substraction.

- The TEM characterizations were performed at Ecole Polytechnique on a Titan-Themis electron microscope operating at 200 kV equipped with a Cs probe corrector with a spatial resolution within nm range using the scanning transmission electron microscopy-high angle annular dark field (STEM-HAADF) imaging mode. For all the studied samples, cross-section-lamellas have been prepared using a standard lift-out procedure within a focused-ion, dual-beam microscope (FIB, FEI-Scios DualBeam).

- The FTIR spectroscopy was carried out at Air Liquid R&D lab on a Nicolet 6700 spectrometer.

All the other characterizations (QSSPC, SE, 4PP, Raman spectroscopy, TDS, confocal microscopy, COCOS), data treatment (FTIR), and depositions were made by the PhD candidate. The various characterization techniques are shortly described in Appendix A2.

2.2 Tunnel oxide layer

In this section we study the tunnel oxide layer situated between the poly-Si layer and the c-Si wafer (for the TOPCon structure, see Figure 1.11a). The oxide was made by two different techniques: PECVD and wet chemical oxidation.

2.2.1 PECVD oxide

The PECVD process had to be developed in order to deposit a silicon oxide layer. The gases used for the deposition were dihydrogen (H_2, also simply called "hydrogen" later on), silane (SiH_4) and carbon dioxide (CO_2) as an oxidizing agent. The CO_2/SiH_4 gas flow rate ratio was varied in order to get a silicon oxide material close to stoechiometry. SE measurements were analyzed using a Tauc-Lorentz model [143] to extract the refractive indices (n) and extinction coefficients (k) of the deposited materials. Results are shown in Figure 2.4. When increasing the CO_2/SiH_4 ratio, the optical indices decrease due to a higher incorporation of oxygen within the matrix. A ratio of 10 was chosen in the following sections for its relatively low optical indices while not introducing too much CO_2 in the plasma. Indeed, CO_2 plasma can lead to defect creation at the surface of the silicon wafer due to vacuum UV emission [144], [145].

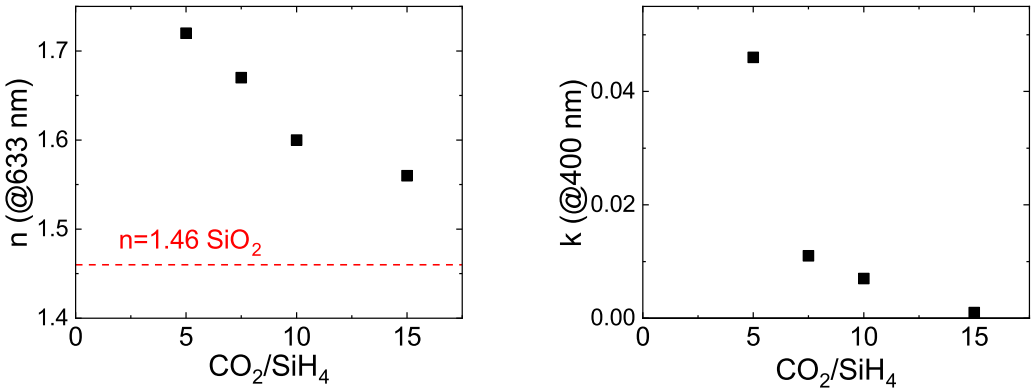

(a) (b)

Figure 2.4: Variation of the (a) refractive index and (b) extinction coefficient of a PECVD SiO_x layer with CO_2/SiH_4 gas flow rate ratio.

XPS analysis on this specific material allowed to measure an oxygen content of 55.5 ± 1.6 at% and a silicon content of 41.4 ± 1.6 at%, giving a-SiO_x:H with $x = 1.3$. The 30 nm-thick layer contains 3 at% of carbon (probably due to CO_2 being the oxidizing agent) as shown in Figure 2.5a. These values do not take into account the contribution of hydrogen - which, however, would not impact the value of x. Figure 2.5b shows the Si_{2p} orbital signal of the oxide layer. It can be seen that the material is mainly composed of bivalent silicon atoms bonded to oxygen atoms (see the peak at 103.0 eV, related to Si^{4+} chemical state) but is not perfectly stoechiometric: substoechiometric oxides SiO_x are indicated by the shoulder at lower energy (for the correspondence of peak energy values, see the work of Park *et al.* [146]). This was expected since the refractive index obtained does not reach the one of pure thermal silicon dioxide (see Figure 2.4a). XPS analysis also shows that the C_{1s} peak sits around 284.0 eV. This low binding energy position of C_{1s} is not usual and is close to the energy position of a C-Si environment, which is expected

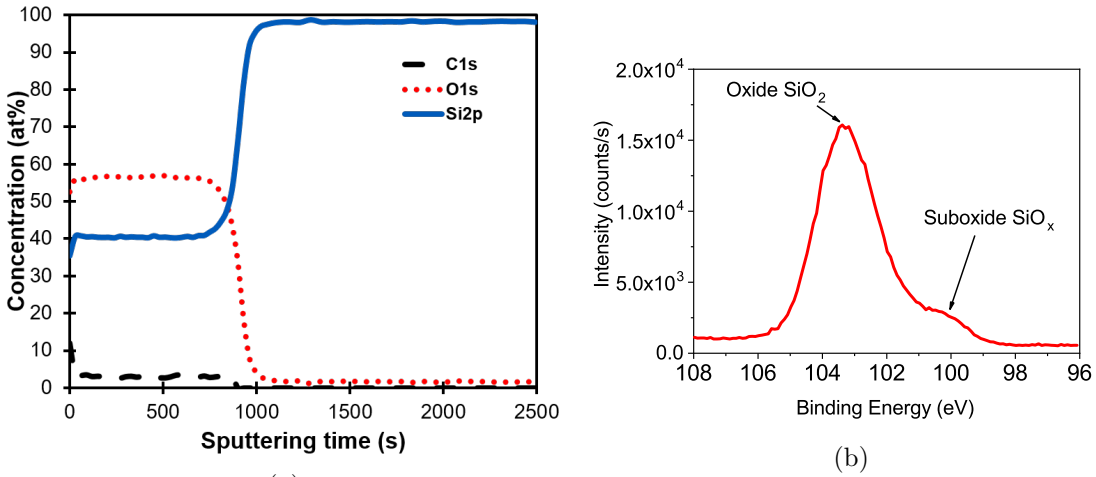

(a) (b)

Figure 2.5: XPS spectra of the SiO_x thin film deposited by PECVD on a DSP n-type Cz c-Si wafer. (a) In-depth profile of the atomic concentration of a 30 nm-thick PECVD deposited SiO_x layer and (b) XPS signal coming from the Si_{2p} orbital in the middle of this layer (after 500 s of sputtering time).

around 283.0 eV. The C-Si contribution is minor and the Si atomic network must be considered as mainly composed of O-type neighbor atoms and C-type atoms in some sites. This organization may explain the higher energy position of the C-Si contribution. This observation is consistent with other CO_2 + SiH_4 plasma processes [147].

2.2.2 Wet-chemical oxide

Wet chemical oxidation of the surface of the silicon wafer is obtained by dipping the clean c-Si wafer having hydrogen terminated silicon bonds in a H_2O_2 + HCl aqueous solution at 75 °C for 10 min, allowing the growth of a chemical tunnel oxide of thickness 1.4 ± 0.2 nm. This oxidation step corresponds to the second standard cleaning step SC-2 of the RCA cleaning procedure [139] detailed in section 2.1.2.

Figure 2.6 shows the difference in the Si_{2p} XPS signal at the surface of the wet-chemical and PECVD SiO_x layers before the deposition of any additional layer. The silicon oxide peak around 103.0 eV can be clearly seen in both the samples. The double peak at 98.8 eV comes from the c-Si wafer beneath the SiO_x layer. It is visible because the probing depth of the XPS method - 10 nm - is bigger than the oxide thickness. The lower intensity of the peak around 103.0 eV for the wet-chemical oxide layer is due to a thinner layer (1.3 nm against 2.4 nm for the PECVD oxide), which consequently produces a weaker signal with respect to the one coming from the wafer. It is worth noting that even though the SiO_2 chemical environment is dominating, the signal does not go back to 0 between photopeaks corresponding to the c-Si and SiO_2: this is again the result of the presence of suboxides.

The passivation properties provided by the PECVD and wet-chemically grown SiO_x layers will be compared later on.

2.3 Boron-doped silicon layer resistant to firing

The next step of the FPC fabrication consists in depositing a doped silicon layer by PECVD on top of the tunnel oxide. It needs to be exempt of blisters after undergoing the

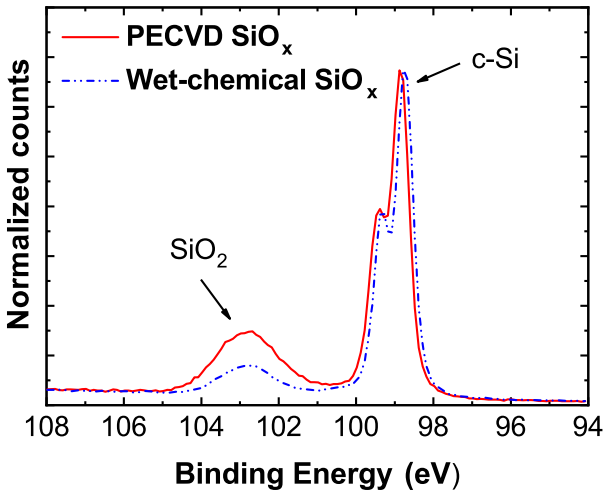

Figure 2.6: XPS Si_{2p} spectra measured on thin wet-chemical (1.3 nm-thick) and PECVD (2.4 nm-thick) oxide layers deposited on a c-Si wafer, in the as-deposited state (no additional deposition).

firing step: a fast temperature ramp up to 800 °C for a few seconds.

2.3.1 Avoiding blistering

Blistering is a common problem when annealing a-Si:H at high temperatures for crystallization purposes [99], [148]. It is most often attributed to stress relaxation [137], hydrogen diffusion and molecular hydrogen accumulation [148]. In some cases, the aforementioned annealing step can be performed using a slow temperature ramp up, thus limiting the constraints on the material, which can prevent the blisters from appearing. However, this solution is not chosen in our process flow (Figure A3.4b) since the silicon layer is directly subject to a high-temperature, fast annealing step with a heating rate up to 100 °C/s, which is even more favorable for the formation of blisters. As an example, the typical temperature profile we use during a firing step in a JETFIRST furnace by Jipelec™ is shown in Figure 2.7.

The fixed PECVD deposition conditions of the boron doped layers presented in this section are shown in Table 2.1. We use trimethylborane $B(CH_3)_3$ (TMB) as the boron doping gas, diluted at a 1.0 % concentration in H_2. In order to deposit the boron doped silicon layer, silane (SiH_4) is used as a silicon precursor. A way to prevent the layers from blistering during high-temperature annealing is to use a high dilution of SiH_4 into H_2 during the PECVD deposition [149]. In the following, 4 different deposition conditions are systematically compared: gas flow rate ratios $R = H_2/SiH_4$ ranging from 50 to 125.

Table 2.1: Fixed conditions during the deposition of the boron doped layers by PECVD.

Temperature (°C)	RF Power (W)	Pressure (mbar)	Interelectrode distance (mm)	H_2 flow rate (sccm)	TMB flow rate (sccm)
175	50	2.5	15	500	0.8

Hereafter, the boron doped silicon layers are deposited on top of a 2.4 nm-thick PECVD a-SiO_x:H layer on c-Si (n-type Cz wafer). Figure 2.8 shows confocal microscope images

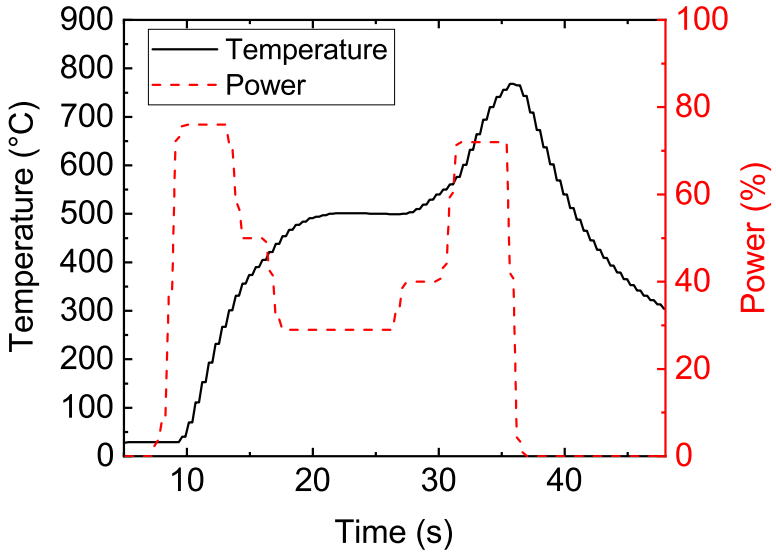

Figure 2.7: Temperature of the substrate and light bulb power during a firing step in a JETFIRST system by Jipelec™.

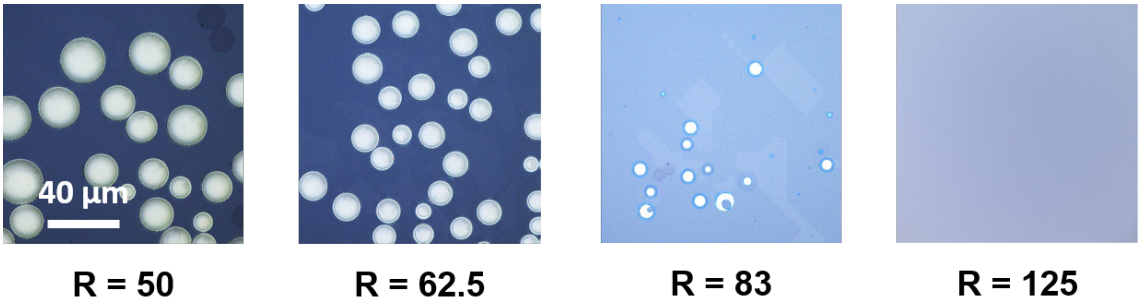

Figure 2.8: Confocal microscope images of the surface of PECVD deposited silicon layers on SiO_x after firing step, for increasing $R = H_2/SiH_4$ flow rate ratios.

of the surface of the samples after undergoing a firing step. As expected, the density of blisters strongly decreases with the dilution of SiH_4 into H_2. A blister-free layer is obtained for $R = 125$. Similar results were obtained with an underlying 1.3 nm-thick wet chemical oxide instead of the PECVD oxide layer.

The inhibition of the blister formation is related to the structural change of the deposited silicon layer, from hydrogenated amorphous silicon (a-Si:H) to hydrogenated microcrystalline silicon (µc-Si:H) as can be seen from the Raman spectra in Figure 2.9. Indeed, the increase of the signal from the crystalline phase at 522 cm^{-1} and the decrease of the one coming from the amorphous phase at 470 cm^{-1} are both visible (for the correspondence of peaks, see the work of Saleh *et al.* [150]). Consequently, in these deposition conditions ($R = 125$), the layer is crystallized in the as-deposited state, making any dedicated crystallization step superfluous.

The optical properties of the layers were additionally measured by SE. Figure 2.10a shows the imaginary part of the pseudo-dielectric function $\varepsilon_i(E)$ for the different dilution ratios. A double Tauc-Lorentz model allowed to extract the accurate optical properties

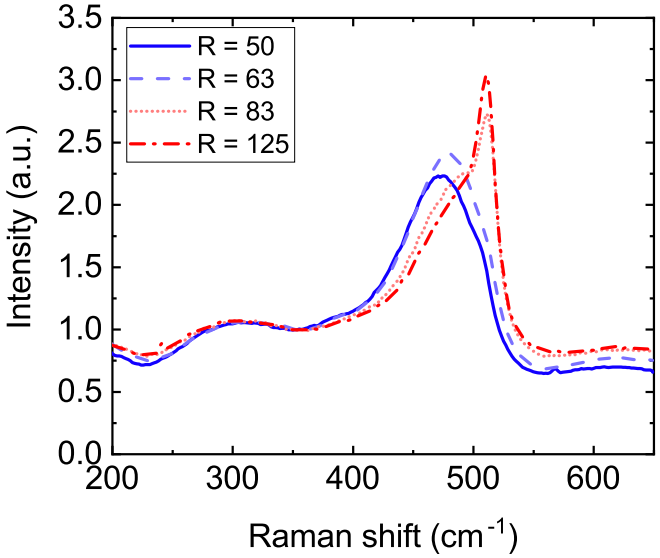

Figure 2.9: Raman intensity of boron doped silicon layers deposited on a glass slide for different $R = H_2/SiH_4$ ratios. The layers have a thickness of 115 ± 3 nm.

of the deposited material, such as its absorptivity, shown in Figure 2.10b. As expected, a higher crystallinity also leads to a higher transparency and, consequently, lower parasitic absorption losses.

The crystalline fraction was also assessed by modeling the SE data of the deposited stack using an effective medium approximation (Brüggemann model [151]). The silicon layer is assumed to be a mixture of a-Si:H, small-grain µc-Si:H called "psi-ud" from Jellison [152] and voids, split into three layers: a buried crystallized phase that may contain some voids, a growth layer with a larger portion of a-Si:H, and some roughness, as was proposed by Kalache *et al.* [153] (see Figure 2.11a). By fitting the material fractions as well as the thicknesses of the different layers, we can plot the evolution of the total crystalline fraction as well as the thickness of the underlying oxide layer. Here, "crystalline fraction" relates to the amount of crystallized phase versus amorphous phase $F_c/(F_a+F_c)$ with F_c the fraction of psi-ud and F_a the fraction of a-Si:H in the stack.

One can notice the expected increase of the crystalline fraction with the silane-to-hydrogen dilution ratio R, which leads to a lower absorptivity and is consistent with the Raman spectra of Figure 2.9. However and more surprisingly, there also seems to be a decrease of the underlying SiO_x layer thickness (Figure 2.11b). It must be noted that before deposition of the µc-Si:H layer, the PECVD SiO_x layer thickness was measured to be 2.4 nm (represented by the dotted line). This rises the question of the impact of the (p) µc-Si:H deposition conditions on the underlying oxide, and of the accuracy of the optical model of this complex stack.

2.3.2 Impact of µc-Si:H deposition on the tunnel oxide layer

In order to verify the presence and nature of the oxide interlayer, XPS depth profiling was employed. It consists in making an XPS spectrum, then sputtering the surface of the sample, and repeating this sequence in order to get a profile. Despite the high surface sensitivity of XPS, the detection of this ultra-thin SiO_x layer is challenging since its

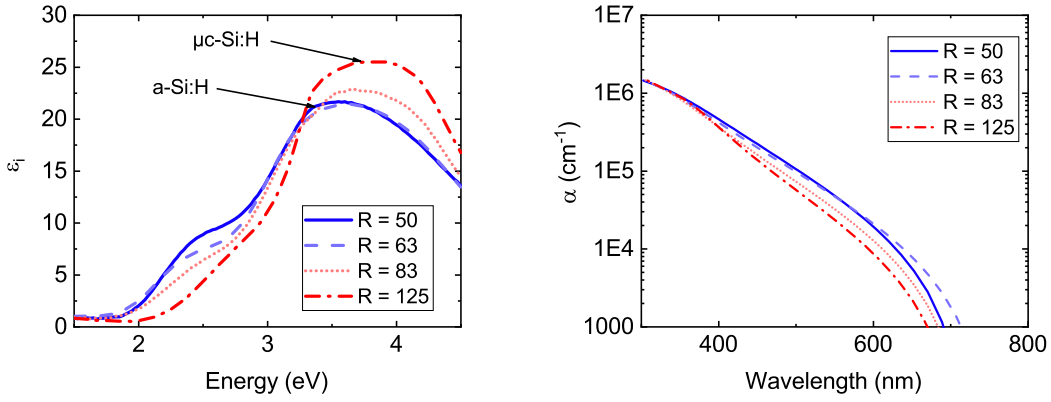

(a) (b)

Figure 2.10: (a) Imaginary part of the dielectric function and (b) absorptivity of the deposited layers for different $R = H_2/SiH_4$ dilution ratios. The layers have a thickness of 32 ± 2 nm.

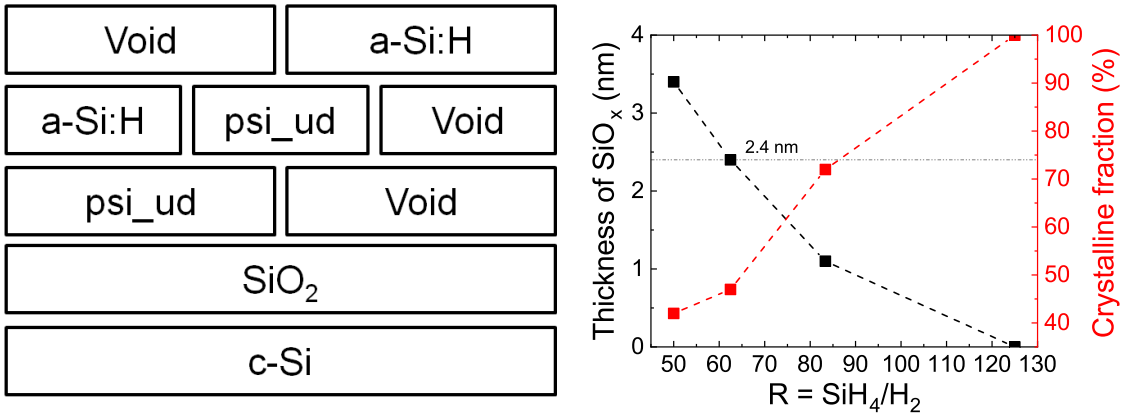

(a) (b)

Figure 2.11: (a) Stack of the ellipsometric Brüggemann model. (b) Evolution of the crystalline fraction and the buried oxide thickness with R.

thickness - close to 2 nm - is inferior to the escape depth of the emitted photoelectrons. It thus required the optimization of the abrasion sequence in order not to cross over the layer during one single sequence.

The composition profile for the sample produced with a silane-to-hydrogen dilution ratio $R = 125$ can be observed on Figure A3.5a. At the surface of the sample, at the beginning of the acquisition, a higher concentration of oxygen (and carbon, not shown here) is detected due to the impact of ambient atmosphere on the µc-Si:H layer (oxidation and organic pollution). The profile evidences three regions in agreement with the corresponding µc-Si:H, SiO_x and c-Si stack structure. Contrary to what was estimated by SE, the oxide layer - characterized by the bump in the concentration of oxygen after 800 s of sputtering - is still present even for the sample with $R = 125$.

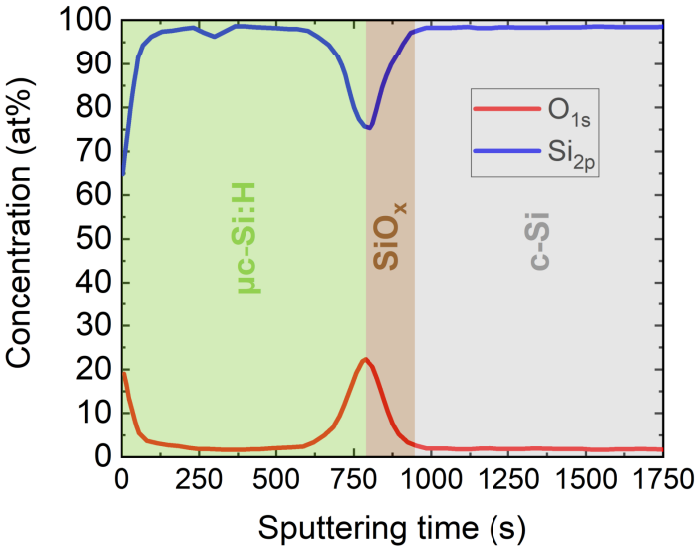

Figure 2.12: Concentration profile of silicon (blue) and oxygen (red) of the SiO_x/(p) µc-Si:H stack with $R = 125$ deposited on c-Si, measured by XPS. The background green, brown and grey areas represent the position of the different materials of the stack.

The presence of the SiO_x layer at the interface is additionally confirmed by transmission electron microscopy (TEM). As seen in Figure 2.13, the oxide layer is present for both deposition conditions $R = 50$ and $R = 125$, and the thickness does not seem impacted by the µc-Si:H deposition process. It is worth noting that, in the case of the sample deposited with $R = 125$, an amorphous silicon layer is observed below the SiO_x layer. This is likely due to the fact that the tougher deposition conditions of (p) µc-Si:H lead to more hydrogen incorporation below the SiO_x layer, thus weakening the crystalline structure of the c-Si wafer. This weakened region may have become amorphous as a result of the focused ion beam (FIB) sample preparation.

Figure A3.5 compares the XPS analyses of the buried oxide layer in a (p) µc-Si:H/SiO_x/c-Si stack for different values of $R = H_2/SiH_4$ used during the deposition of the overlying silicon layer: $R = 50$ (blue), $R = 125$ (red). They are obtained at the maximum intensity of the O_{1s} peak (see depth profile in Figure A3.5a), which means that the entire overlying a-Si:H or µc-Si:H layer has been etched. These are compared with the photopeaks of the PECVD oxide layer (2.4 nm) before the silicon deposition (black). The Si_{2p} and O_{1s} signals obtained by high-resolution XPS measurements (20 eV pass energy) are shown

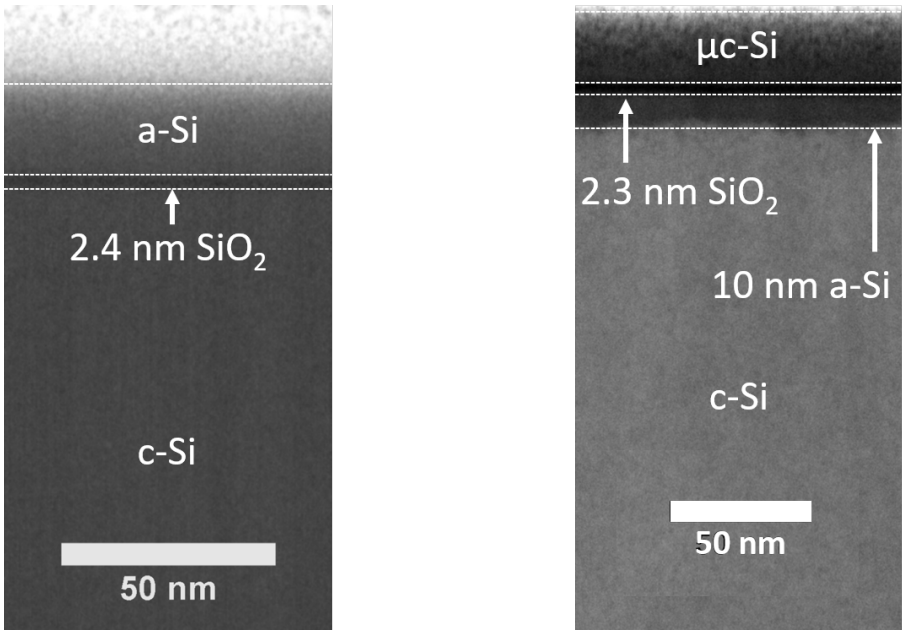

(a) (b)

Figure 2.13: TEM images of the cross section of a c-Si/SiO_x/(p) µc-Si:H stack for deposition conditions with (a) $R = 50$ and (b) $R = 125$.

respectively on Figures A3.5b and A3.5c. As seen above, the reference oxide is not perfect and contains a small amount of suboxides. Additionally, the double-peak at 98.8 eV of the Si_{2p} signal is related to the Si-Si bonds of the c-Si wafer and its unchanged absolute intensity in the three samples supports the fact that the thickness of the SiO_x layer has not changed significantly, contrary to the SE effective medium model. These observations (XPS and TEM) imply that the SE model used is not adapted for the assessment of the thickness of such a thin buried layer.

By comparing the spectra of the SiO_x PECVD layer before and after the silicon deposition, notable changes are observed. Figure A3.5b shows that the stoechiometry of the oxide layer has been modified for both the aforementioned deposition conditions and goes along with a strong decrease of the oxygen content of the layer (see Figure A3.5c). In order to make sure that the observations are process-related and not due to the Ar^+ abrasion process, a depth profile was also realized on the 2.4 nm-thick PECVD SiO_x reference layer (no silicon growth on top). High-Resolution XPS Si_{2p} and O_{1s} spectra are acquired. The Si_{2p} signals are deconvoluted, and the areas of four different contributions are monitored: (i) "O1s", (ii) "Si_{2p} main" (double-peak around 98.8 eV), (iii) "Si_{2p} oxide" (contributions around 102-103 eV), and (iv) "Si_{2p} suboxide" (contributions around 101 eV). The evolution of these contributions during the abrasion of the thin oxide is shown in Figure 2.15 (duration of one sputtering sequence: 10 s).

The decrease of the Si_{2p} oxide and O_{1s} contributions simultaneous with the slight increase of the "Si_{2p} suboxide" contribution evidences a preferential abrasion phenomenon (O release) leading to the creation of suboxides. This modification remains low, as the suboxide contribution does not increase significantly and remains fairly constant during the sputtering. Since the suboxides are already present before sputtering, the measured suboxide contribution is a combination of suboxides resulting from the abrasion sequence and of suboxides present in the initial state. However, the "Si_{2p} suboxide" contribution

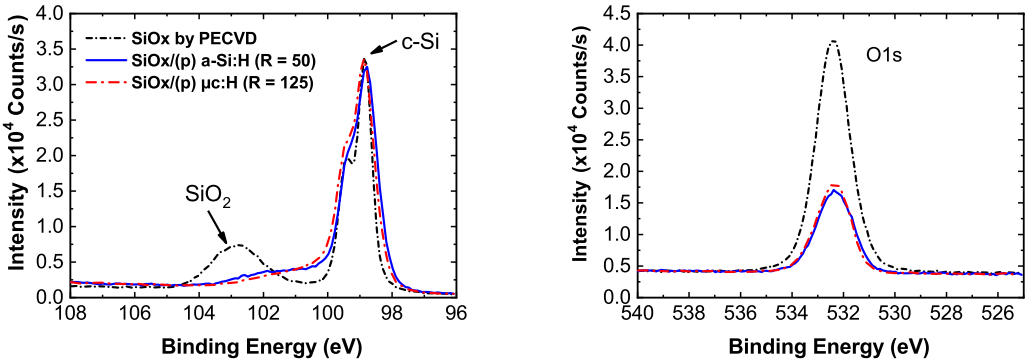

(a) (b)

Figure 2.14: XPS analysis of the buried oxide layer in a (p) µc-Si:H/SiO_x/c-Si stack for different values of $R = H_2/SiH_4$ during the silicon layer deposition. (a) Si_{2p} and (b) O_{1s} spectra obtained at the maximum intensity of the O_{1s} peak (see depth profile in Figure A3.5a) for different deposition conditions of the overlying silicon layer ($R = 50$ (blue), $R = 125$ (red)). The photopeaks of the PECVD oxide layer (2.4 nm) before the silicon deposition are shown in comparison (black).

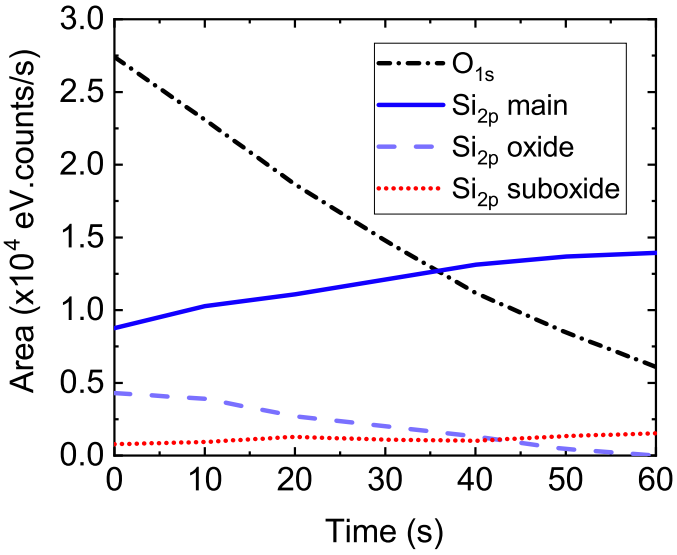

Figure 2.15: Integration of XPS signals during the sputtering of a 2 nm-thick SiO_x layer deposited by PECVD. Four contributions are represented: (i) Si_{2p} main (double-peak around 99 eV), (ii) O1s, (iii) Si_{2p} oxide (contributions around 102-103 eV), and (iv) Si_{2p} suboxide (contributions round 101 eV).

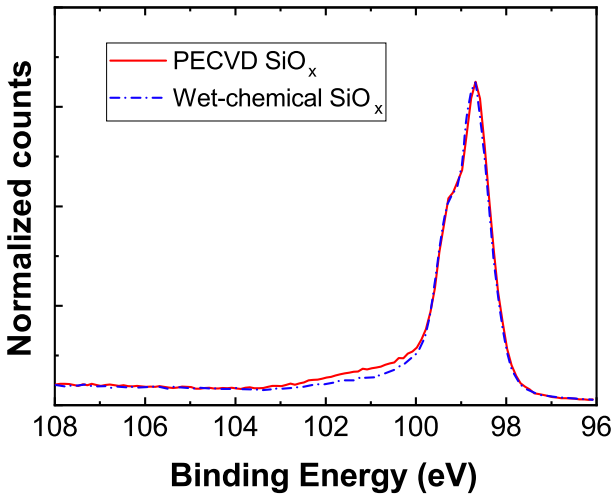

Figure 2.16: Normalized Si_{2p} XPS signals at the surface of the SiO_x layer for wet-chemical and PECVD oxides after the complete sputtering of the µc-Si:H layer ($R = 125$).

in Figure A3.5b is significantly higher in the samples subject to a subsequent PECVD deposition than for the reference sample. This high amount of suboxide cannot be entirely explained by the initial suboxide concentration or the abrasion effect. We can thus conclude that the deposition of a silicon layer on top of the SiO_x changes its chemical composition by increasing the amount of suboxides in the layer.

Similar conclusions can be drawn when using a 1.3 nm-thick wet-chemical tunnel oxide layer instead of a 2.4 nm-thick PECVD SiO_x layer as shown in Figure 2.16. In both cases, no peak can be observed around 103 eV, while a shouldering appears around 101 eV. The lower intensity of the suboxide contribution in the case of the wet-chemical oxide is once again due to the smaller thickness of the oxide layer.

From this section, we conclude that the thickness of the SiO_x layer in the passivating stack is not directly impacted by the PECVD deposition of the overlying (p) µc-Si:H layer (whatever the deposition conditions). Consequently, the thin buried SiO_x layer is not accurately described in the previous spectroscopic ellipsometry model. However, XPS measurements highlighted that the deposition of the (p) µc-Si:H layer decreases the oxygen content and modifies the stoechiometry of the tunnel oxide layer (for both wet-chemical and PECVD SiO_x).

2.3.3 Optimization of the passivation properties of (p) µc-Si:H

The passivation quality provided by the deposited stack is a feature that is of paramount importance since it is an indicator of the parasitic electrical losses in the solar cell. The values of implied Open-Circuit Voltage (iV_{oc}) measured by QSSPC are shown in Figure 2.17b for a wet-chemical oxide and different dilution ratios R during the deposition of (p) µc-Si:H, and in Figure 2.17a for both PECVD and wet-chemical SiO_x (for $R = 125$). From these results we can draw three main conclusions: (i) the wet-chemical SiO_x provides a passivation that is far better than PECVD SiO_x, (ii) increasing the dilution ratio R allows to improve the passivation quality, and (iii) the deposition of an additional a-SiN_x:H layer significantly increases the passivation.

The first (i) observation could be explained by plasma induced damages in the chosen

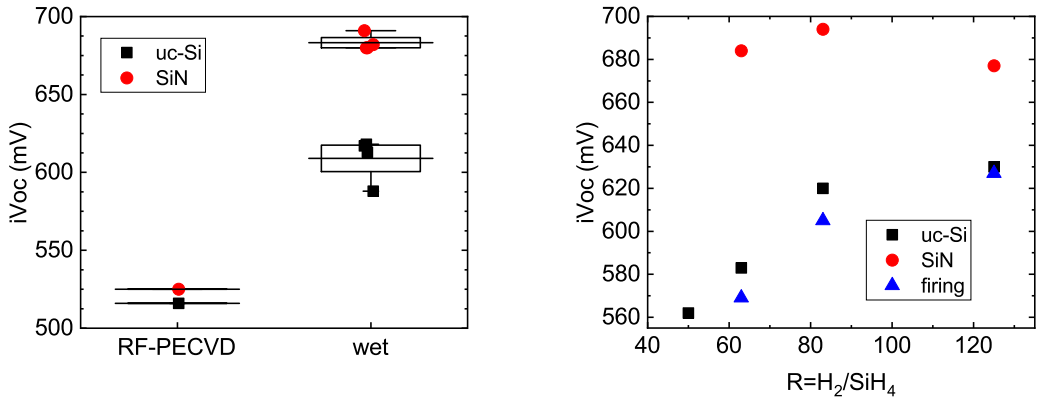

Figure 2.17: Variation of iV_{oc} for (a) both PECVD and wet-chemical ("wet") oxides at a given $R = 125$ value and (b) a wet-chemical tunnel oxide and different dilution ratios R during the deposition of (p) µc-Si:H. "uc-Si" stands for the c-Si/SiO_x/(p) µc-Si:H stack (black squares), "SiN" for the c-Si/SiO_x/(p) µc-Si:H/a-SiN_x:H stack (red circles), and "firing" this last stack after a firing step.

SiO_x PECVD deposition conditions, related to ion bombardment or surface defect formation due to the UV emission from the plasma [145], [154]. It is worth noting that the despite very little difference observed in the previous section between the PECVD and wet-chemical oxide regarding the chemical composition, the gap between the passivation provided by these layers is significant. This is due to the fact that the electrical properties are very sensitive to interface defects, and are impacted by defect densities that are not visible through standard chemical characterization techniques. As a consequence, the wet-chemical SiO_x layer is used in all the FPC samples studied later on.

A possible explanation of the second (ii) is that µc-Si:H has a doping efficiency about 100 times higher than a-Si:H [155], [156], thus providing a better field-effect passivation. To support this statement, the conductivity results from 4PP measurements are also shown in Figure 2.18. The higher the dilution ratio, the higher the crystalline fraction, and the higher the conductivity of the layer. As a consequence of all previous results, we use the dilution ratio $R = 125$ for all the following deposition conditions, since it provides the highest passivation quality (up to 695 mV), transparency, and conductivity (5 S/cm for a 35 nm-thick layer). For comparison purposes, Lehmann *et al.* [87] obtained up to 706 mV of iV_{oc} for a FPC with a wet-chemical SiO_x layer after (p) a-SiC_x:H deposition, firing, a-SiN_x:H and annealing on a hotplate for hydrogenation purposes.

The third point (iii) may be explained by the SiN_x:H deposition temperature (350 °C) that anneals the (p) µc-Si:H layer and further activates dopants in the layer. It can additionally drive more hydrogen to the c-Si/SiO_x interface, thus providing a better chemical passivation. Further investigations will be carried out in section 2.5 dedicated to capping layers.

The TMB gas flow rate was additionally varied in order to estimate the best condition for passivation purposes. As can be seen in Figure 2.19, there is no major impact of this parameter on the passivation properties after capping the sample with a-SiN_x:H. For later depositions, a TMB flow rate of 0.8 sccm is chosen (the same as in the previous sections).

As exposed in section 1.5 the fabrication process should be ended by a high-temperature

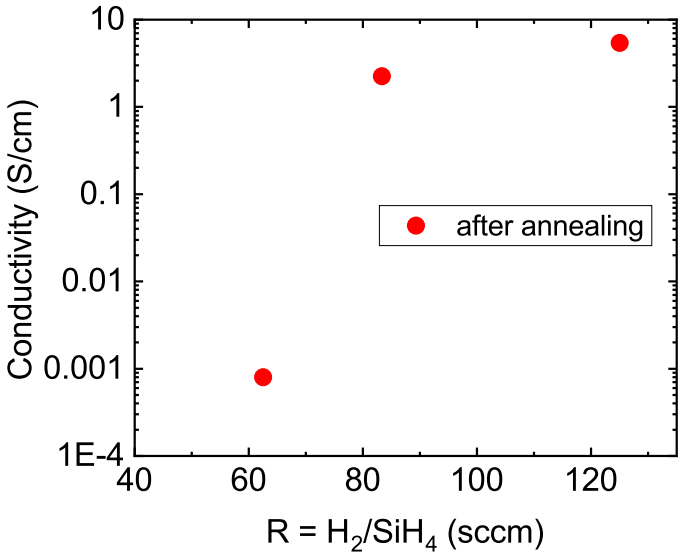

Figure 2.18: Evolution of the conductivity of the boron doped silicon layers with R, after an annealing step at 250 °C for 10 min.

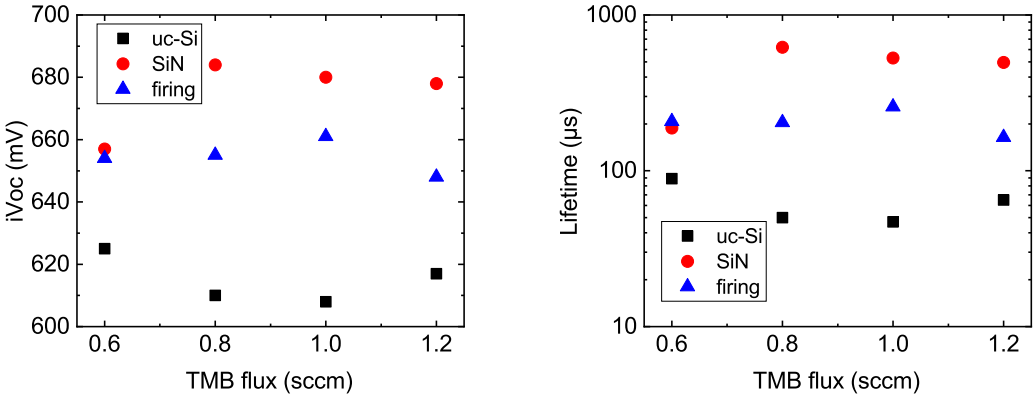

(a) (b)

Figure 2.19: Variation of (a) iV_{oc} and (b) lifetime τ_{eff} - measured by QSSPC - with the flow rate of TMB used during the deposition of the (p) µc-Si:H layer at three different stages of the process: (i) in the as-deposited step ("uc-Si" = c-Si/SiO_x/(p) µc-Si:H stack, black squares), (ii) after SiN deposition ("SiN" = c-Si/SiO_x/(p) µc-Si:H/a-SiN_x:H stack, red circles), and (iii) after a final firing step (blue triangles).

firing step for standard screen printing metallization. However, the firing step dramatically damages the passivation properties as can be seen in Figures 2.17b and 2.19: the iV_{oc} drops by more than 20 mV. This phenomenon has been largely reported on in the literature [157], [158], and will be investigated further later in this chapter. Since the passivation properties obtained in the as-deposited state are comparable to literature results, the main objective is to manage to maintain the passivation properties after the firing step.

2.3.4 µc-SiO$_x$:H

Even though µc-Si:H is far better than a-Si:H in terms of absorption losses, its absorption coefficient in the visible range is still high. This can induce relatively large optical losses due to parasitic absorption [159], [160]. One way to reduce these losses is to add oxygen into the matrix. The addition of a source of oxygen in the PECVD gas box (CO_2, O_2, N_2O, ...) allows to deposit hydrogenated micro-crystalline silicon oxide (µc-SiO$_x$:H) which is a mixed phase of silicon micro-crystals, amorphous silicon and amorphous silicon oxide [155]. The impact of the CO_2 flow rate on the properties of the thin film are studied in this section. As shown in Figure 2.20a the deposited material becomes more and more transparent with the addition of CO_2. As a comparison, the most transparent sample in Figure 2.10b, corresponds to the 0 sccm line in Figure 2.20a, so to the material that shows the highest absorptivity. However, the better transparency of (p) µc-SiO$_x$ comes at the price of a lower electrical conductivity (see Figure 2.20b). No data point was available for the sample deposited with 2 sccm of CO_2 due to the detection limit of the 4PP acquisition setup, which is around 5×10^{-4} S.cm^{-1} for our samples of thickness between 60 and 70 nm.

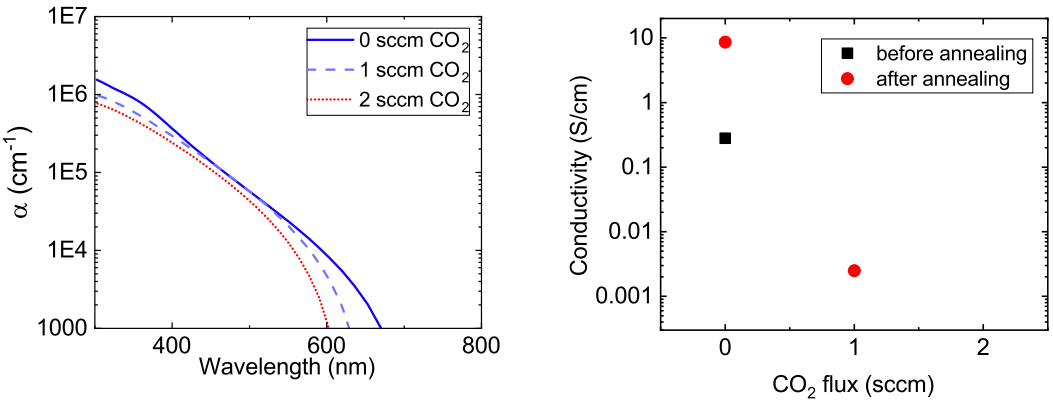

(a) (b)

Figure 2.20: Evolution of (a) the absorptivity and (b) the conductivity of the (p) µc-SiO$_x$:H layer with the flow rate of CO_2.

But on the brighter side, one very important feature of this kind of material is the better passivation it provides, along with a higher thermal stability as can be seen in Figure 2.21. Indeed, despite lower passivation properties in the as-deposited state (10 µs versus 100 µs for (p) µc-Si:H), iV_{oc} and lifetime values as high as 700 mV and 1.1 ms have been reached after a-SiN$_x$:H deposition. More importantly, passivation losses after firing are significantly reduced for (p) µc-SiO$_x$:H compared with (p) µc-Si:H. For future depositions, the material deposited with 1 sccm of CO_2 was chosen since it provides the best balance between conductivity and passivation properties. This material is noted as (p) µc-SiO$_x$:H in the rest of this work.

In order to get a better understanding of the higher thermal stability of the passivation properties of (p) µc-SiO$_x$ versus (p) µc-Si:H, thermal desorption spectrocsopy (TDS) experiments were carried out in a homemade exo-diffusion setup. The samples are put in a vacuum chamber pumped down to 1.10^{-5} Pa. The ion current of H, H_2 and H_2O are monitored in real-time by a PRISMA 80 mass spectrometer. A heating rate of 10 °C/s was used, from ambient temperature to 800 °C. The sample stays at 800 °C for 30 min

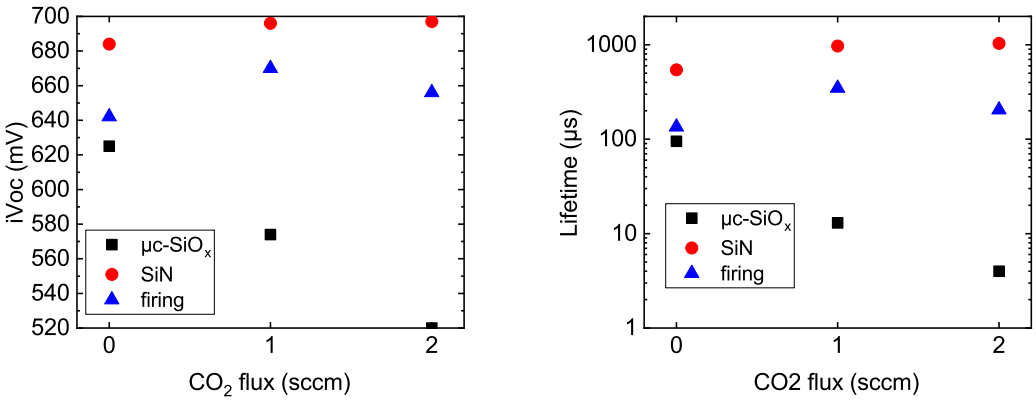

(a) (b)

Figure 2.21: Variation of (a) iV_{oc} and (b) τ_{eff} with the flow rate of CO_2 used during the deposition of the (p) µc-SiO_x:H layer at three different stages of the process: (i) in the as-deposited step ("µc-SiO_x" = c-Si/SiO_x/(p) µc-SiO_x:H stack, black squares), (ii) after SiN deposition ("SiN" = c-Si/SiO_x/(p) µc-SiO_x:H/a-SiN_x:H stack, red circles), and (iii) after a final firing step (blue triangles).

and then gradually cools down to ambient temperature. One run was made without any sample in the chamber in order to acquire the background ion currents. This background is removed from the results showed hereafter.

H_2 ion currents from (p) µc-Si:H and (p) µc-SiO_x are compared (corresponding to H effusion from the sample) and are shown in Figure 2.22. One can notice two main differences: (i) the (p) µc-Si:H material seems to release more hydrogen than (p) µc-SiO_x at lower temperatures (from 100 to 200 °C), and (ii) for (p) µc-SiO_x hydrogen effuses more at higher temperatures, with another TDS peak around 500 °C and a significant hydrogen release up to 600 to 650 °C. This last difference in behavior partially explains the higher thermal stability of the passivation properties provided by (p) µc-SiO_x, since more hydrogen can be kept in the FPC passivating stack at higher temperature compared with (p) µc-Si:H-based FPC. The various peaks between 150 and 450 °C may be linked to the contribution of some impurities inside the exodiuffusion chamber, or to different hydrogen bonding strengths in the difference phases of the material: within the nano-crystals, or in the amorphous-phase and grain boundaries [161], [162].

Additionally to the intrinsic characteristics of (p) µc-SiO_x:H the thickness of the film might impact the final properties of the device. In most of TOPCon solar cells with standard screen-printing metallization, the thickness of poly-Si sits around 100-200 nm [163]–[165] which is significantly thicker than the 35 nm-thick layers studied so far. In order to evaluate the impact of the thickness of (p) µc-SiO_x:H on the passivation properties, we vary the duration of deposition from 12 min to 60 min. This corresponds to thicknesses ranging from 30 nm to 140 nm as shown in Figure 2.23. The deposition rate of this material is thus calculated to be 0.39 Å/s.

Figure 2.24 shows the evolution of the passivation properties with the deposition duration. Neither iV_{oc} nor τ_{eff} are impacted by a change in the deposition time for the complete passivating stack SiO_x/(p) µc-SiO_x:H/a-SiN_x:H in the as-deposited state. However, thicker (p) µc-SiO_x seem to grant a better maintain of the passivation after the firing step (430 µs and 677 mV for 140 nm against 106 µs and 637 mV for 30 nm). A possible

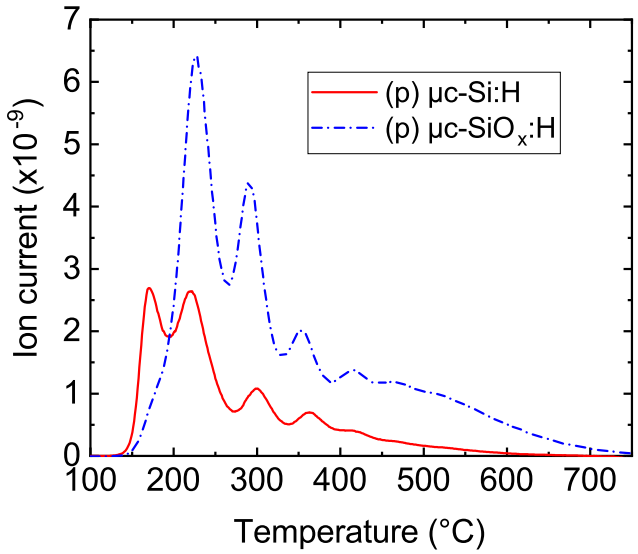

Figure 2.22: Comparison of the H_2 ion currents measured by Thermal Desorption Spectrometry (TDS) for (p) µc-Si:H and (p) µc-SiO_x:H.

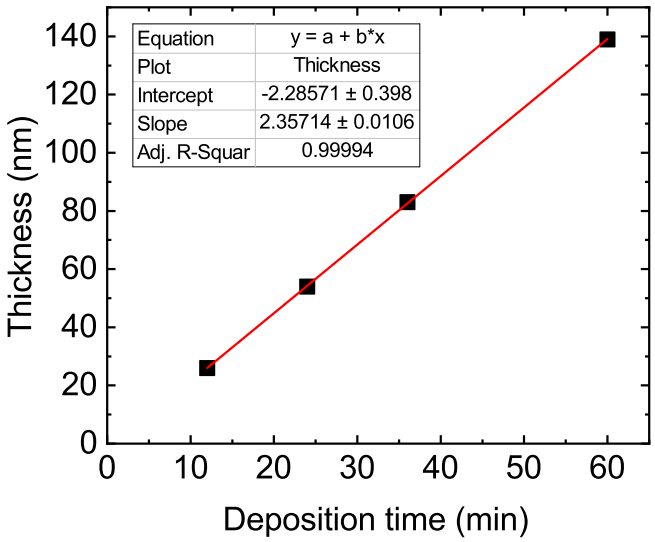

Figure 2.23: Thickness of (p) µc-SiO_x:H deposited as a function of the duration of deposition.

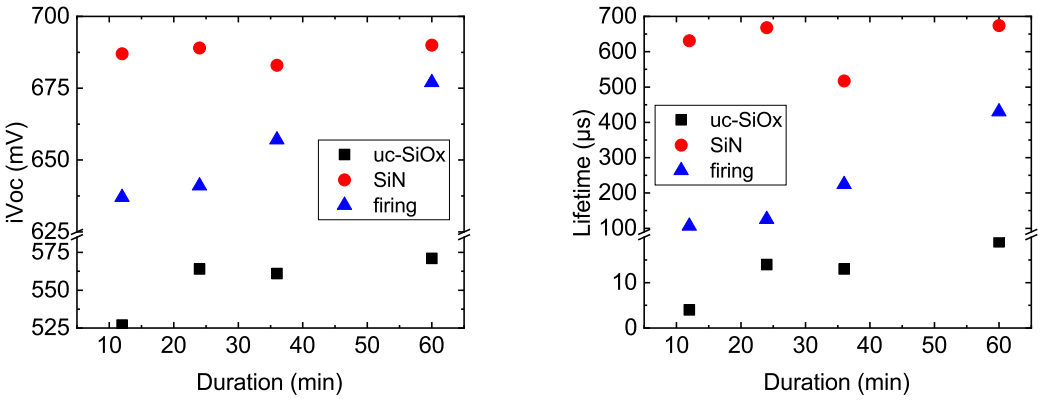

(a) (b)

Figure 2.24: Variation of (a) iV_{oc} and (b) τ_{eff} with the (p) µc-SiO_x layer deposition time at three different stages of the process: (i) in the as-deposited step ("µc-SiO_x" = c-Si/SiO_x/(p) µc-SiO_x:H stack, black squares), (ii) after SiN deposition ("SiN" = c-Si/SiO_x/(p) µc-SiO_x:H/a-SiN_x:H stack, red circles), and (iii) after a final firing step (blue triangles).

explanation of this feature is that the hydrogen atoms most significantly contributing to the passivation properties - situated at the c-Si/SiO_x interface - are better capped by thicker layers, which hinders their diffusion out of the sample.

In this section we showed that the deposition of the boron-doped silicon layer on top of the tunnel oxide has an impact on its stoechiometry. The formation of blisters could be avoided by using a high dilution of SiH_4 into H_2 which lead to the deposition of µc-Si:H, a material providing better passivation and higher transparency than a-Si:H. However the SiO_x/(p) µc-Si:H/a-SiN_x:H suffered from significant passivation losses after the final firing step of the process. The deposition of (p) µc-SiO_x allowed to reach higher passivation, a greater thermal stability, and less absorption losses but at the expense of the electrical conductivity. It was shown additionally that thicker (p) µc-SiO_x layer provide a better maintain of the passivation properties after firing.

2.4 Phosphorous-doped silicon layer

So far, boron-doped layers were developed for the fabrication of TOPCon solar cells. However, n-type FPC can also be of interest if one needs to make electron-selective passivating contacts either for TOPCon (with a front emitter formed by the diffusion of boron) or for both sides contacted solar cells with passivated contacts. Consequently, an optimization was carried out for n-type, phosphorous-doped µc-Si:H, similarly to what was done in the previous section. The fixed conditions for the deposition of these layers are shown in Table 2.2.

Table 2.2: Fixed conditions during the deposition of the n-type layers by PECVD.

Temperature (°C)	RF Power (W)	Pressure (mbar)	Interelectrode distance (mm)	H_2 flow rate (sccm)	PH_3 flow rate (sccm)
175	50	2.5	15	500	0.8

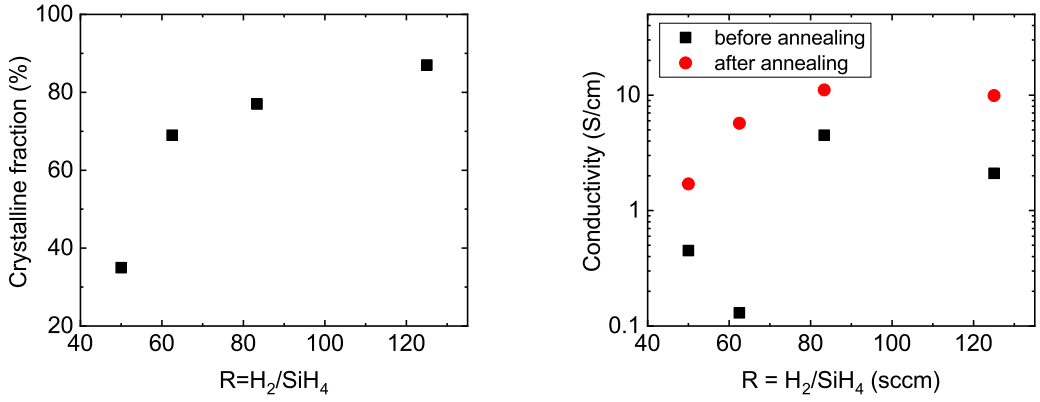

(a) (b)

Figure 2.25: (a) Evolution of the crystalline fraction of the n-type silicon layer with the dilution ratio R. The results are given in the as-deposited state.

Once more, the $R = H_2/SiH_4$ dilution ratio is being varied (see Figure 2.25a): a higher dilution of silane in hydrogen leads to a higher crystalline fraction.

However, the conductivity of the layer with $R = 83$ seems to be slightly higher compared with $R = 125$ (see Figure 2.25b). Additionally, the dilution ratio resulting in the highest passivation properties was also $R = 83$, as shown in Figure 2.26. Thus, the dilution ratio chosen for the future depositions of (n) µc-Si:H layers is $R = 83$. The very best passivation properties obtained for a passivating stack SiO_x/(n) µc-Si:H/a-SiN_x:H on p-type FZ DSP wafers (in another batch) were $\tau_{eff} = 3$ ms and $iV_{oc} = 726$ mV. No direct comparison can be drawn for these structures with literature results. Ingenito *et al.* showed iV_{oc} values reaching 746 mV, on (n) SiC_x but with the addition of a thermal treatment of 8 min at 850 °C for crystallization purposes followed by a hydrogenation step (a-SiN_x:H deposition + annealing at 450 °C for 30 min) [63].

The use of (n) µc-Si:H shows again its limitation after the firing step with an SiO_x/(n) µc-Si:H/a-SiN_x:H passivation stack with a dramatic degradation of the passivation. Hence, an (n) µc-SiO_x:H layer is also optimized. Figure 2.27 displays the evolution of the passivation properties of the (n) µc-SiO_x:H layer with an increasing CO_2 flow rate during the deposition. Once more, too high a CO_2 flow leads to a decrease in the passivation properties. Henceforth, 1 sccm of CO_2 is chosen for the deposition of so-called (n) µc-SiO_x:H later on. Indeed, it maintains high passivation properties (up to 717 mV and 1.7 ms) while providing a higher thermal stability than (n) µc-Si:H.

Similarly to (p) µc-SiO_x, a greater transparency is achieved with the addition of CO_2 (see Figure 2.28a), which conversely significantly decreases the conductivity of the (n) µc-SiO_x layers. Figure 2.28b shows that the latter drops from 10 S/cm for (n) µc-Si:H to 1.10^{-3} S/cm for (n) µc-SiO_x with 1 sccm of CO_2. The conductivity value is below the detection limit when using 2 sccm of CO_2.

In this section we optimized the deposition conditions of (n) µc-Si:H and (n) µc-SiO_x in order to get the best passivation properties and conductivity. Like for boron doped layers, the µc-Si:H layer shows higher conductivity while the µc-SiO_x:H mixed phase provides a higher thermal stability of passivation and a better transparency.

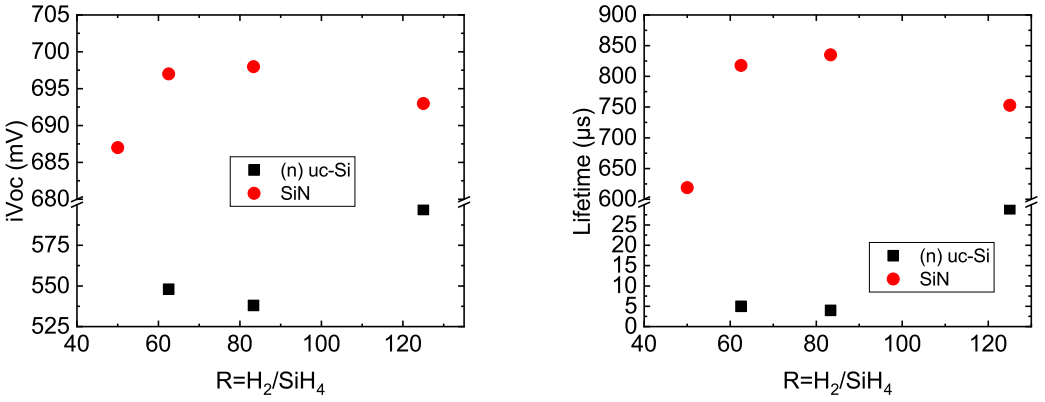

(a) (b)

Figure 2.26: Variation of (a) iV_{oc} and (b) τ_{eff} with the flow rate of SiH_4 used during the deposition of the (n) µc-Si:H layer at two different stages of the process: (i) in the as-deposited state ("(n) uc-Si" = c-Si/SiO_x/(n) µc-Si:H stack, black squares), and (ii) after SiN deposition ("SiN" = c-Si/SiO_x/(n) µc-Si:H/a-SiN_x:H stack, red circles).

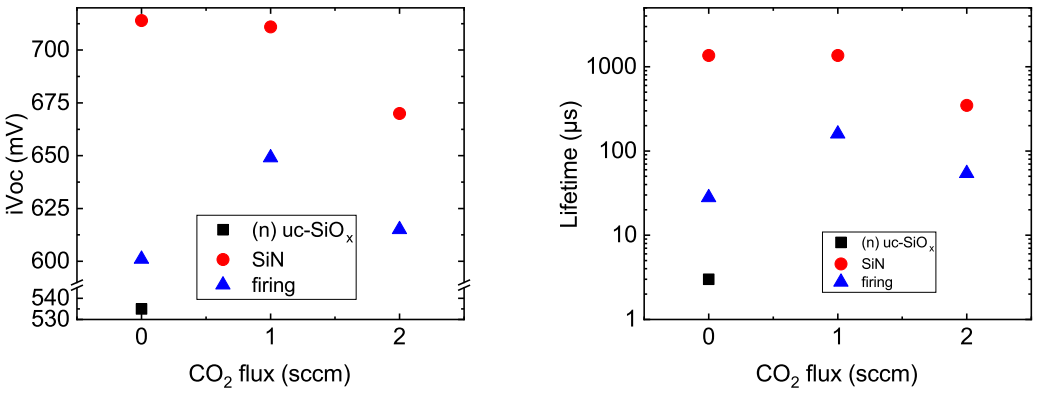

(a) (b)

Figure 2.27: Variation of (a) iV_{oc} and (b) τ_{eff} with the flow rate of CO_2 used during the deposition of the (n) µc-SiO_x:H layers at three different stages of the process: (i) in the as-deposited step ("(n) uc-SiOx" = c-Si/SiO_x/(n) µc-SiO_x:H stack, black squares), (ii) after SiN deposition ("SiN" = c-Si/SiO_x/(n) µc-SiO_x:H/a-SiN_x:H stack, red circles), and (iii) after a final firing step (blue triangles).

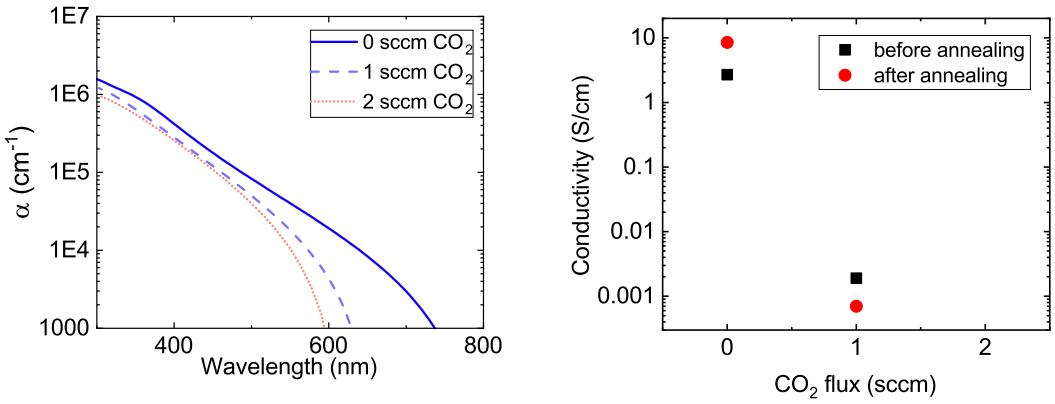

(a) (b)

Figure 2.28: (a) Absorbtivity and (b) conductivity of the (n) µc-SiO_x layers for different CO_2 flow rates during the deposition.

2.5 Capping layer

From the beginning of this chapter, an a-SiN_x:H capping layer is deposited on top of the passivating stack, which greatly improves the overall properties of the FPC. In this section, the role and properties of the different capping layers that are being used on top of the doped µc-Si layers are being studied. We first focus on the optimization of silicon nitride, and then discuss the impact of the nature of the capping layer to identify the different phenomena at play.

2.5.1 Hydrogenated amorphous silicon nitride (a-SiN_x:H) layer

Optimization of optical properties and chemical composition

The hydrogenated amorphous silicon nitride (a-SiN_x:H) layer that is deposited on top of the SiO_x/(p) µc-Si:H stack serves several purposes. It may act as a hydrogen source that can reduce the defect density at the c-Si/SiO_x interface [23], [87] as well as in the c-Si wafer [166]. It also acts as an anti-reflection coating and a capping layer that should help maintain high passivation properties after the final firing step. In this section, we optimize the deposition conditions of silicon nitride in order to get adequate optical properties and density. As mentioned in section 2.1.1, the layers were deposited in a PECVD chamber, in a capacitively coupled plasma, parallel plate configuration and with an electromagnetic excitation at a frequency of 13.56 MHz.

The studies started with standard deposition conditions previously developed in the laboratory [137]. The starting conditions lead to a layer with optical indices of n(633 nm) = 1.81 and k(400 nm) = 0. These are very low values, and most of the SiN_x:H capping layers have a refraction index larger than 2 [167] (and sometimes greater than 3 [168]). Even more importantly, Steinhauser *et al.* showed that in their configuration, increasing the refractive index of the capping a-SiN_x:H layer from 1.98 to 2.06 allowed to improve the thermal stability of the passivating stack, reaching iV_{oc} values 10 mV higher [157]. Based on previous studies working on SiN_x:H deposition in a similar deposition tool (CCP RF PECVD) [169], a new optimization of the optical properties was carried out, by varying H_2 flow rate, RF power, pressure and NH_3/SiH_4 ratio, at a fixed temperature of 350 °C. The results are shown in Figure 2.29.

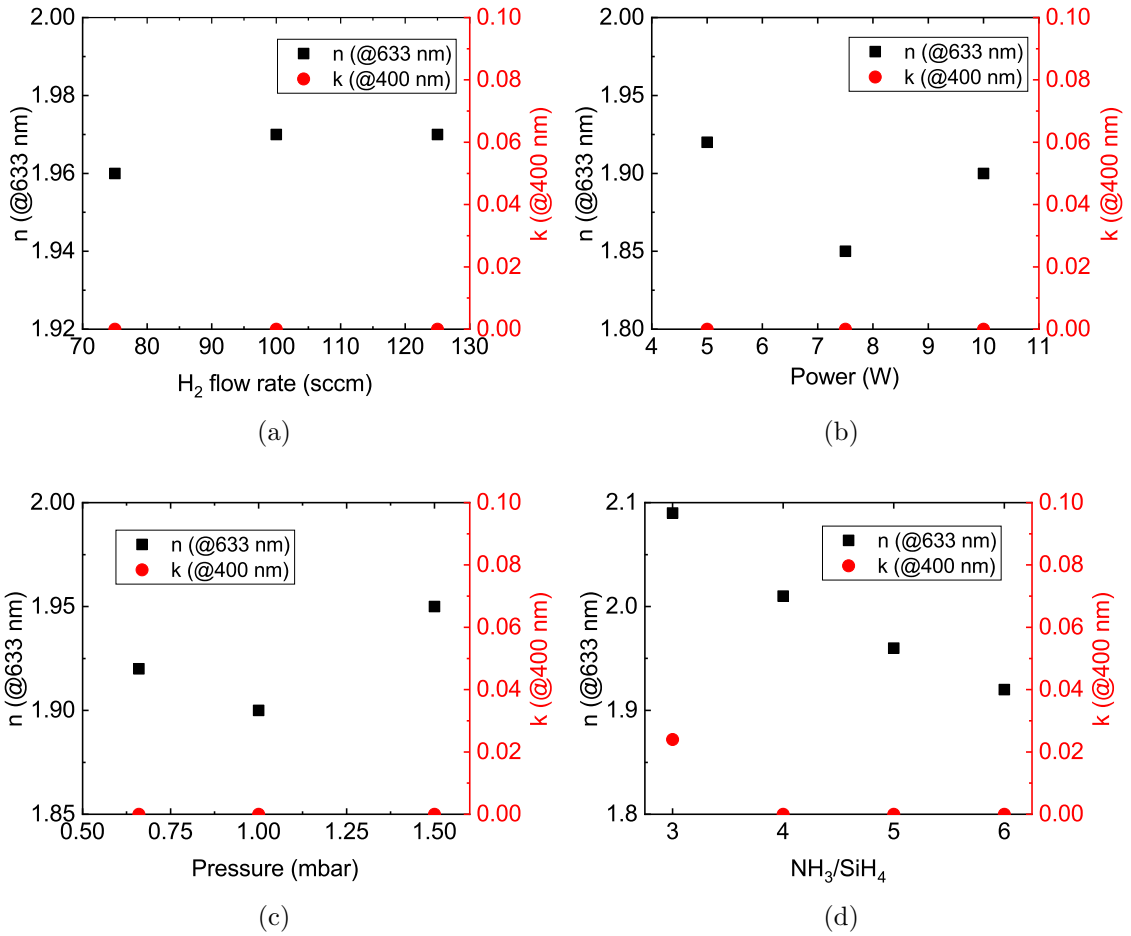

Figure 2.29: Evolution of n and k with (a) H_2 flow rate, (b) RF Power, (c) Pressure, and (d) NH_3/SiH_4 flow rate ratio for the a-SiN_x:H deposition.

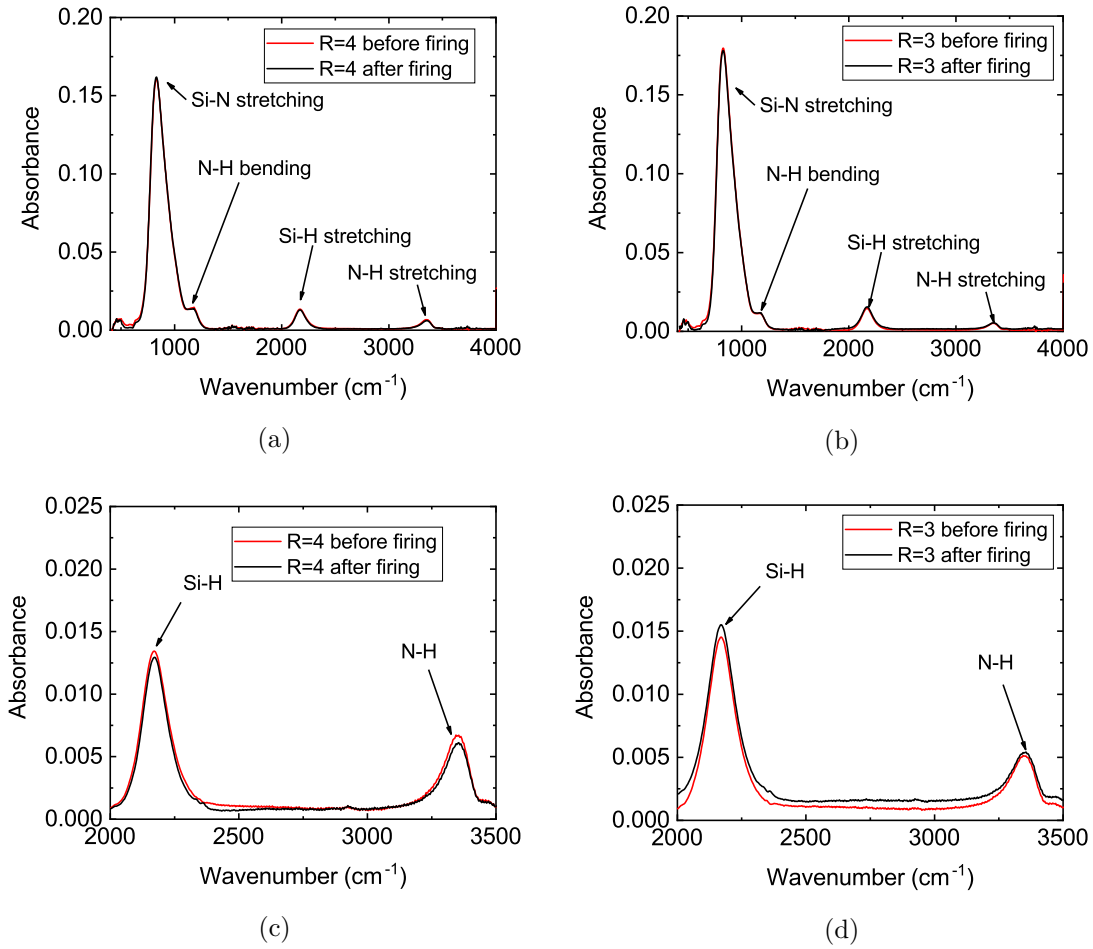

Figure 2.30: FTIR spectra before and after a firing step for samples with (a) NH_3/SiH_4 = 4 and (b) NH_3/SiH_4 = 3. (c) and (d) are the same spectra zoomed on Si-H and N-H stretching modes, between 2000 and 3500 cm^{-1}.

Varying the H_2 flow rate or the pressure seems to change the optical properties only marginally, and did not allow to reach a higher refractive index. A lower RF power usually leads to higher optical indices and a denser material because of a lower deposition rate, even though this was not observed in Figure 2.29b. When decreasing the NH_3/SiH_4 flow rate ratio, thus depositing silicon-richer a-SiN_x:H material, the refractive index and extinction coefficient increase. In order to obtain a refractive index greater than 2, two different deposition conditions may be used: NH_3/SiH_4 = 3 or 4, for 75 sccm of H_2, 5 W of RF power and a pressure of 0.66 mbar. In this range of deposition conditions, going to even lower NH_3/SiH_4 ratios would lead to higher refractive indices, but also to higher extinction coefficients, which is not desirable since a-SiN_x:H acts as a window layer and should be highly transparent.

Fourier transform infrared spectroscopy (FTIR) measurements were carried out for the two conditions mentioned above. The experiments were done before and after firing to assess the impact of this high temperature process on the layer, and are shown in Figure 2.30. The main peak around 850 cm^{-1} corresponds to the Si-N bonds (stretching mode), the shoulder around 1100 cm^{-1} to the N-H bending mode, the peak at 2100 cm^{-1} to the Si-H stretching mode, and the one at 3400 cm^{-1} to the N-H stretching mode. The N-H

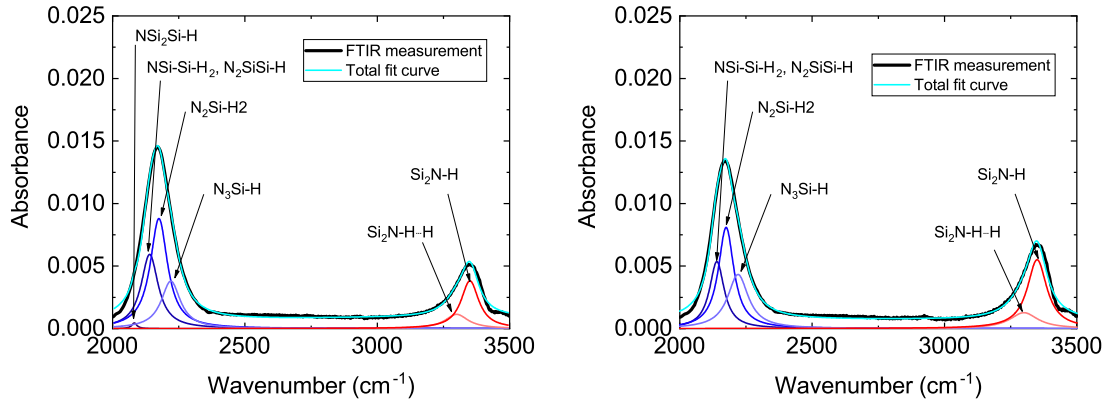

(a) (b)

Figure 2.31: Deconvolution of the FTIR signals before firing for the NH_3/SiH_4 ratios (a) 3 and (b) 4. The deconvolution is processed to identify the chemical environments of the Si and N atoms in the deposited materials.

peak is stronger for R = 4 than for R = 3, which is expected due to a higher amount of NH_3 in the gas mixture. No major change can be noticed after firing for either one of the samples.

The concentrations of the Si-H and N-H bonds are extracted from the integration of the FTIR absorbance peaks and the use of IR-scattering cross sections determined by Lanford and Rand ($\sigma_{Si-H} = 7.4\times10^{-18}$ cm^2 and $\sigma_{N-H} = 5.3\times10^{-18}$ cm^2) according to Equation 2.1 as described in [170]:

$$[X-H] = \frac{A_{XH}}{\sigma_{X-H} \times t} \tag{2.1}$$

where $[X-H]$ is the concentration in $X-H$ bonds (with X being either Si or N), A_{XH} is the area of the $X-H$ stretching mode peak (at 2100 cm^{-1} for Si-H and at 3400 cm^{-1} for N-H), and t the thickness of the film.

Deconvolutions of the $Si-H$ and $N-H$ stretching mode absorption peaks are shown in Figure 2.31. This allows to identify the contributions from specific chemical environments of $Si-H$ and $N-H$ bonds. In 2019, Kim *et al.* varied the deposition conditions of the a-SiN$_x$:H capping layers for TOPCon applications, and carried out a thorough analysis of the FTIR spectra and mass densities with respect to the final passivation properties [171]. Three different ratios were investigated: $R_1 = [Si-H]/([Si-H] + [N-H])$, $R_2 = [N_2Si-H_2]/([N_2Si-H_2] + [N_3Si-H])$, and $R_3 = [Si_2N-H^{\cdots}H]/([Si_2N-H^{\cdots}H] + [Si_2N-H])$. The final passivation properties were shown to increase for both R_1 and R_2 values increasing from 0.2 to 0.7. For all the samples presented in their study, R_3 sat between 0.4 and 0.5 and did not seem to have any impact on the final iV_{oc}. The best samples were achieved for a-SiN$_x$:H layers with densities from 2.5 to 2.7 g.cm^{-3}.

For our samples, these values extracted from the FTIR spectra are shown in Table 2.3. Both R_1 and R_2 values are relatively high, meaning that the deposited layers are silicon-rich. However, the values for R_3 are only around 0.2, which is half of what was obtained in the study described above. Additionally, the contribution from $NSi-Si-H_2$ and $N_2SiSi-H$ is far from being negligible contrary to what is obtained by *Kim et al.* X-ray reflectometry (XRR) was used to measure the density of the deposited layers. Both samples had a similar density of 2.5 g.cm^{-3}. From these results, we conclude that the

Table 2.3: Bond absolute concentrations and ratios in the a-SiN_x:H thin films deposited for NH_3/SiH_4 = 4 and 3.

	$NH_3/SiH_4 = 4$	$NH_3/SiH_4 = 3$
$[Si-H]$ in cm^{-3}	3.9×10^{22}	4.0×10^{22}
$[N-H]$ in cm^{-3}	2.7×10^{22}	1.6×10^{22}
$R_1 = \frac{[Si-H]}{[Si-H]+[N-H]}$	0.59	0.72
$R_2 = \frac{[N_2Si-H_2]}{[N_2Si-H_2]+[N_3Si-H]}$	0.68	0.72
$R_3 = \frac{[Si_2N-H^{\cdots}H]}{[Si_2N-H^{\cdots}H]+[Si_2N-H]}$	0.20	0.22
Density in $g.cm^{-3}$	2.48	2.50

chemical environment of hydrogen atoms in our deposited layers is relatively close to the materials investigated in the literature. However, given that the process flow studied in this thesis significantly differs from standard high thermal budget processes for TOPCon fabrication, no conclusion can be drawn on whether this is the most favorable type of layer.

In the following of this thesis, the deposition conditions with a flow rate ratio NH_3/SiH_4 = 4 is chosen because of the lower extinction coefficient of the resulting material (thus lower optical losses), and because the spectroscopic signature of Si-H bonds is closer to the best conditions achieved in the literature.

Passivation properties and firing step

As shown in the previous section, the passivating stack SiO_x/(p) µc-Si:H/a-SiN_x:H yields good passivation properties in the as-deposited state, but is subject to a severe degradation after a firing step. This phenomenon has already been observed in the literature [157], [158], [172]. In order to evaluate the thermal stability of this stack, various firing steps were carried out with increasing firing peak temperatures. The results are shown in Figure A3.6. The passivation properties remain fairly constant for firing profiles with peak temperatures up to 700 °C. However, from 750 °C up, significant losses in the passivation properties are observed.

These results are shown for 75 nm-thick a-SiN_x:H layers. Since the main objective is to keep hydrogen in the sample during the firing step, samples with thicker layers of a-SiN_x:H are studied. A comparison of the passivation properties provided by the SiO_x/(p) µc-Si:H/a-SiN_x:H stack before and after firing is shown in Figure 2.33 for a-SiN_x:H layers of 75 nm and 100 nm. Both samples show equivalent passivation quality before the firing step. However, a thicker layer of a-SiN_x:H shows a lower drop of passivation during the firing step (from 25 to 10 mV of loss in iV_{oc}). Consequently, if the passivated contact is at the rear side of the solar cell, it may be beneficial to deposit thicker layers of a-SiN_x:H for a better thermal stability.

Thicker layers might induce a slightly worse optical response in the high energy part of the solar spectrum. In order to improve the thermal stability and get a better diffusion barrier [173] while staying as transparent as possible, the addition of CO_2 for the deposition of a-SiN_xO_y:H is investigated. The passivation results after deposition and after firing are shown in Figure 2.34. They are significantly worsen by the increase in CO_2 flow rate during the deposition of a-SiN_xO_y:H in both the as-deposited state and after firing. This

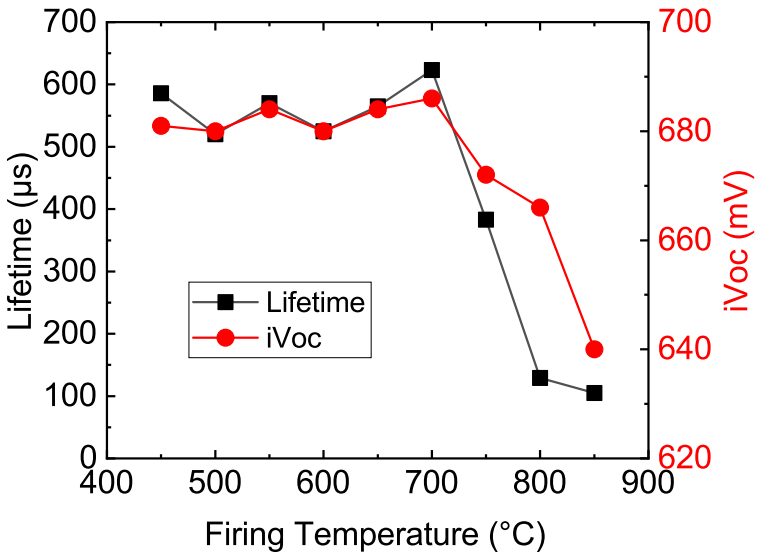

Figure 2.32: Evolution of iV_{oc} and τ_{eff} for various firing peak temperatures on a sample coated with a SiO_x/(p) µc-Si:H/SiN_x:H passivating stack.

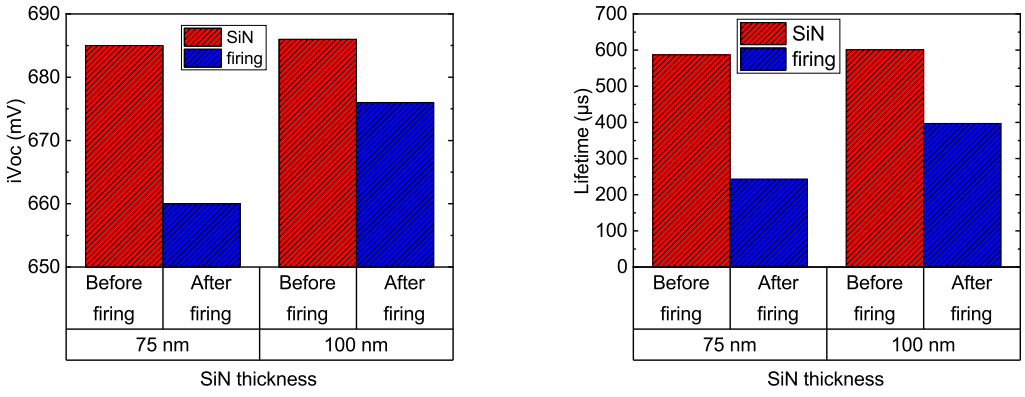

(a) (b)

Figure 2.33: Variation of (a) iV_{oc} and (b) τ_{eff} with the thickness of a-SiN_x:H deposited before and after a firing step at 850 °C.

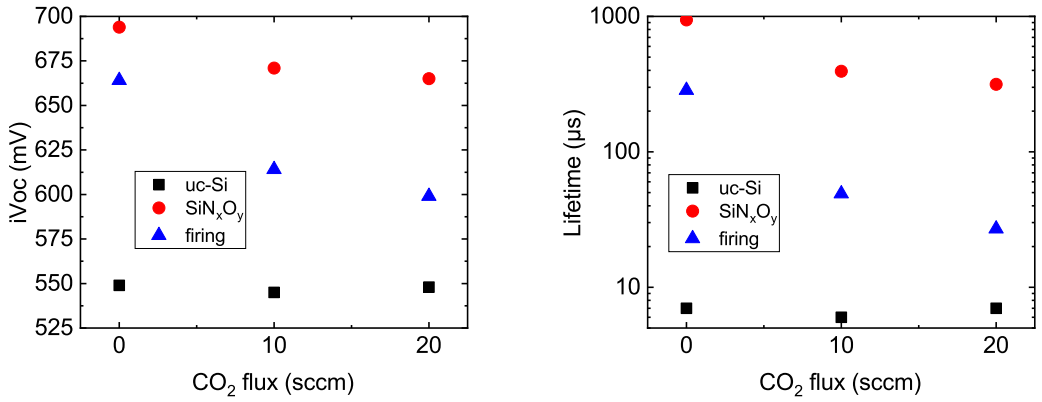

(a) (b)

Figure 2.34: Variation of (a) iV_{oc} and (b) τ_{eff} with the flow rate of CO_2 used during the deposition of the a-SiN_xO_y:H layer at three different stages of the process: (i) in the as-deposited step ("uc-Si" = c-Si/SiO_x/(p) µc-Si:H stack, black squares), (ii) after SiN deposition ("SiN_xO_y" = c-Si/SiO_x/(p) µc-Si:H/a-SiN_xO_y:H stack, red circles), and (iii) after a final firing step (blue triangles).

might come from the high energy UV emission from the CO_2 plasma that may create more defects at the surface of the silicon wafer. Consequently, the simple a-SiN_x:H material is kept for the rest of the depositions.

2.5.2 Comparison of different capping layers

As previously shown, the silicon nitride deposition step increases significantly the passivation properties, while the firing step degrades them for the passivating stack developed so far. Different capping layers are now studied in order to assess the impact of the nature of the top layer. 4 different samples were tested: (i) a sample with no capping layer (only the SiO_x/(p) µc-Si:H stack) in the as-deposited state, (ii) one with no capping layer but annealed at 350 °C with the same temperature profile as during the a-SiN_x:H deposition, (iii) a sample capped with AlO_x deposited by plasma-assisted atomic layer deposition (PA-ALD) and annealed at 350 °C, and (iv) a sample capped with a 75 nm-thick layer of the previously optimized a-SiN_x:H material. The results are shown in Figure 2.35 before and after a firing step at 850 °C. It can be seen that a simple annealing (20 min at 350 °C) already significantly improves the passivation properties of the SiOx/(p) µc-Si:H stack by 40 mV. This may be due to dopant activation, better crystallization of µc-Si:H, and hydrogen diffusion. A higher passivation is reached when adding AlO_x or a-SiN_x:H on top of it, likely due to capping properties and additional hydrogen intake.

After the firing step, the passivation properties drop significantly for the samples with no capping layer and with the a-SiN_x:H layer as expected after the observations of the previous section dedicated to a-SiN_x:H. However, the passivation properties of the sample capped with the ALD AlO_x layer remain high and even improve with the firing step. This proves the possibility of making Fired Passivating Contacts with the process flow proposed in Figure A3.4b, as long as the capping layer is adapted. For process flow reasons, the AlO_x solution is not investigated further in the rest of this thesis, and this set of experiments was mainly a proof of the feasibility of the simple process flow studied in this thesis.

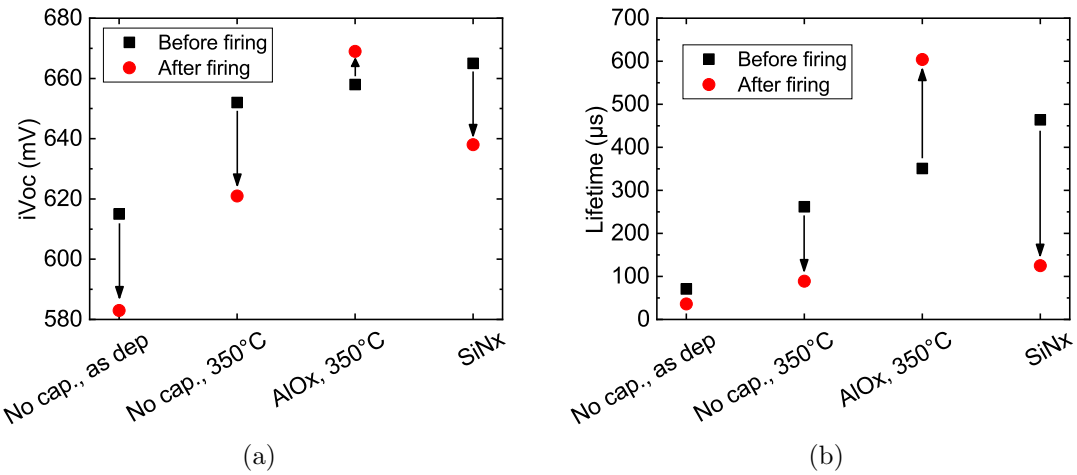

Figure 2.35: Variation of (a) iV_{oc} and (b) τ_{eff} before and after a firing step for different capping layers on a SiO_x/(p) µc-Si:H passivating stack.

2.6 Summary

This chapter describes the optimization of the different layers of the passivating contact. The wet-chemical SiO_x was chosen for the rest of this thesis for the better passivation properties it provides. Micro-crystallized layers were used in order to limit parasitic absorption and avoid blister formation during the rapid thermal annealing steps. A thorough investigation of the composition of the oxide after deposition of the (p) µc-Si:H layer was carried out by XPS analysis, and showed that the deposition changed the morphology of the underlying oxide layer. Yet no relationship could be drawn between the passivation properties and the composition of the tunnel oxide measured with this technique. Boron and phosphorous doped µc-Si:H and µc-SiO_x:H deposition conditions were optimized to get the best possible trade-off between conductivity, transparency, passivation properties and thermal stability. After the optimization of the a-SiN_x:H layer, further characterizations were done in order to gain a better knowledge of its chemical and optical properties. The passivation provided by the SiO_x/(p) µc-Si:H/a-SiN_x:H stack was shown to start degrading for firing steps with peak temperatures exceeding 700 °C. A better thermal stability was finally achieved by replacing the a-SiN_x:H layer with an AlO_x layer. A summary of the best deposition conditions for the different materials optimized in this chapter can be found in Table 2.4.

Table 2.4: Optimized deposition conditions for the different materials studied in chapter 2.

Material	Temperature (°C)	RF Power (W)	Pressure (mbar)	Interelectrode distance (mm)	SiH_4 flow rate (sccm)	H_2 flow rate (sccm)	TMB flow rate (sccm)	PH_3 flow rate (sccm)	CO_2 flow rate (sccm)	NH_3 flow rate (sccm)
(p) µc-Si:H	175	50	2.5	15	4	500	0.8	0	0	0
(p) µc-SiO_x:H	175	50	2.5	15	4	500	0.8	0	1	0
(n) µc-Si:H	175	50	2.5	15	6	500	0	0.8	0	0
(n) µc-SiO_x:H	175	50	2.5	15	4	500	0	0.8	1	0
SiN_x:H	350	5	0.66	20	7.5	75	0	0	0	30

This section focused on the optimization of the deposition conditions of the various materials used for the fabrication of the Fired Passivating Contacts. A loss of passivation properties was observed during the firing step, and two strategies compatible with the

investigated process flow were found to hinder it: replacing µc-Si:H by µc-SiO_x:H layers and depositing thicker layers of µc-SiO_x:H and/or a-SiN_x:H. The complexity of the stack and the impact of the deposition steps on the whole structure motivate the use of real-time characterization techniques. Consequently, *in situ* characterization is used in the following chapters in order to optimize the process steps more efficiently and gain a better understanding on the kinetics of the passivation properties.

Chapter 3

In situ modulated photoluminescence for AlO_x

Modulated photoluminescence (MPL) allows to measure the minority carrier lifetime in a sample. In situ*, real-time lifetime measurement is extremely interesting since it gives some insight on the evolution of the passivation properties during a given process step. In this section, an* in situ *MPL measurement tool is described along with the improvements that have been made during this doctoral thesis. We also report on a case study dealing with AlO_x passivated samples undergoing an annealing step. These allow to show that the combined action of light and temperature activates stable positive fixed charges in the layer, which is highly unusual for this kind of material.*

Contents

3.1 *In situ* MPL coupled to a PECVD reactor

3.1.1 Introduction to modulated photoluminescence

As discussed in section 1.1.3, 4 main recombination mechanisms can be identified: radiative, Auger, SRH, and surface recombinations. Specific recombination rates can be attributed to each of them, respectively R_{rad}, R_{Auger}, R_{SRH}, and R_{surf}, the latter including the contribution of all surface recombinations. The total effective recombination rate R_{eff} (expressed in $\mathrm{cm}^{-3}.\mathrm{s}^{-1}$) is defined as the sum of these contributions:

$$R_{eff} = R_{bulk} + R_{surf} = R_{rad} + R_{Auger} + R_{SRH} + R_{surf} \tag{3.1}$$

with R_{bulk} the recombination rate accounting for all recombination mechanisms in the bulk of the silicon wafer. To each of these phenomena, one can attribute a related characteristic carrier lifetime $\tau = \dfrac{\Delta n}{R}$. This allows to define an effective minority carrier lifetime τ_{eff} in the material, such as described in Equation 3.2:

$$\frac{1}{\tau_{eff}} = \frac{R_{eff}}{\Delta n} = \frac{1}{\tau_{rad}} + \frac{1}{\tau_{Auger}} + \frac{1}{\tau_{SRH}} + \frac{1}{\tau_{surf}} \tag{3.2}$$

This is (under a few minor approximations) the value derived from QSSPC measurements and used in the previous section. At this point, it is worth reminding that the recombination rates depend on the charge carrier density. Typically, the rate of Auger recombination events dramatically increase at high excess carrier densities (see Equation 1.10).

Harmonically modulated photoluminescence consists in illuminating a sample with a monochromatic light of modulated intensity [174]. The illumination intensity varies at an angular frequency ω and can be expressed as the superposition of a continuous and a time-depend contribution:

$$I = I_0 + I_1 e^{i\omega t} \tag{3.3}$$

As a consequence of this modulated intensity and by linearity of the electron-hole pair generation with the incident photon flux, the generation rate G (in $\mathrm{cm}^{-3}.\mathrm{s}^{-1}$) and the excess carrier densities Δn and Δp (in cm^{-3}) also follow this harmonic modulation.

$$\begin{cases} G = G_0 + G_1 e^{i\omega t} \\ \Delta n = \Delta n_0 + \Delta n_1 e^{i\omega t} \\ \Delta p = \Delta p_0 + \Delta p_1 e^{i\omega t} \end{cases} \tag{3.4}$$

Radiative recombinations govern the luminescence intensity. The luminescence photon flux j_{PL} coming out of the sample is given by the expression:

$$j_{PL} = Bnp \tag{3.5}$$

with B the radiative coefficient depending on the material properties and np the product of electron and hole densities. As a consequence of the excitation of the sample, the modulated photoluminescence intensity can be written:

$$j_{PL} = B(n_0 + \Delta n)(p_0 + \Delta p) \tag{3.6}$$

where n_0 and p_0 are respectively the electron and hole densities in the material under no excitation (thermal equilibrium). Assuming that the modulated part of the laser intensity

is relatively small compared to the continuous contribution, one can assume $\Delta n_1 \ll \Delta n_0$, along with $\Delta n_0 = \Delta p_0$ and $\Delta n_1 = \Delta p_1$. From Equation 3.4 one can induce that the first order term $j_{PL,1}$ can be expressed under the form:

$$j_{PL,1} = B\left(n_0 + p_0 + 2\Delta n_0\right)\Delta n_1 \tag{3.7}$$

The continuity equation for the excess minority carrier lifetime in p-type semiconductors is given by:

$$\frac{\partial \Delta n}{\partial t} = G(\mathbf{r},t) - R(\mathbf{r},t) - \nabla \mathbf{j}_{\Delta n}(\mathbf{r},t) \tag{3.8}$$

where $\nabla \mathbf{j}_{\Delta n}$ is the gradient of the excess carrier current density. In uniform materials under uniform illumination, this last contribution is null. When deriving the continuity equation (Equation 3.8) with respect to time, one gets:

$$\begin{aligned}\frac{d^2\Delta n(t)}{dt^2} &= \frac{dG}{dt} - \frac{dR}{dt} \\ &= \frac{dG}{dt} - \frac{dR}{d\Delta n}\frac{d\Delta n}{dt}\end{aligned}$$

$$\frac{d^2\Delta n(t)}{dt^2} = \frac{dG}{dt} - \frac{1}{\tau_{eff,diff}}\frac{d\Delta n}{dt} \tag{3.9}$$

with the introduction of the differential lifetime $\tau_{eff,diff} = \dfrac{d\Delta n}{dR}$. When using the set of Equations 3.4 to account for the time dependence of the various quantities, one can rewrite equation 3.9:

$$\begin{aligned}(i\omega)^2\Delta n_1 e^{i\omega t} &= i\omega G_1 e^{i\omega t} - \frac{1}{\tau_{eff,diff}}(i\omega)\Delta n_1 e^{i\omega t} \\ i\omega\Delta n_1 &= G_1 - \frac{1}{\tau_{eff,diff}}\Delta n_1 \\ \Delta n_1\left(i\omega + \frac{1}{\tau_{eff,diff}}\right) &= G_1\end{aligned}$$

$$\Delta n_1 = \frac{G_1\tau_{eff,diff}}{1 + i\omega\tau_{eff,diff}} \tag{3.10}$$

From Equation 3.10, one can finally derive the module and phase shift of Δn_1:

$$|\Delta n_1| = \frac{G_1\tau_{eff,diff}}{\sqrt{1 + (\omega\tau_{eff,diff})^2}} \tag{3.11}$$

$$\phi = -\arctan(\omega\tau_{eff,diff}) \tag{3.12}$$

This relates directly to the photoluminescence intensity as Equation 3.7 shows. As a consequence, a simple measurement of the phase-shift between the excitation and the photoluminescence signal allows to extract a measured lifetime τ_m which corresponds to the differential effective lifetime $\tau_{eff,diff}$. For simplification purposes, the notation τ_m will be used to relate to the differential effective lifetime in the rest of this chapter.

3.1.2 *In situ* modulated photoluminescence experimental setup

Real-time measurements are extremely interesting for the understanding of physical phenomena occurring during different process steps. As shown above, a quantitative assessment of the passivation quality can be obtained by measuring the modulated photoluminescence (MPL) of a sample. The purpose of the following sections is to describe the acquisition and data treatment routine in order to extract the effective carrier lifetime τ_{eff} at a specific photogenerated carrier density (typically 1×10^{15} cm^{-3}) in real time during the sample processing.

The setup presented hereafter has been developed during the doctoral thesis of M. Sreng [169] and is an evolution of an *in situ* photoluminescence (PL) system previously described by S. Abolmasov [175]. The PECVD reactor has a grounded electrode with a 9 mm-diameter hole in its center. This electrode is used as a substrate holder, and the hole allows (i) the illumination of the sample in order to photogenerate carriers, and (ii) the MPL signal collection. The illumination source is a laser which delivers a continuous wave beam centered on a wavelength of 785 nm with a spot size corresponding to the full 9 mm-diameter hole aforementioned. The optical power output and modulation frequencies are controlled through a programmable current/temperature controller from Thorlabs. The modulation depth represents 6 % of the laser intensity, and the modulation frequencies range from 225 Hz to 625 Hz. A parabolic mirror was used in order to maximize the collection of the MPL signal. The signal is then converted by an InGaAs photodiode. Finally, the phase shift between the MPL signal and the excitation is measured by a lock-in amplifier. This whole setup is schematically represented in Figure 3.1.

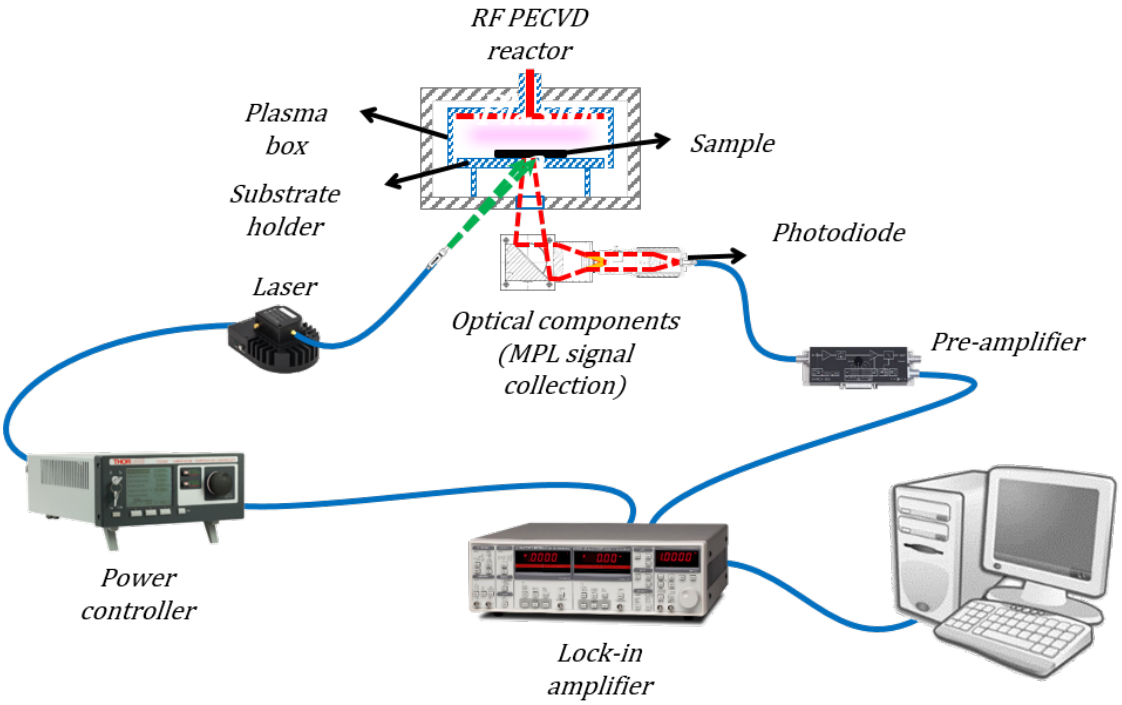

Figure 3.1: Schematic representation of the *in situ* MPL acquisition setup coupled with a PECVD reactor, Figure from [169].

LiTe algorithm

Given Equation 3.12, the experimental data that need to be collected are phase shifts between the laser excitation and the MPL signal. These are acquired for different illumination intensities, modulation frequencies and at different times of the process step investigated. LiTe© algorithm previously developed can be described by the diagram shown in Figure 3.2 adapted from [169].

It consists in exciting a sample for every combination of laser intensity and modulation frequency in a given ensemble $\{I_{0,i}; i \in [1,n]\} \times \{\omega_j; j \in [1,p]\}$. For each couple $(I_{0,i}, \omega_j)$, the phase shift $\phi_{i,j}$ between excitation and MPL is measured and corrected (the "Phase shift correction" removes the contribution from the intrinsic phase shift induced by the optical path of the light in the setup).

Then for each laser intensity $I_{0,i}$, a few elements are calculated in order to get the final effective lifetime value.

- The first step consists in calculating the generation rate $G_{0,i}$ in the sample at a given illumination intensity.
- The second step consists in extracting the corresponding measured lifetime values $\tau_{m,i}$. These can be derived from Equation 3.12: $\tau_{m,i} = \tan(-\phi_{i,j})/\omega_j$. Several modulation frequencies ω_j are used for a better reliability of the lifetime measurement.
- The third step consists in deducing the excess carrier density. In this algorithm, it is first approximated with the relationship $\Delta n_{G,i} = G_{0,i}\tau_{m,i}$ (red rectangle).

Then, one can get a curve of $\tau_m(\Delta n_G)$. However, the lifetime measured by MPL is the differential effective carrier lifetime $\tau_m = \tau_{eff,diff} = \dfrac{d\Delta n}{dR_{eff}}$, which differs from the effective lifetime τ_{eff} measured by QSSPC. The effective lifetime can be derived from the Equation 3.13 (see the work of Giesecke *et al.* [176]):

$$\tau_{eff}(G) = \tau_m(G)\left(1 - G\left.\frac{d\tau_{eff}}{d\Delta n}\right|_{\Delta n}\right) \tag{3.13}$$

An updated calculation of the values $\Delta n_{G,i} = G_{0,i}\tau_{eff,i}$ can be made, which leads to a function $\tau_{eff}(\Delta n_G)$. These elements are represented respectively by blue dots and the red dotted line in Figure 3.3. In the end, this allows to extract the value of lifetime at the standard excess carrier density of 1×10^{15} cm^{-3} represented by the green dot in the same Figure.

3.1.3 Diffusion phenomena

The method described above is based on the assumption that all the carriers generated in the illuminated region stay in that area and recombine. This is most likely not the case in non-uniformly illuminated samples due to diffusion phenomena. In our case, the non-uniform illumination is inherent to the local excitation of the acquisition setup presented in Section 3.1.2. We make a first estimation of the impact of diffusion on the evaluation of the minority carrier density. Afterwards a first attempt to implement the diffusion phenomena in the data treatment algorithm is described.

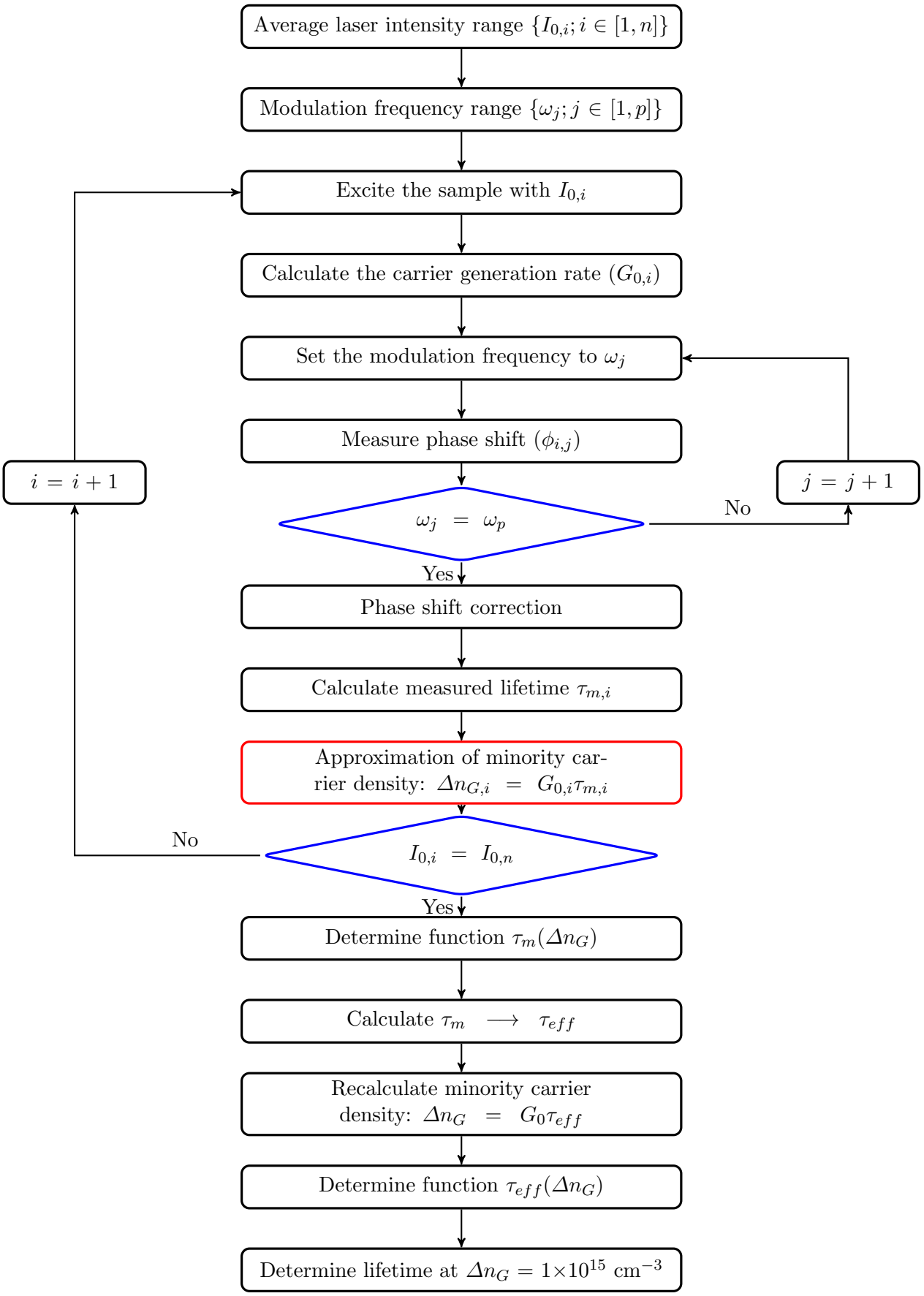

Figure 3.2: LiTe algorithm, adapted from [169].

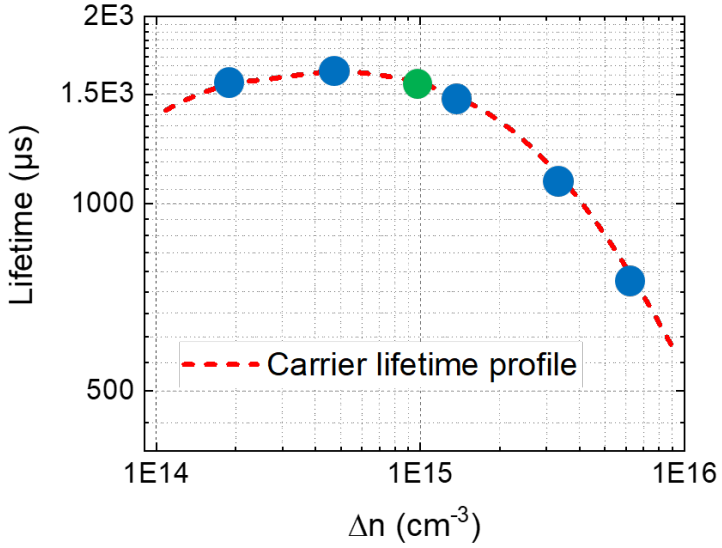

Figure 3.3: Various measurements (blue dots) and extrapolation of the function $\tau_{eff}(\Delta n)$ to derive the minority carrier lifetime at a specific injection level of 1×10^{15} cm^{-3} (green dot) [169].

The impact of lateral diffusion

A simple diffusion model is used hereafter in order to evaluate the impact of the lateral diffusion on the actual excess carrier density in the illuminated area - which corresponds to the collection area in our experimental setup.

The continuity equation in steady-state and one dimension, for $x \in [0;\infty[$, accounting from diffusion phenomena (see Equation 3.8) gives:

$$\frac{d^2\Delta n}{dx^2} - \frac{1}{D\tau_{eff}}\Delta n = -\frac{G(x)}{D} \tag{3.14}$$

The physical problem is schematically represented in Figure 3.4. The spacial profile of the generation rate, represented by a red line, is superimposed to the scheme and assumed to follow a step-like function with a constant generation rate in the illuminated area. From this model of the problem, one gets the following set of boundary conditions:

$$\left.\frac{\partial\Delta n}{\partial x}\right|_{x=0} = 0 \tag{3.15}$$

$$\lim_{x\to+\infty} \Delta n(x) = 0 \tag{3.16}$$

$$\lim_{\substack{x\to d/2\\ x<d/2}} \Delta n(x) = \lim_{\substack{x\to d/2\\ x>d/2}} \Delta n(x) \tag{3.17}$$

$$\lim_{\substack{x\to d/2\\ x<d/2}} \frac{\partial\Delta n(x)}{\partial x} = \lim_{\substack{x\to d/2\\ x>d/2}} \frac{\partial\Delta n(x)}{\partial x} \tag{3.18}$$

For a first assessment of the impact of lateral diffusion on the excess carrier density, a few assumptions are made:

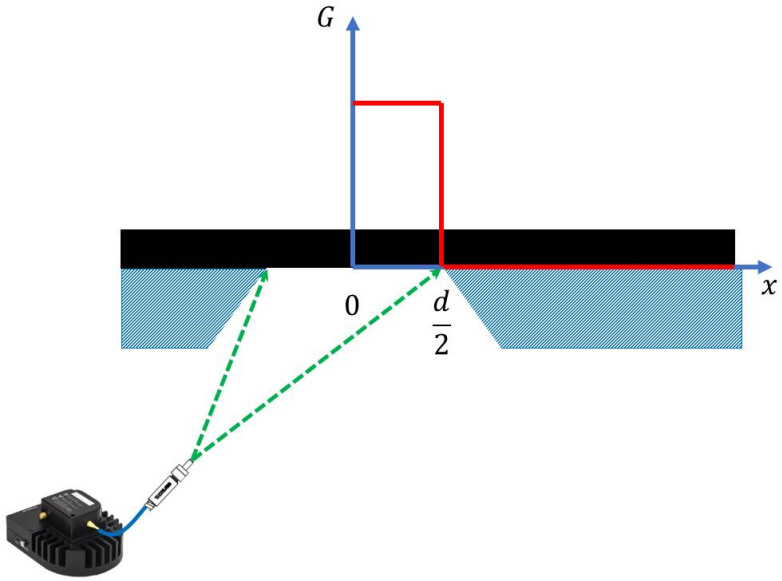

Figure 3.4: Schematic representation of the MPL measurement setup. The black rectangle represents the sample, the blue striped area represents the substrate holder with the hole that allows the rear side illumination. This figure is superimposed with the assumed spacial distribution of the generation rate in red.

- the lifetime is constant in the illuminated area $x \in \left[0; \frac{d}{2}\right]$:

$$\begin{cases} \tau_{eff}(x) = \tau_1 \\ \dfrac{\partial \tau_{eff}}{\partial x} = 0 \end{cases}$$

- the lifetime is constant in the dark area $x \in \left]\frac{d}{2}; +\infty\right[$:

$$\begin{cases} \tau_{eff}(x) = \tau_2 \\ \dfrac{\partial \tau_{eff}}{\partial x} = 0 \end{cases}$$

- D the diffusion coefficient related to the diffusion phenomenon studied is supposed to be constant $\forall x \in [0; +\infty[$ and taken equal to 27 $cm^2.s^{-1}$ which is the diffusion coefficient of electrons in n-type silicon with a doping level around 5×10^{15} cm^{-3}.

Under these conditions, equation 3.14 leads to the following excess carrier profile:

$$\begin{cases} \Delta n(x) = G\tau_1 \left[1 + 2C_1 \cosh\left(\dfrac{x}{\lambda_1}\right)\right] & \text{for } x \in \left[0; \frac{d}{2}\right] \\ \Delta n(x) = C_2 \exp\left(\dfrac{-x}{\lambda_1}\right) & \text{for } x \in \left]\frac{d}{2}; +\infty\right[\end{cases} \tag{3.19}$$

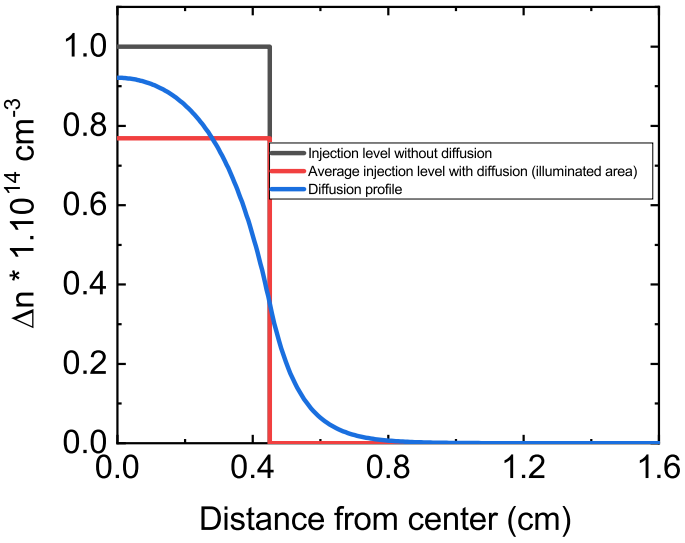

Figure 3.5: Spacial distribution of the excess carrier density in the sample with a simple diffusion model. The black curve corresponds to neglecting diffusion, the blue curve is the diffusion profile, and the red is the averaged value of the diffusion profile in the illuminated area.

with

$$\begin{cases} C_1 = \dfrac{-\lambda_1}{\lambda_2\left[\exp\left(\dfrac{d}{2\lambda_1}\right) - \exp\left(\dfrac{-d}{2\lambda_1}\right)\right] + \lambda_1\left[\exp\left(\dfrac{d}{2\lambda_1}\right) + \exp\left(\dfrac{-d}{2\lambda_1}\right)\right]} \\ C_2 = G\tau_1 \dfrac{\exp\left(\dfrac{d}{2\lambda_2}\right)}{1 + \dfrac{\lambda_1}{\lambda_2}\tanh^{-1}\left(\dfrac{d}{2\lambda_1}\right)} \end{cases} \text{ and } \begin{cases} \lambda_1 = \sqrt{D\tau_1} \\ \lambda_2 = \sqrt{D\tau_2} \end{cases} \tag{3.20}$$

These equations show that the overestimation of the minority carrier density in the center of the sample, corresponding to C_1, depends mostly on λ_1 - the diffusion length of the carriers at the center of the sample - and is proportional to the square root of the lifetime in that point. This means that the higher the lifetime in the center, the greater the impact of diffusion on the actual value of the excess carrier density.

For a generation rate $G = 1{\times}10^{17}$ cm^{-3}.s^{-1}, $\tau_1 = 1000$ µs, $\tau_2 = 300$ µs, and $d = 9$ mm, Figure 3.5 displays the diffusion profile (blue curve), the average value of this profile in the illuminated area (red curve), and the assumed injection level in the illuminated area when not taking diffusion into account (black curve).

This simple analytic diffusion model shows that the excess carrier density is overestimated by up to 23 % for the specific numerical values chosen. In Figure 3.6, we make a screening of τ_1 from 100 to 5000 µs at a fixed value of $\tau_2 = 300$ µs. For high lifetime samples (around 5000 µs), neglecting diffusion can lead to an overestimation of Δn by up to 60 %. As a consequence, the implementation of such diffusion phenomena in the treatment of the MPL data seems necessary to get an accurate value of the lifetime.

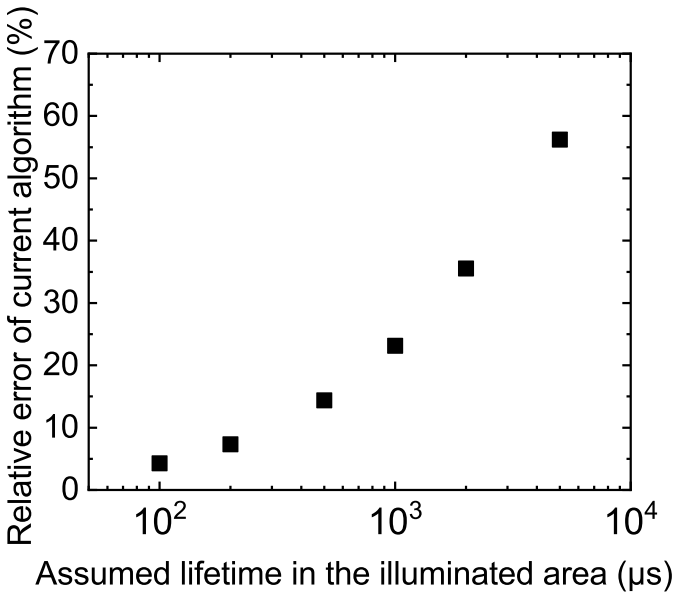

Figure 3.6: Variation of the relative error in excess carrier lifetime of the current algorithm (assuming no diffusion). The values are given for a lifetime in the dark of 300 µs.

Implementing diffusion phenomena in the algorithm

In this section we describe the diffusion model implemented as an improvement of the algorithm presented in Section 3.1.2. We modify this method by taking into account the lateral diffusion and calculating the spacial profile of the excess carrier density. This replaces the step "Determine the minority carrier density" in red in Figure 3.2.

The new algorithm is represented in Figure 3.7. It adds the calculation of the diffusion profile of the excess carrier density in the sample in order to extract the average excess carrier density in the area of collection of the MPL signal. For an easier reading, in the following equation we note $\Delta n = N$. The space is discretized in K space bins of width Δx. The value of a property X at a space bin k and a time step i is written X_k^i. Hence a vector $\mathbf{X^i}$ is written $\mathbf{X^i} = \begin{pmatrix} X_1^i & X_2^i & ... & X_{K-1}^i & X_K^i \end{pmatrix}^T$ and describes the spacial distribution of a property X at the i^{th} time step of duration Δt. The excess carrier density diffusion profile for a given lifetime distribution in the sample is obtained by solving the matrix equation 3.21 until convergence.

$$\mathbf{N^{i+1}} = (\mathbf{M_1} + \mathbf{M_2})^T \left(\mathbf{M_3 N}^i + \Delta t \mathbf{G}\right) \tag{3.21}$$

with

$$\mathbf{M_1} = \begin{pmatrix} 1 & -1 & & & 0 \\ -A & 1+2A & -A & & \\ & \ddots & \ddots & \ddots & \\ & & -A & 1+2A & -A \\ 0 & & & & 1 \end{pmatrix} \quad \mathbf{M_2} = \begin{pmatrix} 0 & & & & 0 \\ 0 & \Delta t/\tau_2 & 0 & & \\ & \ddots & \ddots & \ddots & \\ & & 0 & \Delta t/\tau_{K-1} & 0 \\ 0 & & & 0 & 0 \end{pmatrix}$$

$$\mathbf{M_3} = \begin{pmatrix} 0 & 0 & & & 0 \\ 0 & 1 & 0 & & \\ & \ddots & \ddots & \ddots & \\ & & 0 & 1 & 0 \\ 0 & & & 0 & 0 \end{pmatrix} \quad \mathbf{G} = \begin{pmatrix} 0 \\ G_0 \\ \vdots \\ G_0 \\ 0 \\ \vdots \\ 0 \end{pmatrix}$$

- $\mathbf{M_1}$ matrix is related to diffusion phenomena, with $A = \dfrac{D\Delta t}{\Delta x^2}$,
- $\mathbf{M_2}$ matrix is related to recombination phenomena, with τ_2 to τ_{K-1} the lifetime values in each space bin,
- $\mathbf{G}$ vector corresponds to the generation rate distribution in the sample (G_0 in the illuminated area, 0 in the dark area).

After convergence, the spacial distribution of the excess carrier density Δn is obtained for one given value of illumination intensity and one acquisition time step. $\Delta n_{end,i}$ is then taken as the average value of the newly calculated excess carrier density in the collection area. It is necessary to make this calculation for every laser excitation intensity and every time step of the studied process. After this correction, one finally gets a function $\tau_{eff}(\Delta n)$ that takes diffusion into account. Last but not least, after this correction, it is possible to extract the effective minority carrier lifetime at an excess carrier density of 1.10^{15} cm^{-3}.

This correction induces a change in the final effective carrier lifetime at 1×10^{15} cm^{-3}. The difference between the previous scheme and the new one is shown in Figure 3.8. One can see that taking diffusion into account does not result in a major difference in the final lifetime values due to the relatively low evolution of the lifetime with the excess minority carrier density (see Figure 3.3). In the sample studied here, the lifetime is high, and at an excess carrier density of 1×10^{15} cm^{-3}, a significant amount of Auger recombinations already take place. Consequently, an overestimation of the minority carrier lifetime results in an underestimation of τ_{eff}.

It is worth mentioning that a strong approximation is made in the calculation of the diffusion profile: the phenomenon is considered to happen only in 1D, and does not take into account the circular symmetry. Consequently, the results obtained in this section correspond once again to an overestimation of the minority carrier density.

3.1.4 Temperature correction

τ_{eff} additionally depends on temperature, since the bulk lifetime does [177]. In this chapter, in order to take into account this dependence, the lifetime was assumed to follow a power law [178] determined experimentally, given by:

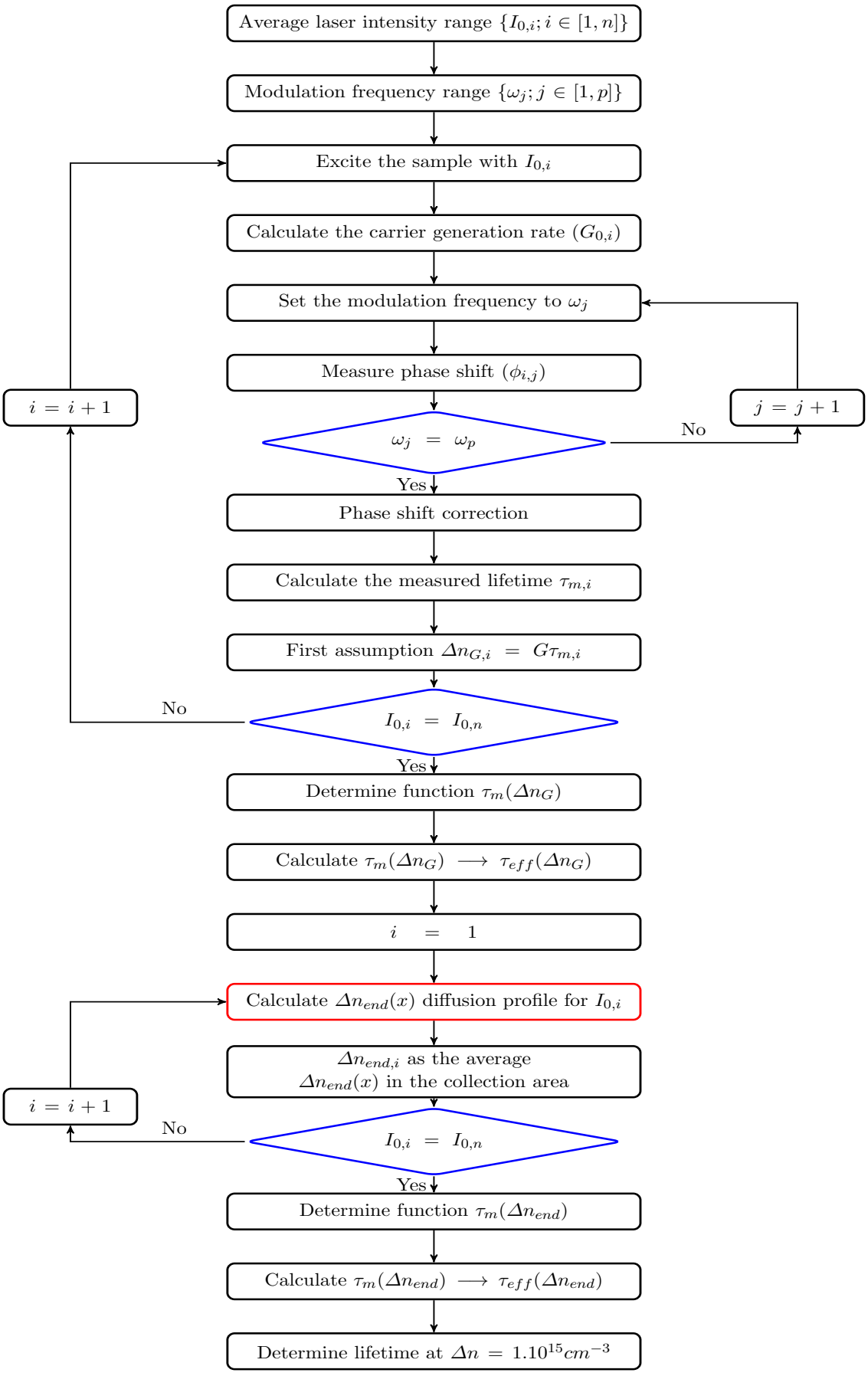

Figure 3.7: Modified algorithm, taking lateral diffusion into account.

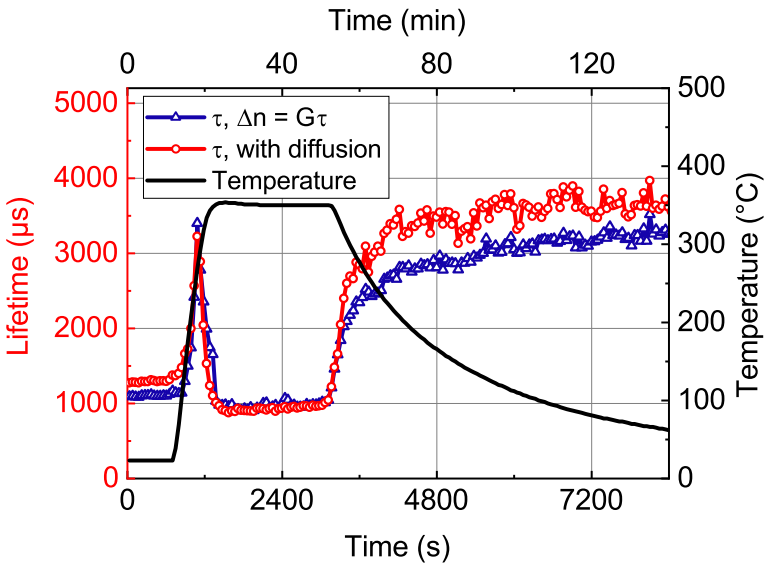

Figure 3.8: Comparison of the previous (blue) and new scheme (red) for the calculation of the lifetime by MPL. Evolution of the minority carrier lifetime (at $\Delta n = 1{\times}10^{15}$ cm^{-3}) of an Al_2O_3-passivated c-Si wafer during annealing at 350 °C for 30 minutes in H_2. The black curve shows the temperature profile. The lifetime values follow the temperature correction detailed in Section 3.1.4.

$$\tau_{eff}(T) = \tau_{eff}(300\text{ K}) \left(\frac{T}{300}\right)^{\alpha} \tag{3.22}$$

Where T is the temperature in K and α a constant which value was determined to be $\alpha = 1.0026$. This value was measured by annealing at 300 °C an n-type TOPSil FZ wafer provided by Fraunhofer ISE, that was passivated with a SiO_x/(n) poly-Si processed at high temperature (> 800 °C), and measuring the decrease in lifetime during the cooling phase (see Figure 3.9). The changes in τ_{eff} measured by MPL are assumed to reflect the evolution of the bulk lifetime. The initial and final τ_{eff} in the sample have been checked to be identical by QSSPC.

This temperature correction is applied to all subsequent data in this chapter, in order to plot the effective minority carrier lifetime at an equivalent temperature of 300 K, in order to get rid of the contribution of the bulk lifetime, and focus on the evolution of the properties of the passivation layer. At this point, it is worth noting that the fitting is done on a range between ambient temperature and 160 °C while the correction is extrapolated to higher temperatures (up to 350 °C).

3.2 AlO_x passivated samples: a case study

3.2.1 Context

Aluminum oxide (AlO_x) is a widely used material for surface passivation in crystalline silicon (c-Si) solar cells. It is indeed the base material for rear surface passivation in PERC cells (see Section 1.1.4) and numerous research teams are also attempting to include it in TOPCon [158], [179]–[181] or HIT [182] solar cells. The application of this material to PV technologies has already been extensively studied over the last decade [137], [183]–[185],

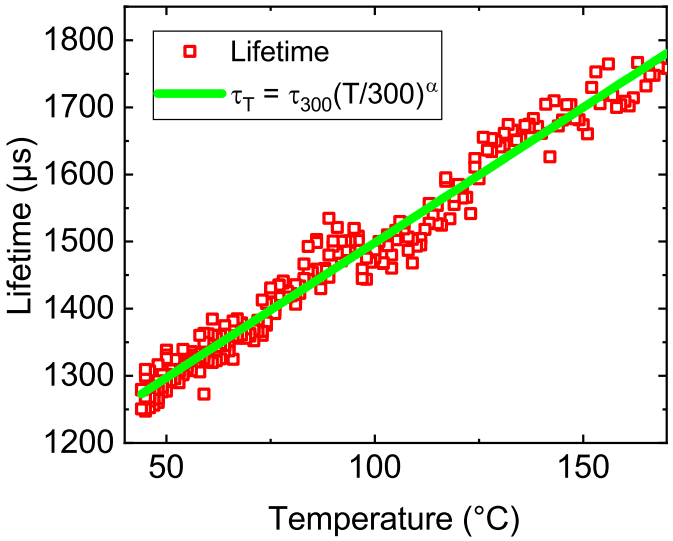

Figure 3.9: Evolution of the minority carrier lifetime (at $\Delta n = 1{\times}10^{15}$ cm^{-3}) with temperature of an n-type FZ wafer (1-5 Ω.cm) passivated with a SiO_x/(n) poly-Si stack processed at high temperature (> 800 °C) during the cooling phase of an annealing at 300 °C for 1 minutes in H_2. The green line is the fitting of the lifetime with a power low of coefficient $\alpha = 1.0026$. Adapted from [169].

and is recently being further pushed towards industrialization by the development of high throughput ALD techniques [186]. Its outstanding passivation properties are due to a low surface defect density (D_{it}), along with a high negative fixed charge density (Q_f), thus providing a high quality of both chemical and field-effect passivation. In order to achieve this, an annealing step after ALD deposition was shown to be necessary [187]–[189].

In order to get a better understanding of the passivation mechanisms during this last annealing step, the *in situ* MPL technique is used and allows to track the effective carrier lifetime during the process.

3.2.2 Experimental methods

In this work, AlO_x layers were deposited at LPICM by Thermal ALD. The deposition is done in a reactor by Picosun at 150 °C, with alternating pulses of trimethylaluminum $Al(CH_3)_3$ (TMA) and water vapor, and is carried out for 99 cycles which results in a thickness of 9 nm. These layers are deposited symmetrically on 1/4 n-type FZ wafers (100 mm of diameter, 280 µm of thickness, 1-5 Ω.cm) which undergo a 30 s HF clean immediately before the deposition. The samples subsequently experience an annealing step with *in situ* MPL measurements in the setup described in Section 3.1.2.

Some characterizations result from collaborations with researchers from various research units.

- The TEM characterizations were performed at Ecole Polytechnique on a Titan-Themis electron microscope operating at 200 kV equipped with a Cs probe corrector with a spatial resolution within nm range using the STEM-HAADF imaging mode. For all the studied samples, cross-section-lamellas have been prepared using a standard lift-out procedure within a Focused Ion Dual beam microscope (FIB, FEI-Scios

DualBeam).

All the other characterizations (QSSPC, annealing with *in situ* MPL, COCOS, PL Images) were made by the PhD candidate.

3.2.3 *In situ* MPL measurements during annealing

The standard annealing step that previously showed the best results for the AlO_x passivated samples made at LPICM consists in a 30 min-long plateau at 350 °C [137]. Figure A3.7a shows the evolution of τ_{eff} during such thermal treatment under 1 Torr of H_2. The lifetime starts to increase at the beginning of the heating step and reaches a peak at a temperature around 250 °C ($\tau_{peak} \approx 3.2$ ms). Then, when the temperature further increases, τ_{eff} drops back close to its initial value and only slightly increases during the 30 minutes of high temperature plateau. Finally, when the sample starts cooling down, the lifetime recovers, and reaches $\tau_{eff} = 3.5$ ms at the end of the annealing step. A measurement of the effective minority carrier lifetime by QSSPC at the end of the process confirms the final value of $\tau_{eff} = 3.2$ ms, which is close to the value obtained with the MPL method, thus confirming the validity and accuracy of the different corrections. This kind of kinetics (increase, decrease, low lifetime plateau, recovery) is very reproducible, and was observed on all the samples annealed at 350 °C for 30 minutes.

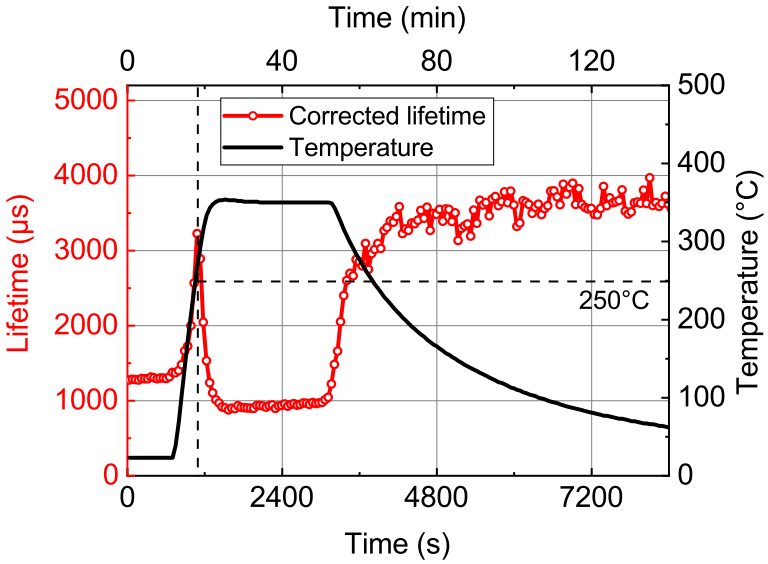

Figure 3.10: Evolution of the minority carrier lifetime (at $\Delta n = 1{\times}10^{15}$ cm^{-3}) of an Al_2O_3-passivated c-Si wafer during annealing at 350 °C for 30 minutes in H_2. The black curve shows the temperature profile. The black curve shows the temperature profile. The lifetime values follow the temperature correction detailed in Section 3.1.4.

The decrease of lifetime at temperatures higher than 250 °C will be investigated further in the next chapter (Section 4.1.3). The kinetics of passivation shown in Figure A3.7a raise at least two questions. (i) Since we did not witness any significant change during the 30 min-long plateau, what is the impact of a shorter annealing step? (ii) Reaching temperatures up to 350 °C seems to be detrimental: what happens if the annealing is stopped at the peak of lifetime: 250 °C? In order to answer these questions, two more temperature profiles are investigated: (i) annealing at 350 °C for 1 min (Figure 3.11) and (ii) annealing at 250 °C for 1 min (Figure A3.7b).

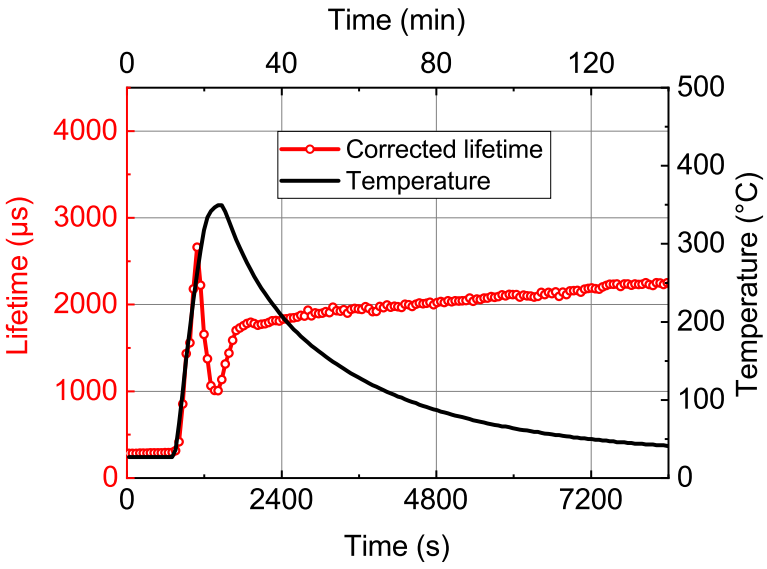

Figure 3.11: Evolution of the minority carrier lifetime (at $\Delta n = 1{\times}10^{15}$ cm^{-3}) of an Al_2O_3-passivated c-Si wafer during annealing at 350 °C for less than 1 minute in H_2. The black curve shows the temperature profile. The black curve shows the temperature profile. The lifetime values follow the temperature correction detailed in Section 3.1.4.

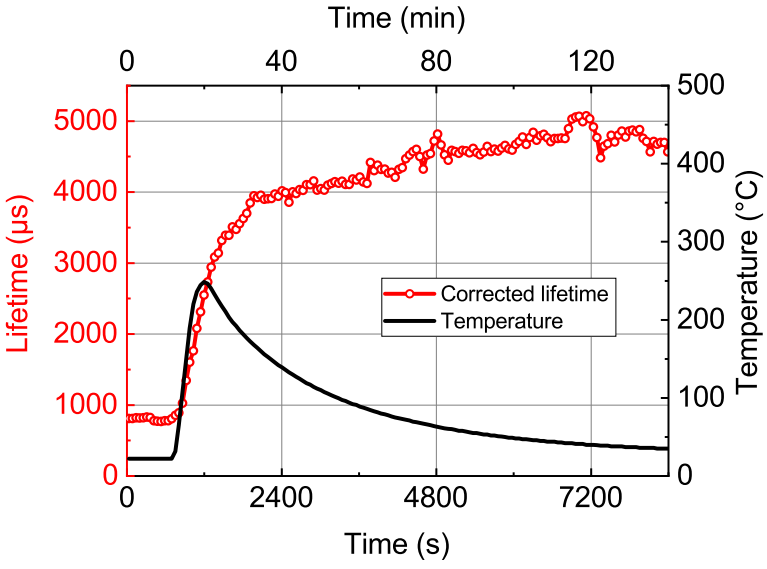

Figure 3.12: Evolution of the minority carrier lifetime (at $\Delta n = 1{\times}10^{15}$ cm^{-3}) of an Al_2O_3-passivated c-Si wafer during annealing at 250 °C for less than 1 minute in H_2. The black curve shows the temperature profile. The black curve shows the temperature profile. The lifetime values follow the temperature correction detailed in Section 3.1.4.

The graph obtained for the one-minute-long annealing at 350 °C (Figure 3.11) shows a similar peak of lifetime at 250 °C as in Figure 3.9, followed by a drop in lifetime when the temperature is further increased. When the temperature starts to decrease, τ_{eff} increases again, but reaches significantly lower values (2.5 ms) at room temperature than for the 30 min-long annealing step.

When the annealing is stopped at 250 °C (Fig. A3.7b), the kinetics of the lifetime is significantly different. Indeed, τ_{eff} increases up to 2.5 ms at 250 °C, but the lifetime does not decrease afterwards since the temperature does not exceed this threshold value. Surprisingly, τ_{eff} keeps increasing during the cooling phase, reaching 4.7 ms at room temperature, at the end of the MPL measurements. This excellent result shows the importance of *in situ* characterizations: it allowed to choose specific annealing conditions that would otherwise not have been investigated. However, the lifetime value measured by QSSPC after the annealing step is significantly different from this last result: only 500 μs. This discrepancy will be investigated further in section 3.2.6.

3.2.4 Chemical passivation

One hypothesis reported in the literature to explain the improvement in passivation properties provided by AlO_x thin-films upon annealing is the formation of a thin silicon oxide (SiO_x) layer at the AlO_x/c-Si interface [180], [190]. Therefore we have performed STEM-HAADF images of the c-Si/AlO_x interface (see Figure 3.13). These show that a thin SiO_x layer is already present in the as-deposited state. The oxide thickness seems to be decreasing with the thermal budget: 1.5 nm for the sample in the as-deposited state, 1 nm for the sample annealed at 250 °C for 1 min, and 0.8 nm for the sample annealed at 350 °C for 30 min. This indicates that the enhancement in passivation cannot be directly related to the formation of a SiO_x layer at the interface. However, this analysis does not provide information on the passivation quality of the SiO_x thin film: some densification, rearrangements in the Si-O bonds and hydrogen effusion may explain the thinning of the layer and could lead to a change in chemical passivation.

3.2.5 Field-effect passivation

Another important aspect in AlO_x annealing is the activation of fixed charges. Table 3.1 displays the fixed charge density and the surface defect density measured in our AlO_x thin films for the three samples obtained in section 3.2.3. For the sample annealed at 350 °C for 30 min, a negative fixed charge density of -2.1×10^{12} cm^{-2} was measured by COCOS. A slightly lower value of -1.2×10^{12} cm^{-2} was obtained after annealing for only 1 min at 350 °C. This difference could mean that the annealing step was too short to activate as many fixed charges inside the material, which could have a share in the difference between the two final minority carrier lifetime values (see Fig. A3.7a and Fig. 3.11). For the sample annealed at 250 °C for 1 min, however, the fixed charge density is +3×10^{10} cm^{-2}. This low absolute value means that the negative fixed charges have not been activated at such low temperature. The absence of charge activation could explain the low final lifetime measured by QSSPC for the sample annealed at 250 °C (500 µs), but is not consistent with the high values obtained from the MPL measurement. Despite this large difference in fixed charge densities, the surface defect densities are similar between the different samples (around 1×10^{11} cm^{-2}). These values show that most of the difference in lifetime between the samples is expected to come from field-effect passivation.

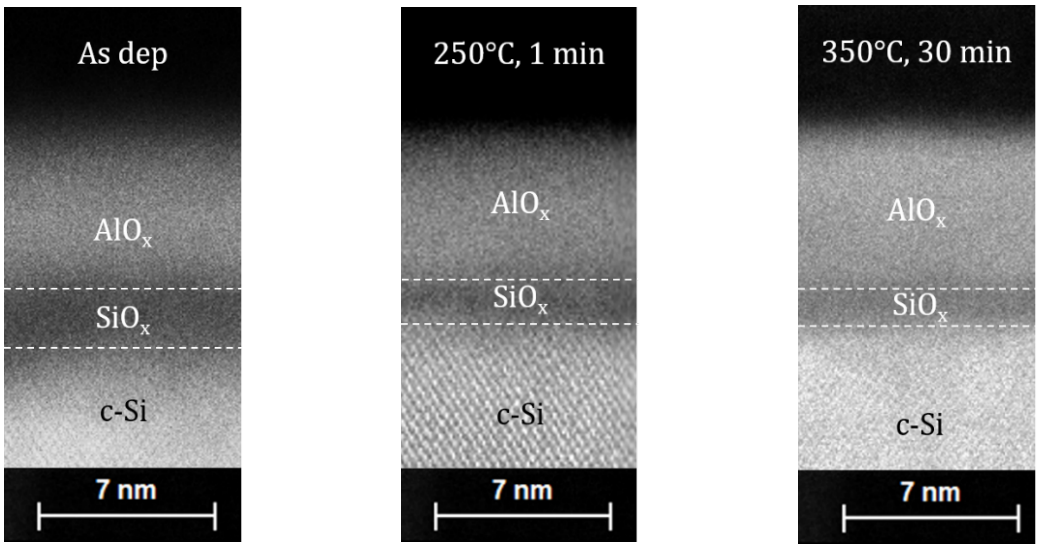

(a) (b) (c)

Figure 3.13: STEM-HAADF images of the c-Si/AlO_x interface for (a) the as-deposited sample, (b) the sample annealed at 250 °C for 1 min, and (c) the one annealed 30 min at 350 °C.

Table 3.1: Fixed charge and surface defect densities measured by corona charge experiments on AlO_x films after different thermal treatments in the PECVD chamber with *in situ* MPL.

Annealing	Fixed charge density Q_f (cm^{-2})	Surface defect density D_{it} (cm^{-2})
350 °C for 30 min	-2.1×10^{12}	1×10^{11}
350 °C for 1 min	-1.2×10^{12}	2×10^{11}
250 °C for 1 min	+3×10^{11}	1×10^{11}

3.2.6 Investigation of the discrepancy between QSSPC and MPL

In order to understand the difference between the MPL and QSSPC results, we investigate the homogeneity of the passivation properties; PL images of the samples are shown in Figure 3.14. It can be seen that for the sample annealed at 350 °C for 30 minutes, the PL signal is relatively spacially homogeneous – despite a slightly brighter spot near the center, and damaged areas due to manipulation. On the other hand, the PL image of the sample annealed for 1 min at 250 °C shows significant spacial variations. In particular, a very bright spot can be noticed at the center of the sample, whereas the rest emits a weaker PL signal in comparison. This explains the discrepancy noticed between the MPL and QSSPC measurements, since the QSSPC measures the average effective minority carrier lifetime on a rather large area (most of the sample) whereas the bright spot corresponds exactly to the area from which the MPL signal is collected.

One hypothesis for this inhomogeneity in the passivation properties is that the charges may have been locally activated by the laser illumination [137], [191], [192]. In order to investigate this feature, a map of the fixed charge density has been measured on a similar sample (full 100 mm FZ wafer) annealed at 250 °C for 1 minute. The map in Figure A3.8b shows that the fixed charge density around the spot of high PL signal intensity surprisingly

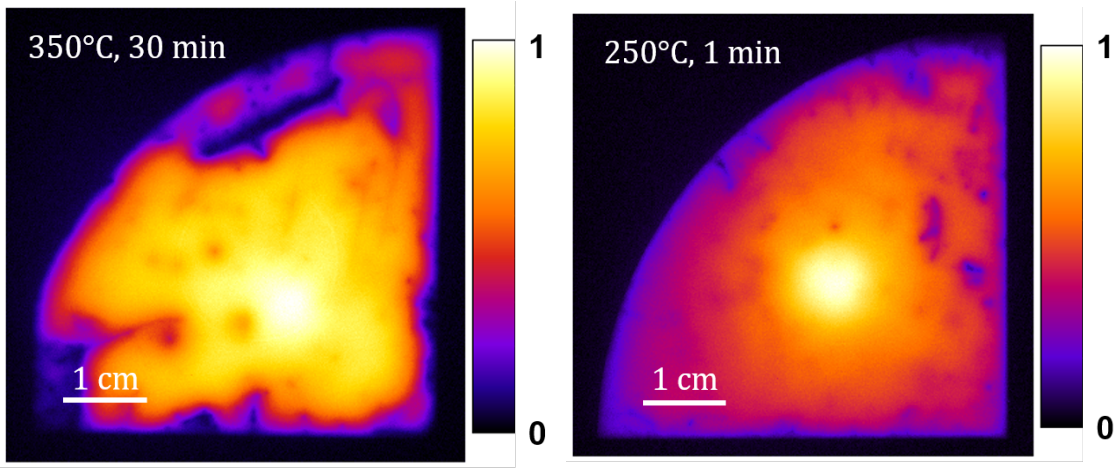

(a) (b)

Figure 3.14: PL Images for samples annealed at (a) 350 °C for 30 min and (b) 250 °C for 1 min. *In situ* MPL was used during the annealing step.

corresponds to a high positive fixed charge density of around $+1\times10^{12}$ cm^{-2}. This result has been observed and verified on different samples: in all of them the fixed charge density reached similar values. D_{it} stays homogeneous at values around 2×10^{-11} cm^{-2}. The high positive fixed charge density is very unusual and mostly witnessed in samples having several nanometers of interface layer of SiO_x or another dielectric [193], [194].

This positive fixed charge density could explain the better passivation properties measured by MPL, because the deposition of the AlO_x layers were done on phosphorous doped silicon wafers, so field-effect passivation with positive fixed charges is more favorable. As mentioned above, this may not be the only process taking place, since some degradation may be occurring while the temperature gets higher than 250 °C. Additionally, we notice that after 2 months of storage in the dark, the PL images obtained in Figure 3.14 remain unchanged, which means that the high positive fixed charges are stable, contrarily to reversible negative fixed charge activation through light soaking reported at room temperature [191].

We have shown in this section that the combined action of light and temperature could lead to the formation of a highly passivating AlO_x layer containing a large positive fixed charge density which is stable in time. The annealing under illumination of the full wafer still remains to be investigated. The advantage of such a process is that it only requires the addition of a light source during the annealing step in order to activate fixed charges in AlO_x. The process is simple, low temperature and short, and leads to the formation of very interesting positive fixed charges that are stable in time.

3.3 Summary

In this chapter, an *in situ* MPL setup mounted on a PECVD reactor allowing the measurement in real time of the minority carrier lifetime at the minority carrier density of 1×10^{15} cm^{-3} has been described, along with the improvement made to the data treatment procedure in order to take lateral diffusion of charge carriers into account. This characterization tool gives the possibility to investigate a thermal annealing treatment or a thin-film deposition step. The annealing step following the deposition of an AlO_x pas-

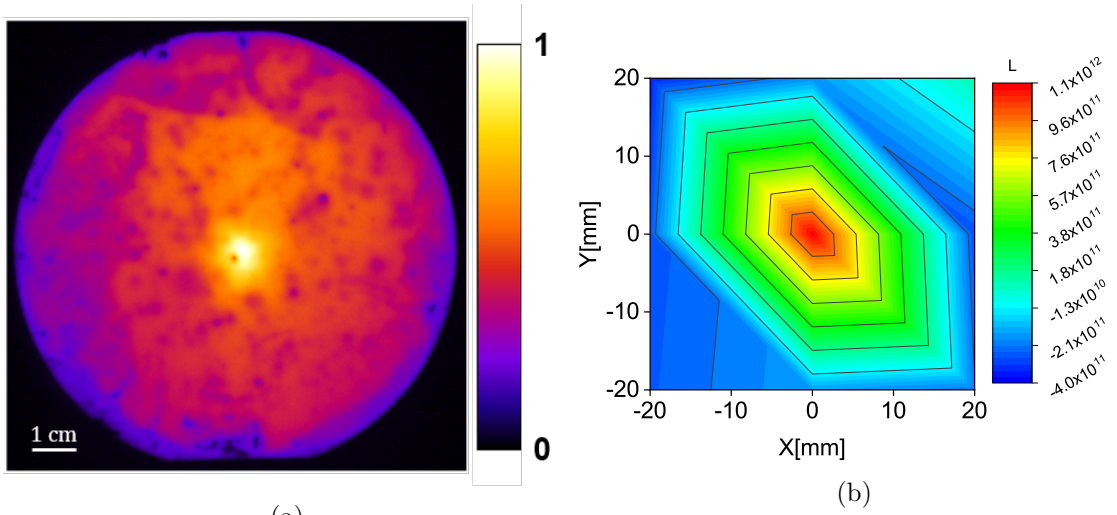

(a) (b)

Figure 3.15: (a) PL Images and (b) fixed charge density map for a sample annealed at 250°C for 1 min. *In situ* MPL was used during the annealing step.

sivation layer was studied. The experiments carried out evidenced the rich kinetics of the passivation during the annealing. A large drop of lifetime is observed when the AlO_x passivated sample reaches a temperature greater than 250 °C. This spurred the investigation of a faster annealing step at lower temperature (1 min at 250 °C instead of 30 min at 350 °C). Such a thermal profile allowed to achieve an effective lifetime of 5 ms, but only locally, on the area where the laser used for the MPL measurement was shining the sample. The combined action of light and temperature was shown to activate a high density of fixed charges, which were both positive and stable. This could lead to an additional interest in the use of AlO_x for passivating both n-type and p-type semiconductors. This study shows that annealing under illumination provides a simple and fast way to get positively charged AlO_x layers. As a perspective, it would be interesting to add a light source to shine the whole sample during the thermal annealing. This could allow more thorough investigations on this state of the alumina layer.

This chapter shows the advantage of using *in situ* MPL in order to highlight specific mechanisms during some process steps. However, in the process flow for FPC fabrication studied in this thesis, we do not focus on AlO_x deposited by ALD. Consequently, in the following chapters, we focus on using this newly developed *in situ* MPL technique for the optimization of the FPC fabrication processes.

Chapter 4

In situ MPL for fired passivating contacts

In this chapter, in situ *MPL is used in order to investigate the kinetics of the passivation properties of fired passivated contact (FPC) at different stages of the fabrication process. A first section describes the post-firing hydrogenation step of FPC samples processed at EPFL. This investigation will allow to pinpoint some limitations in the lifetime measurement technique at temperatures greater than 300 ˚C. A second section focuses on FPC samples based on the process flow considered since the beginning of this manuscript, with hydrogenation before the firing step. For these samples, the MPL measurements are done during plasma processes: NH_3/H_2 plasma and a-SiN_x:H deposition.*

Contents

4.1 Hydrogenation after firing

4.1.1 Context and experimental methods

The process investigated in this first section is the one developed by Ingenito *et al.* in [46] and shown on Figure A3.4a. The samples were processed at EFPL. Shiny etched p-type FZ wafers (100 mm of diameter, 200 µm of thickness, 2 Ω.cm) were wet chemically cleaned, with a final hot nitric acid (HNO_3) treatment (69 % in H_2O, 80 °C, 10 min) in order to grow a ≈ 1.3 nm-thick tunnel oxide layer. Then a 25 nm-thick (p) a-SiC_x:H (with ≈ 2.5 at.% of carbon) was deposited at 200 °C by PECVD and the sample was subject to a 3 s-long, 800 °C firing process. The final hydrogenation of the sample was made by depositing an a-SiN_x:H layer by PECVD, and required a final annealing step in order to allow hydrogen to diffuse into the wafer.

The evolution of the passivation properties at each process step was described by Lehmann et al. [87] and is shown in Figure 4.1 for both n-type and p-type FPC. The iV_{oc} values remain low in the as-deposited state (SiO_x/doped SiC_x stack), after firing and after the a-SiN_x:H layer deposition. The subsequent "Hotplate" annealing step is carried out at 450 °C for 30 min, and allows the passivation properties to improve dramatically. In this specific graph, the oxide layer is a 25 nm-thick thermally grown oxide layer of very high quality instead of a 1.3 nm-thick wet-chemically grown oxide layer. This explains the outstanding iV_{oc} values (up to 740 mV). However, the overall trend of the properties and more specifically the improvement during the "Hotplate" annealing step should not differ upon the change in the nature of the oxide layer.

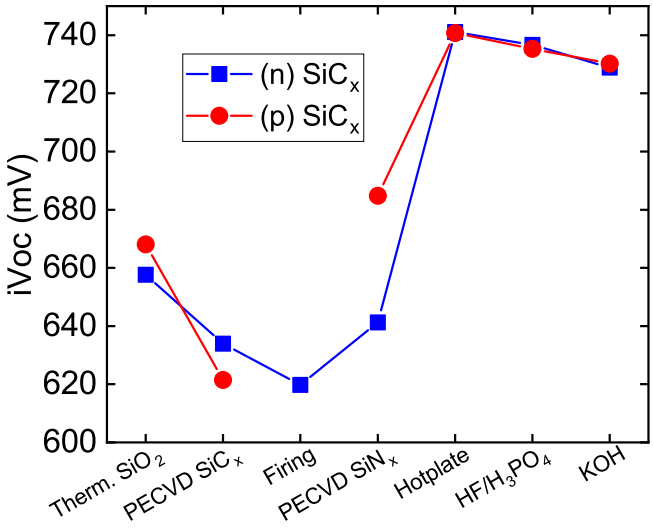

Figure 4.1: iV_{oc} values as a function of the processing step of samples fabricated with a p-type or n-type SiC_x layer on p-type shiny etched wafers with a 25 nm-thick thermal oxide. The passivation quality of the (p) SiC_x sample after firing was too low to measure an iV_{oc} value. Figure and caption adapted from Lehmann *et al.* [87].

Further investigations on the annealing duration and temperature have been carried out and are shown respectively in Figures 4.2a and 4.2b. On the one hand, when putting the samples abruptly on a hotplate at 450 °C, the lifetime increases up to a maximum value that is reached after relatively short annealing times (less than 10 min). On the other

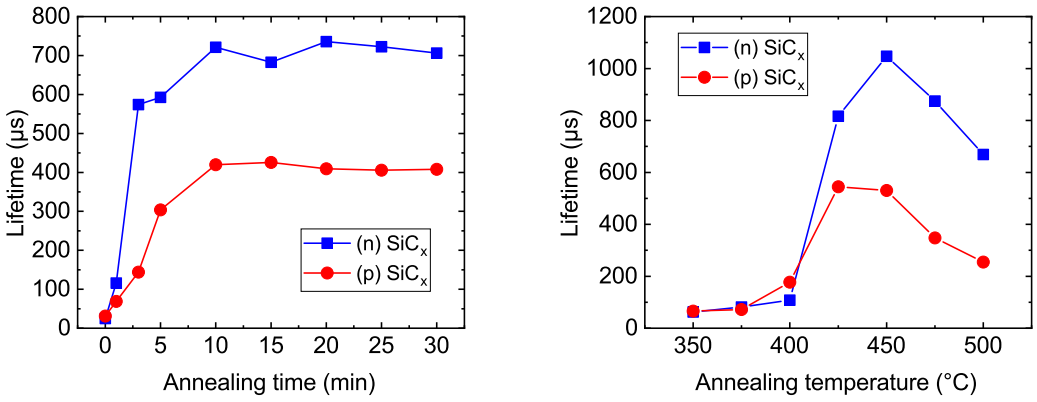

(a) (b)

Figure 4.2: Lifetime values of EPFL samples after the annealing step of the hydrogenation process for various (a) annealing times (at 450 °C) and (b) annealing temperatures (for 30 min-long annealing steps). Courtesy of M. Lehmann.

hand, the maximum lifetime obtained is strongly dependent on the annealing temperature, with the best value obtained when heating the sample at 450 °C. The combination of the a-SiN_x:H deposition and of the annealing step is called "hydrogenation", because the silicon nitride layer acts as a hydrogen source, and during the annealing step, the hydrogen diffuses to the c-Si/SiO_x interface and inside the bulk of the silicon wafer [87].

In order to get more information on the kinetics of the passivation properties during the hydrogenation process, *in situ* MPL measurements are made at IPVF with the setup described in Section 3.1.2. Annealing steps are made in this reactor under an atmosphere of 1 Torr of H_2. In this chapter, we present the lifetime values without any temperature correction (contrary to the previous chapter with the temperature correction described in Section 3.1.4). This is done in order to work with less hypotheses and display all the contributions in the graphs presented.

The annealing steps with *in situ* MPL, the PL Images, the QSSPC measurements, the data treatment and the modeling were carried out by the PhD candidate.

4.1.2 Annealing temperature and hydrogen diffusion

In situ MPL measurements are made on p-type FPC samples during 30 min-long annealing steps. In the light of the values obtained in Figure 4.2b, two different annealing temperatures are investigated: 400 °C and 450 °C (see respectively Figures 4.3a and 4.3b).

- For the sample annealed at 400 °C (see Figure 4.3a), the lifetime stays around 100 µs. The behavior is comparable to the one obtained for AlO_x passivated samples: after an initial increase of the lifetime, it then decreases when the temperature exceeds 300 °C. During the temperature plateau, the lifetime improves only marginally. When the sample starts to cool down, an improvement of the lifetime is observed. Overall the absolute variations and lifetime values remain low.

- The sample heated at 450 °C for 30 min shows an evolution of lifetime displayed in Figure 4.3b. Once the temperature reaches 450 °C, the lifetime increases faster and faster, up to a maximum value of 230 µs after 20 min and remains constant until the end of the 450 °C annealing step. It then dramatically improves during the first few

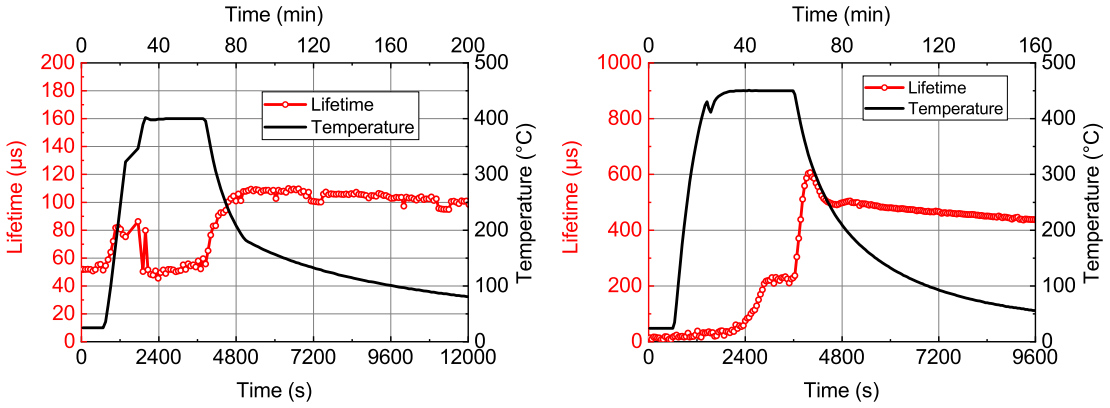

Figure 4.3: Evolution of the minority carrier lifetime of a p-type FPC sample made at EPFL measured *in situ* by MPL during an annealing at (a) 400 °C and (b) 450 °C for 30 min. The black curves display the temperature profiles, the red dots are the lifetime values measured by MPL.

minutes of the cooling step. The final lifetime for this sample annealed at 450 °C measured by QSSPC is 512 µs, and is similar to the results obtained by annealing the samples on a hotplate at EPFL (≈ 500 µs).

The lifetime is very low in the as-deposited state (28 µs), slightly higher after the annealing at 400 °C (90 µs) and significantly improved after the annealing at 450 °C (512 µs). The difference in final lifetime between these two samples is consistent with the observation of Figure 4.2b. For the second sample, the plateau of lifetime is reached after 20 min at 450 °C, which is later than the 10 min expected from the measurements after annealing on a hoptlate (see Figure 4.2a). This might be due to dynamic effects since, in the *in situ* MPL experiment, the temperature rises relatively slowly (around 30 °C/min) while the sample annealed at EPFL is directly put on a hotplate which is already at 450 °C. The decreasing trend during the cooling step in both graphs is likely due to evolutions of the lifetime with temperature (evolution of defects hole and electron capture cross-sections [177], thermal phenomena ...), that were taken into account in the "temperature correction" in the previous chapter.

Photoluminescence images calibrated in lifetime are shown in Figure 4.4. The passivation properties are relatively homogeneous in the samples annealed at 450 °C and in the as-deposited state. However, the sample annealed at 400 °C for 30 min shows a ring-shaped distribution of the minority carrier lifetime. Grant *et al.* [195] also observed such a ring-shape in FZ wafers, with defects related to vacancies appearing in the center of the sample upon rapid thermal annealing at temperatures ranging from 450 °C to 700 °C. These defects were shown to be cured upon annealing at temperatures higher than 1000 °C. Hiller *et al.* [196] showed that one type of defect causing the low values of lifetime is a silicon vacancy with a nitrogen atom in a substitutional position, called V_1N_1 center. These defects are characterized by the formation of a silicon dangling bond (due to the fact that silicon atoms are tetravalent and nitrogen atoms are trivalent), that can be passivated by hydrogenation at lower temperatures. The ring shape originates from the uneven distribution of point-defects during the growth of the silicon ingot [197] (larger defect density in the center than on the edge), that are being stabilized through nitrogen doping during the float-zone process.

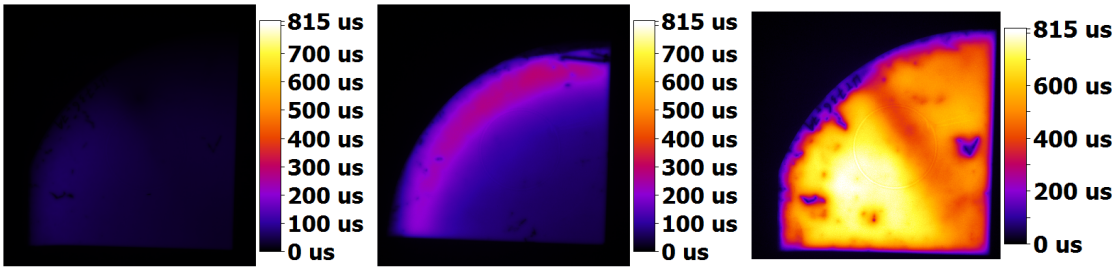

(a) (b) (c)

Figure 4.4: Lifetime calibrated PL images of p-type FPC samples (a) in the as-deposited state, (b) annealed for 30 min at 400 °C, and (c) annealed for 30 min at 450 °C.

One important remark is that the MPL acquisition is made in the center of the sample. Consequently the evolution of the lifetime at the edge of the samples would probably have a slightly different behavior (faster increase of lifetime). From these observations, we conclude that the higher temperature of annealing allows to provide a better final effective lifetime, along with a more homogeneous passivation of the sample. In our experiments, the wafers damaged by the firing step are slowly passivated by hydrogen diffusing from the a-SiN_x:H layer to the inside of the bulk. Once the defects have been cured, the passivation becomes homogeneous again.

Another heat treatment at 450 °C for 30 min of a sample pre-annealed on a hotplate at EPFL at 450 °C for 2 min was investigated. The evolution of the effective lifetime is shown in Figure 4.5. At the beginning, there is a phase of improvement of the lifetime, followed by a decrease when the temperature exceeds 300 °C. Then, as expected, and similarly to Figure 4.3b, the lifetime improves at the beginning of the temperature plateau at 450 °C until saturation at 250 µs, which is close to the lifetime measured at 450 °C in the previous sample (230 µs). The kinetics during the cooling phase is also similar. The lifetime measured by QSSPC goes from 417 µs before annealing to 666 µs after annealing. The PL images before (Figure 4.5b) and after (Figure 4.5c) the annealing step show that after 2 min of annealing at 450 °C, the wafer is not completely cured in its center. The lifetime in the center of the FZ silicon wafer was greatly improved thanks to hydrogen diffusion during this high temperature annealing step: it passivates the active defects remaining in the center of the sample.

In this section, we saw that the FZ silicon wafer was degraded by the firing step carried out before the hydrogenation process. This degradation reportedly results from the formation of defects in the bulk of the silicon wafer (unpassivated V_1N_1 recombination centers and others). All the measurements are in agreement with the fact that these defects are passivated by hydrogen diffusion: there is a higher density of defects in the center of the silicon wafer (PL images) and annealing steps that are either too short or at too low temperature do not manage to passivate all the defects. This is consistent with the temperature dependence of the hydrogen diffusion coefficient

$$D_H = D_{H,0} \exp\left(-\frac{E_0}{k_B T}\right) \tag{4.1}$$

Typically, for values of $D_{H,0} = 2.8\times10^{-3}$ $cm^2.s^{-1}$ and of activation energy $E_0 = 0.49$ eV from the literature [198], a difference in temperature from 400 °C to 450 °C induces an increase of 79 % of the diffusion coefficient (from 6×10^{-7} to 11×10^{-7} $cm^2.s^{-1}$). So far, the kinetics of the hydrogenation process was investigated for p-type FPC samples. The

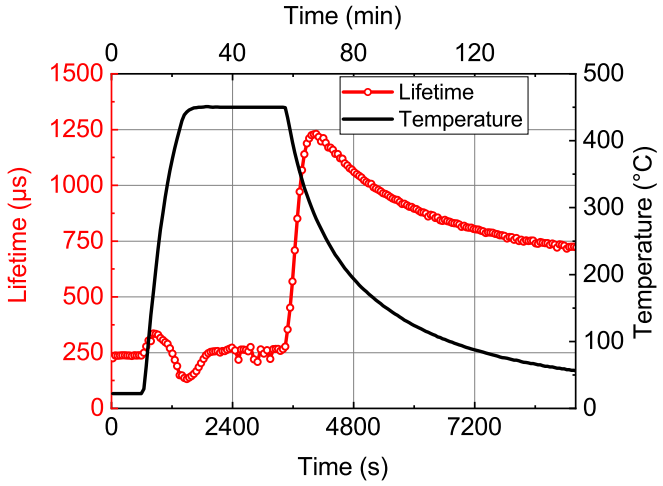

(a)

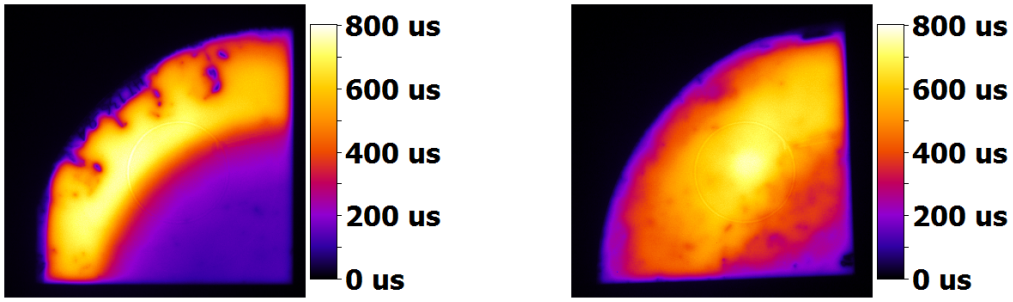

(b) (c)

Figure 4.5: (a) Evolution of the minority carrier lifetime of a p-type FPC sample made at EPFL, and pre-annealed for 2 min at 450 °C, during an annealing step at 450 °C for 30 min. Lifetime calibrated PL images of the sample (b) after the pre-annealing step and (c) after annealing for 30 min at 450 °C.

impact of the temperature and duration of annealing were also evidenced.

4.1.3 Identification of the different contributions

In this section we will investigate the low lifetime plateau that is observed in all the samples when the temperature reaches values above 300 °C.

Reversible drop of lifetime at T > 300 °C

A single sample was subject to 4 consecutive thermal annealing processes of 30 min each. The respective temperature setpoints were 450 °C, 350 °C, 250 °C and finally 450 °C once again. These temperatures were chosen in order to, first, hydrogenate the whole wafer, measure the impact of lower annealing temperature, and check the stability of the sample and the reproducibility of the measurement with a final annealing at again 450 °C. The effective lifetime values measured by MPL during the processes are shown in Figure 4.6.

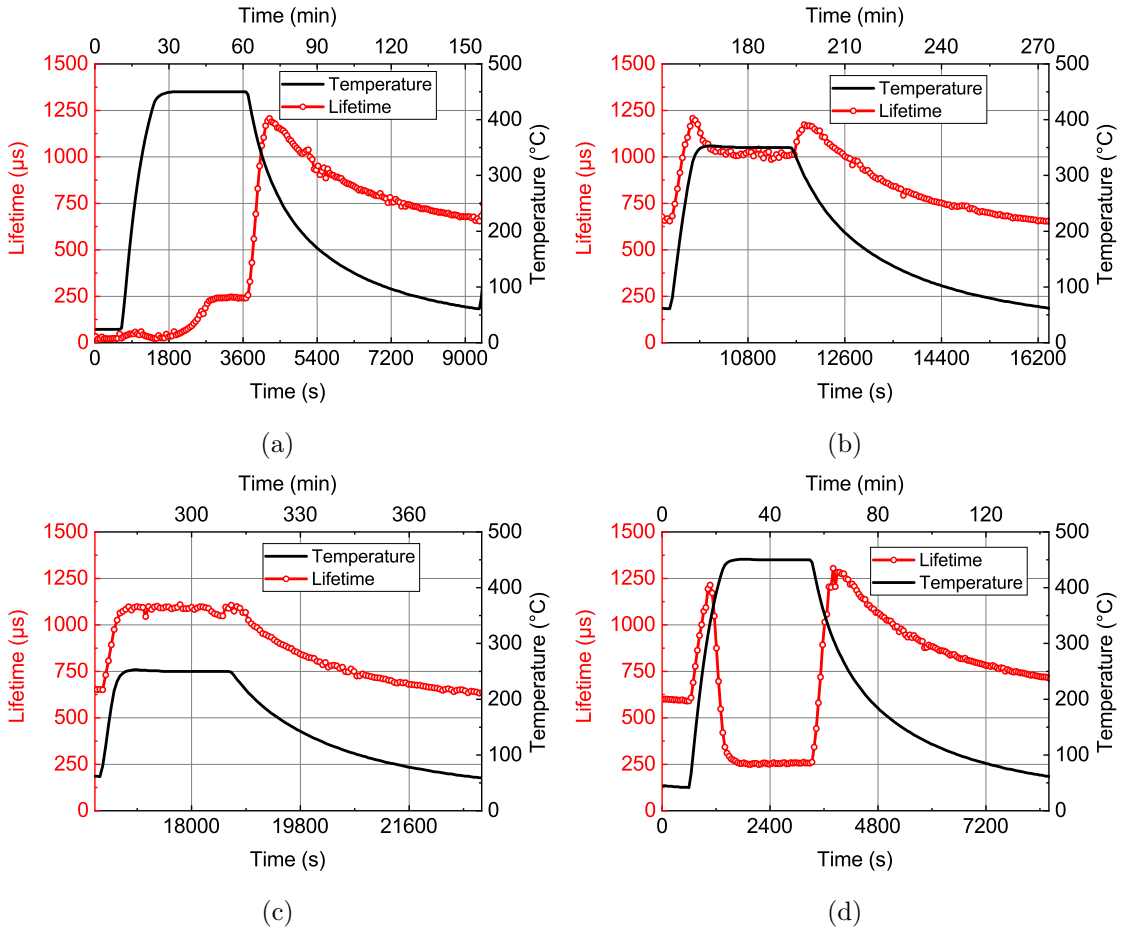

Figure 4.6: Evolution of the minority carrier lifetime of a p-type FPC sample made at EPFL during consecutive annealing steps at (a) 450 °C, (b) 350 °C, (c) 250 °C, and (d) 450 °C for 30 min.

- During the first annealing step (Figure 4.6a), the lifetime follows the same trend as in Figure 4.3b which means that the bulk is likely to have been largely cured at this step. This shows the reproducibility of our observations.

- The lifetime during the subsequent step at 350 °C starts by increasing, and decreases when the temperature exceeds 300 °C (see Figure 4.6b). It stays constant during the temperature plateau.

- In Figure 4.6c, the 250 °C annealing step, no decrease in the measured lifetime can be observed. The lifetime simply follows the temperature profile.

- The evolution of the effective lifetime during the last annealing step at 450 °C for 30 min is shown in Figure 4.6d. First, the lifetime increases for temperatures going up to 300 °C. When exceeding that temperature, the lifetime drops. It is then followed by a quick recovery at the beginning of the cooling phase and then by a decrease in lifetime during the slow decrease of temperature (below 300 °C).

First, in all the samples of this chapter, the increase of lifetime at the beginning of the heating and the decrease during the cooling phase (at temperatures lower than 300 °C) can be, once again, linked to thermal phenomena leading to a change in the minority carrier lifetime of the sample with temperature.

The lifetime measured by QSSPC on the sample before and after the last annealing step (450 °C) stays fairly constant, going from 687 to 744 µs. The last annealing step hence only resulted in a marginal change of the final passivation properties while the lifetime measured by MPL shows significant variations during the process. This is the case for the three last annealing steps. As a consequence, the drop of lifetime at temperatures greater than 300 °C is a reversible phenomenon contrary to the bulk degradations evidenced in the studies mentioned above [195], [197], [199], [200]. Interestingly, when comparing the annealing steps at 350 °C and 450 °C, one can see that the lifetime has a similar behavior, but the values measured at 450 °C are significantly lower (250 µs) than the ones measured at 350 °C (1000 µs). One of the most plausible explanations for this observation is that, when the temperature increases, the amount of thermally generated electron-hole pairs rises dramatically, which puts the sample in conditions where Auger and SRH are significantly increased and become limiting for the measurement of the effective minority carrier lifetime. This is shown in the following paragraphs.

The intrinsic minority carrier density n_i as a function of temperature [201] is given by the equation

$$n_i(T) = AT^{3/2} \exp\left(-\frac{E_g(T)}{2kT}\right) \tag{4.2}$$

where A is a constant depending on the electron and hole effective masses (assumed independent of temperature), T the temperature of the sample, $k = 1.38\times10^{-23}$ J.K^{-1}, and E_g the energy band gap which varies with temperature, following the equation

$$E_g(T) = E_g(0\text{ K}) - \frac{\alpha T^2}{T+\beta} \tag{4.3}$$

with $E_g(0\text{ K}) = 1.170$ eV, $\alpha = 4.73\times10^{-4}$ eV.K^{-1}, and $\beta = 636$ K for silicon [202]. Knowing that $n_i(300\text{ K}) = 1.08\times10^{10}$ cm^{-3}, the value of n_i can be derived in all the range of temperatures investigated during the various processes. The function $n_i(T)$ is shown in Figure 4.7a. For the temperature profile of an annealing at 450 °C for 30 min, the minority carrier density of an intrinsic semiconductor $n = \Delta n + n_i$ is plotted in Figure 4.7b (with $\Delta n = 1\times10^{15}$ cm^{-3} the photo-generated electron-hole pair density).

In order to get a better visualization of the impact of the higher minority carrier density generated during the annealing process, we use the $\tau_{eff}(n)$ plot measured by QSSPC for

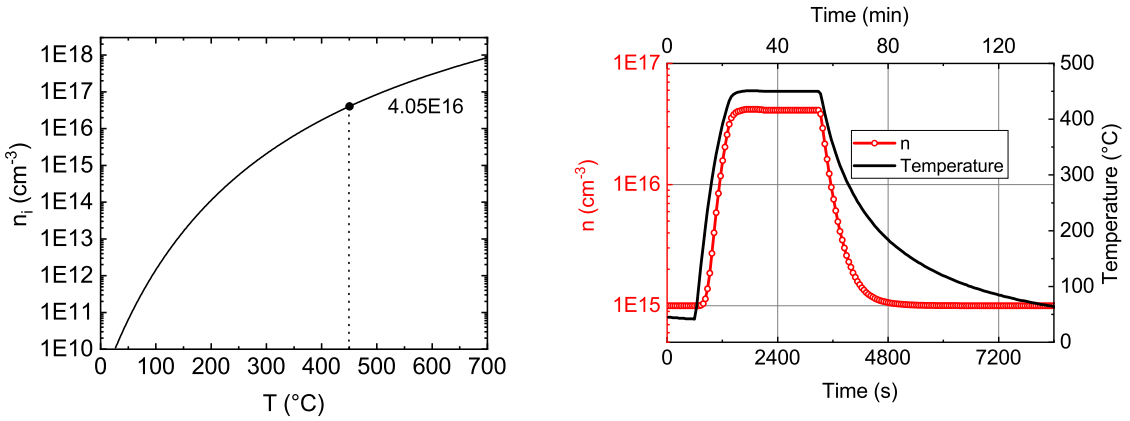

(a) (b)

Figure 4.7: (a) Evolution of the intrinsic carrier density as a function of temperature (adapted from [202]). (b) Variation of the minority carrier density at a fixed value of $\Delta n = 1\times10^{15}$ cm^{-3} during an annealing step at 450 °C for 30 min (black solid line: temperature profile).

the studied sample at the end of the 4^{th} annealing step (see Figure 4.8a). We then link the lifetime values to the evolution of the total minority carrier density shown in Figure 4.7b. This evolution of the lifetime is shown in Figure 4.8b and does not take into account any thermal phenomenon other than electron-hole pair generation. Due to the limited range of minority carrier density measured in the QSSPC experiment, the values of the lifetime for minority carrier densities greater than 2.5×10^{16} cm^{-3} are not available. Even without these values, this graph supports the assumption that the reversible drop of lifetime at high temperatures is due to Auger and SRH recombinations linked to a high intrinsic minority carrier density. Indeed, this shows that, even if the passivation properties of the sample did not change at all, the evolution of the thermally generated minority carrier density alone during the annealing would result in the large lifetime variations shown in Figure 4.8b.

We can then conclude that the large variations of lifetime observed in Figure 4.6d are due to two main competing phenomena: (i) the evolution of the effective minority carrier lifetime in the sample due to thermal phenomena (increase when the temperature rises) and (ii) the variation of the intrinsic minority carrier density with temperature, which induces a large drop of the lifetime due to high injection levels.

The algorithm and the measurement procedure would need to be adapted in order to take this contribution into account. Indeed, the values displayed in the various graphs shown so far are actually lifetime values extracted at minority carrier densities that can be significantly different from one another due to thermally generated charge carriers. Only the photogenerated electron-hole pair density is identical. Consequently the values do not describe the sample in similar conditions - which is the original purpose of displaying the lifetime value at a minority carrier density of 1×10^{15} cm^{-3}. Strictly comparing the results measured by MPL at very different temperatures is thus not physically meaningful. A simple addition of the intrinsic carrier density would not be particularly helpful since at 450 °C, the intrinsic carrier density is equal to 4×10^{16} cm^{-3}, which is very large compared to 1×10^{15} cm^{-3} and would make the extrapolation of the $\tau_{eff}(n)$ function unreliable. Further work on the acquisition routine would need to be carried out.

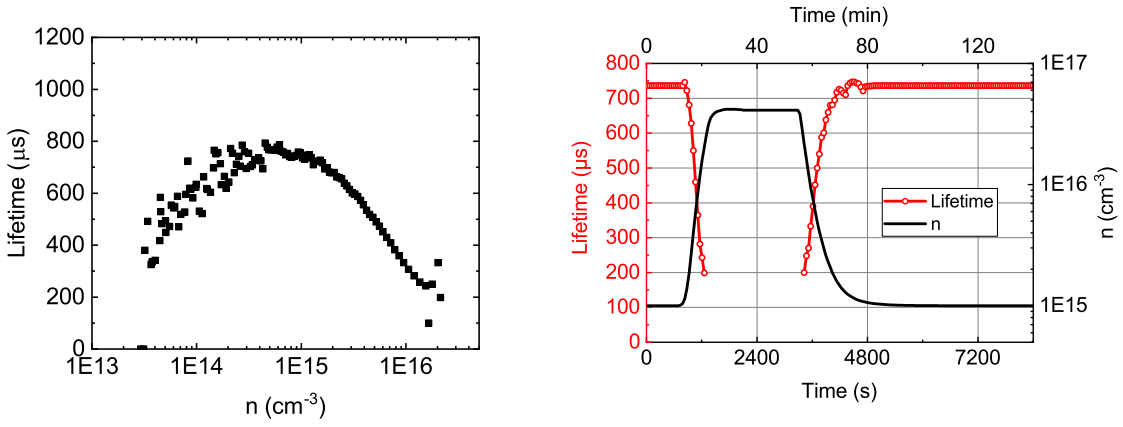

(a) (b)

Figure 4.8: (a) Lifetime versus minority carrier density of the sample after the last annealing step (measured by QSSPC). (b) Evolution of the lifetime with time (in red), by simply taking into account the increase in minority carrier density (back solid line).

Bulk lifetime

We are now trying to isolate the evolution of the bulk lifetime in order to focus on the hydrogenation kinetics. As seen above, the effective lifetime values displayed in the various graphs of this section result from the combination of various contributions. For better clarity, the contribution coming from the bulk lifetime, related to the N_1V_1 centers and other firing-related defects, is to be isolated. For simplification purposes, we assume that the variation of this so called "bulk lifetime" τ_{bulk} is strictly independent of the variations observed in Figure 4.6d, which are assumed to be variations of lifetime from other contributions written τ_{other}. This means that this "bulk" lifetime is actually an equivalent bulk lifetime at ambient temperature (the temperature-related changes being taken into account in the τ_{other} contribution).

Similarly to Equation 3.2, we assume the effective lifetime to follow the expression:

$$\frac{1}{\tau_{eff}} = \frac{1}{\tau_{bulk}} + \frac{1}{\tau_{other}} \tag{4.4}$$

Consequently, the bulk lifetime can be re-written:

$$\tau_{bulk} = \frac{\tau_{other}\tau_{eff}}{\tau_{other} - \tau_{eff}} \tag{4.5}$$

As seen previously, the fourth annealing step at 450 °C of the studied sample has a negligible impact on the overall passivation properties (marginal change in the lifetime measured by QSSPC). Consequently, this fourth annealing will be considered as reference process step "0". For this reference, we assume that the "reference bulk lifetime" $\tau_{bulk,0}$ is constant during the whole annealing step. In order to extract the evolution of the bulk lifetime during an investigated process step 1 with a similar temperature profile, we assume that the passivation properties "other" than the aforementioned firing-related "bulk" lifetime are similar to the ones of the reference sample, hence $\tau_{other,0} = \tau_{other,1} =$

τ_{other}. Consequently

$$\tau_{bulk,1} = \frac{\frac{\tau_{bulk,0}\tau_{eff,0}}{\tau_{bulk,0}-\tau_{eff,0}}\tau_{eff,1}}{\frac{\tau_{bulk,0}\tau_{eff,0}}{\tau_{bulk,0}-\tau_{eff,0}} - \tau_{eff,1}}$$
$$= \frac{\tau_{bulk,0}\tau_{eff,0}\tau_{eff,1}}{\tau_{bulk,0}\tau_{eff,0} + \tau_{eff,0}\tau_{eff,1} - \tau_{bulk,0}\tau_{eff,1}}$$
$$\tau_{bulk,1} = \frac{\tau_{eff,0}\tau_{eff,1}}{\tau_{eff,0} - \tau_{eff,1} + \frac{\tau_{eff,0}\tau_{eff,1}}{\tau_{bulk,0}}} \tag{4.6}$$

Figure 4.9a shows the superposition of the lifetime values measured by MPL during the "reference" annealing step (last annealing) and the studied hydrogenation process (first annealing step). The temperature profile (identical for both annealing treatments) is once more represented by a black solid line. Thanks to Equation 4.6, these effective lifetime values are used in order to calculate the evolution of an equivalent bulk lifetime $\tau_{bulk,1}$ at ambient temperature during the hydrogenation process in Figure 4.9b. The bulk lifetime in the reference sample is assumed to be equal to $\tau_{bulk,0} = 2000$ µs. The arbitrary choice of $\tau_{bulk,0}$ value does not have a dramatic impact on the observed behavior of the bulk lifetime, as further investigated in Appendix A1. This allows to identify more clearly the accelerating increase in lifetime during the hydrogenation process.

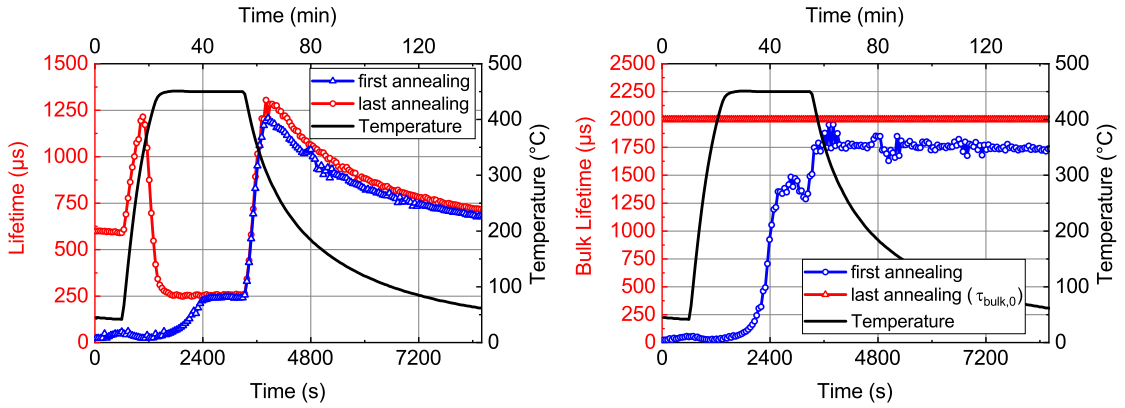

(a) (b)

Figure 4.9: (a) Superposition of the first (blue) and last (red) annealing steps for 30 min at 450 °C (see Figure 4.6). (b) Bulk lifetime evolution calculated with Equation 4.6, under the assumption that the bulk lifetime in the reference sample is $\tau_{bulk,0} = 2000$ µs (red points).

The larger noise and jumps starting from the lifetime plateau after 2450 s are due to the fact that $\tau_{bulk,1}$ depends on the difference $\tau_{eff,0} - \tau_{eff,1}$ (even more so if $\tau_{eff} \ll \tau_{bulk,0}$). Consequently, a slight shift in the alignment of the profiles can lead to a significant change in the calculated bulk lifetime values.

The aforementioned fast increase in $\tau_{bulk,1}$ when the temperature reaches 450 °C is consistent with the Shockley-Read-Hall theory. We assume that:

$$\frac{1}{\tau_{bulk}} = \frac{1}{\tau_{firing}} + \frac{1}{\tau_{rest}} \tag{4.7}$$

with $\tau_{rest} = 2000$ µs, and $\tau_{firing} = 1/(CN_{firing})$ with C a proportionality constant and N_{firing} the density in recombination centers created during the firing step (V_1N_1 centers and others). The defects are assumed to be represented as one single kind of defect (see equation 1.11 from Shockley-Read-Hall). This implies that:

$$\tau_{bulk} = \frac{\tau_{rest}}{\tau_{rest} C N_{firing} + 1} \tag{4.8}$$

During the hydrogenation process, if one assumes a linear decrease of the defect density N_{firing} until saturation, this model results in an evolution of the lifetime such as shown in Figure 4.10, which follows the same trend as the one observed in Figure 4.9b. Consequently, this SRH assumption of an increase of the recombination rate proportional to the defect density is quite consistent with the results observed in the MPL experiments.

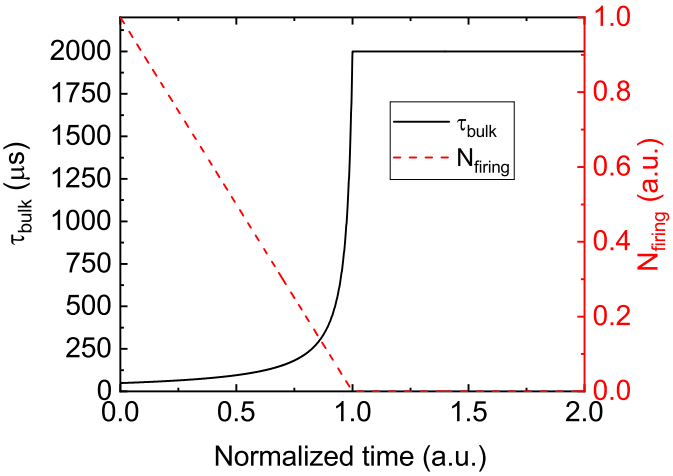

Figure 4.10: Simulated evolution of the bulk lifetime value for a linear decrease of the defect density N_{firing}. This profile results from Shockley-Read-Hall theory, under the assumption that there is only one type of bulk defect.

This section allowed to isolate the hydrogenation contribution from the other contributions (Auger, SRH, thermal effects, ...) in a physically comprehensive manner. We showed that the increase in lifetime follows an accelerating behavior consistent with a constant hydrogen flux provided by the a-SiN_x:H layer, that would come cure defects in the bulk of the wafer according to Shockley-Read-Hall theory.

Influence of a-SiC_x:H doping

The 450 °C annealing step for 30 min was also carried out on a FPC sample with (n) a-SiC_x:H deposited on the SiO_x tunnel layer instead of (p) a-SiC_x:H. The *in situ* MPL measurement is shown in Figure 4.11a. The behavior is similar to the p-type FPC, with an increasing lifetime during the temperature plateau at 450 °C. QSSPC measurements confirm the dramatic increase of the sample lifetime from 3 µs to 1858 µs. The passivation of the sample is also relatively homogeneous despite some defects on the bottom right hand corner of the sample due to manipulation (see Figure 4.11b). This similarity in the passivation kinetics is, once more, consistent with the hydrogen diffusion process at the origin of the passivation of the wafer bulk defects: the doping of the a-SiC_x:H layer is not expected to have a significant impact on the in-diffusion of hydrogen.

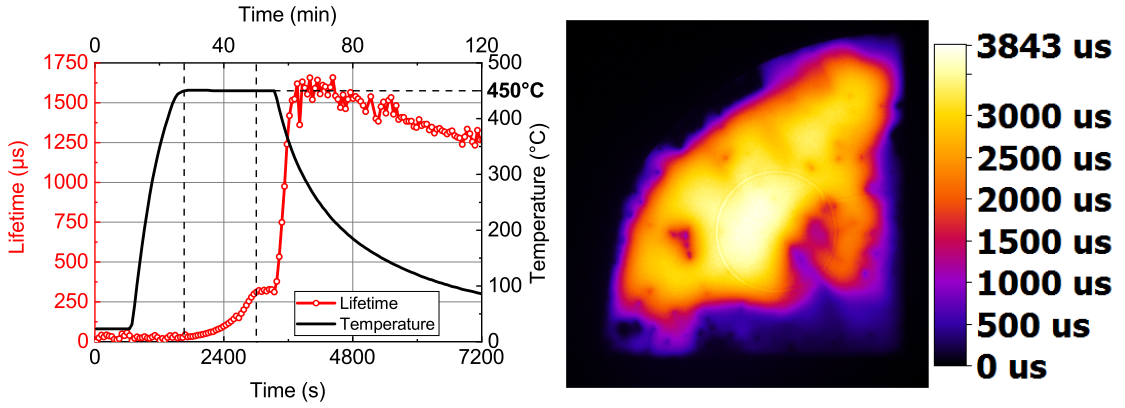

(a) (b)

Figure 4.11: (a) Evolution of the minority carrier lifetime of a n-type FPC sample made at EPFL during an annealing at 450 °C and (b) PL Image of the sample after the annealing step.

Interestingly, as mentioned before, the lifetime measured at the end of the temperature plateau is equal to 230 µs for the p-type FPC sample (see Figure 4.3b), while this value reaches 350 µs for the n-type FPC. Since the only difference between these two samples is the surface passivation, one can assume that all the other contributions are equal. By assuming them (bulk, Auger, other thermal contributions) to lead to a lifetime of 400 µs, this would imply the equivalent lifetimes due to surface recombinations to be equal to $\tau_{surf,p}$ = 540 µs and $\tau_{surf,n}$ = 1600 µs. These calculated values are consistent with the ones measured at the end of *in situ* MPL experiments.

In this section, we showed that the FPC fabrication process used at EPFL gives rise to the formation of defects during the firing step. The subsequent hydrogenation process allows to passivate these defects after spending around 20 min at 450 °C, and the evolution of the lifetime is consistent with the bulk defect theory of Shockley-Read-Hall, assuming a linear decrease of the bulk defect density. A series of annealing experiments allowed to study the origin of the low lifetime values systematically measured at high temperature. These were shown to be due to thermally generated electron-hole pairs during the high temperature processes, which leads to minority carrier densities significantly larger than 1×10^{15} cm^{-3} and consequently boosts Auger and SRH recombinations.

4.2 Hydrogenation before firing

After the investigation of the samples processed at EPFL with a hydrogenation step after firing, this section studies the fabrication process described in Chapter 2. More specifically, the evolution of the passivation properties during the hydrogenation step - following the deposition of the doped µc-Si:H or µc-SiO_x layer - and before the firing step is investigated. The different layers and stacks used in this section are the ones that were previously optimized.

4.2.1 *In situ* MPL setup for acquisition during a PECVD process

The silicon nitride deposition step described in Chapter 2 was optimized in a PECVD chamber of the MVS cluster tool. In order to use equivalent deposition conditions and

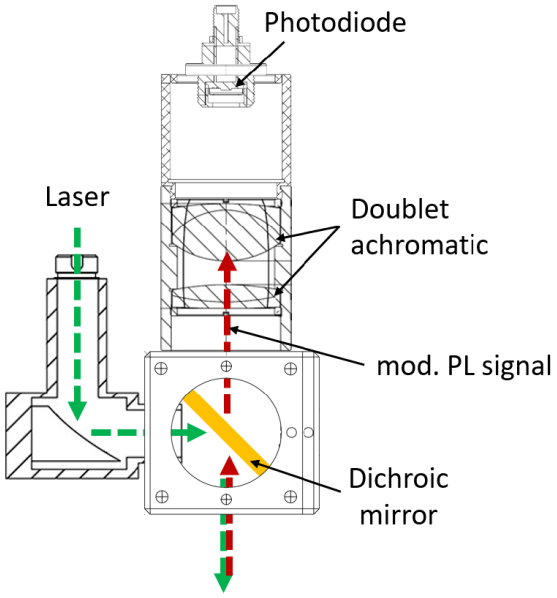

Figure 4.12: Optical system designed for the integration of *in situ* MPL into the MVS cluster tool (extracted from [169]).

keep the same deposited material, an *in situ* MPL setup mounted on the same MVS cluster is used. This setup is more thoroughly described in the thesis of M. Sreng [169]. The working principle is the same as what was described in Section 3.1.2. However, the optical system is slightly different, and is shown in Figure 4.12. This change is due to the fact that only one single window could be drilled in the PECVD reactor, which requires the MPL signal to be collected in the same direction as the incident laser beam, thus requiring the use of a dichroic mirror. The MPL is focused on the InGaAs photodiode thanks to the doublet achromatic pair, and the reflected light is optically removed thanks to a longpass filter.

In the rest of this chapter, the measurements will display the evolution of the minority carrier lifetime during different process steps in a PECVD chamber which has a setpoint temperature of 350 °C. Contrary to the experiments done previously, the temperature of the sample is not supposed to vary significantly during the process. However, when the sample is put in the chamber, it is initially at ambient temperature, and quickly heats up to reach the setpoint temperature of 350 °C. In order to estimate the duration of this increase in temperature, a sample that was previously processed at 350 °C is put back in the PECVD chamber. The lifetime should not be significantly impacted by this additional heating experiment. Figure 4.13 shows the evolution of the lifetime measured by *in situ* MPL during this second annealing step. It can be seen that the lifetime increases for up to 2 minutes when the sample is put in the PECVD chamber. After this initial increase, one can assume that the sample has reached thermal equilibrium. Consequently, caution must be taken when observing changes during the first 2 minutes of the process since these can be induced by the thermalization of the sample.

As discussed in the previous section, the lifetime at 350 °C is not equivalent to what will be measured at ambient temperature. However, all the following measurements are done at 350 °C. Consequently, the interpretations will mostly focus on the evolution of the lifetime, and not on the absolute lifetime values displayed in the figures. Additionally, the samples processed are, for the most part, symmetric samples. In order to obtain a

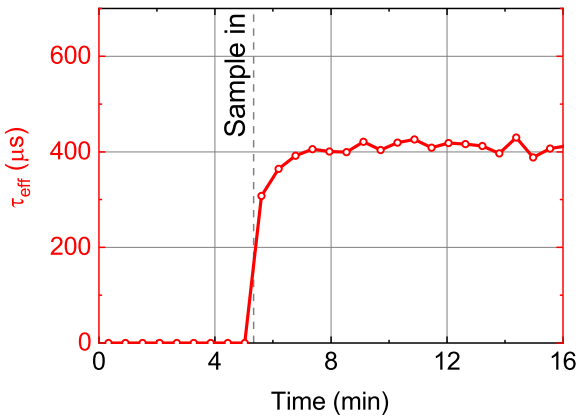

Figure 4.13: Evolution of the lifetime for a passivated sample after its introduction in the PECVD chamber at 350 °C.

reliable QSSPC measurement of the passivation quality provided by the deposited stacks, the process steps (plasma treatment or deposition steps) are carried out twice: once on each side of the sample. Consequently, most of the figures later on will be composed of 2 measurements, one on each side ((a) putting the sample in, pre-heat, deposition, post-heat, taking sample out, (b) flipping sample, putting the sample in, pre-heat, deposition, post-heat, taking sample out).

4.2.2 (p) µc-Si:H and (p) µc-SiO_x:H under NH_3 + H_2 plasma exposure

The final considerations of Chapter 2 discuss the role of the capping layer, and more specifically the improvement of the passivation properties along with their maintain after a subsequent firing step. In this section we focus on the evolution of the passivation properties during an NH_3 + H_2 plasma.

During one experiment, the silane tank ran out of silane, and the a-SiN_x:H deposition step on a SiO_x/(p) µc-Si:H passivating stack was carried out with no SiH_4 in the gas mixture. Interestingly, this step allowed to reach a passivation that was close to the one obtained after a normal a-SiN_x:H deposition. However, when trying this NH_3 + H_2 plasma step on a SiO_x/(p) µc-SiO_x sample, the passivation properties remained extremely low (see Figure 4.14). When depositing a-SiN_x:H instead (adding 7.5 sccm of SiH_4 to the previous exact same conditions), the lifetime increase dramatically in both samples.

Two factors are expected to have an impact on the passivation properties: the temperature of the deposition chamber (annealing) and the NH_3 + H_2 plasma itself. In order to get a better understanding of the role of these different contributions in the evolution of the passivation properties, the process step is investigated by *in situ* MPL.

Figure 4.15 shows the effect of the exposure of a SiO_x/(p) µc-SiO_x symmetrically passivated sample to an NH_3 + H_2 plasma. One can observe that when the sample is put in the chamber, the lifetime directly starts to increase. Indeed, the PECVD chamber being at 350 °C, this anneals the sample, which improves the passivation quality of the stack. However, when the NH_3 + H_2 plasma is switched on, the lifetime decreases continuously, and irreversibly: despite a tiny recovery when the plasma is stopped, the lifetime remains low. During the exposure of the second side of the sample, the lifetime remains at very

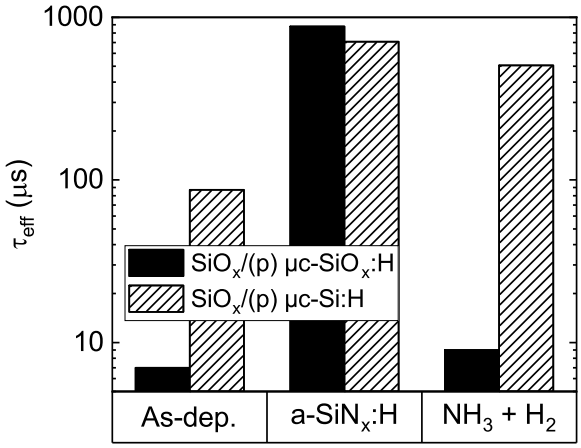

Figure 4.14: Effective lifetime measured by QSSPC of either SiO_x/(p) µc-SiO_x (black squares) or SiO_x/(p) µc-Si:H (red circles) passivating stacks after different process steps: (i) in the as-deposited state, (ii) after exposure to an NH_3 + H_2 plasma, or (iii) after a-SiN_x:H deposition instead. The lines are provided as a guide to the eye.

low values, and seems to degrade even further when the plasma is switched on once again. As shown in Figure 4.14, the lifetime goes from 7 to 9 µs, which is extremely low.

Figure 4.16 shows the effect of the exposure of a SiO_x/(p) µc-Si:H symmetrically passivated sample to the same NH_3 + H_2 plasma. When the sample is put in the chamber, the lifetime increases only marginally during the pre-heating phase (10 min). It then increases steadily during the exposure to NH_3 + H_2 plasma. However, at the very beginning of the NH_3 + H_2 plasma step, the lifetime displays a small decrease. During the processing of the second side of the sample, the lifetime does not change significantly, but seems to slightly degrade during the exposure to NH_3+H_2 plasma. The lifetime measured by QSSPC goes from 87 to 507 µs.

In order to tell apart the annealing and the plasma contributions for (p) µc-Si:H, a sample is simply put in the PECVD chamber at 350 °C, and the evolution of the lifetime is measured by *in situ* MPL. In Figure A3.11, this measurement is superimposed to the one shown in Figure 4.16a. One can see that the trend is similar for both samples, implying that most of the improvement observed in Figure 4.16 is due to the annealing. This is consistent with the fact that no improvement can be seen when exposing the second side of the sample to the plasma. On the contrary and similarly to (p) µc-SiO_x, the plasma only seems to be detrimental for the passivation properties. The higher final lifetime value measured by QSSPC (766 µs vs 507 µs) of the sample simply annealed supports this statement.

An experiment similar to the one Figure 4.16 is carried out, but with a RF power twice as high (10 W instead of 5 W). The results are shown in Figure 4.18. In this sample, the lifetime starts to increase a bit earlier than in the previous experiments, but what is more noticeable is the larger decrease in lifetime when the plasma is switched on. The final lifetime measured by QSSPC is τ_{eff} = 272 µs. This means that the plasma-related degradation is more detrimental to the passivation properties at higher power densities.

This degradation could be related to the UV emission from the NH_3 plasma (many strong emission peaks in the 300-400 nm range, and more precisely at 336 nm for the NH*

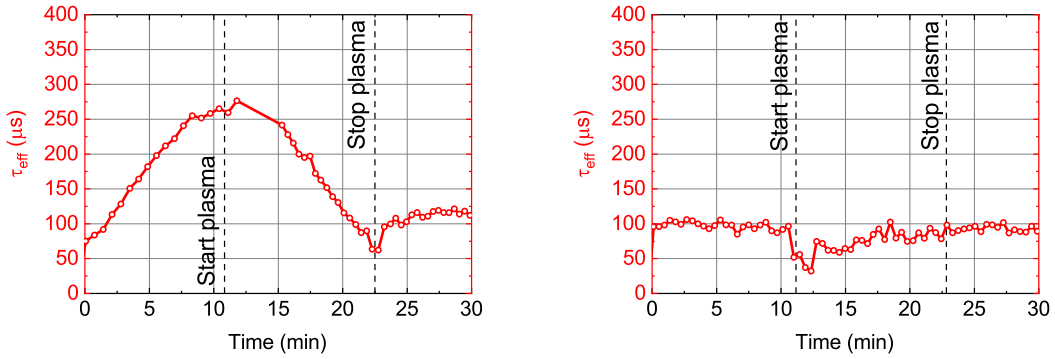

(a) (b)

Figure 4.15: Evolution of the minority carrier lifetime of a sample passivated with a SiO_x/(p) µc-SiO_x:H symmetric stack, exposed to an NH_3 + H_2 plasma of 5 W at 350 °C on (a) the first side of the sample and subsequently on (b) the second side.

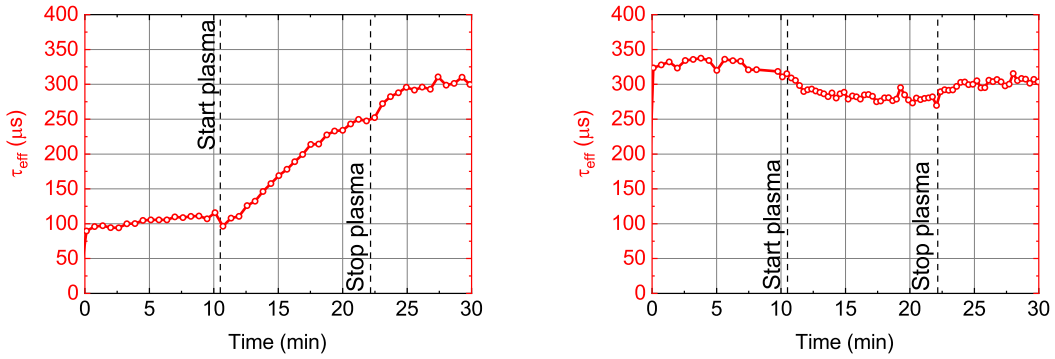

(a) (b)

Figure 4.16: Evolution of the minority carrier lifetime of a sample passivated with a SiO_x/(p) µc-Si:H symmetric stack, exposed to an NH_3 + H_2 plasma of 5 W at 350 °C on (a) the first side of the sample and subsequently on (b) the second side.

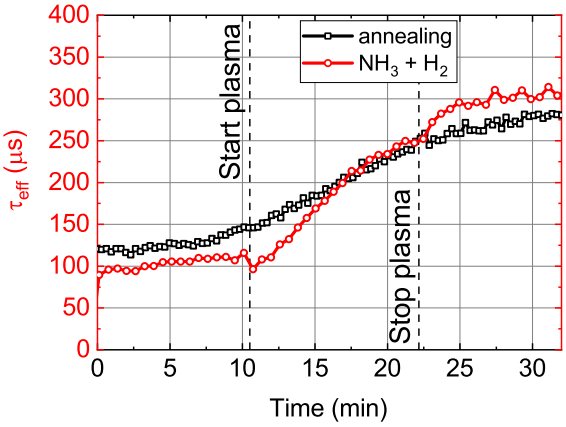

Figure 4.17: Evolution of the minority carrier lifetime of a sample passivated with a SiO_x/(p) µc-Si:H symmetric stack, (i) either exposed to an NH_3 + H_2 plasma at 350 °C (in black) or (ii) simply put in the PECVD chamber at 350 °C (in red).

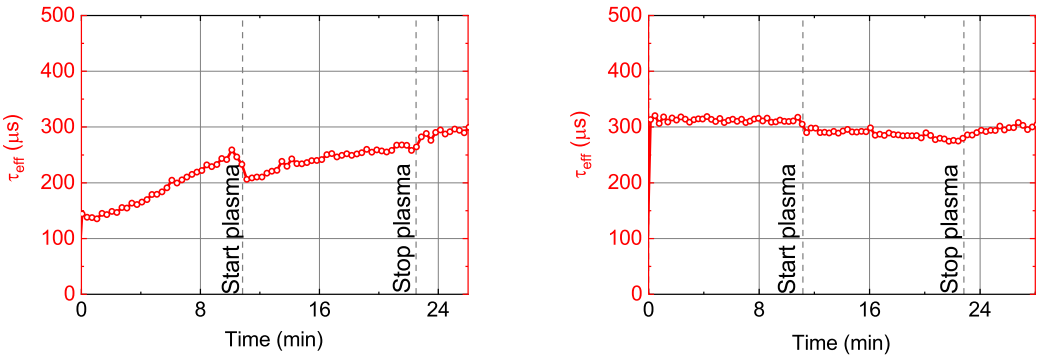

(a) (b)

Figure 4.18: Evolution of the minority carrier lifetime of a sample passivated with a SiO_x/(p) µc-Si:H symmetric stack, exposed to a NH_3/H_2 plasma of 10 W at 350 °C on (a) the first side of the sample and subsequently on (b) the second side.

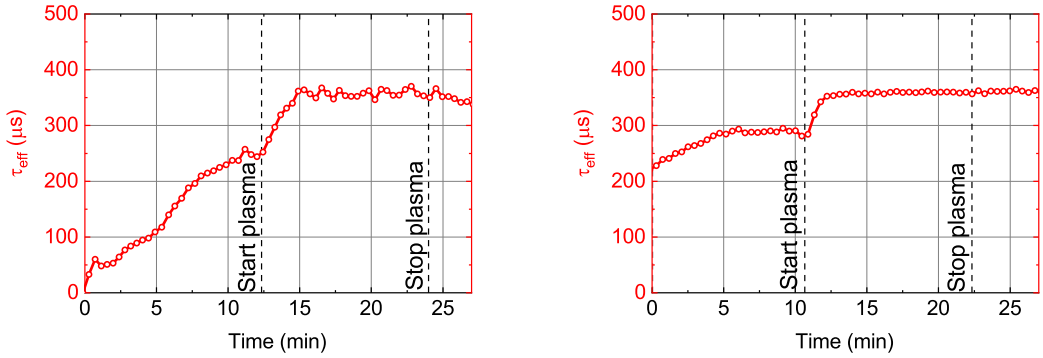

Figure 4.19: Evolution of the minority carrier lifetime of a sample passivated with a SiO_x/(p) µc-SiO_x:H symmetric stack, during the deposition of a-SiN_x:H at 350 °C on (a) the first side of the sample and subsequently on (b) the second side.

ammonia peak [203]), which can induce the breaking of Si-H bonds [145]. The difference between the degradation rates of (p) µc-Si:H and (p) µc-SiO_x could then be partially explained by the higher transparency of the latter, thus allowing more UV light to reach the c-Si/SiO_x interface.

In this section, we showed that the passivation properties of the FPC samples increase upon annealing at 350 °C, and that removing the SiH_4 precursor required for the a-SiN_x:H deposition (NH_3 + H_2 plasma) had a detrimental effect on the passivation properties, which is even more dramatic in the case of (p) µc-SiO_x-based FPC.

4.2.3 Evolution of the passivation during a-SiN_x:H deposition

The silicon nitride deposition showed its importance for the activation of the passivation of the FPC samples. Such a layer is deposited on a SiO_x/(p) µc-SiO_x symmetrically passivated sample, and the evolution of the lifetime is measured by *in situ* MPL in Figure 4.19. When the sample enters in the PECVD chamber at 350 °C, its lifetime increases as previously observed in Figure 4.15. More interestingly, when the SiH_4 + NH_3 + H_2 plasma is switched on, the lifetime slightly drops at the very beginning, increases significantly over the 2 first minutes of deposition, and then stays fairly constant. This overall increase is equally observed during the deposition on the second side of the sample.

The fact that both depositions improve the passivation properties implies that, in this case, the increase in lifetime is related to an improvement of the surface passivation, along with the general improvement of the passivation properties through thermal annealing (as shown in the previous section). While the lifetime of the sample exposed to a NH_3 + H_2 went from 7 to 9 µs, the one exposed to a SiH_4 + NH_3 + H_2 plasma (all else being equal) goes from 6 to 879 µs.

Similar measurements were made on (n) µc-Si:H and (n) µc-SiO_x respectively in Figures 4.20 and 4.21. The behavior remains generally the same: (i) the lifetime is very low at the beginning, increases during the first deposition due to a combination of the annealing temperature and of the SiH_4 + NH_3 + H_2 plasma, and (ii) significantly increases once again during the first minutes of SiN_x:H deposition on the second side of the sample.

It is worth noticing two important features. First, the lifetime seems to be still increas-

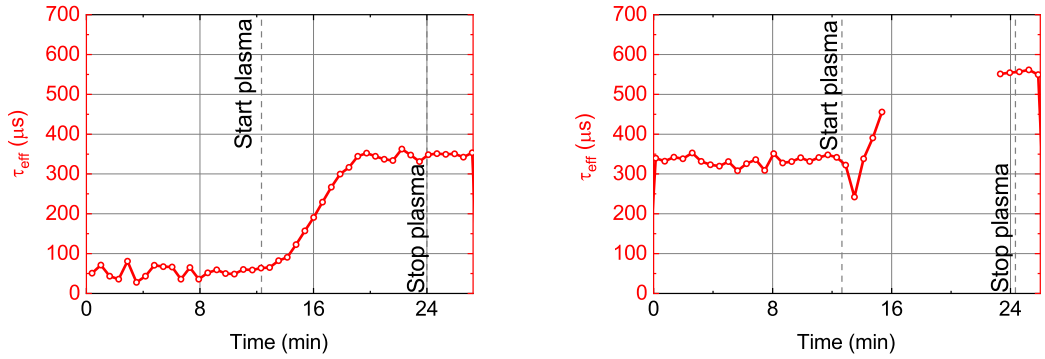

Figure 4.20: Evolution of the minority carrier lifetime of a sample passivated with a SiO_x/(n) µc-Si:H symmetric stack, during the deposition of a-SiN_x:H at 350 °C on (a) the first side of the sample and subsequently on (b) the second side.

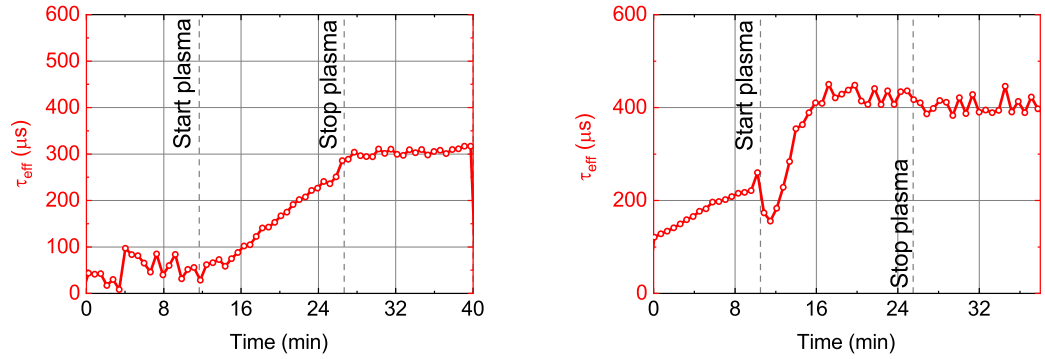

Figure 4.21: Evolution of the minority carrier lifetime of a sample passivated with a SiO_x/(n) µc-SiO_x:H symmetric stack, during the deposition of a-SiN_x:H at 350 °C on (a) the first side of the sample and subsequently on (b) the second side.

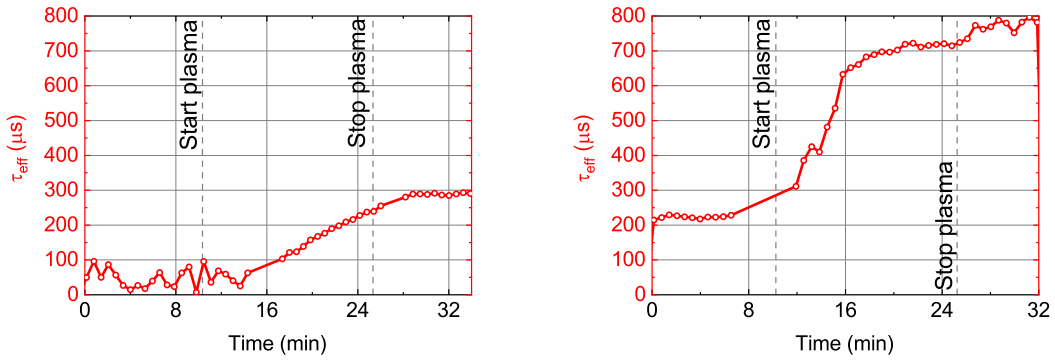

Figure 4.22: Evolution of the minority carrier lifetime of a sample passivated with a SiO_x/(n) µc-SiO_x:H symmetric stack, during the deposition of a-SiN_x:H at 350 °C on (a) the first side of the sample and subsequently on (b) the second side. In this sample, the (n) µc-SiO_x:H layer is 140 nm-thick.

ing during the pre-heating step of the second deposition for (n) µc-SiO_x and (p) µc-SiO_x while it is constant for (n) µc-Si:H. This may mean that the µc-SiO_x layers would need longer annealing times in order to reach the maximum lifetime compared to µc-Si:H for equivalent thicknesses (30 nm). Second, in both n-type samples, a drop of lifetime is observable when the SiH_4+NH_3+H_2 plasma is switched on. This observation is not very surprising since, at the beginning of the deposition, the sample is still coated with a simple SiO_x/(n) µc-Si(O_x):H passivating stack and the plasma is likely to emit UV radiations due to the presence of NH_3. The drop of lifetime is mainly visible during the second deposition since, for the first deposition, the initial lifetime is very low and does not allow this kind of observation. However after less than 2 minutes of deposition, the sample is coated by an additional thin a-SiN_x:H layer, which likely protects the sample from degrading further (optical and physical barrier).

The a-SiN_x:H layer has a high positive fixed charge density ($+3\times10^{12}$ cm^{-2}, measured by COCOS). In order to make sure that the improvement is not due to field effect passivation provided by the silicon nitride layer, we measure the lifetime by *in situ* MPL for a sample with a 140 nm-thick layer of (n) µc-SiO_x which should screen the field-effect from the charges in the a-SiN_x:H layer. Figure 4.22 shows that the dynamics of the lifetime is identical to the one with a thinner layer. The lifetime measured by QSSPC goes from 0 to 2333 µs. The final lifetime value is even higher in this case than in the previous sample, which implies that the passivation properties are not provided by fixed charges sitting in the a-SiN_x:H layer, which effect on the passivation would be hindered by a thicker (n) µc-SiO_x layer. In this sample, the lifetime could not be measured at the beginning of the a-SiN_x:H deposition step due to acquisition issues (from 700 to 950 s).

So far, we studied by *in situ* MPL the evolution of the passivation properties provided by a FPC structure during the deposition of the a-SiN_x:H capping layer. This allowed to evidence the strong impact of this step during which the lifetime is improved both by the deposition of the layer itself and by the annealing of the underlying layers. The behavior between n-type and p-type FPC is quite similar, but the degradation observed when the plasma is started is more noticeable for n-type layers. This might be partially explained by the higher lifetime values in n-type FPC samples which may make the degradation more

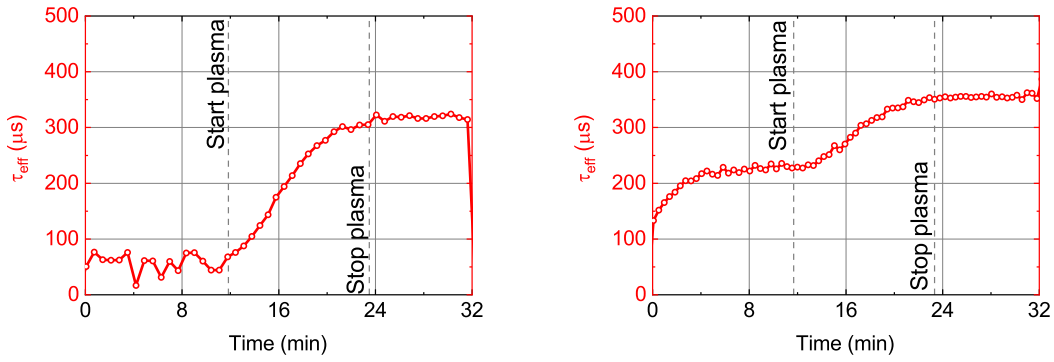

Figure 4.23: Evolution of the minority carrier lifetime of a sample passivated with a SiO_x/(p) µc-SiO_x:H on side 1 and (n) µc-Si:H on side 2, during the deposition of a-SiN_x:H at 350 °C on (a) the first side of the sample and subsequently on (b) the second side.

visible. We showed that the improvement due to the annealing of the layers is larger and takes more time for µc-SiO_x than for µc-Si:H. The deposition of the a-SiN_x:H layer itself gives a boost to the measured lifetime values during the first few minutes of deposition, which is not linked to the fixed charge density embedded in this material. Consequently, the increase in passivation during this deposition must be due to an increase in chemical passivation.

4.2.4 Cell precursors with p-type and n-type FPC

In order to get first solar cell precursors, despite the loss of passivation during the firing step, in this section we study samples with a p-type FPC on the rear side and an n-type FPC on the front side. Since the sample is not symmetric anymore, the question of the order of the deposition steps rises. Two identical samples are investigated: the front side is capped with a 30 nm-thick (n) µc-Si:H layer, and the rear side is capped with a 45 nm-thick (p) µc-SiO_x layer. In the first sample in Figure 4.23, the silicon nitride is first deposited on the (p) µc-SiO_x:H layer ("Side 1 = (p) µc-SiO_x"), then on the (n) µc-Si:H. For the second sample in Figure 4.24, the silicon nitride is first deposited on the (n) µc-Si:H layer ("Side 1 = (p) µc-SiO_x"), then on the (p) µc-SiO_x:H.

The evolution of the lifetime follows a similar trend for the two samples: important increase during the first a-SiN_x:H deposition (due to the combined action of the SiH_4+NH_3+H_2 and of the deposition temperature), and an additional boost in lifetime at the beginning of the second deposition step (side 2).

However, a significant difference in the final lifetime measured by QSSPC is observed: while the first sample only reached τ_{eff} = 550 µs and iV_{oc} = 685 mV, the second sample (starting a-SiN_x:H deposition on the (n) µc-Si:H layers) shows significantly higher passivation properties with τ_{eff} = 940 µs and iV_{oc} = 699 mV. Consequently, the order of the deposition steps has an impact on the passivation properties. This should be taken into account in the final process flow chosen for the fabrication of a both-sides FPC contacted cell.

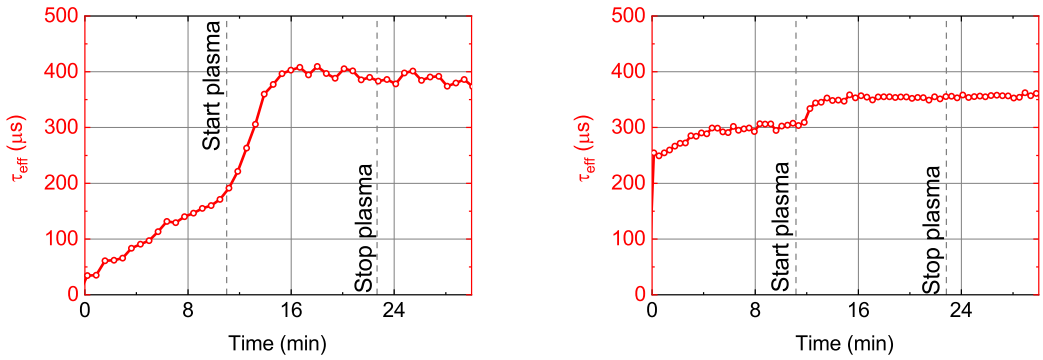

Figure 4.24: Evolution of the minority carrier lifetime of a sample passivated with a SiO_x/(n) µc-Si:H on side 1 and (p) µc-SiO_x:H on side 2, during the deposition of a-SiN_x:H at 350 °C on (a) the first side of the sample and subsequently on (b) the second side.

4.3 Summary

In this chapter, the hydrogenation process step of Fired Passivating Contacts is studied by *in situ* Modulated Photoluminescence. Two types of samples are studied.

- The first type, processed at EPFL, undergoes first a firing step after the deposition of the SiO_x/doped SiC_x stack, and then a SiN_x:H layer deposition. The hotplate annealing step that follows is studied. The measurements allowed to validate that the lifetime before annealing is limited by bulk defects, and that the annealing allows the hydrogenation of the bulk and the curing of the defects. This first section also lead to the conclusion that the recurrent low lifetime values obtained at high temperature are due to the thermal generation of electron-hole pairs. This increases the total minority carrier density and boosts Auger and SRH recombinations, which limits the lifetime at temperatures greater than 300 °C.

- The second type, processed at IPVF, is the one developed in Chapter 2. The hydrogenation step (before any firing step) is investigated, either by a NH_3 + H_2 plasma, or by the deposition of a silicon nitride layer. The process temperature of 350 °C was showed to have a significant impact on the lifetime, through the simple annealing of the passivating stack. The NH_3 + H_2 plasma damages the passivation properties in any case, but significantly more in the case of FPC samples with (p) µc-SiO_x. The addition of the SiH_4 precursor to the gas mixture allows to deposit silicon nitride and dramatically improves the final lifetime. This improvement taking place during the first few minutes of deposition, this seems to give a wider freedom on the material deposited after 5 minutes, and a a-SiN_x:H/a-SiN_xO_y:H capping stack could be implemented for a better resistance to the subsequent firing step. Additionally, the order of the deposition steps must be carefully chosen in order to get the best final passivation properties.

So far, all the optimization and MPL studies were carried out on high quality, lab scale FZ DSP wafers. It is necessary to check that the process is transferable on large-area industrial wafers.

Chapter 5

Towards large area FPC cells

In this chapter, the FPC solar cell upscale from the 50×50 mm^2 FZ wafers to industrial 156×156 mm^2 Cz and cast-mono wafers is investigated. The integration of the previously optimized passivating stack is deposited on both textured and polished surfaces. iV_{OC} values up to 691 mV are achieved on cast-mono wafers, which is a very promising result. A first attempt of a complete solar cell is finally made on a lab scale FZ wafer.

Contents

5.1 Process transfer on Cz and cast-mono wafers

5.1.1 Context and experimental methods

Standard solar cells are made from industrial silicon wafers which areas are larger than lab scale samples. Nowadays, standard wafers have an area of 156×156 mm^2 and are named M2 wafers. The size of industrial wafers tends to increase and M6 wafers (166×166 mm^2) or greater - up to G12+ (217×217 mm^2) - are expected to account for more than 50 % of the market shares by 2027 according to the projections of the International Technology Roadmap for Photovoltaics [204]. However, such large wafers require the adaptation of some processing tools which are currently designed for M2 wafers.

In this thesis, M2 wafers were used due to their current availability and the dimensions of the deposition tools. Two kinds of silicon bulks were used: Cz and cast-mono silicon crystals. The Cz crystals were bought from a supplier under the form of silicon ingots. The cast-mono ingots were grown at Photowatt™ in G5 furnaces by ECM Greentech. These two kinds of silicon ingots underwent the same process steps in order to end up with textured silicon wafers: diamond sawing, saw-damage removal (SDR) and texturization (in a chemical bath of KOH and additives). The final M2 wafers obtained have textured surfaces with a random-pyramid pattern. They are 170 µm thick and have a resistivity around 1.6 Ω.cm for cast-mono wafers and 2.3 Ω.cm for Cz wafers. All these steps were carried out by the technical and research staff of Photowatt™.

Once at IPVF, some of the wafers were polished (see Section 5.1.3), and all the samples were cleaned with a RCA cleaning procedure. Like previously, for safety reasons, all the wet-chemical steps were carried out by the EDF R&D research team.

The wafers are subsequently coated with the passivating layers developed previously in this PhD thesis. The confocal microscope images were acquired with an Olympus OLS5000 microscope. The PECVD deposition of the passivating layers, metallic evaporation, the confocal microscope images, QSSPC measurements, lifetime calibrated photoluminescence images, and IV measurement were made by the PhD candidate.

5.1.2 Textured wafers

The thorough RCA cleaning procedure on the textured surfaces of industrial wafers is a challenge because of the high aspect ratio of the pyramids, which makes the second cleaning step (SC-2) very hard to rinse due to the viscosity of the solution. Figure 5.1 shows a couple of PL images that result from a bad rinsing procedure. Figure 5.1a shows a wafer that got accidentally stuck to another sample right before the rinsing step: the large liquid surface tension due to a thin water film between the two samples makes their separation tedious, resulting in a longer exposure of the sample to the reaction medium, hence the large chemical traces in the PL image. In Figure 5.1b, an improper rinsing along with projections during the drying step resulted in drops of the reaction medium landing on the wafer and forming black dots on the PL image. These problems were tackled by using several rinsing beakers and a larger spacing between the wafers.

The cleaning and SiO_x growth steps were initially not adapted to large area wafers (due to the use of relatively small beakers) and was limited to 50×50 mm^2 of surface area. Consequently, the SiO_x/(p) µc-Si:H/a-SiN_x:H passivating stacks were initially deposited on 50×50 mm^2 Cz and cast-mono samples, cut inside larger (M2) silicon wafers. Similar iV_{OC} values (650 mV) were obtained for the two kinds of wafers. The cast-mono wafers reached slightly lower lifetime values than Cz wafers (48 µs *vs.* 67 µs), most likely because of the difference in doping and impurity levels. Lifetime calibrated images are shown in

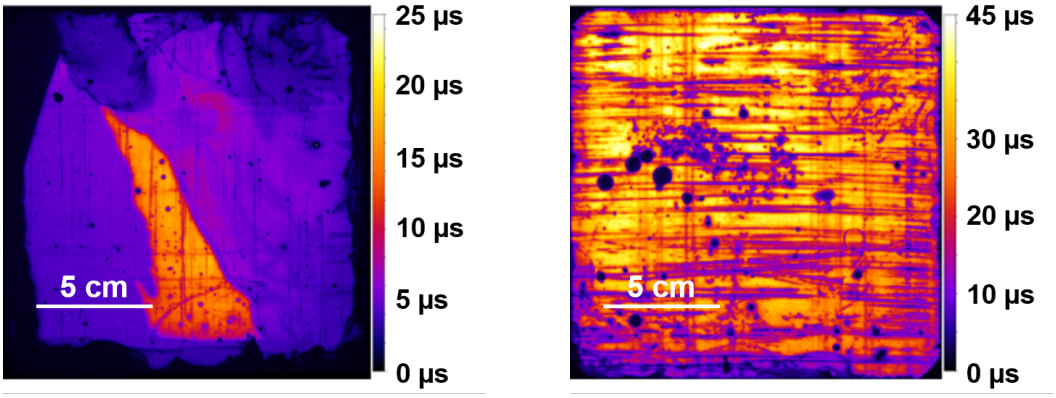

(a) (b)

Figure 5.1: Lifetime calibrated PL images of a textured cast-mono wafers of area 156×156 mm^2 passivated by a SiO_x/(p) µc-Si:H/a-SiN_x:H stack on both sides after a bad cleaning procedure.

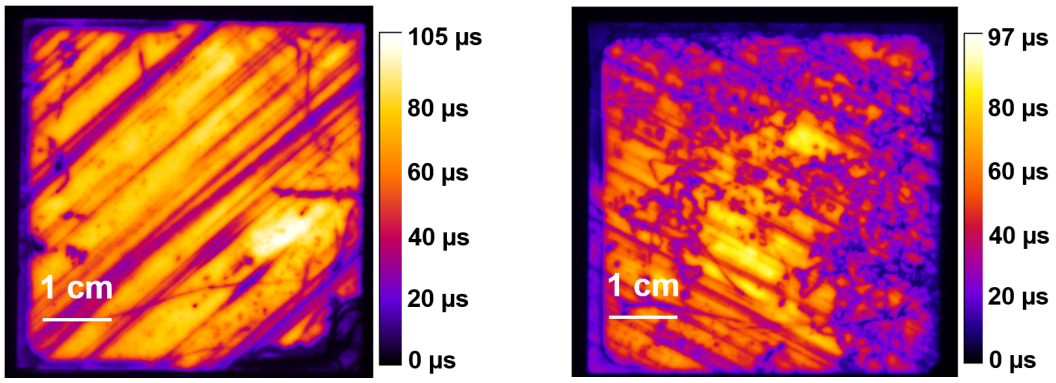

(a) (b)

Figure 5.2: Lifetime calibrated PL images of a textured (a) Cz and (b) cast-mono wafer of area 50×50 mm^2 passivated by a SiO_x/(p) µc-Si:H/a-SiN_x:H stack on both sides.

Figure 5.2. These show that the diamond saw damages are still present, under the form of dark diagonal lines of low lifetime. The passivation was not high enough to get rid of these mechanical defects. We can also notice one main difference between the two samples: while the Cz wafer looks relatively homogeneous, small twisted lines can be seen in the cast-mono sample. These are dislocations that appear sometimes during the cast-mono crystallization processes [205]. The final lifetimes are low even compared to the ones obtained with a simple standard SiO_x/a-SiN_x:H passivation stack (up to 70 µs and 670 mV on cast-mono at Photowatt).

A setup for cleaning larger samples was installed in the lab, with a new wet-bench. Equivalent passivation properties were obtained on M2 wafers with best samples at 651 mV for Cz wafers and 655 mV for cast-mono wafers. The corresponding lifetime calibrated PL images are shown in Figure 5.3. These measurements validate the new cleaning setup and procedure: no major difference is seen between the large and small samples. Indeed, (i) the PL intensity is relatively homogeneous despite the presence of the areas damaged by the diamond sawing step and (ii) the passivation properties obtained are similar for large and small samples. They are even slightly better for the large-area with values up to 92 µs and

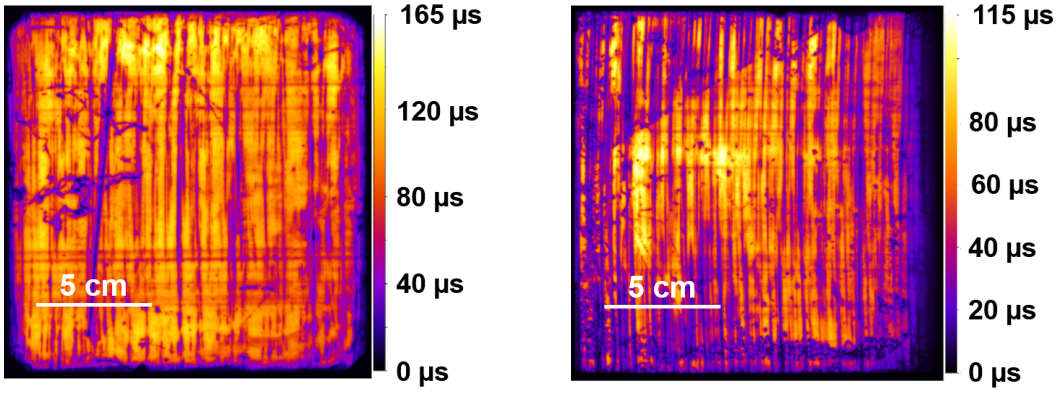

(a) (b)

Figure 5.3: Lifetime calibrated PL images of a textured (a) Cz and (b) cast-mono wafer of area 156×156 mm^2 passivated by a SiO_x/(p) µc-Si:H/a-SiN_x:H stack on both sides.

651 mV for the Cz wafer and 74 µs and 655 mV for the cast-mono wafer. Consequently, either of these sizes can be used in order to evaluate the passivation properties on these wafers.

This shows that the cleaning of large samples is now possible at IPVF. Up to this point, the final passivation properties on textured wafers (655 mV) are not very high for the p-type FPC passivating stack, and there is a large difference between the results obtained on textured wafers and on FZ wafers. This confirms the fact that the passivation by a FPC stacks is very sensitive to the crystalline orientation and the quality of the surface passivation (conformal oxide layer) of the sample that is to be passivated. Consequently, other kinds of surface preparation are investigated on these industrial wafers for the fabrication of large area solar cells.

5.1.3 Polished surfaces

In the literature, passivating contacts are often integrated on polished surfaces [31], [32] since the passivation provided on textured surfaces is usually lower [95]. This was shown to be at least partially related to the <111> crystal orientation of textured samples which is harder to passivate than <100> crystal planes [54]. Consequently the samples from Photowatt were polished at IPVF. In order to do so, we used a wet-chemical solution containing:

- 330 mL of HF (concentration: 40 %),
- 990 mL of HNO_3 (concentration: 65 %),
- 660 mL of CH_3COOH (concentration: 100 %).

The reaction is strong, exothermal, and etches in an isotropic way the surface of the sample. One proposed reaction mechanism is [206]:

$$3Si_{(s)} + 4HNO_{3(aq)} \longrightarrow 3SiO_{2(s)} + 4NO_{(aq)} + 2H_2O_{(l)}$$

$$SiO_{2(s)} + 6HF_{(aq)} \longrightarrow H_2\,[SiF_6]_{(aq)} + 2H_2O_{(l)}$$

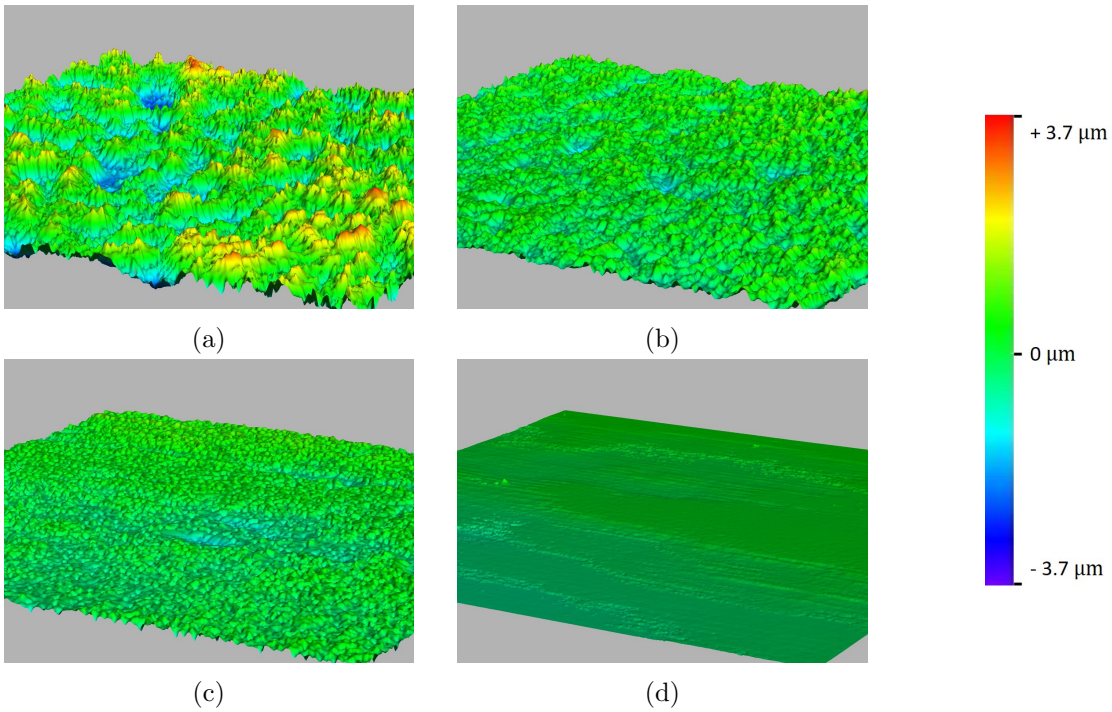

Figure 5.4: 3D confocal images of the surface of Cz wafers polished for (a) 0 min, (b) 1 min, (c) 2 min, and (d) 5 min.

The CH_3COOH is considered to improve the wettability of the surface, and to act as a complementary oxidizing agent. Four immersion times were investigated in order to get various values of surface roughness: 0, 1, 2, and 5 min. Confocal microscope images of the surface of theses samples are shown in Figure 5.4. The surface becomes flatter and flatter for longer immersion times, which shows that the etching has the desired effect.

In order to assess the polishing efficiency of the etching process, the surface roughness is quantified by calculating the quadratic mean of the roughness. Typically, along a line of length l_r, with z the surface height profile along this line, this value is given by the equation:

$$R_{ms} = \sqrt{\frac{1}{l_r}\int_0^{l_r} z(x)^2 dx} \tag{5.1}$$

As displayed in Figure 5.5, the surface roughness is being reduced further and further with the polishing duration (red circles). However, this goes along with a significant reduction of the wafer thickness (black squares). A longer etching time is thus better in order to get a flatter surface, but the additional thinning of the wafer may be detrimental for light trapping efficiency and for mechanical resistance (easy breakage).

A polishing time of 2 minutes is chosen: it gives a flatter surface ($R_{ms} = 0.28$ µm) and does not decrease the thickness of the wafer too dramatically (145 µm). Cz and cast-mono M2 silicon wafers were consequently polished and symmetrically passivated by a SiO_x/(p) µc-Si:H/a-SiN_x:H stack. Their thickness was measured to be 155 ± 5 µm instead of 145 µm as measured in Figure 5.5 (this may be due to a slight difference in the time laps between the removal from the etching bath and the rinsing). The lifetime calibrated photoluminescence images of these samples are shown in Figure 5.6: the saw damages have

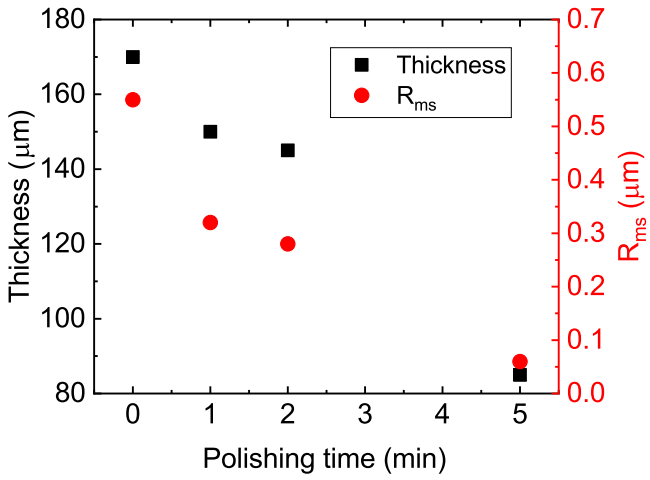

Figure 5.5: Evolution of the surface roughness and of the silicon wafer thickness of a Cz wafer initially textured, after (a) 0 min, (b) 1 min, (c) 2 min, and (d) 5 min of chemical polishing in $HF/HNO_3/CH_3COOH$.

disappeared and the lifetime is way more homogeneous than on the textured surfaces. The passivation provided by the layers on the smooth surfaces is significantly higher than on textured surfaces: QSSPC measurements gave τ_{eff} = 196 µs and iV_{oc} = 684 mV on the Cz wafer and τ_{eff} = 224 µs and iV_{oc} = 691 mV on the cast-mono wafer. These are very promising results since the iV_{oc} values obtained (especially for cast-mono wafers) are very close to the ones obtained on FZ wafers.

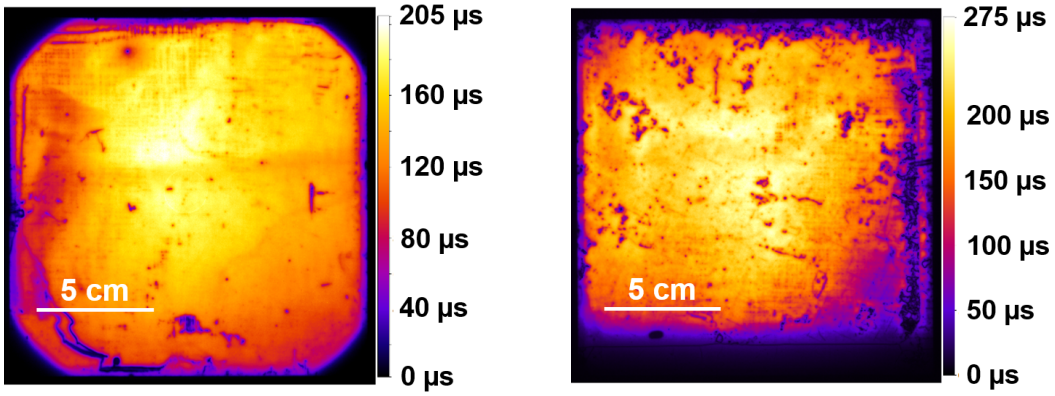

(a) (b)

Figure 5.6: Lifetime calibrated PL images of a polished (a) Cz and (b) cast-mono wafer of area 156×156 mm^2 passivated by a SiO_x/(p) µc-Si:H/a-SiN_x:H stack on both sides.

The large difference in final passivation properties between textured and polished wafers supports the statement that the FPC contacts are particularly sensitive to the quality and morphology of the wafer surface. A textured surface could show a less conformal growth of the wet-chemical oxide, which would significantly impact the resulting lifetime.

5.2 Solar cell fabrication

A first attempt of solar cell fabrication is presented in this section. We used a high-quality, p-type, DSP FZ wafer with a resistivity of 2.3 Ω.cm. After a RCA cleaning procedure and the growth of a thin wet-chemical oxide layer (1.3 nm), a (p) µc-SiO_x:H layer was deposited on the rear side and an (n) µc-SiO_x:H layer was deposited on the front side of the solar cell. At this point, the passivation properties were still very low (τ_{eff} = 5 µs and iV_{oc} < 545 mV). As seen in the previous sections, the a-SiN_x:H deposition is needed in order to activate the passivation properties of the passivating stack.

Before the a-SiN_x:H deposition, so that no additional laser scribing step is needed, metallic grids were directly evaporated on the µc-SiO_x:H layers. 200 nm of silver were evaporated on the (n) µc-SiO_x:H layer and 150 nm of aluminum was evaporated on the (p) µc-SiO_x:H layer, with a grid-patterned mask. An 85 nm-thick a-SiN_x:H layer was deposited on both sides of the sample: first on the (n) µc-SiO_x:H layer, then on the (p) µc-SiO_x:H. Finally, the sample was annealed for 10 minutes at 200 °C. A photoluminescence image of the samples after this step can be seen on Figure 5.7a. It is necessary to have metallic grids on both sides (and not full side metallization) because silicon nitride needs to be deposited in order to "activate" the passivation properties of each FPC stack. The grid used for the measurement of the I-V characteristic is the one visible on the bottom right hand side of the image. It is worth noting that the grid on the front and rear FPC stacks are not aligned and are actually perpendicular to one another. The evaporation of the metallic layer does not seem to have resulted in a significant decrease in the PL intensity, and the losses (dark areas) look mostly due to shading.

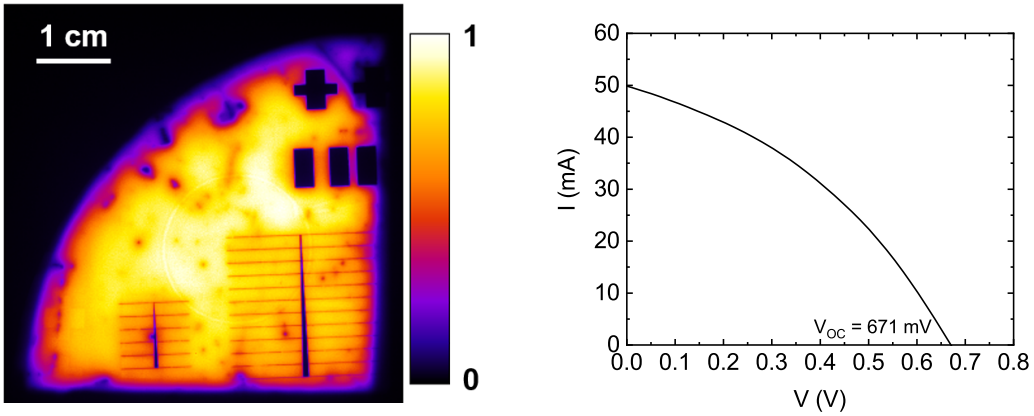

(a) (b)

Figure 5.7: (a) PL images of a double-sided FPC solar cell after metallization and a-SiN_x:H deposition. (b) I(V) characteristic of the solar cell.

An I-V measurement was subsequently carried out, and the characteristic is shown in Figure 5.7b. Since the grid pattern is present on both sides of the sample, for contacting the rear side, copper tape was stuck to the rear aluminum grid and brought to the front side. In the IV curve, the fill-factor is very poor, which is likely due to metallization problems: delamination of the evaporated metals was clearly visible, and aluminum-copper tape contact might have been defective. Despite these problems of metallization, a V_{oc} value of up to 671 mV was reached, which is encouraging.

Other tests are needed to know if some part of the large resistive losses seen in the I-V curve is due to the relatively low conductivity of the µc-SiO_x:H layers. The metallization

step needs to be improved. Screen-printing metallization of a fire-through paste could allow for the deposition of a-SiN_x:H on the full area of the wafer, thus simplifying the fabrication process, and making the contact easier for large area I-V characterization. This, however, requires the FPC to maintain its passivation properties during the firing step.

5.3 Summary

In this chapter, p-type FPC were integrated on industrial Cz and cast-mono wafers, reaching similar iV_{oc} values. This highlights the interest of integrating FPC on cast-mono wafers, that are both cheaper and require less energy for the cell fabrication. This study additionally pinpoints the sensitivity of the FPC passivating stacks to the surface preparation, which needs a high-quality, conformal SiO_x layer in order to provide good passivation properties. An encouraging iV_{oc} value of 691 mV for the integration of p-type FPC on a polished cast-mono wafer was even reached, which is close to the maximum values obtained on p-type DSP, FZ wafers.

A first prototype of solar cell was made, with an (n) µc-SiO_x:H layer on the front side and a (p) µc-SiO_x:H on the rear side. A V_{oc} of 671 mV was achieved, despite large resistive losses. Some improvements of the metallization process are required to unravel the full potential of the FPC integration on silicon solar cells.

Conclusion and perspectives

This doctoral work focused on the study of a simplified process flow for the fabrication of tunnel oxide passivated contact (TOPCon) called fired passivated contact (FPC). This solar cell fabrication process has the advantage of being simple (few steps) and requiring a low thermal budget, thus reducing the carbon intensity of the photovoltaic energy produced. In order to carry out this comprehensive study, various characterization techniques were used and optimized, among which *in situ* modulated photoluminescence (MPL) which allowed the measurement in real time of the minority carrier lifetime in solar cell precursors during a specific process step. The major contributions of this thesis are listed below.

Optimization of the FPC stack

A layer-by-layer optimization of the passivating stack was carried out in order to develop the FPC cell fabrication process at IPVF and LPICM laboratories. This optimization coupled with several characterization techniques allowed to measure the various physical properties of the layers chosen for the final passivating stack: SiO_x, doped µc-Si:H and µc-SiO_x:H, and a-SiN_x:H. During this thesis µc-Si:H and µc-SiO_x:H materials were chosen as carrier transport layers, since they degrade less than a-Si:H during the final high-temperature firing step. These materials were optimized in order to get the best possible trade-off between transparency, conductivity and passivation properties. Notably, XPS analyses allowed to show that the deposition of (p) µc-Si:H on top of the thin SiO_x layer leads to a rearrangement of the tunnel oxide, that forms substoechiometric oxides. The final firing step systematically degraded the passivation properties, but this detrimental effect could be mitigated by the use of µc-SiO_x:H instead of µc-Si:H, and depositing thicker layers of either µc-SiO_x:H or a-SiN_x:H. The use of an AlO_x layer deposited by ALD allowed to show the feasibility of our process, while maintaining the passivation properties after firing. The complexity of the stack and the interactions of the consecutive process steps on the properties of the whole structure motivated the use of real-time measurements of the passivation properties.

In situ modulated photoluminescence for AlO_x

An *in situ* MPL acquisition setup mounted on a PECVD reactor is described, along with the data treatment necessary to extract the minority carrier lifetime at the specific excess minority carrier density of 1×10^{15} cm^{-3}. New corrections were made in order to take lateral diffusion into account in the data treatment procedure, which is shown to result in significant overestimations of the minority carrier density for a very local illumination of highly passivated samples.

A case study of the evolution of AlO_x passivated n-type silicon wafers was carried out using the *in situ* MPL setup. We showed that the negative fixed charge density is not

activated at 250 °C, while it is fully activated after a 30 min-long annealing step at 350 °C. Interestingly we showed that the combined action of temperature (250 °C) and light (laser illumination needed for the MPL measurement) activates a large amount of stable positive fixed charges in AlO_x, which is a phenomenon never reported before.

In situ MPL for Fired Passivating Contacts

In situ MPL measurements were also carried out on silicon wafers coated with FPC passivating stacks. The hydrogenation process of samples made at EPFL was investigated. Their team showed that the firing step creates bulk defects in the FZ silicon wafers. The real-time lifetime measurements allowed to evidence that bulk defects are cured during a 30 min-long annealing at 450 °C after the deposition of a hydrogen-rich a-SiN_x:H layer. This dynamics was shown to strongly depend on temperature, which is consistent with the hypothesis of the diffusion of hydrogen and a decrease of the bulk defect density. In our experiments, the *in situ* MPL experiments allowed to show that 20 minutes of annealing were enough to completely passivate the bulk.

The lifetime measured by MPL were shown to strongly vary with temperature even for samples which passivation properties were not impacted by annealing steps. Increases of lifetime were observed during the beginning of the increase of temperature, and low lifetime values were systematically measured in all samples when the temperature exceeded 300 °C. These variations were shown to result from two competing phenomena: (i) the increase of the effective minority carrier lifetime of the sample with temperature (due to variations of the electron and hole trap capture cross sections, ...) and (ii) the strong increase of the thermally generated minority carrier density at high temperatures (4×10^{16} cm^{-3} at 450 °C) which boosts recombinations losses. Consequently, at very high temperatures, the evolution of the actual passivation properties is harder to measure.

Finally, *in situ* MPL was used during PECVD processes for the fabrication of FPC at IPVF. $NH_3 + H_2$ plasmas were shown to degrade the passivation provided by FPC samples in all cases, but more dramatically for FPC with µc-SiO_x:H than FPC with µc-Si:H, while the annealing of the samples at 350 °C boosts the passivation of the samples. The addition of SiH_4 in the gas mixture allows to deposit a-SiN_x:H and leads to a dramatic increase of the effective lifetime, especially during the first few minutes of deposition. It must also be noted that the order of the deposition sequence in the case of solar cells with both n-type and p-type FPC is reported to be of importance: a deposition of a-SiN_x:H first on the n-type FPC could lead to better performances.

Towards large area FPC cells

A first integration of the p-type FPC stack with (p) µc-Si:H was carried out on textured and polished Cz and cast-mono wafers of area 156×156 mm^2. This confirmed that FPC passivating stacks depend dramatically on the quality of the c-Si/SiO_x interface. They provide iV_{OC} values around 655 mV on textured wafers, while 684 mV on Cz and 691 mV on cast-mono polished wafers were reached, which are very promising results. It is thus of significant interest to keep implementing the newest solar cell architectures on cast-mono wafers to show the potential of such wafers

Perspectives

As a sum up, we showed that in complex passivating stacks, each processing step modifies the overall properties of the sample and the deposition of the layers impact one another (see XPS and ellipsometry measurements). Because of the critical role of interfaces in the performances of our devices, standard optical and chemical characterization techniques are not sufficient, and electronic measurements are necessary: a slight change in the deposition conditions of materials can lead to completely different electronic properties (see the characterization of positively charged AlO_x). Electrical characterization on final devices is not enough to understand the mechanisms at stake, which motivated the use of real-time, *in situ* MPL measurements for a finer tuning of the processing times and conditions. It must be stressed out that what counts in the end are the properties after the final firing step in FPC samples: the *in situ* MPL measurements can help find the best combination of materials to maximize both the final passivation properties and the thermal stability. Many interesting studies can be made in order to push further the understanding and improvements achieved during this thesis.

Thorougher investigations must be carried out on the surprising positively charged AlO_x thin films: XPS analyses in order to learn more about the chemical configuration of the AlO_x layer with such positive fixed charges, variations of the light source (spectral distribution, photon flux, ...) to narrow down the possible mechanisms at stake, and finally a verification of the possibility to get positively charged AlO_x on larger areas.

An improvement of the MPL acquisition routine and data treatment should be made in order to better take temperature variations into account. The treatment should be fully rethought for high-temperature measurements (higher than 350 °C) if one wants to visualize only the evolution of the surface and bulk passivation. However, it is worth reminding that, at fixed temperature, the variations of the lifetime that are being measured still account for real variations of the passivation properties.

A more extensive study on the capping layer should be carried out for future improvements. The increase in lifetime occurring exclusively during the first few minutes of a-SiN_x:H deposition, this paves the way for the development of new capping stacks: the deposition of the first few nm of a hydrogen-rich material that could increase the passivation of the c-Si/SiO_x interface (such as a-SiN_x:H) until the maximum lifetime value could be followed by the deposition of a layer which could increase the thermal stability of the passivating stack upon firing (such as a-$SiN_xO_yC_z$:H) while not impacting directly the passivation properties. These bi-layers should be investigated using *in situ* MPL during their deposition in order to optimize the duration of deposition and get a better understanding of the impact of the different species present inside the plasma.

A full study on the metallisation and on the optimal firing temperature profile should be made in order to allow for the integration of FPC on industrial size silicon wafers. Additionally, it would be of great interest to investigate the long-term stability and aging of FPC solar cells, and compare it with the lifetime of passivated contact solar cells made with other fabrication processes.

The investigation of solar cell manufacturing processes that have lower and lower environmental impacts is of major importance, and is fundamental for the acceptability and the larger adoption of photovoltaic devices. Fundamental and comprehensive research on fabrication processes should spur the photovoltaic industry to adopt abstemious methods in order to contribute to a more sustainable future.

Bibliography

[1] U. N. D. Program, "Human Development Data (1990-2018)," Tech. Rep., 2019.

[2] W. E. Council, *World Energy Trilemma Index 2019*. 2019.

[3] IEA, "Key World Energy Statistics," p. 81, 2019.

[4] I. P. o. C. Change, "6th assessment report, climate change 2021: The physical science basis," IPCC, Tech. Rep., Aug. 2021.

[5] ——, "IPCC Special Report on Renewable Energy Sources and Climate Change Mitigation," IPCC, Tech. Rep., 2011.

[6] ITRPV, "International Technology Roadmap for Photovoltaic (ITRPV) 10th edition," Tech. Rep. 10th edition, Mar. 2019, p. 80.

[7] IRENA, "Renewable Energy Statistics 2019," International Renewable Energy Agency, Abu Dhabi, Tech. Rep., 2019, p. 398.

[8] C. Kost, S. Shammugam, V. Jülch, H.-T. Nguyen, and T. Schlegl, "Levelized Cost of Electricity- Renewable Energy Technologies," Fraunhofer ISE, Tech. Rep., Mar. 2018, p. 42.

[9] R. Fu, D. Feldman, and R. Margolis, "U.S. Solar Photovoltaic System Cost Benchmark: Q1 2018," NREL, Tech. Rep., 2018, p. 63.

[10] S. Europe, "Solar Sustainability: Best Practices Benchmark," p. 54, 2021.

[11] ISE, "Photovoltaics Report," Fraunhofer ISE, Tech. Rep., Jul. 2021.

[12] D. Chen, Y. Chen, Z. Wang, J. Gong, C. Liu, Y. Zou, Y. He, Y. Wang, L. Yuan, W. Lin, R. Xia, L. Yin, X. Zhang, G. Xu, Y. Yang, H. Shen, Z. Feng, P. Altermatt, and P. Verlinden, "24.58% total area efficiency of screen-printed, large area industrial silicon solar cells with the tunnel oxide passivated contacts (i-TOPCon) design," *Solar Energy Materials and Solar Cells*, vol. 206, p. 110 258, Mar. 2020. DOI: 10.1016/j.solmat.2019.110258.

[13] Photowatt, *PW2450F Crystal Advanced sur Photowatt*. [Online]. Available: http://www.photowatt.com/produits/modules/pw2450f-crystal-advanced.

[14] P. Wurfel and U. Wurfel, *Physics of Solar Cells: From Basic Principles to Advanced Concepts*, 3rd. Wiley-VCH, 2016.

[15] U. Wurfel, A. Cuevas, and P. Wurfel, "Charge Carrier Separation in Solar Cells," *IEEE Journal of Photovoltaics*, vol. 5, no. 1, pp. 461–469, Jan. 2015. DOI: 10.1109/JPHOTOV.2014.2363550.

[16] W. Shockley and H. Queisser, "Detailed Balance Limit of Efficiency of p-n Junction Solar Cells," *Journal of Applied Physics*, vol. 32, no. 3, pp. 510–519, Mar. 1961. DOI: 10.1063/1.1736034.

[17] M. Rodrıguez-Meza and J. Carrillo, "Thermalization process of a photo-generated plasma in semiconductors," *Revista Mexicana de Fisica*, vol. 48, no. 1, pp. 52–60, 2002.

[18] M. Hudedmani, V. Soppimath, and C. Jambotkar, "A Study of Materials for Solar PV Technology and Challenges," *European Journal of Applied Engineering and Scientific Research*, vol. 1, no. 5, pp. 1–13, 2017.

[19] A. Richter, M. Hermle, and S. Glunz, "Reassessment of the Limiting Efficiency for Crystalline Silicon Solar Cells," *IEEE Journal of Photovoltaics*, vol. 3, no. 4, pp. 1184–1191, Oct. 2013. DOI: 10.1109/JPHOTOV.2013.2270351.

[20] K. Yoshikawa, H. Kawasaki, W. Yoshida, T. Irie, K. Konishi, K. Nakano, T. Uto, D. Adachi, M. Kanematsu, H. Uzu, and K. Yamamoto, "Silicon heterojunction solar cell with interdigitated back contacts for a photoconversion efficiency over 26%," *Nature Energy*, vol. 2, no. 5, May 2017. DOI: 10.1038/nenergy.2017.32.

[21] W. Gerlach, H. Schlangenotto, and H. Maeder, "On the radiative recombination rate in silicon," *Physica Status Solidi (a)*, vol. 13, no. 1, pp. 277–283, Sep. 1972. DOI: 10.1002/pssa.2210130129.

[22] W. Shockley and W. T. Read, "Statistics of the Recombinations of Holes and Electrons," *Physical Review*, vol. 87, no. 5, pp. 835–842, Sep. 1952. DOI: 10.1103/PhysRev.87.835.

[23] A. Aberle, "Surface passivation of crystalline silicon solar cells: A review," *Progress in Photovoltaics: Research and Applications*, vol. 8, no. 5, pp. 473–487, Sep. 2000. DOI: 10.1002/1099-159X(200009/10)8:5<473::AID-PIP337>3.0.CO;2-D.

[24] M. Sajjad, X. Yang, P. Altermatt, N. Singh, U. Schwingenschlögl, and S. De Wolf, "Metal-induced gap states in passivating metal/silicon contacts," *Applied Physics Letters*, vol. 114, no. 7, p. 071 601, Feb. 2019. DOI: 10.1063/1.5066423.

[25] A. Aberle, "Overview on SiN surface passivation of crystalline silicon solar cells," *Solar Energy Materials and Solar Cells*, vol. 65, no. 1-4, pp. 239–248, Jan. 2001. DOI: 10.1016/S0927-0248(00)00099-4.

[26] T. Allen, J. Bullock, X. Yang, A. Javey, and S. De Wolf, "Passivating contacts for crystalline silicon solar cells," *Nature Energy*, Sep. 2019. DOI: 10.1038/s41560-019-0463-6.

[27] M. Tanaka, M. Taguchi, T. Matsuyama, T. Sawada, S. Tsuda, S. Nakano, H. Hanafusa, and Y. Kuwano, "Development of New a-Si/c-Si Heterojunction Solar Cells: ACJ-HIT (Artificially Constructed Junction-Heterojunction with Intrinsic Thin-Layer)," *Japanese Journal of Applied Physics*, vol. 31, no. Part 1, No. 11, pp. 3518–3522, Nov. 1992. DOI: 10.1143/JJAP.31.3518.

[28] R. Varache, A. Valla, N. Nguyen, and D. Muñoz, "Front Side Recombination Losses Analysis in Rear Emitter Silicon Heterojunction Solar Cells," *Energy Procedia*, vol. 55, pp. 302–309, 2014. DOI: 10.1016/j.egypro.2014.08.089.

[29] F. Feldmann, M. Bivour, C. Reichel, H. Steinkemper, M. Hermle, and S. Glunz, "Tunnel oxide passivated contacts as an alternative to partial rear contacts," *Solar Energy Materials and Solar Cells*, vol. 131, pp. 46–50, Dec. 2014. DOI: 10.1016/j.solmat.2014.06.015.

[30] P. Spinelli, M. Sen, E. Hoek, B. Kikkert, G. Yang, O. Isabella, A. Weeber, and P. Bronsveld, "Moly-poly solar cell: Industrial application of metal-oxide passivating contacts with a starting efficiency of 18.1%," 2018, p. 040 021. DOI: 10.1063/1.5049284.

[31] S. Duttagupta, N. Nandakumar, P. Padhamnath, J. Buatis, R. Stangl, and A. Aberle, "monoPolyTM cells: Large-area crystalline silicon solar cells with fire-through screen printed contact to doped polysilicon surfaces," *Solar Energy Materials and Solar Cells*, vol. 187, pp. 76–81, Dec. 2018. DOI: 10.1016/j.solmat.2018.05.059.

[32] F. Feldmann, M. Simon, M. Bivour, C. Reichel, M. Hermle, and S. Glunz, "Efficient carrier-selective p- and n-contacts for Si solar cells," *Solar Energy Materials and Solar Cells*, vol. 131, pp. 100–104, Dec. 2014. DOI: 10.1016/j.solmat.2014.05.039.

[33] U. Römer, R. Peibst, T. Ohrdes, B. Lim, J. Krügener, E. Bugiel, T. Wietler, and R. Brendel, "Recombination behavior and contact resistance of n+ and p+ poly-crystalline Si/mono-crystalline Si junctions," *Solar Energy Materials and Solar Cells*, vol. 131, pp. 85–91, Dec. 2014. DOI: 10.1016/j.solmat.2014.06.003.

[34] U. Römer, "Polycrystalline silicon / monocrystalline silicon junctions and their application as passivated contacts for Si solar cells," PhD Thesis, 2015.

[35] R. Peibst, U. Römer, Y. Larionova, M. Rienäcker, A. Merkle, N. Folchert, S. Reiter, M. Turcu, B. Min, J. Krügener, D. Tetzlaff, E. Bugiel, T. Wietler, and R. Brendel, "Working principle of carrier selective poly-Si/c-Si junctions: Is tunnelling the whole story?" *Solar Energy Materials and Solar Cells*, vol. 158, pp. 60–67, Dec. 2016. DOI: 10.1016/j.solmat.2016.05.045.

[36] A. Kale, W. Nemeth, H. Guthrey, E. Kennedy, A. Norman, M. Page, M. Al-Jassim, D. Young, S. Agarwal, and P. Stradins, "Understanding the charge transport mechanisms through ultrathin SiOx layers in passivated contacts for high-efficiency silicon solar cells," *Applied Physics Letters*, vol. 114, no. 8, p. 083 902, Feb. 2019. DOI: 10.1063/1.5081832.

[37] A. Kale, W. Nemeth, S. Nanayakkara, H. Guthrey, M. Page, M. Al-Jassim, S. Agarwal, and P. Stradins, "Tunneling or Pinholes: Understanding the Transport Mechanisms in SiOx Based Passivated Contacts for High-Efficiency Silicon Solar Cells," 2018, p. 5.

[38] Z. Zhang, Y. Zeng, C.-S. Jiang, Y. Huang, M. Liao, H. Tong, M. Al-Jassim, P. Gao, C. Shou, X. Zhou, B. Yan, and J. Ye, "Carrier transport through the ultrathin silicon-oxide layer in tunnel oxide passivated contact (TOPCon) c-Si solar cells," *Solar Energy Materials and Solar Cells*, vol. 187, pp. 113–122, Dec. 2018. DOI: 10.1016/j.solmat.2018.07.025.

[39] G. R. Wolstenholme, N. Jorgensen, P. Ashburn, and G. R. Booker, "An investigation of the thermal stability of the interfacial oxide in polycrystalline silicon emitter bipolar transistors by comparing device results with high-resolution electron microscopy observations," *Journal of Applied Physics*, vol. 61, no. 1, pp. 225–233, Jan. 1987. DOI: 10.1063/1.338861.

[40] I. Post, P. Ashburn, and G. Wolstenholme, "Polysilicon emitters for bipolar transistors: A review and re-evaluation of theory and experiment," *IEEE Transactions on Electron Devices*, vol. 39, no. 7, pp. 1717–1731, Jul. 1992. DOI: 10.1109/16.141239.

[41] T. Matsushita, N. Oh-uchi, H. Hayashi, and H. Yamoto, "A silicon heterojunction transistor," *Applied Physics Letters*, vol. 35, no. 7, pp. 549–550, Oct. 1979. DOI: 10.1063/1.91174.

[42] E. Yablonovitch, T. Gmitter, R. M. Swanson, and Y. H. Kwark, "A 720 mV open circuit voltage SiOx / c-Si/SiOx double heterostructure solar cell," *Applied Physics Letters*, vol. 47, no. 11, pp. 1211–1213, Dec. 1985. DOI: 10.1063/1.96331.

[43] F. Feldmann, M. Bivour, C. Reichel, M. Hermle, and S. Glunz, "Passivated rear contacts for high-efficiency n-type Si solar cells providing high interface passivation quality and excellent transport characteristics," *Solar Energy Materials and Solar Cells*, vol. 120, pp. 270–274, Jan. 2014. DOI: 10.1016/j.solmat.2013.09.017.

[44] R. Peibst, U. Romer, K. Hofmann, B. Lim, T. Wietler, J. Krugener, N.-P. Harder, and R. Brendel, "A Simple Model Describing the Symmetric IV Characteristics of p Polycrystalline Si/n Monocrystalline Si, and n Polycrystalline Si/p Monocrystalline Si Junctions," *IEEE Journal of Photovoltaics*, vol. 4, no. 3, pp. 841–850, May 2014. DOI: 10.1109/JPHOTOV.2014.2310740.

[45] M. Stodolny, M. Lenes, Y. Wu, G. Janssen, I. Romijn, J. Luchies, and L. Geerligs, "N-Type polysilicon passivating contact for industrial bifacial n-type solar cells," *Solar Energy Materials and Solar Cells*, vol. 158, pp. 24–28, Dec. 2016. DOI: 10.1016/j.solmat.2016.06.034.

[46] A. Ingenito, G. Nogay, Q. Jeangros, E. Rucavado, C. Allebé, S. Eswara, N. Valle, T. Wirtz, J. Horzel, T. Koida, M. Morales-Masis, M. Despeisse, F.-J. Haug, P. Löper, and C. Ballif, "A passivating contact for silicon solar cells formed during a single firing thermal annealing," *Nature Energy*, vol. 3, no. 9, pp. 800–808, Sep. 2018. DOI: 10.1038/s41560-018-0239-4.

[47] A. Richter, J. Benick, F. Feldmann, A. Fell, M. Hermle, and S. Glunz, "N-Type Si solar cells with passivating electron contact: Identifying sources for efficiency limitations by wafer thickness and resistivity variation," *Solar Energy Materials and Solar Cells*, vol. 173, pp. 96–105, Dec. 2017. DOI: 10.1016/j.solmat.2017.05.042.

[48] F. Haase, C. Hollemann, S. Schäfer, A. Merkle, M. Rienäcker, J. Krügener, R. Brendel, and R. Peibst, "Laser contact openings for local poly-Si-metal contacts enabling 26.1%-efficient POLO-IBC solar cells," *Solar Energy Materials and Solar Cells*, vol. 186, pp. 184–193, Nov. 2018. DOI: 10.1016/j.solmat.2018.06.020.

[49] N. Nandakumar, J. Rodriguez, T. Kluge, T. Groβe, L. Fondop, P. Padhamnath, N. Balaji, M. König, and S. Duttagupta, "Approaching 23% with large-area monoPoly cells using screen-printed and fired rear passivating contacts fabricated by inline PECVD," *Progress in Photovoltaics: Research and Applications*, Dec. 2018. DOI: 10.1002/pip.3097.

[50] Y. Chen, D. Chen, C. Liu, Z. Wang, Y. Zou, Y. He, Y. Wang, L. Yuan, J. Gong, W. Lin, X. Zhang, Y. Yang, H. Shen, Z. Feng, P. P. Altermatt, and P. J. Verlinden, "Mass production of industrial tunnel oxide passivated contacts (i-TOPCon) silicon solar cells with average efficiency over 23% and modules over 345 W," *Progress in Photovoltaics: Research and Applications*, Jul. 2019. DOI: 10.1002/pip.3180.

[51] C. Maritan and N. Tarr, "Polysilicon emitter p-n-p transistors," *IEEE Transactions on Electron Devices*, vol. 36, no. 6, pp. 1139–1144, Jun. 1989. DOI: 10.1109/16.24359.

[52] T. Yamamoto, K. Uwasawa, and T. Mogami, "Bias Temperature Instability in Scaled p Polysilicon Gate p-MOSFET's," *IEEE TRANSACTIONS ON ELECTRON DEVICES*, vol. 46, no. 5, p. 6, 1999.

[53] A. Kale, W. Nemeth, H. Guthrey, M. Page, M. Al-Jassim, D. Young, S. Agarwal, and P. Stradins, "Modifications of Textured Silicon Surface Morphology and Its Effect on Poly-Si/SiOx Contact Passivation for Silicon Solar Cells," *IEEE Journal of Photovoltaics*, pp. 1–9, 2019. DOI: 10.1109/JPHOTOV.2019.2937230.

[54] Y. Larionova, M. Turcu, S. Reiter, R. Brendel, D. Tetzlaff, J. Krügener, T. Wietler, U. Höhne, J.-D. Kähler, and R. Peibst, "On the recombination behavior of p-type polysilicon on oxide junctions deposited by different methods on textured and planar surfaces.," *physica status solidi (a)*, vol. 214, no. 8, p. 1 700 058, Aug. 2017. DOI: 10.1002/pssa.201700058.

[55] G. Nogay, A. Ingenito, E. Rucavado, Q. Jeangros, J. Stuckelberger, P. Wyss, M. Morales-Masis, F.-J. Haug, P. Loper, and C. Ballif, "Crystalline Silicon Solar Cells With Coannealed Electron- and Hole-Selective SiCx Passivating Contacts," *IEEE Journal of Photovoltaics*, vol. 8, no. 6, pp. 1478–1485, Nov. 2018. DOI: 10.1109/JPHOTOV.2018.2866189.

[56] C. Allebe, C. Ballif, J. Leon, A. Ingenito, A. Descoeudres, G. Nogay, P. Wyss, F.-J. Haug, M. Despeisse, and S. Nicolay, "PECVD based layers for improved high temperature industrial Solar cell processes," IEEE, Jun. 2019, pp. 2196–2199. DOI: 10.1109/PVSC40753.2019.8980583.

[57] P. Padhamnath, J. Buatis, A. Khanna, N. Nampalli, N. Nandakumar, V. Shanmugam, A. Aberle, and S. Duttagupta, "Characterization of screen printed and fire-through contacts on LPCVD based passivating contacts in monoPoly™ solar cells," *Solar Energy*, vol. 202, pp. 73–79, May 2020. DOI: 10.1016/j.solener.2020.03.087.

[58] B. Min, N. Wehmeier, T. Brendemuehl, A. Merkle, F. Haase, Y. Larionova, L. David, H. Schulte-Huxel, R. Peibst, and R. Brendel, "A 22.3% Efficient p-Type Back Junction Solar Cell with an Al-Printed Front-Side Grid and a Passivating n+ -Type Polysilicon on Oxide Contact at the Rear Side," *Solar RRL*, p. 2 000 435, Sep. 2020. DOI: 10.1002/solr.202000435.

[59] F. Feldmann, G. Nogay, J.-I. Polzin, B. Steinhauser, A. Richter, A. Fell, C. Schmiga, M. Hermle, and S. Glunz, "A Study on the Charge Carrier Transport of Passivating Contacts," *IEEE Journal of Photovoltaics*, vol. 8, no. 6, pp. 1503–1509, Nov. 2018. DOI: 10.1109/JPHOTOV.2018.2870735.

[60] J.-I. Polzin, F. Feldmann, B. Steinhauser, M. Hermle, and S. Glunz, "Realization of TOPCon using industrial scale PECVD equipment," 2018, p. 040 018. DOI: 10.1063/1.5049281.

[61] W. Chen, T. Truong, H. Nguyen, C. Samundsett, S. Phang, D. MacDonald, A. Cuevas, L. Zhou, Y. Wan, and D. Yan, "Influence of PECVD deposition temperature on phosphorus doped poly-silicon passivating contacts," *Solar Energy Materials and Solar Cells*, vol. 206, p. 110 348, Mar. 2020. DOI: 10.1016/j.solmat.2019.110348.

[62] Q. Yang, M. Liao, Z. Wang, J. Zheng, Y. lin, X. Guo, Z. Rui, D. Huang, L. Lu, M. Feng, P. Cheng, C. Shou, Y. Zeng, B. Yan, and J. Ye, "In-situ phosphorus-doped polysilicon prepared using rapid-thermal anneal (RTA) and its application for polysilicon passivated-contact solar cells," *Solar Energy Materials and Solar Cells*, vol. 210, p. 110 518, Jun. 2020. DOI: 10.1016/j.solmat.2020.110518.

[63] A. Ingenito, G. Nogay, J. Stuckelberger, P. Wyss, L. Gnocchi, C. Allebe, J. Horzel, M. Despeisse, F.-J. Haug, P. Loper, and C. Ballif, "Phosphorous-Doped Silicon Carbide as Front-Side Full-Area Passivating Contact for Double-Side Contacted c-Si Solar Cells," *IEEE Journal of Photovoltaics*, pp. 1–9, 2018. DOI: 10.1109/JPHOTOV.2018.2886234.

[64] T. Gao, Q. Yang, X. Guo, Y. Huang, Z. Zhang, Z. Wang, M. Liao, C. Shou, Y. Zeng, B. Yan, G. Hou, X. Zhang, Y. Zhao, and J. Ye, "An industrially viable TOPCon structure with both ultra-thin SiOx and n+-poly-Si processed by PECVD for p-type c-Si solar cells," *Solar Energy Materials and Solar Cells*, vol. 200, p. 109 926, Sep. 2019. DOI: 10.1016/j.solmat.2019.109926.

[65] G. Limodio, G. Yang, H. Ge, P. Procel, Y. De Groot, L. Mazzarella, O. Isabella, and M. Zeman, "Front and rear contact Si solar cells combining high and low thermal budget Si passivating contacts," *Solar Energy Materials and Solar Cells*, vol. 194, pp. 28–35, Jun. 2019. DOI: 10.1016/j.solmat.2019.01.039.

[66] A. Morisset, R. Cabal, B. Grange, C. Marchat, J. Alvarez, M.-E. Gueunier-Farret, S. Dubois, and J.-P. Kleider, "Highly passivating and blister-free hole selective poly-silicon based contact for large area crystalline silicon solar cells," *Solar Energy Materials and Solar Cells*, vol. 200, p. 109 912, Sep. 2019. DOI: 10.1016/j.solmat.2019.109912.

[67] M. Stodolny, J. Anker, C. Tool, M. Koppes, A. Mewe, P. Manshanden, M. Lenes, and I. Romijn, "Novel Schemes of p+ poly-Si Hydrogenation Implemented in Industrial 6" Bifacial Front-and-Rear Passivating Contacts Solar Cells," *35th European Photovoltaic Solar Energy Conference and Exhibition; 414-417*, 2018. DOI: 10.4229/35theupvsec20182018-2co.10.3.

[68] Z. Xu, K. Tao, S. Jiang, R. Jia, W. Li, Y. Zhou, Z. Jin, and X. Liu, "Application of polycrystalline silicon carbide thin films as the passivating contacts for silicon solar cells," *Solar Energy Materials and Solar Cells*, vol. 206, p. 110 329, Mar. 2020. DOI: 10.1016/j.solmat.2019.110329.

[69] N. Nandakumar, J. Rodriguez, T. Kluge, T. Grosse, D. Landgraf, N. Balaji, M. Esber, P. Padhamnath, and S. Duttagupta, "21.6% monoPolyTM cells with in-situ interfacial oxide and poly-Si layers deposited by inline PECVD," Waikoloa Village, HI, USA, Jun. 2018, p. 4. DOI: 10.1109/PVSC.2018.8547271.

[70] J. Temmler, J.-I. Polzin, F. Feldmann, L. Kraus, B. Kafle, S. Mack, A. Moldovan, M. Hermle, and J. Rentsch, "Inline PECVD Deposition of Poly-Si-Based Tunnel Oxide Passivating Contacts," *physica status solidi (a)*, vol. 215, no. 23, p. 1 800 449, Dec. 2018. DOI: 10.1002/pssa.201800449.

[71] M. Koehler, F. Finger, U. Rau, K. Ding, M. Pomaska, A. Zamchiy, A. Lambertz, W. Duan, F. Lentz, S. Li, V. Smirnov, and T. Kirchartz, "Optimization of Transparent Passivating Contact for Crystalline Silicon Solar Cells," *IEEE Journal of Photovoltaics*, pp. 1–8, 2019. DOI: 10.1109/JPHOTOV.2019.2947131.

[72] E. Khorani, T. Scheul, A. Tarazona, J. Nutter, T. Rahman, and S. Boden, "P+ polycrystalline silicon growth via hot wire chemical vapour deposition for silicon solar cells," *Thin Solid Films*, p. 137 978, Apr. 2020. DOI: 10.1016/j.tsf.2020.137978.

[73] Y. Tao, V. Upadhyaya, C.-W. Chen, A. Payne, E. Chang, A. Upadhyaya, and A. Rohatgi, "Large area tunnel oxide passivated rear contact n-type Si solar cells with 21.2% efficiency," *Progress in Photovoltaics: Research and Applications*, vol. 24, no. 6, pp. 830–835, Jun. 2016. DOI: 10.1002/pip.2739.

[74] G Yang, A. Ingenito, N. van Hameren, O. Isabella, and M. Zeman, "Design and application of ion-implanted polySi passivating contacts for interdigitated back contact c-Si solar cells," *Applied Physics Letters*, vol. 108, no. 3, p. 033 903, Jan. 2016. DOI: 10.1063/1.4940364.

[75] D. Yan, A. Cuevas, Y. Wan, and J. Bullock, "Passivating contacts for silicon solar cells based on boron-diffused recrystallized amorphous silicon and thin dielectric interlayers," *Solar Energy Materials and Solar Cells*, vol. 152, pp. 73–79, Aug. 2016. DOI: 10.1016/j.solmat.2016.03.033.

[76] M. K. Stodolny, J. Anker, B. Geerligs, G. Janssen, B. van de Loo, J. Melskens, R. Santbergen, O. Isabella, J. Schmitz, M. Lenes, J.-M. Luchies, W. Kessels, and I. Romijn, "Material properties of LPCVD processed n-type polysilicon passivating contacts and its application in PERPoly industrial bifacial solar cells," *Energy Procedia*, vol. 124, pp. 635–642, Sep. 2017. DOI: 10.1016/j.egypro.2017.09.250.

[77] Y. Chen, Y. Yang, G. Xu, J. K. Marmon, Z. Feng, and H. Shen, "Optimization of micron size passivated contact and doping level for high efficiency interdigitated back contact solar cells," *Solar Energy*, vol. 178, pp. 308–313, Jan. 2019. DOI: 10.1016/j.solener.2018.12.049.

[78] X. Guo, M. Liao, Z. Rui, Q. Yang, Z. Wang, C. Shou, W. Ding, X. Luo, Y. Cao, J. Xu, L. Fu, Y. Zeng, B. Yan, and J. Ye, "Comparison of different types of interfacial oxides on hole-selective p+-poly-Si passivated contacts for high-efficiency c-Si solar cells," *Solar Energy Materials and Solar Cells*, vol. 210, p. 110 487, Jun. 2020. DOI: 10.1016/j.solmat.2020.110487.

[79] Q. Li, K. Tao, Y. Sun, R. Jia, S.-M. Wang, Z. Jin, and X.-Y. Liu, "Replacing the amorphous silicon thin layer with microcrystalline silicon thin layer in TOPCon solar cells," *Solar Energy*, vol. 135, pp. 487–492, Oct. 2016. DOI: 10.1016/j.solener.2016.06.012.

[80] Z. Xin, Z. Ling, P. Wang, J. Ge, C. Ke, K. Choi, A. Aberle, and R. Stangl, "Ultra-thin atomic layer deposited aluminium oxide tunnel layer passivated hole-selective contacts for silicon solar cells," *Solar Energy Materials and Solar Cells*, vol. 191, pp. 164–174, Mar. 2019. DOI: 10.1016/j.solmat.2018.11.011.

[81] A. Desthieux, J. Posada, P.-P. Grand, C. Broussillou, B. Bazer-Bachi, G. Goaer, D. Messou, M. Bouttemy, E. Drahi, and P. Roca i Cabarrocas, "Impact of PECVD µc-Si:H deposition on tunnel oxide for passivating contacts," *EPJ Photovoltaics*, vol. 11, no. 3, M. Guenier-Farret and J. Alvarez, Eds., 2020. DOI: 10.1051/epjpv/2020001.

[82] H. Park, S. Bae, S. Park, J. Hyun, C. Lee, D. Choi, D. Kang, H. Han, Y. Kang, H.-S. Lee, and D. Kim, "Role of polysilicon in poly-Si/SiOx passivating contacts for high-efficiency silicon solar cells," *RSC Advances*, vol. 9, no. 40, pp. 23 261–23 266, 2019. DOI: 10.1039/C9RA03560E.

[83] A. Kale, W. Nemeth, S. Harvey, M. Page, D. Young, S. Agarwal, and P. Stradins, "Effect of silicon oxide thickness on polysilicon based passivated contacts for high-efficiency crystalline silicon solar cells," *Solar Energy Materials and Solar Cells*, vol. 185, pp. 270–276, Oct. 2018. DOI: 10.1016/j.solmat.2018.05.011.

[84] Y. Huang, M. Liao, Z. Wang, X. Guo, C. Jiang, Q. Yang, Z. Yuan, D. Huang, J. Yang, X. Zhang, Q. Wang, H. Jin, M. Al-Jassim, C. Shou, Y. Zeng, B. Yan, and J. Ye, "Ultrathin silicon oxide prepared by in-line plasma-assisted N2O oxidation (PANO) and the application for n-type polysilicon passivated contact," *Solar Energy Materials and Solar Cells*, vol. 208, p. 110 389, May 2020. DOI: 10.1016/j.solmat.2019.110389.

[85] Z. Rui, Y. Zeng, X. Guo, Q. Yang, Z. Wang, C. Shou, W. Ding, J. Yang, X. Zhang, Q. Wang, H. Jin, M. Liao, S. Huang, B. Yan, and J. Ye, "On the passivation mechanism of poly-silicon and thin silicon oxide on crystal silicon wafers," *Solar Energy*, vol. 194, pp. 18–26, Dec. 2019. DOI: 10.1016/j.solener.2019.10.064.

[86] S. Chao, Y. Takagi, G. Lucovsky, P. Pai, R. Custer, J. Tyler, and J. Keem, "Chemical states study of Si in SiOx films grown by PECVD," *Applied Surface Science*, vol. 26, no. 4, pp. 575–583, Oct. 1986. DOI: 10.1016/0169-4332(86)90128-5.

[87] M. Lehmann, N. Valle, J. Horzel, A. Pshenova, P. Wyss, M. Döbeli, M. Despeisse, S. Eswara, T. Wirtz, Q. Jeangros, A. Hessler-Wyser, F.-J. Haug, A. Ingenito, and C. Ballif, "Analysis of hydrogen distribution and migration in fired passivating contacts (FPC)," *Solar Energy Materials and Solar Cells*, vol. 200, Sep. 2019. DOI: 10.1016/j.solmat.2019.110018.

[88] F.-J. Haug, A. Ingenito, F. Meyer, S. Libraro, N. Bolis, J. Leon, C. Allebe, and C. Ballif, "Contributions to the Contact Resistivity in Fired Tunnel-Oxide Passivating Contacts for Crystalline Silicon Solar Cells," *IEEE Journal of Photovoltaics*, pp. 1–6, 2019. DOI: 10.1109/JPHOTOV.2019.2939880.

[89] A. Moldovan, F. Feldmann, M. Zimmer, J. Rentsch, J. Benick, and M. Hermle, "Tunnel oxide passivated carrier-selective contacts based on ultra-thin SiO2 layers," *Solar Energy Materials and Solar Cells*, vol. 142, pp. 123–127, Nov. 2015. DOI: 10.1016/j.solmat.2015.06.048.

[90] M. Hayes, B. Martel, S. Dubois, A. Morisset, and O. Palais, "Study of non fire-through metallization processes of boron-doped polysilicon passivated contacts for high efficiency silicon solar cells," 2019, p. 040 006. DOI: 10.1063/1.5123833.

[91] M. Lozac'h, S. Nunomura, H. Umishio, T. Matsui, and K. Matsubara, "Hydrogen passivation effect on p-type poly-Si/SiOx stack for crystalline silicon solar cells," 2019, p. 040 010. DOI: 10.1063/1.5123837.

[92] M. Lozac'h, S. Nunomura, and K. Matsubara, "Double-sided TOPCon solar cells on textured wafer with ALD SiOx layer," *Solar Energy Materials and Solar Cells*, vol. 207, p. 110 357, Apr. 2020. DOI: 10.1016/j.solmat.2019.110357.

[93] G. Kaur, T. Dutta, Z. Xin, Z. Ling, M. John Naval, M. Saifullah, R. Stangl, and A. Danner, "Ultra-thin LPCVD SiNx/n+poly-Si passivated contacts – A possibility?," Chiago: IEEE, Jun. 2019, pp. 2679–2683. DOI: 10.1109/PVSC40753.2019.8980624.

[94] D. Yan, A. Cuevas, J. Bullock, Y. Wan, and C. Samundsett, "Phosphorus-diffused polysilicon contacts for solar cells," *Solar Energy Materials and Solar Cells*, vol. 142, pp. 75–82, Nov. 2015. DOI: 10.1016/j.solmat.2015.06.001.

[95] Z. Ling, Z. Xin, P. Wang, R. Sridharan, C. Ke, and R. Stangl, "Double-Sided Passivated Contacts for Solar Cell Applications: An Industrially Viable Approach Toward 24% Efficient Large Area Silicon Solar Cells," p. 45, 2019. DOI: 10.5772/intechopen.85039.

[96] J. Schmidt, R. Peibst, and R. Brendel, "Surface passivation of crystalline silicon solar cells: Present and future," *Solar Energy Materials and Solar Cells*, vol. 187, pp. 39–54, Dec. 2018. DOI: 10.1016/j.solmat.2018.06.047.

[97] R. van der Vossen, F. Feldmann, A. Moldovan, and M. Hermle, "Comparative study of differently grown tunnel oxides for p-type passivating contacts," *Energy Procedia*, vol. 124, pp. 448–454, Sep. 2017. DOI: 10.1016/j.egypro.2017.09.273.

[98] Y. Tao, E. Chang, A. Upadhyaya, B. Roundaville, Y.-W. Ok, K. Madani, C.-W. Chen, K. Tate, V. Upadhyaya, F. Zimbardi, J. Keane, A. Payne, and A. Rohatgi, "730 mV implied Voc enabled by tunnel oxide passivated contact with PECVD grown and crystallized n+ polycrystalline Si," IEEE, Jun. 2015, pp. 1–5. DOI: 10.1109/PVSC.2015.7356218.

[99] H. Kim, S. Bae, K.-S. Ji, S. Kim, J. Yang, C. Lee, K. Lee, S. Kim, Y. Kang, H.-S. Lee, and D. Kim, "Passivation properties of tunnel oxide layer in passivated contact silicon solar cells," *Applied Surface Science*, vol. 409, pp. 140–148, Jul. 2017. DOI: 10.1016/j.apsusc.2017.02.195.

[100] A. Morisset, R. Cabal, B. Grange, C. Marchat, J. Alvarez, M.-E. Gueunier-Farret, S. Dubois, and J.-P. Kleider, "Conductivity and Surface Passivation Properties of Boron-Doped Poly-Silicon Passivated Contacts for c-Si Solar Cells," *physica status solidi (a)*, p. 1 800 603, Oct. 2018. DOI: 10.1002/pssa.201800603.

[101] J. Shewchun, D. Burk, and M. Spitzer, "MIS and SIS solar cells," *IEEE Transactions on Electron Devices*, vol. 27, no. 4, pp. 705–716, Apr. 1980. DOI: 10.1109/T-ED.1980.19926.

[102] J. Bullock, M. Hettick, J. Geissbühler, A. Ong, T. Allen, C. Sutter-Fella, T. Chen, H. Ota, E. Schaler, S. De Wolf, C. Ballif, A. Cuevas, and A. Javey, "Efficient silicon solar cells with dopant-free asymmetric heterocontacts," *Nature Energy*, vol. 1, no. 3, Mar. 2016. DOI: 10.1038/nenergy.2015.31.

[103] J. Meyer, S. Hamwi, M. Kröger, W. Kowalsky, T. Riedl, and A. Kahn, "Transition Metal Oxides for Organic Electronics: Energetics, Device Physics and Applications," *Advanced Materials*, vol. 24, no. 40, pp. 5408–5427, Oct. 2012. DOI: 10.1002/adma.201201630.

[104] L. Gerling, C. Voz, R. Alcubilla, and J. Puigdollers, "Origin of passivation in hole-selective transition metal oxides for crystalline silicon heterojunction solar cells," *Journal of Materials Research*, vol. 32, no. 2, pp. 260–268, Jan. 2017. DOI: 10.1557/jmr.2016.453.

[105] C. Battaglia, S. de Nicolás, S. De Wolf, X. Yin, M. Zheng, C. Ballif, and A. Javey, "Silicon heterojunction solar cell with passivated hole selective MoOx contact," *Applied Physics Letters*, vol. 104, no. 11, p. 113 902, Mar. 2014. DOI: 10.1063/1.4868880.

[106] M. Bivour, "Principles of carrier-selective contacts based on induced junctions," p. 5, 2017.

[107] M. Bivour, J. Temmler, H. Steinkemper, and M. Hermle, "Molybdenum and tungsten oxide: High work function wide band gap contact materials for hole selective contacts of silicon solar cells," *Solar Energy Materials and Solar Cells*, vol. 142, pp. 34–41, Nov. 2015. DOI: 10.1016/j.solmat.2015.05.031.

[108] J. Dréon, Q. Jeangros, J. Cattin, J. Haschke, L. Antognini, C. Ballif, and M. Boccard, "23.5%-efficient silicon heterojunction silicon solar cell using molybdenum oxide as hole-selective contact," *Nano Energy*, vol. 70, p. 104 495, Apr. 2020. DOI: 10.1016/j.nanoen.2020.104495.

[109] L. Gerling, S. Mahato, A. Morales-Vilches, G. Masmitja, P. Ortega, C. Voz, R. Alcubilla, and J. Puigdollers, "Transition metal oxides as hole-selective contacts in silicon heterojunctions solar cells," *Solar Energy Materials and Solar Cells*, vol. 145, pp. 109–115, Feb. 2016. DOI: 10.1016/j.solmat.2015.08.028.

[110] S. Avasthi, W. E. W.E., G. Man, A. Kahn, J. Schwartz, and J. Sturm, "Hole-blocking titanium-oxide/silicon heterojunction and its application to photovoltaics," *Applied Physics Letters*, vol. 102, no. 20, p. 203 901, May 2013. DOI: 10.1063/1.4803446.

[111] X. Yang, Q. Bi, H. Ali, K. Davis, W. Schoenfeld, and K. Weber, "High-Performance TiO2 -Based Electron-Selective Contacts for Crystalline Silicon Solar Cells," *Advanced Materials*, vol. 28, no. 28, pp. 5891–5897, Jul. 2016. DOI: 10.1002/adma.201600926.

[112] K. Nagamatsu, S. Avasthi, G. Sahasrabudhe, G. Man, J. Jhaveri, A. Berg, J. Schwartz, A. Kahn, S. Wagner, and J. Sturm, "Titanium dioxide/silicon hole-blocking selective contact to enable double-heterojunction crystalline silicon-based solar cell," *Applied Physics Letters*, vol. 106, no. 12, p. 123 906, Mar. 2015. DOI: 10.1063/1.4916540.

[113] W. Liang, J. Tong, P. Narangari, S. Armand, T. Kho, M. Ernst, D. Walter, S. Surve, K. McIntosh, M. Stocks, K. Weber, A. Blakers, and K. Fong, "Impact of Al Doping on Surface Passivation of TiOx on Si," *IEEE Journal of Photovoltaics*, pp. 1–5, 2020. DOI: 10.1109/JPHOTOV.2020.2982169.

[114] B. Macco, L. Black, J. Melskens, B. van de Loo, W.-J. H. Berghuis, M. Verheijen, and W. Kessels, "Atomic-layer deposited Nb2O5 as transparent passivating electron contact for c-Si solar cells," *Solar Energy Materials and Solar Cells*, vol. 184, pp. 98–104, Sep. 2018. DOI: 10.1016/j.solmat.2018.04.037.

[115] B. W. H. van de Loo, B. Macco, J. Melskens, W. Beyer, and W. M. M. Kessels, "Silicon surface passivation by transparent conductive zinc oxide," *Journal of Applied Physics*, vol. 125, no. 10, p. 105 305, Mar. 2019. DOI: 10.1063/1.5054166.

[116] J. Heng, "23% High-Efficiency Tunnel Oxide Junction Bifacial Solar Cell With Electroplated Cu Gridlines," *IEEE JOURNAL OF PHOTOVOLTAICS*, vol. 5, no. 1, pp. 82–86, 2015.

[117] M. Green, "Photovoltaic technology and visions for the future," *Progress in Energy*, vol. 1, no. 1, p. 013 001, Jul. 2019. DOI: 10.1088/2516-1083/ab0fa8.

[118] G. Group, *Screen Printing For The Industrial User*. Mar. 1997. [Online]. Available: http://www.gwent.org/gem_screen_printing.html.

[119] E. Bruhat, T. Desrues, D. Blanc-Pélissier, B. Martel, R. Cabal, and S. Dubois, "TCO contacts on poly-Si layers: High and low temperature approaches to maintain passivation and contact properties," 2019, p. 040 001. DOI: 10.1063/1.5123828.

[120] A. Faes, A. Lachowicz, A. Bettinelli, P.-J. Ribeyron, J.-F. Lerat, D. Munoz, J. Geissbühler, H.-Y. Li, C. Ballif, and M. Despeisse, "Metallization and interconnection for high-efficiency bifacial silicon heterojunction solar cells and modules," p. 12,

[121] J. Zhang, H. Li, H. Tong, S. Xiong, Y. Yang, X. Yuan, H. Li, and C. Liu, "Influence of Glass Phase in Silver Paste on Metallized Contact Resistance between Rear Silver and Aluminum Electrodes of Crystalline Silicon PERC Cells," *Applied Sciences*, vol. 9, no. 5, p. 891, Mar. 2019. DOI: 10.3390/app9050891.

[122] A. Z. O. Materials, *Front-side Metallization Pastes for Photovoltaic Manufacture*. Apr. 2020. [Online]. Available: https://www.azom.com/article.aspx?ArticleID=10081.

[123] A. Ebong and N. Chen, "Metallization of crystalline silicon solar cells: A review," IEEE, Dec. 2012, pp. 102–109. DOI: 10.1109/HONET.2012.6421444.

[124] P. Padhamnath, J. Wong, B. Nagarajan, J. Buatis, L. Ortega, N. Nandakumar, A. Khanna, V. Shanmugam, and S. Duttagupta, "Metal contact recombination in monoPolyTM solar cells with screen-printed & fire-through contacts," *Solar Energy Materials and Solar Cells*, vol. 192, pp. 109–116, Apr. 2019. DOI: 10.1016/j.solmat.2018.12.026.

[125] M. Stodolny, K. Tool, B. Geerligs, J. Loffler, A. Weeber, Y. Wu, J. Anker, X. Lu, J. Liu, P. Bronsveld, A. Mewe, G. Janssen, and G. Coletti, "PolySi Based Passivating Contacts Enabling Industrial Silicon Solar Cell Efficiencies up to 24%," IEEE, Jun. 2019, pp. 1456–1459. DOI: 10.1109/PVSC40753.2019.8980806.

[126] A. Luque López and S. Hegedus, Eds., *Handbook of photovoltaic science and engineering*, 2. ed., [fully rev. and updated]. Chichester: Wiley, 2011.

[127] A. R. Barron, "Chemistry of the Main Group Elements," pp. 336–344, 2014. [Online]. Available: http://cnx.org/content/col11124/1.25/.

[128] W. Zulehner, "Historical overview of silicon crystal pulling development," *Materials Science and Engineering: B*, vol. 73, no. 1-3, pp. 7–15, Apr. 2000. DOI: 10.1016/S0921-5107(99)00427-4.

[129] W. Ammon, P. Dreier, W. Hensel, U. Lambert, and L. Köster, "Influence of oxygen and nitrogen on point defect aggregation in silicon single crystals," *Materials Science and Engineering: B*, vol. 36, no. 1-3, pp. 33–41, Jan. 1996. DOI: 10.1016/0921-5107(95)01295-8. [Online]. Available: https://linkinghub.elsevier.com/retrieve/pii/0921510795012958.

[130] N. Stoddard, B. Wu, I. Witting, M. Wagener, Y. Park, G. Rozgonyi, and R. Clark, "Casting Single Crystal Silicon: Novel Defect Profiles from BP Solar's Mono Wafers," *Solid State Phenomena*, vol. 131-133, pp. 1–8, Oct. 2007. DOI: 10.4028/www.scientific.net/SSP.131-133.1.

[131] I. Takahashi, S. Joonwichien, T. Iwata, and N. Usami, "Seed manipulation for artificially controlled defect technique in new growth method for quasi-monocrystalline Si ingot based on casting," *Applied Physics Express*, vol. 8, no. 10, p. 105 501, Oct. 2015. DOI: 10.7567/APEX.8.105501.

[132] S. Riepe, S. Nold, P. Brailovsky, P. Krenckel, L. Friedrich, S. Janz, and R. Preu, "Cast-Mono Silicon Wafers For A Sustainable PV Market Growth," 2020, p. 5.

[133] N. R. Council, *Plasma Science: Advancing Knowledge in the National Interest*. Washington, D.C.: National Academies Press, 2007. DOI: 10.17226/11960.

[134] P. Roca i Cabarrocas, "Deposition Techniques and Processes Involved in the Growth of Amorphous and Microcrystalline Silicon Thin Films," in *Physics and Technology of Amorphous-Crystalline Heterostructure Silicon Solar Cells*, W. G. J. H. M. van Sark, L. Korte, and F. Roca, Eds., vol. 0, Berlin, Heidelberg: Springer Berlin Heidelberg, 2012, pp. 131–160. DOI: 10.1007/978-3-642-22275-7_5.

[135] N. S. J. Braithwaite, "Introduction to gas discharges," *Plasma Sources Science and Technology*, vol. 9, no. 4, pp. 517–527, Nov. 2000. DOI: 10.1088/0963-0252/9/4/307.

[136] M. Chrostowski, "Growth of doped epitaxial silicon at low temperature by RF-PECVD for photovoltaic applications," Ph.D. dissertation, Institut Polytechnique de Paris, Palaiseau, France, 2020.

[137] F. Lebreton, "Silicon surface passivation properties of aluminum oxide grown by atomic layer deposition for low temperature solar cells processes," PhD thesis, Université Paris-Saclay, Dec. 2017.

[138] J. C. Looney and M. C. McFeely, "Thermal growth and chemical etching of silicon dioxide films (dimensional control of oxide films on n- and p-type silicon by thermal oxidation and chemical etching in hf)," *Semiconductor products and solid state technology*, vol. 9, pp. 19–24, 1966.

[139] W Kern and D. Puotinen, "Cleaning solutions based on hydrogen peroxide for use in silicon semiconductor technology," vol. 31, no. 2, pp. 187–206, 1970.

[140] F. J. Himpsel, F. R. McFeely, A. Taleb-Ibrahimi, J. A. Yarmoff, and G. Hollinger, "Microscopic structure of the SiO 2 /Si interface," *Physical Review B*, vol. 38, no. 9, pp. 6084–6096, Sep. 1988. DOI: 10.1103/PhysRevB.38.6084.

[141] Z. H. Lu, M. J. Graham, D. T. Jiang, and K. H. Tan, "SiO2/Si(100) interface studied by Al Kα x-ray and synchrotron radiation photoelectron spectroscopy," *Applied Physics Letters*, vol. 63, no. 21, pp. 2941–2943, Nov. 1993. DOI: 10.1063/1.110279.

[142] O. Sublemontier, C. Nicolas, D. Aureau, M. Patanen, H. Kintz, X. Liu, M.-A. Gaveau, J.-L. Le Garrec, E. Robert, F.-A. Barreda, A. Etcheberry, C. Reynaud, J. Mitchell, and C. Miron, "X-ray Photoelectron Spectroscopy of Isolated Nanoparticles," *The Journal of Physical Chemistry Letters*, vol. 5, no. 19, pp. 3399–3403, Oct. 2014. DOI: 10.1021/jz501532c.

[143] G. E. Jellison and F. A. Modine, "Parameterization of the optical functions of amorphous materials in the interband region," *Applied Physics Letters*, vol. 69, no. 3, pp. 371–373, Jul. 1996. DOI: 10.1063/1.118064.

[144] L. Yan, S. Huang, H. Ren, D. Zhang, W. Liu, Y. Zhao, and X. Zhang, "Bifunctional CO2 Plasma Treatment at the i/p Interface Enhancing the Performance of Planar Silicon Heterojunction Solar Cells," *physica status solidi (RRL) – Rapid Research Letters*, p. 2 100 010, Feb. 2021. DOI: 10.1002/pssr.202100010.

[145] M. Sreng, F. Silva, and P. Roca i Cabarrocas, "In situ Photoluminescence Study of Plasma Effects on Passivation of Crystalline Silicon Coated with Aluminum Oxide," *physica status solidi (a)*, vol. 216, no. 10, p. 1 800 612, May 2019. DOI: 10.1002/pssa.201800612.

[146] C. Park, N. Balaji, S. Ahn, J. Park, E.-C. Cho, and J. Yi, "Effects of tunneling oxide defect density and inter-diffused carrier concentration on carrier selective contact solar cell performance: Illumination and temperature effects," *Solar Energy*, vol. 211, pp. 62–73, Nov. 2020. DOI: 10.1016/j.solener.2020.09.060.

[147] L. Shen, J. Zhou, C. Liu, H. Li, Y. Gong, Y. Bao, and J. Fang, "Investigation and characterization of silicon concentration in N-free anti-reflective layer films," IEEE, Jun. 2020, pp. 1–3. DOI: 10.1109/CSTIC49141.2020.9282476.

[148] S. Choi, O. Kwon, K. Min, M. Jeong, K. Jeong, M. Kang, S. Park, K. Hong, H. Song, and K. Kim, "Formation and suppression of hydrogen blisters in tunnelling oxide passivating contact for crystalline silicon solar cells," *Scientific Reports*, vol. 10, no. 1, Dec. 2020. DOI: 10.1038/s41598-020-66801-4.

[149] A. Morisset, R. Cabal, B. Grange, C. Marchat, J. Alvarez, M.-E. Gueunier-Farret, S. Dubois, and J.-P. Kleider, "Improvement of the conductivity and surface passivation properties of boron-doped poly-silicon on oxide," 2018, p. 040 017. DOI: 10.1063/1.5049280.

[150] R. Saleh and N. Nickel, "Raman spectroscopy of B-doped microcrystalline silicon films," *Thin Solid Films*, vol. 427, no. 1-2, pp. 266–269, Mar. 2003. DOI: 10.1016/S0040-6090(02)01203-8.

[151] D. A. G. Bruggeman, "Berechnung verschiedener physikalischer Konstanten von heterogenen Substanzen. I. Dielektrizitätskonstanten und Leitfähigkeiten der Mischkörper aus isotropen Substanzen," *Annalen der Physik*, vol. 416, no. 7, pp. 636–664, 1935. DOI: 10.1002/andp.19354160705.

[152] G. E. Jellison, M. F. Chisholm, and S. M. Gorbatkin, "Optical functions of chemical vapor deposited thin-film silicon determined by spectroscopic ellipsometry," *Applied Physics Letters*, vol. 62, no. 25, pp. 3348–3350, Jun. 1993. DOI: 10.1063/1.109067.

[153] B. Kalache, A. I. Kosarev, R. Vanderhaghen, and P. R. i Cabarrocas, "Ion bombardment effects on microcrystalline silicon growth mechanisms and on the film properties," *Journal of Applied Physics*, vol. 93, no. 2, pp. 1262–1273, Jan. 2003. DOI: 10.1063/1.1524707.

[154] F. Lebreton, S. N. Abolmasov, F. Silva, and P. Roca i Cabarrocas, "In situ photoluminescence study of plasma-induced damage at the a-Si:H/c-Si interface," *Applied Physics Letters*, vol. 108, no. 5, p. 051 603, Feb. 2016. DOI: 10.1063/1.4941298.

[155] R. Martins, I. Ferreira, and E. Fortunato, "Wide Band Gap Microcrystalline Silicon Thin Films," *Solid State Phenomena*, vol. 44-46, pp. 299–346, Jul. 1995. DOI: 10.4028/www.scientific.net/SSP.44-46.299.

[156] S. Hamma and P. Roca i Cabarrocas, "Low-temperature growth of thick intrinsic and ultrathin phosphorous or boron-doped microcrystalline silicon films: Optimum crystalline fractions for solar cell applications," *Solar Energy Materials and Solar Cells*, vol. 69, no. 3, pp. 217–239, Oct. 2001. DOI: 10.1016/S0927-0248(00)00391-3.

[157] B. Steinhauser, F. Feldmann, D. Ourinson, H. Nagel, T. Fellmeth, and M. Hermle, "On the Influence of the SiNx Composition on the Firing Stability of Poly-Si/SiNx Stacks," *physica status solidi (a)*, vol. 217, no. 21, p. 2 000 333, Nov. 2020. DOI: 10.1002/pssa.202000333.

[158] C. Hollemann, F. Haase, J. Krügener, R. Brendel, and R. Peibst, "Firing stability of n-type poly-Si on oxide junctions formed by quartz tube annealing," in *46th IEEE PVSC*, Online, 2020, p. 5.

[159] C. Messmer, A. Fell, F. Feldmann, N. Wohrle, J. Schon, and M. Hermle, "Efficiency Roadmap for Evolutionary Upgrades of PERC Solar Cells by TOPCon: Impact of Parasitic Absorption," *IEEE Journal of Photovoltaics*, vol. 10, no. 2, pp. 335–342, Mar. 2020. DOI: 10.1109/JPHOTOV.2019.2957642.

[160] M. Khokhar, S. Chowdhury, D. Pham, S. Hussain, E.-C. Cho, and J. Yi, "Improving passivation properties using a nano-crystalline silicon oxide layer for high-efficiency TOPCon cells," *Infrared Physics & Technology*, vol. 115, p. 103 723, Jun. 2021. DOI: 10.1016/j.infrared.2021.103723. [Online]. Available: https://linkinghub.elsevier.com/retrieve/pii/S1350449521000955.

[161] B. Pan and R. Biswas, "Simulation of hydrogen evolution from nano-crystalline silicon," *Journal of Non-Crystalline Solids*, vol. 333, no. 1, pp. 44–47, Jan. 2004. DOI: 10.1016/j.jnoncrysol.2003.09.058.

[162] S. Lebib and P. Roca i Cabarrocas, "Effects of ion energy on the crystal size and hydrogen bonding in plasma-deposited nanocrystalline silicon thin films," *Journal of Applied Physics*, vol. 97, no. 10, p. 104 334, May 2005. DOI: 10.1063/1.1913803.

[163] P. Padhamnath, A. Khanna, N. Balaji, V. Shanmugam, N. Nandakumar, D. Wang, Q. Sun, M. Huang, S. Huang, B. Fan, B. Ding, A. Aberle, and S. Duttagupta, "Progress in screen-printed metallization of industrial solar cells with SiOx/poly-Si passivating contacts," *Solar Energy Materials and Solar Cells*, vol. 218, p. 110 751, Dec. 2020. DOI: 10.1016/j.solmat.2020.110751.

[164] Y.-W. Ok, A. Tam, Y.-Y. Huang, V. Yelundur, A. Das, A. Payne, V. Chandrasekaran, A. Upadhyaya, A. Jain, and A. Rohatgi, "Screen printed, large area bifacial N-type back junction silicon solar cells with selective phosphorus front surface field and boron doped poly-Si/SiOx passivated rear emitter," *Applied Physics Letters*, vol. 113, no. 26, p. 263 901, Dec. 2018. DOI: 10.1063/1.5059559.

[165] H. Çiftpınar, M. Stodolny, Y. Wu, G. Janssen, J. Löffler, J. Schmitz, M. Lenes, J.-M. Luchies, and L. Geerligs, "Study of screen printed metallization for polysilicon based passivating contacts," *Energy Procedia*, vol. 124, pp. 851–861, Sep. 2017. DOI: 10.1016/j.egypro.2017.09.242.

[166] H. Dekkers, S. De Wolf, G. Agostinelli, F. Duerinckx, and G. Beaucarne, "Requirements of PECVD SiNx:H layers for bulk passivation of mc-Si," *Solar Energy Materials and Solar Cells*, vol. 90, no. 18-19, pp. 3244–3250, Nov. 2006. DOI: 10.1016/j.solmat.2006.06.024. [Online]. Available: https://linkinghub.elsevier.com/retrieve/pii/S0927024806002443.

[167] S. Duttagupta, F.-J. Ma, B. Hoex, and A. G. Aberle, "Excellent surface passivation of heavily doped p+ silicon by low-temperature plasma-deposited SiOx/SiNy dielectric stacks with optimised antireflective performance for solar cell application," *Solar Energy Materials and Solar Cells*, vol. 120, pp. 204–208, Jan. 2014. DOI:

10.1016/j.solmat.2013.09.004. [Online]. Available: https://linkinghub.elsevier.com/retrieve/pii/S092702481300456X.

[168] S. Gatz, T. Dullweber, V. Mertens, F. Einsele, and R. Brendel, "Firing stability of SiNy/SiNx stacks for the surface passivation of crystalline silicon solar cells," *Solar Energy Materials and Solar Cells*, vol. 96, pp. 180–185, Jan. 2012. DOI: 10.1016/j.solmat.2011.09.051.

[169] M. Sreng, "Development of in-situ photoluminescence characterization tools for the real-time study of semiconductor materials for photovoltaic application," PhD thesis, IPParis, Palaiseau, France, Oct. 2019.

[170] D. Benoit, P. Morin, and J. Regolini, "Determination of silicon nitride film chemical composition to study hydrogen desorption mechanisms," *Thin Solid Films*, vol. 519, no. 19, pp. 6550–6553, Jul. 2011. DOI: 10.1016/j.tsf.2011.04.130.

[171] J. Kim, S. Park, J. Hyun, H. Park, S. Bae, K.-S. Ji, H. Kim, K. Lee, Y. Kang, H.-S. Lee, and D. Kim, "Characterization of SiNx:H thin film as a hydrogen passivation layer for silicon solar cells with passivated contacts," *Thin Solid Films*, vol. 675, pp. 109–114, Apr. 2019. DOI: 10.1016/j.tsf.2019.02.016.

[172] X. Yan, F. Suhaimi, M. Xu, J. Yang, X. Zhang, Q. Wang, H. Jin, V. Shanmugam, and S. Duttagupta, "Development of ultra-thin doped poly-Si via LPCVD and ex-situ tube diffusion for passivated contact solar cell applications," *Solar Energy Materials and Solar Cells*, vol. 209, p. 110 458, Jun. 2020. DOI: 10.1016/j.solmat.2020.110458.

[173] V. Shanmugam, N. Chen, X. Yan, A. Khanna, B. Nagarajan, J. Rodriguez, N. Nandakumar, H. Knauss, H. Haverkamp, A. Aberle, and S. Duttagupta, "Impact of the manufacturing process on the reverse-bias characteristics of high-efficiency n-type bifacial silicon wafer solar cells," *Solar Energy Materials and Solar Cells*, vol. 191, pp. 117–122, Mar. 2019. DOI: 10.1016/j.solmat.2018.11.014.

[174] R. Brüggemann and S. Reynolds, "Modulated photoluminescence studies for lifetime determination in amorphous-silicon passivated crystalline-silicon wafers," *Journal of Non-Crystalline Solids*, vol. 352, no. 9-20, pp. 1888–1891, Jun. 2006. DOI: 10.1016/j.jnoncrysol.2005.11.092.

[175] S. Abolmasov, H. Woo, R. Planques, J. Holovský, E. Johnson, A. Purkrt, and P. Roca i Cabarrocas, "Substrate and p-layer effects on polymorphous silicon solar cells," *EPJ Photovoltaics*, vol. 5, p. 55 206, 2014. DOI: 10.1051/epjpv/2014007.

[176] J. A. Giesecke, S. W. Glunz, and W. Warta, "Understanding and resolving the discrepancy between differential and actual minority carrier lifetime," *Journal of Applied Physics*, vol. 113, no. 7, Feb. 2013. DOI: 10.1063/1.4790716.

[177] S. Bernardini, T. Naerland, A. Blum, G. Coletti, and M. Bertoni, "Unraveling bulk defects in high-quality c-Si material via TIDLS: Unraveling bulk defects in high-quality c-Si material," *Progress in Photovoltaics: Research and Applications*, vol. 25, no. 3, pp. 209–217, Mar. 2017. DOI: 10.1002/pip.2847.

[178] P. C. Mathur, R. P. Sharma, P. Saxena, and J. D. Arora, "Temperature dependence of minority carrier lifetime in single-crystal and polycrystalline Si solar cells," *Journal of Applied Physics*, vol. 52, no. 5, pp. 3651–3654, May 1981. DOI: 10.1063/1.329101.

[179] C.-H. Hsu, C.-W. Huang, Y.-S. Cho, W.-Y. Wu, D.-W. Wuu, X.-Y. Zhang, W.-Z. Zhu, S.-Y. Lien, and C.-S. Ye, "Efficiency improvement of PERC solar cell using an aluminum oxide passivation layer prepared via spatial atomic layer deposition and post-annealing," *Surface and Coatings Technology*, Dec. 2018. DOI: 10.1016/j.surfcoat.2018.12.016.

[180] G. Kaur, N. Dwivedi, X. Zheng, B. Liao, L. Peng, A. Danner, R. Stangl, and C. Bhatia, "Understanding Surface Treatment and ALD AlOx Thickness Induced Surface Passivation Quality of c-Si Cz Wafers," *IEEE Journal of Photovoltaics*, vol. 7, no. 5, pp. 1224–1235, Sep. 2017. DOI: 10.1109/JPHOTOV.2017.2717040.

[181] B. van de Loo, B. Macco, M. Schnabel, M. Stodolny, A. Mewe, D. Young, W. Nemeth, P. Stradins, and W. Kessels, "On the hydrogenation of Poly-Si passivating contacts by Al2O3 and SiN thin films," *Solar Energy Materials and Solar Cells*, vol. 215, p. 110 592, Sep. 2020. DOI: 10.1016/j.solmat.2020.110592.

[182] D. Tröger, M. Grube, J. Lehnert, and T. Mikolajick, "Al2O3-TiOx as full area passivating contacts for silicon surfaces utilizing oxygen scavenging titanium interlayers," *Solar Energy Materials and Solar Cells*, vol. 215, p. 110 651, Sep. 2020. DOI: 10.1016/j.solmat.2020.110651.

[183] G. Dingemans and W. M. M. Kessels, "Status and prospects of Al2O3 -based surface passivation schemes for silicon solar cells," *Journal of Vacuum Science & Technology A: Vacuum, Surfaces, and Films*, vol. 30, no. 4, p. 040 802, Jul. 2012. DOI: 10.1116/1.4728205.

[184] B Liao, R Stangl, F Ma, T Mueller, F Lin, A. G. Aberle, C. S. Bhatia, and B Hoex, "Excellent c-Si surface passivation by thermal atomic layer deposited aluminum oxide after industrial firing activation," *Journal of Physics D: Applied Physics*, vol. 46, no. 38, p. 385 102, Sep. 2013. DOI: 10.1088/0022-3727/46/38/385102.

[185] E. Simoen, A. Rothschild, B. Vermang, J. Poortmans, and R. Mertens, "A Deep-Level Transient Spectroscopy Comparison of the SiO2/Si and Al2O3/Si Interface States," *ECS Transactions*, vol. 41, no. 4, pp. 37–44, Dec. 2019. DOI: 10.1149/1.3628607.

[186] J. Melskens, B. W. H. van de Loo, B. Macco, M. F. J. Vos, J. Palmans, S. Smit, and W. M. M. Kessels, "Concepts and prospects of passivating contacts for crystalline silicon solar cells," IEEE, Jun. 2015, pp. 1–6. DOI: 10.1109/PVSC.2015.7355646.

[187] G. Dingemans, P. Engelhart, R. Seguin, F. Einsele, B. Hoex, M. C. M. van de Sanden, and W. M. M. Kessels, "Stability of Al2O3 and Al2O3/a-SiNx:H stacks for surface passivation of crystalline silicon," *Journal of Applied Physics*, vol. 106, no. 11, p. 114 907, Dec. 2009. DOI: 10.1063/1.3264572.

[188] K. Arafune, S. Miki, R. Matsutani, J. Hamano, H. Yoshida, T. Tachibana, H. Lee, A. Ogura, Y. Ohshita, and S.-I. Satoh, "Surface Recombination of Crystalline Silicon Substrates Passivated by Atomic-Layer-Deposited AlOx," *Japanese Journal of Applied Physics*, vol. 51, 04DP06, Apr. 2012. DOI: 10.1143/JJAP.51.04DP06.

[189] J. Töfflinger, A. Laades, C. Leendertz, L. Montañez, L. Korte, U. Stürzebecher, H.-P. Sperlich, and B. Rech, "PECVD-AlOx/SiNx Passivation Stacks on Silicon: Effective Charge Dynamics and Interface Defect State Spectroscopy," *Energy Procedia*, vol. 55, pp. 845–854, 2014. DOI: 10.1016/j.egypro.2014.08.068.

[190] V. Naumann, M. Otto, R. Wehrspohn, and C. Hagendorf, "Chemical and structural study of electrically passivating Al2O3/Si interfaces prepared by atomic layer deposition," *Journal of Vacuum Science & Technology A: Vacuum, Surfaces, and Films*, vol. 30, no. 4, p. 04D106, Jul. 2012. DOI: 10.1116/1.4704601.

[191] B. Liao, R. Stangl, T. Mueller, F. Lin, C. Bhatia, and B. Hoex, "The effect of light soaking on crystalline silicon surface passivation by atomic layer deposited Al2O3," *Journal of Applied Physics*, vol. 113, no. 2, p. 024 509, Jan. 2013. DOI: 10.1063/1.4775595. [Online]. Available: http://aip.scitation.org/doi/10.1063/1.4775595.

[192] F. Lebreton, R. Lachaume, P. Bulkin, F. Silva, S. Filonovich, E. Johnson, and P. Roca i Cabarrocas, "Deleterious electrostatic interaction in silicon passivation stack between thin ALD Al2O3 and its a-SiNx:H capping layer: Numerical and experimental evidences," *Energy Procedia*, vol. 124, pp. 91–98, Sep. 2017. DOI: 10.1016/j.egypro.2017.09.328.

[193] G. Dingemans, N. M. Terlinden, M. A. Verheijen, M. C. M. van de Sanden, and W. M. M. Kessels, "Controlling the fixed charge and passivation properties of Si(100)/Al2O3 interfaces using ultrathin SiO2 interlayers synthesized by atomic layer deposition," *Journal of Applied Physics*, vol. 110, no. 9, p. 093 715, Nov. 2011. DOI: 10.1063/1.3658246.

[194] N. M. Terlinden, G. Dingemans, V. Vandalon, R. H. E. C. Bosch, and W. M. M. Kessels, "Influence of the SiO2 interlayer thickness on the density and polarity of charges in Si/SiO2/Al2O3 stacks as studied by optical second-harmonic generation," *Journal of Applied Physics*, vol. 115, no. 3, p. 033 708, Jan. 2014. DOI: 10.1063/1.4857075.

[195] N. Grant, V. Markevich, J. Mullins, A. Peaker, F. Rougieux, D. Macdonald, and J. Murphy, "Permanent annihilation of thermally activated defects which limit the lifetime of float-zone silicon: Permanent annihilation of thermally activated defects in FZ-Si," *physica status solidi (a)*, vol. 213, no. 11, pp. 2844–2849, Nov. 2016. DOI: 10.1002/pssa.201600360.

[196] D. Hiller, V. Markevich, J. de Guzman, D. König, S. Prucnal, W. Bock, J. Julin, A. Peaker, D. Macdonald, N. Grant, and J. Murphy, "Kinetics of Bulk Lifetime Degradation in Float-Zone Silicon: Fast Activation and Annihilation of Grown-In Defects and the Role of Hydrogen versus Light," *physica status solidi (a)*, vol. 217, no. 17, p. 2 000 436, Sep. 2020. DOI: 10.1002/pssa.202000436.

[197] T. Abe, "Generation and annihilation of point defects by doping impurities during FZ silicon crystal growth," *Journal of Crystal Growth*, vol. 334, no. 1, pp. 4–15, Nov. 2011. DOI: 10.1016/j.jcrysgro.2011.04.017.

[198] A. Hara, "Diffusion Coefficient of Hydrogen in Silicon at an Intermediate Temperature," *Japanese Journal of Applied Physics*, vol. 46, no. 3A, pp. 962–964, Mar. 2007. DOI: 10.1143/JJAP.46.962.

[199] Y. Zhu, F. Rougieux, N. Grant, J. De Guzman, J. Murphy, V. Markevich, G. Coletti, A. Peaker, and Z. Hameiri, "Electrical Characterization of Thermally Activated Defects in n-Type Float-Zone Silicon," *IEEE Journal of Photovoltaics*, vol. 11, no. 1, pp. 26–35, Jan. 2021. DOI: 10.1109/JPHOTOV.2020.3031382.

[200] F. Rougieux, N. Grant, C. Barugkin, D. Macdonald, and J. Murphy, "Influence of Annealing and Bulk Hydrogenation on Lifetime-Limiting Defects in Nitrogen-Doped Floating Zone Silicon," *IEEE Journal of Photovoltaics*, vol. 5, no. 2, pp. 495–498, Mar. 2015. DOI: 10.1109/JPHOTOV.2014.2367912.

[201] S. M. Sze and K. K. Ng, *Physics of semiconductor devices*, 3rd ed. Hoboken, N.J: Wiley-Interscience, 2007.

[202] C. Thurmond, "The Standard Thermodynamic Functions for the Formation of Electrons and Holes in Ge, Si, GaAs , and GaP," *Journal of The Electrochemical Society*, vol. 122, no. 8, pp. 1133–1141, Aug. 1975. DOI: 10.1149/1.2134410.

[203] Y.-B. Park and S.-W. Rhee, "Bulk and interface properties of low-temperature silicon nitride fillms deposited by remote plasma enhanced chemical vapor deposition," *Journal of materials science: materials in electronics*, vol. 12, pp. 515–522, 2001. DOI: https://doi.org/10.1023/A:1012449425744.

[204] ITRPV, "International Technology Roadmap for Photovoltaic (ITRPV) 11th edition," Tech. Rep. 11th edition, Apr. 2020, p. 88.

[205] I. Guerrero, V. Parra, T. Carballo, A. Black, M. Miranda, D. Cancillo, B. Moralejo, J. Jiménez, J.-F. Lelièvre, and C. del Cañizo, "About the origin of low wafer performance and crystal defect generation on seed-cast growth of industrial mono-like silicon ingots: Seed-cast growth of industrial mono-like silicon ingots," *Progress in Photovoltaics: Research and Applications*, vol. 22, no. 8, pp. 923–932, Aug. 2014. DOI: 10.1002/pip.2344.

[206] D. R. Turner, "On the Mechanism of Chemically Etching Germanium and Silicon," *Journal of The Electrochemical Society*, vol. 107, no. 10, p. 810, 1960. DOI: 10.1149/1.2427519.

[207] S. S. LLC, *PV-20000a Operation Manual*, 2013.

[208] I. P. o. C. Change, "Global Warming of 1.5°C, Summary for Polycimakers," IPCC, Tech. Rep., Oct. 2018.

Appendix A1

Choice of $\tau_{bulk,0}$

As exposed in Section 4.1.3, the hydrogenation of the bulk wafer previously degraded by a firing step is studied by observing the evolution of a so called "bulk lifetime" at ambient temperature. This lifetime accounts for the charge carriers recombinations due to N_1V_1 centers and other defects that are activated during the firing step. In order to isolate this contribution from other thermal phenomena (electron and hole trap capture cross sections, Auger recombinations ...), two annealing processes were compared: one during a hydrogenation process, one for a similar annealing step on a sample that is already cured. The evolution of the bulk lifetime during the hydrogenation process is calculated with Equation 4.6

$$\tau_{bulk,1} = \frac{\tau_{eff,0}\tau_{eff,1}}{\tau_{eff,0} - \tau_{eff,1} + \frac{\tau_{eff,0}\tau_{eff,1}}{\tau_{bulk,0}}}$$

using the effective lifetime of the two samples (measured), and by setting a value for the bulk lifetime of the reference sample $\tau_{bulk,0}$. The arbitrary value of 2000 µs was chosen, but the final bulk lifetime might depend on this parameter. The evolution of the behavior for different $\tau_{bulk,0}$ values was assessed in Figure A1.1.

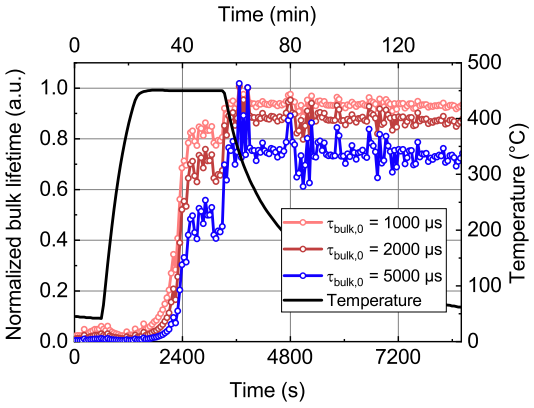

Figure A1.1: Normalized bulk lifetime evolution during the hydrogenation process, for different $\tau_{bulk,0}$ values. The black solid line represents the temperature profile during the hydrogenation process of the sample at 450 °for 30 min.

Obviously, the absolute lifetime value of the studied sample $\tau_{bulk,1}$ is greatly dependent on the $\tau_{bulk,0}$ value chosen since at the end, $\tau_{bulk,1} \approx \tau_{bulk,0}$. However, the behavior of the

normalized bulk lifetime $\tau_{bulk,1}/\tau_{bulk,0}$ is very similar for lifetime values of 1000, 2000, and 5000 µs, which are reasonable guesses of bulk lifetime for a p-type float-zone wafer. The conclusions drawn are consequently not impacted by the arbitrary choice of the value of $\tau_{bulk,0}$.

Appendix A2

Characterization techniques

Quasi Steady-State Photoconductance (QSSPC)

The Quasi Steady-State Photoconductance (QSSPC) technique is the most widely used technique for quantifying the passivation quality of a passivating stack deposited on a silicon wafer. It is convenient since it is a non-destructive technique that does not need metallic contacts and is very fast. It allows to measure various physical values such as the effective minority carrier lifetime τ_{eff}, the implied Open Circuit Voltage iV_{OC} or the recombination current density J_0.

It consists in the following steps

- Subject the sample to a light pulse of known intensity (measured by a photo-diode next to the illuminated sample)
- Measuring the photoconductance decay of the sample that results from the decay of the excess, photo-generated charge carriers (measured by induction thanks to a coil of 4 cm of diameter placed beneath the sample)
- Convert the sheet conductance into an excess carrier density Δn
- Convert the measured light intensity into a generation rate G
- Calculate the effective minority carrier lifetime $\tau_{eff} = \dfrac{\Delta n}{G - \dfrac{d\Delta n}{dt}}$

The iV_{OC} value is calculated following:

$$V_{OC} = \frac{kT}{q} \ln\left(\frac{np}{n_i^2}\right) \tag{A2.1}$$

The J_0 value is calculated with

$$J_0 = J_{0,front} + J_{0,back} = \frac{qn_i^2 W}{N_{dop} + \Delta n}\left(\frac{1}{\tau_{eff}} - \frac{1}{\tau_{bulk}}\right) \tag{A2.2}$$

with N_{dop} the dopant density, $J_{0,front}$ and $J_{0,back}$ the recombination current densities respectively at the front and at the back of the measured sample, and W the thickness of the sample.

Spectroscopic Ellipsometry (SE)

Spectroscopic Ellipsometry (SE) is a characterisation method that allows to extract the optical properties of a material, along with the thickness of the layer that is being studied.

The measurement devices used during this thesis are UVISEL and UVISEL II by Jobin-Yvon. The SE data was treated in DeltaPsi II software in order to carry out the modeling and fitting of the optical model of the layers to characterize.

The acquisition setup consists in shining a sample with a polarized light at a given wavelength. A change of polarization happens when the light is reflected at the surface of the sample. The polarized light is then analyzed in order to measure this change in polarization. The acquisition setup is shown in Figure A2.1. This is done for a range of wavelengths in order to have a spectrum of the variation of the polarization properties.

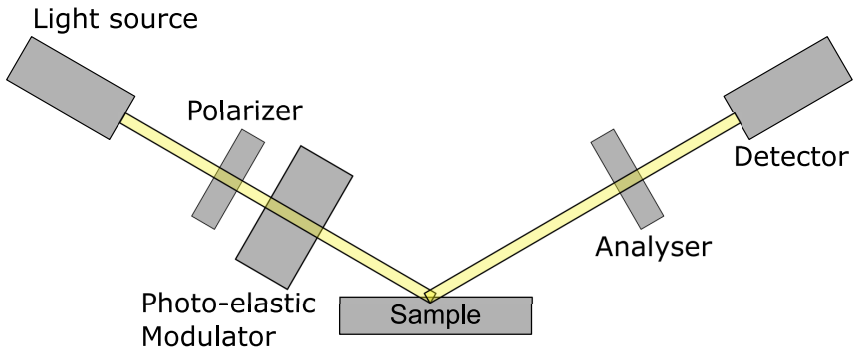

Figure A2.1: Schematic representation of the Spectroscopic Ellipsometry optical system.

A spectroscopic model is then used to assess the optical properties of the stack of materials that is being investigated. The acquired data is subsequently fitted with this model. This can give information on the optical properties (n, k) of the films, their thickness, roughness ...

Photoluminescence (PL) Images

Photoluminescence consists in exciting a semiconductor thanks to a light source, and to measure the luminescence of the sample. The photon flux detected by a photo-detector will be given by:

$$Y_{PL}(E) = \frac{1}{4\pi^2\hbar^3c^2}\frac{a(E)E^2}{\exp\left(\left(E-\Delta\mu\right)/kT\right)-1} \tag{A2.3}$$

With the absorptivity $a(E) = (1-R_f)\left(1-\exp\left(-\alpha(E)d\right)\right)$, R_f the front surface reflectivity, d the sample thickness, α the absorption coefficient, $\hbar$ the reduced Planck constant, and $\Delta\mu$ the electron-hole Fermi level splitting. For a same absorptivity and temperature, a greater photoluminesence intensity results from a larger value of $\Delta\mu$, which can be interpreted as less recombinations, thus a higher surface passivation or a better bulk lifetime.

In PL imaging, a CCD camera collects all the luminescence signal, integrates it and gives a total luminescence intensity. The camera allows to extract an image of the photoluminescence intensity, which provides information on the homogeneity of the effective minority carrier lifetime in the sample.

X-ray Photoelectron Spectroscopy (XPS)

A way to probe the chemical composition of the surface of a film is by X-ray-Photoelectron Spectroscopy. The surface of the sample is exposed to X-rays. The high energy of the photon $h\nu$ can be transferred to a core-level electron that is then expulsed from the sample. These *photoelectrons* are then detected and its kinetic energy E_{kin} is probed. This allows to extract the binding energy of the electron E_B

$$E_B = h\nu - E_{kin} \tag{A2.4}$$

This energy corresponds to the energy position of the electron below the Fermi level as shown in Figure A2.2.

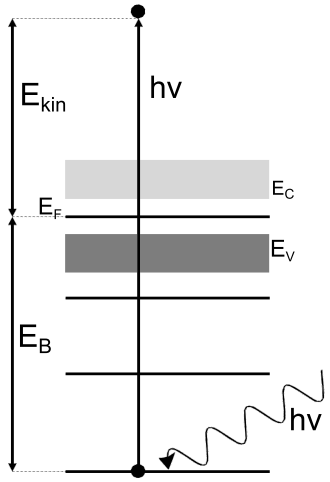

Figure A2.2: Schematic representation of the energy diagram during XPS experiments.

Consequently, this technique allows to probe the occupied states in the matter. The photopeaks that are seen in XPS spectra correspond to dedicated chemical bonds that allow to identify the nature of the atom, as well as the chemical environment of the bond. Since X-rays are mostly absorbed near the surface, and that the photoelectrons emitted below the surface can be reabsorbed by the material, the detected photoelectrons mostly come from a region that is situated less than ≈ 10 nm under the surface of the sample.

Four-Points Probe (4PP)

Four-Points Probe measurements are made to calculate the sheet resistance of a conductive layer. This method is more accurate than a simple two-terminal measurement since it allows to remove the contribution from the contact resistance between the electrode and the studied conductive layer. The equivalent electric circuit of the acquisition setup is shown in Figure A2.3. A known current is sent between the electrodes 1 and 4 while the tension is measured between 2 and 3.

For four electrodes separated by the same distance, the sheet resistivity ρ_{sq} is given by:

$$\rho_{sq} = \frac{\pi}{\ln 2}\frac{U}{I}$$

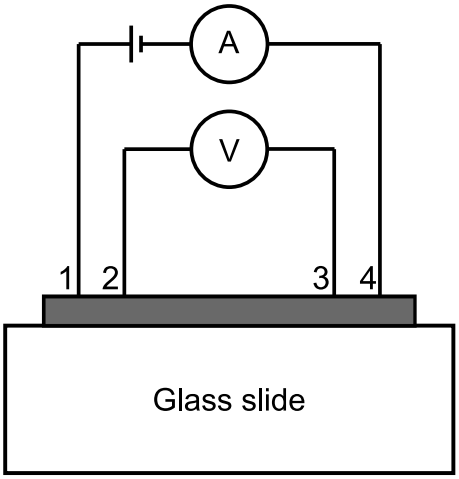

Figure A2.3: Equivalent electric scheme of the 4PP acquisition setup.

Corona Oxide Characterization On Semiconductor (COCOS)

The Corona Oxide Characterization On Semiconductor technique allows to measure the fixed charge density Q_f in a thin film deposited on a silicon wafer. The schemes and explanations described below are extracted from the Semilab PV2000-A User Manual [207].

The measurement sequence in shown in Figure A2.4. It consists in depositing charges on the surface of the sample thanks to a corona gun, and subsequently measuring the contact potential difference V_{cpd} between the surface and the bulk wafer thanks to a vibrating Kelvin probe.

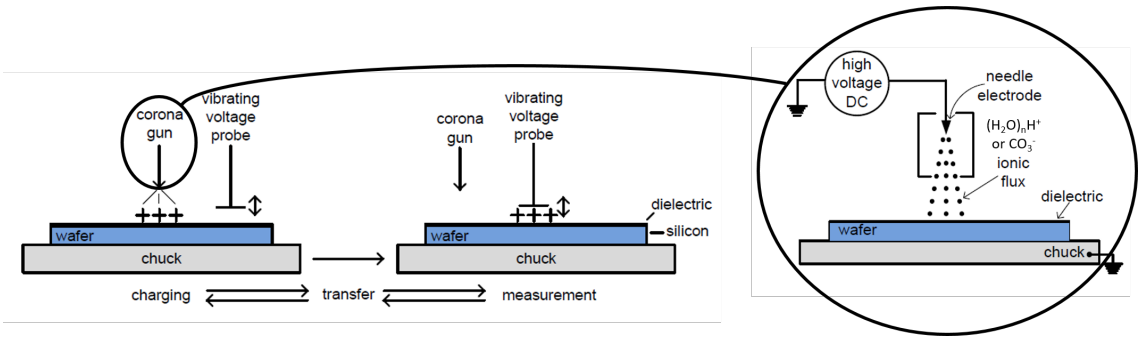

Figure A2.4: Scheme of the COCOS measurement sequence. The right hand graph is a zoom-in on the corona gun [207].

The V_{cpd} measurements include various contributions :

$$V_{cpd} = \phi_{ms} + V_{sb} + V_D \tag{A2.5}$$

with ϕ_{ms} the difference in work function between the metal reference electrode and the c-Si bulk, V_{sb} is the surface potential barrier, and V_D the potential drop in the dielectric layer that is being characterized. The surface barrier V_{sb} being the value of interest, it is necessary to get rid of the $\phi_{ms} + V_D$ contributions. One way to do so is to make one measurement in the dark $V_{cpd,dark}$ and one under strong illumination $V_{cpd,light}$. Indeed, under strong illumination, the large number of electron-pairs flattens the band at the c-Si/dielectric interface, and $V_{sb} = 0$. Consequently $V_{cpd,dark} - V_{cpd,light} = V_{sb}$

When putting more and more corona charge at the surface of the sample, the bands are being bent at the surface of the semiconductor as shown in Figure A2.5.

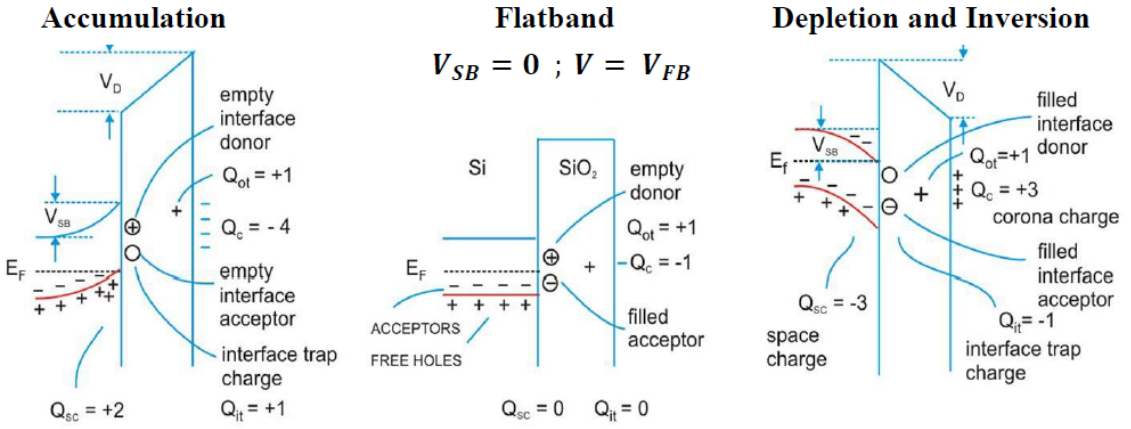

Figure A2.5: Representation of the energy band diagram at the c-Si/dielectric layer interface for different amounts of corona charges deposited at the surface of the dielectric layer [207].

The measurement of the evolution of V_{sb} with the amount of corona charge deposited ΔQ allows to extract both the fixed charge density Q_f in the material and the interface defect density D_{it}.

Raman Spectroscopy

Raman Spectroscopy relies on the physics of photon-phonon interactions. A laser shines the sample to be investigated. It has a specific angular frequency ω. The incident photons have a finite probability of interaction with the phonons (oscillation modes of the crystal). In the following we will focus on one specific oscillation mode of angular frequency Ω. The Raman inelastic scattering can either lead a transfer of energy from the crystal vibration to the photon (phonon-anihilation), that results in a scattered photon of frequency $\omega + \Omega$, or can lead to the creation of a phonon, thus resulting on a scattered photon of frequency $\omega - \Omega$. The first interaction is called *anti-Stokes* and the second is called *Stokes*. The latter having a significantly higher probability of occurrence, and both information being redundant, only the low-frequency part of the spectrum is usually analyzed.

Consequently, Raman spectroscopy gives information on the oscillation modes of the material characterized, which depend on various physical and chemical properties.

Fourier Transform Infrared (FTIR) Spectroscopy

FTIR experiments are useful to measure the chemical composition of a thin film: a wide-spectrum IR source shines the sample, which is the thin film to be characterize deposited on a substrate of silicon (transparent to IR light). The material will absorb the light at the specific energy of vibration of the chemical bonds it contains. The different bonds usually have several modes of vibration that can be excited, such as stretching, bending, rocking ...

A FTIR acquisition setup is usually composed of an IR light source, a Michelson interferometer that allows to modulate each wavelength of the incident beam at a different

frequency. The signal that is measured depends on the position of the Michelson configuration (position of the mirror). This signal actually corresponds to the Fourier transform of the incident light intensity. Consequently, calculating the inverted Fourier transform of the signal allows to get the spectral decomposition of the light intensity. By reflecting the light beam to go through the sample, analyzing this new interferogram and comparing the resulting spectrum with the one of the incident beam, this allows to extract the spectral absorption of the sample.

In our analyzes of the SiN_x:H layers, a FTIR of the bare silicon wafer is carried out in order to remove this contribution (background).

Appendix A3

Résumé en Français

Introduction

L'indice de développement humain (IDH) est un indicateur de l'espérance de vie, de l'éducation et du revenu par habitant des différentes régions du monde. Il est généralement considéré comme un élément de mesure du progrès et du développement des pays. D'après le programme de développement des Nations Unies, il existe une corrélation entre l'IDH et la consommation d'énergie par habitant [1]. L'accès à une énergie abordable est donc capital pour le développement des pays et leur capacité à offrir un meilleur niveau de vie à leurs habitants. Le Conseil Mondial de l'Energie a identifié trois grands défis que l'industrie de l'énergie doit relever : le "trilemme" énergétique [2]. Ces trois piliers sont l'*équité énergétique*, la *sécurité énergétique* et la *durabilité environnementale*.

Sur notre planète, la consommation d'énergie par habitant est répartie de manière très inhomogène d'un pays à l'autre (0,25 tep/hab.[1] pour le Bangladesh contre 16,38 tep/hab. pour le Qatar en 2017 [3]), principalement en raison des différences de produit intérieur brut et d'accès aux ressources. Au sein même des pays, les ménages peuvent être approvisionnés en énergie de manière très inégale en raison de prix élevés ou d'absence de connexion au réseau. Les systèmes énergétiques doivent également être sûrs, flexibles et résilients afin d'éviter les pannes d'électricité qui peuvent avoir des effets désastreux sur la mortalité (blackout dans les hôpitaux) ou sur l'économie. Le Groupe d'experts Intergouvernemental sur l'Evolution du Climat (GIEC) indique en outre que le changement climatique et ses conséquences - tels que le réchauffement de la planète, l'acidification des océans et l'effondrement de la biodiversité - sont principalement dus aux activités humaines et plus particulièrement aux émissions de dioxyde de carbone (CO_2) ou d'autres gaz à effet de serre [208]. En effet, une forte activité économique est corrélée à une consommation d'énergie importante, alors que le mix énergétique mondial actuel est principalement basé sur les combustibles fossiles qui émettent du CO_2 dans l'atmosphère lors de leur utilisation (combustion pour transformer l'énergie chimique en énergie mécanique, thermique ou électrique) [3].

L'énergie solaire photovoltaïque (PV) est une source d'énergie qui pourrait apporter une réponse à au moins deux des problèmes évoqués. Le soleil brille dans tous les pays du globe, ce qui contribue à l'atténuation du problème de la distribution des ressources et permet une meilleure indépendance énergétique des pays (*équité énergétique*). Mais surtout, son principe de fonctionnement ne repose pas sur les combustibles fossiles ce qui en fait un moyen de production d'électricité qui émet beaucoup moins de gaz à effet

[1] tep = tonne d'équivalent pétrole, 1 tep = 11630 kWh, source : Agence Internationale de l'Energie

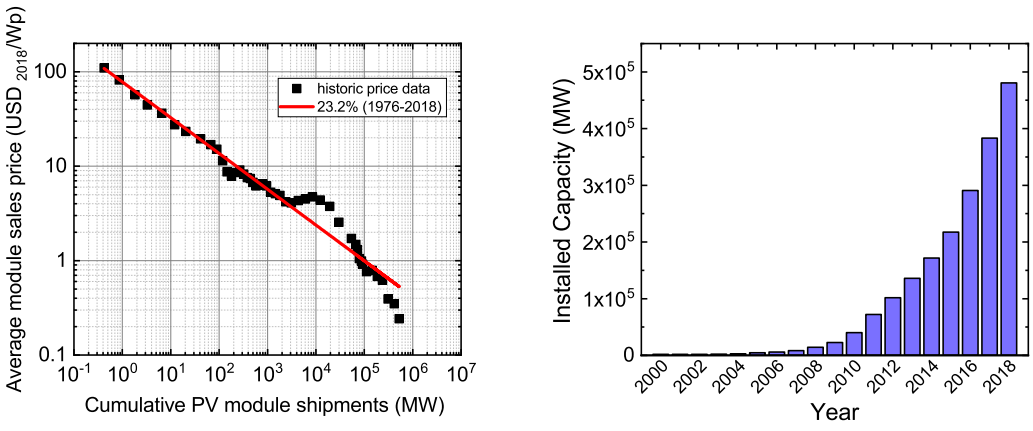

(a) (b)

Figure A3.1: (a) Courbe d'apprentissage des prix de marché d'un module photovoltaïque en fonction de la quantité cumulée de modules vendus [6]. (b) Capacité totale cumulée de puissance photovoltaïque installée dans le monde en MWp de 2000 à 2018 [7].

de serre que les centrales électriques conventionnelles (*durabilité environnementale*). En moyenne en 2011, l'intensité carbone du solaire photovoltaïque était de 48 gCO_2eq/kWh contre 469 gCO_2eq/kWh pour le gaz naturel [5].

Pour que ce moyen de production d'électricité soit pertinent économiquement, il doit être capable de fournir de l'énergie à un coût compétitif. Le prix de vente moyen des modules PV en USD2018/kWp a considérablement diminué au cours de la dernière décennie, avec un taux d'apprentissage de 23,2 % par doublement des expéditions cumulées [6], comme le montre la Figure A3.1a. Cette diminution est due à différents facteurs tels que la délocalisation des activités de production, une industrie dédiée à la fabrication de plaquettes de silicium (wafers) et une augmentation du rendement énergétique des modules. Ces facteurs sont allés de pair avec une forte augmentation de la capacité annuelle installée dans le monde (comme le montre la Figure A3.1b), ce qui a entraîné une baisse significative des coûts marginaux.

Pour évaluer la compétitivité du PV, il convient de comparer le coût actualisé de l'énergie (LCOE pour Levelized Cost of Energy en anglais), c'est-à-dire le coût d'un kWh d'énergie produite, en prenant en compte les coûts d'investissement, la durée de vie du système, les coûts d'exploitation et de maintenance et le combustible. En 2018, en Allemagne, les installations photovoltaïques étaient déjà moins chères que d'autres technologies conventionnelles telles que les centrales à charbon et les turbines à gaz à cycle combiné (CCGT) (voir la Figure A3.2) [8].

Même si les prix sont bas, la pénétration de l'énergie solaire dans le système énergétique mondial reste marginale. En effet, comme le montre la Figure A3.3a, la production mondiale d'énergie est encore largement dominée par les combustibles fossiles (les contributions du gaz naturel, du charbon et du pétrole s'élevant à 81,3 %), et la fraction de cette énergie produite par l'énergie solaire photovoltaïque est d'environ 0,27 % en 2018 (444 TWh ou 38 Mtep par rapport à une production d'énergie totale de 13972 Mtep) [3].

Afin de favoriser ce développement, et notamment si les politiques environnementales changent peu (taxes sur les émissions de carbone, ...), il est primordial de continuer à faire baisser les prix. Cela permettrait à la fois (i) aux fournisseurs d'énergie d'investir davantage dans le photovoltaïque, et (ii) aux États de réduire le montant des subventions,

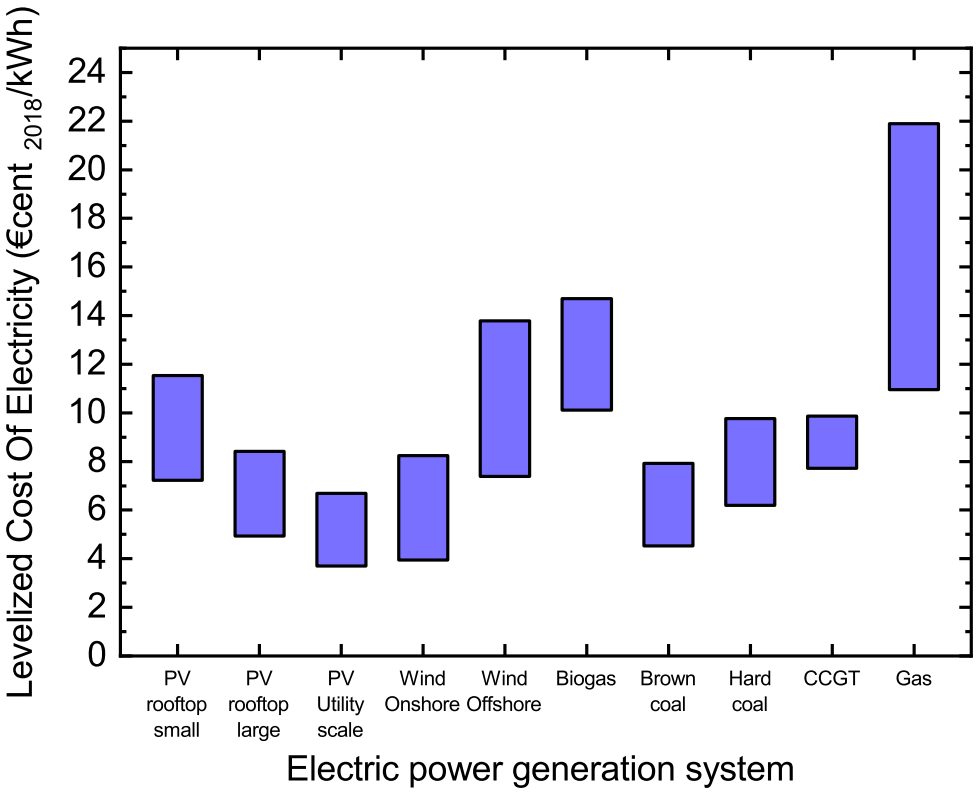

Figure A3.2: Coût actualisé du kWh d'énergie produite pour différentes technologies de production d'électricité, en Allemagne en 2018 [8]. La production PV est calculée en supposant un éclairement horizontal global entre 950 and 1300 kWh.m^2.an^{-1}. Les nombres d'heures d'utilisation à pleine charge (en h/an) sont supposés compris entre : 1800-3200 pour l'éolien terrestre, 3200-4500 pour l'éolien en mer, 5000-7000 pour les biogaz, 6450-7450 pour le charbon (lignite), 5350-6350 pour le charbon (houille), 3000-4000 pour le CCGT, et 500-2000 pour le gaz.

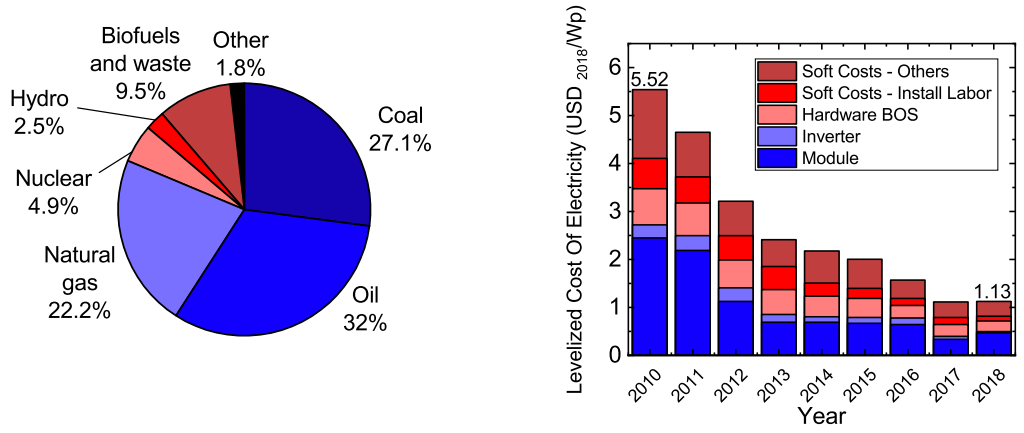

(a) (b)

Figure A3.3: (a) Proportion des différentes sources d'énergie dans le mix énergétique mondial, 2017 [3]. (b) LCOE (ajusté en fonction de l'inflation) de 2010 à 2018 pour les centrales PV avec traqueur à un axe (100 MW) [9].

ce qui réduirait la pression sur le contribuable et permettrait d'investir davantage dans d'autres secteurs clés de la transition énergétique (efficacité énergétique, infrastructures électriques, électrification, adaptation au changement climatique ...). Comme on peut le voir dans la Figure A3.3b, le coût du module représente environ 50 % du LCOE pour les grandes centrales PV, et moins de 10 % pour le PV résidentiel, car les coûts de système sont relativement élevés [9]. Une solution pour réduire de manière significative le LCOE est de fabriquer des modules plus efficaces tout en maintenant de faibles coûts de fabrication et d'investissement. Cela permet de réduire le coût global, car des dispositifs plus efficaces génèrent une plus grande puissance de sortie pour les mêmes coûts de système (acquisition du terrain, coût de la main-d'œuvre, etc.).

Ces arguments sont également valables pour l'intensité carbone de l'électricité photovoltaïque : une plus grande efficacité des modules PV pour la même quantité de gaz à effet de serre émise (pour fabriquer les composants) entraînent moins de CO_2 émis par kWh d'électricité produite [10]. Ce critère devrait être d'une grande importance à l'avenir car si, comme projeté dans les principaux scénarios pour atteindre les objectifs de neutralité carbone à horizon 2050 **iea˙net˙2021**, une grande partie de l'énergie mondiale est produite à terme par des centrales photovoltaïques, la réduction de l'intensité carbone de cette énergie sera essentielle.

Aujourd'hui, l'industrie photovoltaïque est largement basée sur l'utilisation du silicium comme matériau semi-conducteur. Ce type de panneau solaire représente 95 % du marché du photovoltaïque en 2018 [11] et repose sur l'utilisation de wafers de silicium cristallisé. La majorité des cellules solaires actuelles sont basées sur des wafers de silicium monocristallin qui permettent d'obtenir de très bonnes performances, mais sont relativement coûteux et reposent sur des procédés de fabrication énergivores et émettant beaucoup de CO_2. La technologie de cellules solaires PERC, qui est l'architecture de cellule solaire la plus largement industrialisée, repose sur un processus de fabrication simple et permet d'obtenir de bons rendements photovoltaïques.

Il est possible de réduire d'avantage à la fois les coûts de fabrication et les émissions de CO_2 en utilisant des wafers de silicium dit *cast-mono* de haute qualité et faible coût, dont le processus de fabrication est moins énergivore que celui des wafers industriels standards.

En outre, une technologie de cellules solaires très prometteuse pour augmenter encore les rendements tout en maintenant de faibles coûts de fabrication dans un avenir proche est la technologie des *cellules à contacts passivés*. Elle permet d'atteindre des efficacités de cellule solaire plus élevées en réduisant les pertes électriques, et présente l'avantage d'utiliser principalement des machines qui sont déjà présentes dans les lignes de production industrielles actuelles. Cette technologie est déjà en cours d'industrialisation dans certaines entreprises [12]. Néanmoins, le processus de fabrication standard pour cette architecture de cellule solaire à contacts passivés nécessite de nombreuses étapes, ainsi qu'un budget thermique élevé entre autre à cause de la nécessité d'une étape de recuit de plusieurs minutes entre 600 et 1000 °C. C'est pourquoi il convient d'étudier de nouvelles méthodes de fabrication de ce type de cellules solaires, procédés qui seraient moins gourmands en énergie et qui nécessiteraient moins d'étapes de fabrication.

Cette thèse de doctorat porte sur l'étude d'un procédé de fabrication simplifié de contacts passivés, appelé contact passivé avec recuit rapide (FPC pour Fired Passivated Contact en anglais), qui permet de réduire le nombre d'étapes de fabrication et d'exposer la cellule solaire à un budget thermique réduit. Les principales caractéristiques étudiées sont les propriétés de passivation des FPC, qui traduisent les pertes électriques dans le dispositif. Des caractérisations par photoluminescence modulée *in situ* sont réalisées pour atteindre cet objectif : elles permettent de mesurer l'évolution des propriétés de passivation en temps réel pendant une étape spécifique du fabrication. Pour conclure, ces contacts sont intégrés sur des wafers de silicium cast-mono fabriqués par Photowatt™ [13].

Chapitre 1 : Contexte et objectifs

Un procédé de fabrication ne nécessitant pas de longue étape de recuit (5-15 min) à haute température (600-1000 °C) pour la formation de contacts passivés (voir Figure A3.4a) a été proposé par Ingenito *et al.* [46]. Il s'appuie sur l'utilisation du recuit rapide à haute température (*firing*, environ 3 s à 800 °C) déjà nécessaire pour la métallisation de la cellule. Le procédé de fabrication consiste à déposer une couche de silicium résistante au firing. Dans l'étude en question, il s'agit de carbure de silicium amorphe ou nanocristallin hydrogéné (a-SiC_x:H ou nc-SiC_x:H), déposé sur une fine couche d'oxyde de silicium (SiO_x). Pendant le dépôt, la couche de carbure de silicium est dopée au bore ((p) SiC_x:H) pour permettre d'extraire les trous, porteurs de charge positifs. Ensuite, l'échantillon est soumis à l'étape de firing, qui engendre une cristallisation supplémentaire de la couche de (p) a-SiC_x:H et permet la métallisation de la face avant (non étudiée dans cette thèse). Afin d'atteindre une qualité de passivation élevée, un processus d'hydrogénation supplémentaire est nécessaire [87]: de l'hydrogène diffusant à l'intérieur de la cellule permet de passiver des défauts et améliorer la qualité de la cellule. Pour ce faire, une couche de nitrure de silicium amorphe hydrogéné (a-SiN_x:H) est déposée par PECVD, puis recuite à 450 °C pendant 30 minutes. Elle est ensuite gravée par immersion dans de l'acide hydrofluorique, et la cellule est complétée par le dépôt d'une couche d'oxyde transparent conducteur et en sérigraphiant une grille d'argent à basse température.

Cependant, les longues étapes d'hydrogénation ne sont pas souhaitables pour une intégration industrielle (réduction de la cadence de production) et la métallisation à haute température est préférable à la métallisation à basse température pour une meilleure compatibilité avec les outils de production industriels préexistants. Pour outrepasser ces limitations, nous étudions un procédé pour la fabrication de FPC alternatif, illustré dans la Figure A3.4b. Il commence par une étape de nettoyage standard (dit RCA) suivie du dépôt d'une fine couche de SiO_x. Une couche de silicium dopée au bore est ensuite déposée par

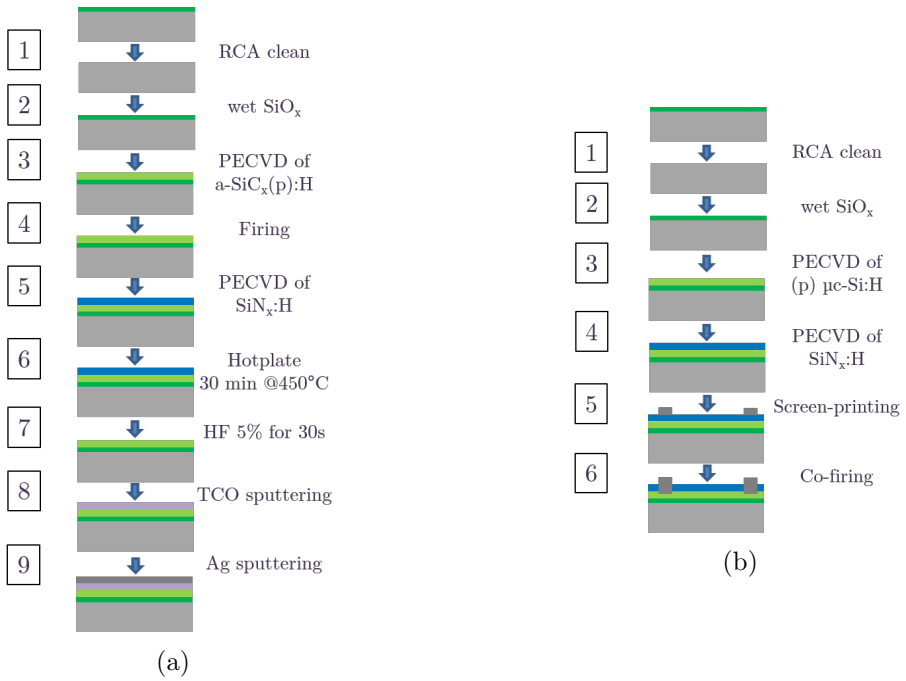

Figure A3.4: (a) Procédé de fabrication des FPC, proposé par l'EPFL [46]. (b) Procédé simplifié pour la fabrication de FPC sans étape d'hydrogénation post-firing.

Dépôt Chimique en phase Vapeur Assisté par Plasma (PECVD, pour le sigle en anglais), suivie d'une couche de a-SiN_x:H. Le tout doit être résistant à l'étape finale de firing qui suit une étape de sérigraphie de pâte de métallisation adaptée pour les hautes températures. Ce procédé, qui réduit le nombre d'étapes de 9 à 6, est représenté schématiquement sur la Figure A3.4b.

L'objectif de cette thèse est d'étudier ce procédé simplifié pour l'intégration de contacts passivés. A terme, nous chercherons à réaliser cette intégration sur des wafers de silicium cast-mono de type p (dopés au bore) car ils ont l'avantage de consommer relativement peu d'énergie lors de leur fabrication, et leur coût de production est réduit par rapport aux wafers industriels standard (Cz). Cela permettrait de limiter le budget thermique et donc la quantité d'énergie nécessaire à la fabrication de la cellule solaire. L'étude de ce procédé consiste d'abord à optimiser les dépôts des différentes couches de l'empilement grâce à des caractérisations multiphysiques des matériaux déposés. Elle est ensuite approfondie en utilisant la technique de photoluminescence modulée (MPL) *in situ*, qui permet de mesurer en temps réel l'évolution de la durée de vie des porteurs de charge minoritaires (électrons ou trous selon la nature du wafer) d'un échantillon pendant une étape donnée du processus de fabrication - ce qui correspond à une mesure des propriétés de passivation. Nous nous attachons tout d'abord à mieux comprendre cette nouvelle technique de caractérisation à travers une étude de cas réalisée sur des wafers de silicium passivés par une couche d'oxyde d'aluminium (AlO_x), puis nous l'utilisons sur des échantillons FPC. Enfin, le transfert de ce procédé de fabrication de contacts passivants sur des wafers industriels de grande taille (Cz et cast-mono) est présenté.

Chapitre 2 : Développement et optimisation des matériaux

Ce chapitre décrit l'optimisation des différentes couches de l'empilement du contact passivé FPC. Des SiO_x chimique et déposés par PECVD ont été comparés. Des couches de silicium micro-cristallisées ont été utilisées afin de limiter l'absorption parasite et d'éviter la formation de cloques lors des étapes de firing. Une étude approfondie de la composition de l'oxyde après le dépôt d'une couche de silicium micro-cristallin hydrogéné ((p) µc-Si:H) a été effectuée par analyse XPS, et a montré que le dépôt a changé la morphologie de la couche d'oxyde. La Figure A3.5a montre qu'il est possible de détecter la présence de l'oxyde tunnel enterré sous la couche de (p) µc-Si:H. Au maximum d'intensité du signal O_{1s} les Figures A3.5b et A3.5c montrent que l'on observe une perte de la quantité d'oxygène détectée dans la couche, et que la structure de l'oxyde tunnel est modifiée par le dépôt de (p) µc-Si:H en changeant d'un oxyde presque stoechiométrique (pic autour de 103 eV) à un ensemble de sous oxydes (augmentation de l'épaulement situé autour de 101 eV).

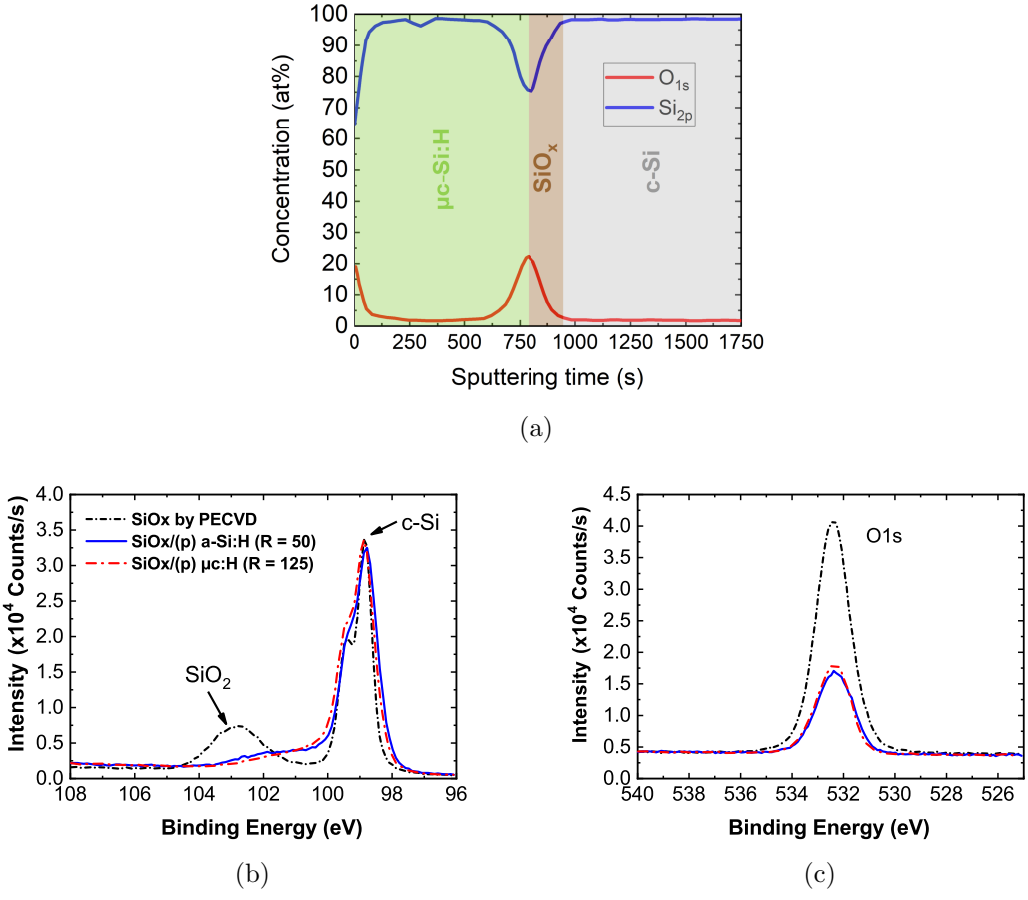

(a)

(b)

(c)

Figure A3.5: (a) Profil de concentration du silicium (bleu) et de l'oxygène (rouge) de l'empilement SiO_x/(p) µc-Si:H déposé sur du c-Si - mesuré par XPS. Les fonds vert, marron et gris représentent la position des différents matériaux de l'empilement. Analyse des spectres XPS (b) Si_{2p} et (c) O_{1s} pour différentes conditions de dépôt de la couche de silicium dopée au bore (courbes bleue et rouge), comparés avec ceux d'un échantillon de référence (pas de dépôt de silicium sur l'oxyde, courbe noire). Ces spectres sont obtenus au maximum d'intensité du photopic O_{1s} (voir Figure A3.5a).

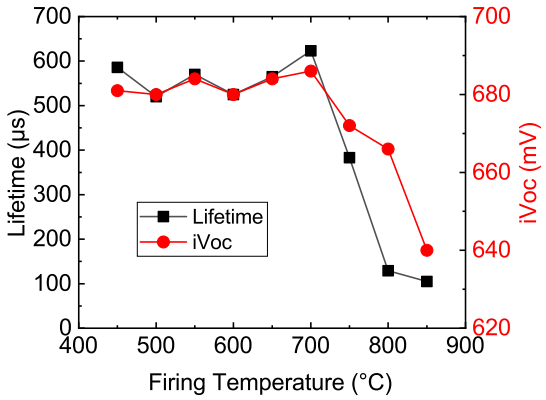

Figure A3.6: Évolution des valeurs d'iV_{oc} et τ_{eff} pour différentes températures maximales lors de l'étape de firing réalisée sur un échantillon passivé par un empilement SiO_x/(p) µc-Si:H/SiN_x:H.

Cependant, aucune relation n'a pu être établie entre les propriétés de passivation et la composition de l'oxyde tunnel mesurée avec cette technique. Celles-ci étant significativement meilleures pour l'oxyde chimique que pour l'oxyde déposé par PECVD, c'est cette première méthode qui est utilisée dans la suite de cette thèse. Les conditions de dépôt de µc-Si:H et µc-SiO_x:H dopés au bore et au phosphore ont été optimisées pour obtenir le meilleur compromis possible entre la conductivité, la transparence, les propriétés de passivation et la stabilité thermique. Après l'optimisation de la couche de a-SiN_x:H, d'autres caractérisations ont été effectuées afin de mieux connaître ses propriétés chimiques et optiques. La passivation fournie par l'empilement SiO_x/(p) µc-Si:H/a-SiN_x:H s'est avérée commencer à se dégrader pour des températures de firing supérieures à 700 °C (voir Figure A3.6). Une meilleure stabilité thermique a finalement été obtenue en remplaçant la couche de a-SiN_x:H par une couche d'AlO_x. Ceci montre que le procédé de fabrication FPC simplifié est réalisable, et qu'il existe des conditions de dépôt et de recuit pour lesquelles la passivation n'est pas trop fortement endommagée après l'étape finale de firing. Cette stabilité est également accrue par l'utilisation de (p) µc-SiO_x:H à la place de (p) µc-Si:H, qui a également l'avantage d'être plus transparent et mieux passiver la surface de l'échantillon, mais qui est significativement moins conducteur. Des couches plus épaisses de (p) µc-SiO_x:H ou de a-SiN_x:H peuvent également être utilisées pour un meilleur maintien des propriétés de passivation après firing.

Ce chapitre souligne la complexité de l'empilement FPC, ainsi que l'impact que peut avoir chaque étape de dépôt sur l'ensemble des autres couches de la structure. Ainsi, une optimisation plus efficace et une meilleure compréhension des processus de passivation peuvent être réalisés en utilisant la caractérisation *in situ*.

Chapitre 3 : Photoluminescence modulée pour AlO_x

Ce chapitre décrit un dispositif d'acquisition MPL *in situ* installé sur un réacteur PECVD qui permet de mesurer en temps réel la durée de vie des porteurs minoritaires à la densité de porteurs minoritaires photogénérés spécifique de 1×10^{15} cm^{-3}. Des améliorations apportées à la procédure de traitement des données afin de prendre en compte la diffusion latérale des porteurs de charge sont également présentées. Cet outil de caractérisation

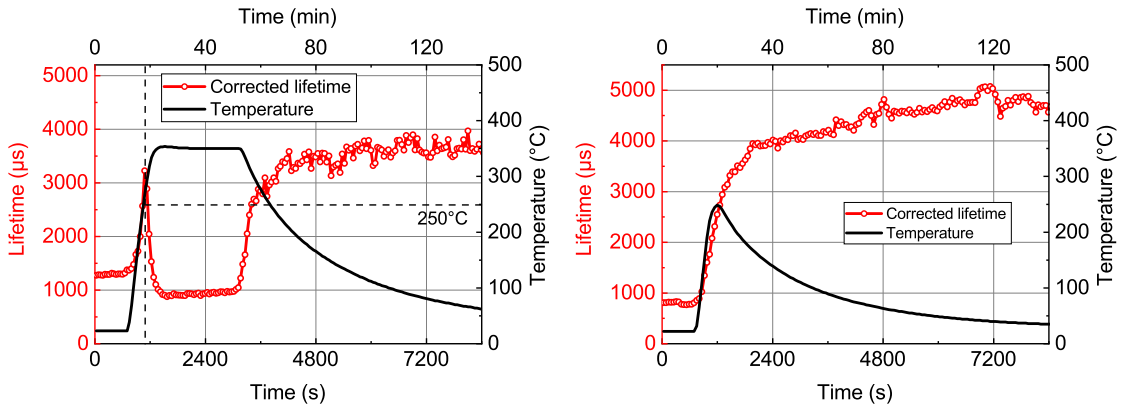

Figure A3.7: Evolution de la durée de vie effective de porteurs de charge minoritaires dans un wafer de silicium passivé par une couche d'Al_2O_3 pendant une étape de recuit (a) à 350 °C pendant 30 minutes ou (b) à 250 °C pour 1 minute sous atmosphère d'hydrogène. La courbe noire montre l'évolution de la température pendant le recuit.

peut être utilisé pendant une étape de recuit ou le de dépôt d'une de couches par PECVD. Une première étude de cas a été réalisée pendant des étapes de recuit réalisées sur des wafers de silicium passivés par des couches d'AlO_x. De fortes variations de la durée de vie effective des porteurs minoritaires mesurée par MPL ont été observées au cours de ces expériences. Lors d'un recuit de 30 min à 350 °C, la durée de vie des porteurs baisse fortement lorsque l'échantillon atteint une température supérieure à 250 °C (voir Figure A3.7a).

Une étape de recuit plus rapide à une température plus basse (1 min à 250 °C au lieu de 30 min à 350 °C, Figure A3.7b) a permis d'atteindre une durée de vie effective de 5 ms, mais seulement localement, sur la zone où le laser utilisé pour la mesure du MPL éclairait l'échantillon. On en déduit que l'action (locale) de la lumière et de la température a un impact sur les propriétés de passivation. Des mesures de défauts et de charges fixes a permis d'identifier que ces conditions (illumination laser et recuit à 250 °C) engendrent l'activation d'une forte densité de charges fixes, positives et stables (voir les Figures A3.8a et A3.8b).

Ce type d'observation est hautement inhabituel, puisque dans la littérature, l'immense majorité des études mesurent la présence de charges fixes négatives dans les couches minces d'alumine après recuit. Ceci pourrait conduire à un nouvel intérêt pour l'utilisation d'AlO_x pour la passivation des semi-conducteurs de type n et de type p. Cette étude montre que le recuit sous illumination est un moyen simple et rapide d'obtenir des couches d'AlO_x chargées positivement. En perspective, il serait intéressant d'ajouter une source lumineuse au dispositif de MPL *in situ* pour éclairer l'ensemble de l'échantillon pendant le recuit thermique. Cela pourrait permettre des investigations plus approfondies sur cet état particulier de la couche d'alumine.

Chapitre 4 : Photoluminescence modulée pour FPC

Dans ce chapitre, l'étape du processus d'hydrogénation des contacts FPC est étudiée par photoluminescence modulée *in situ*. Deux types d'échantillons sont étudiés:

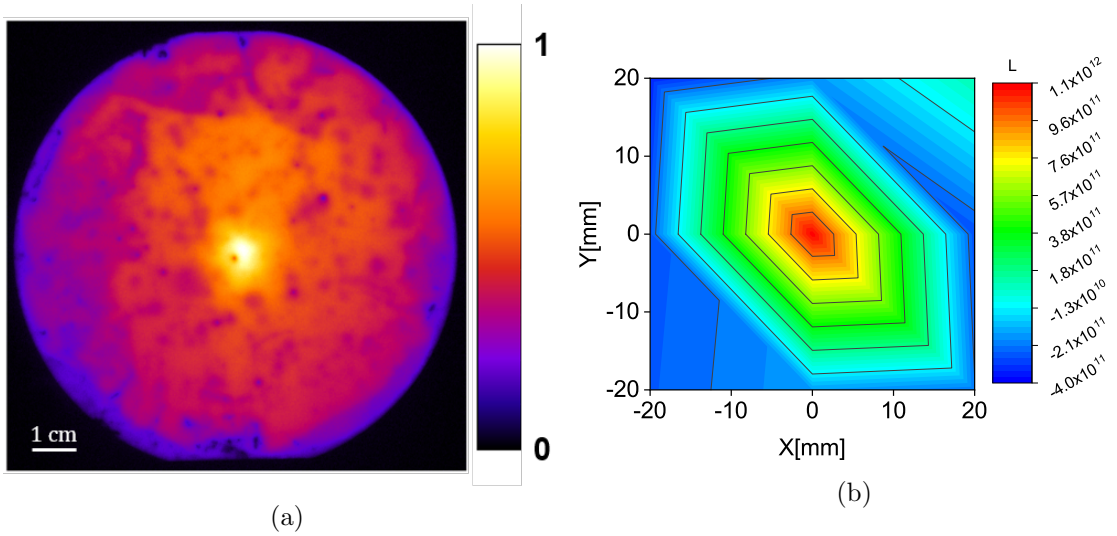

(a) (b)

Figure A3.8: (a) Images PL et (b) cartographie de la densité de charges fixes pour un échantillon recuit à 250 °C pendant 1 min. MPL *in situ* a été utilisée pendant l'étape de recuit.

- Pour le premier, fabriqué à l'EPFL (Suisse), un empilement de SiO_x/aSiC_x:H dopé est déposé, puis subit une étape de firing. Pour améliorer les propriétés de passivation qui sont très faibles suite à cette étape, il s'en suit un dépôt d'une couche de a-SiN_x:H. L'étape de recuit sur plaque chauffante de cette structure est étudiée par MPL. Lors des mesures de durée de vie durant la montée en température, de larges variations réversibles sont observées (voir Figure A3.9). Elles ont pu être attribuées à deux phénomènes qui rentrent en compétition : la variation des vitesses de recombinaison des porteurs avec la température (augmentation de la durée de vie), et l'augmentation significative de la densité de porteurs minoritaires lorsque la température dépasse 300 °C (diminution de la durée de vie). Comme ces variations

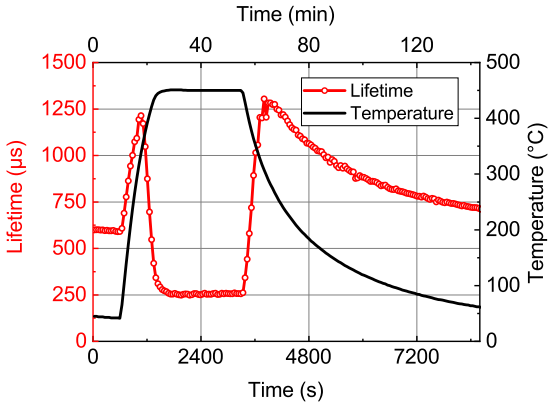

Figure A3.9: Évolution de la durée de vie des porteurs de charge mesurée par MPL *in situ* pendant l'étape d'hydrogénation (recuit 30 min à 450 °C après le dépôt d'une couche de a-SiN_x:H). La courbe noire montre l'évolution de la température pendant le recuit.

réversibles n'ont pas d'intérêt majeur pour la mesure des propriétés de passivation dans l'échantillon étudié, les mesures de durée de vie ont été recalculées pour ne

pas prendre en compte ces phénomènes thermiques, et sont présentées en Figure A3.10. L'évolution de la durée de vie obtenue peut être qualitativement expliquée par une diminution de la densité de défauts dans le volume du wafer de silicium. Cette mesure est en adéquation avec d'autres observations réalisées par photoluminescence résolue spatialement et avec la littérature scientifique. Ainsi, les mesures de MPL *in situ* ont permis de valider que la durée de vie avant recuit est limitée par les défauts volumiques dans le wafer de silicium, et que le recuit permet l'hydrogénation du wafer, et donc la passivation de ces défauts.

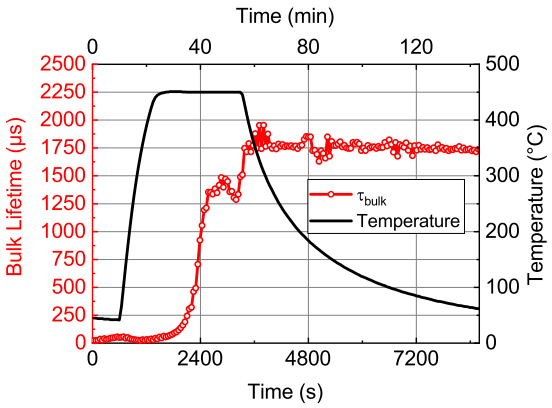

Figure A3.10: Mesure des évolutions irréversibles de la durée de vie des porteurs de charge dans le volume du wafer pendant l'étape d'hydrogénation (recuit 30 min à 450 °C après le dépôt d'une couche de a-SiN_x:H). La courbe noire montre l'évolution de la température pendant le recuit.

- Le deuxième type de FPC, faits à l'IPVF, est celui développé au Chapitre 2. Les méthodes d'hydrogénation (avant firing) étudiées sont l'exposition à un plasma NH_3 + H_2, et le dépôt d'une couche de nitrure de silicium. Il est observé que dans tous les échantillons, la température de consigne de 350 °C de la chambre de dépôt augmente significativement la durée de vie, puisque cela recuit les couches de passivation des échantillons (voir Figure A3.11). Le plasma NH_3 + H_2 endommage les propriétés de passivation dans tous les échantillons, mais de façon beaucoup plus marquée dans le cas des échantillons de FPC avec (p) µc-SiO_x (voir Figure A3.12a). La dégradation peut être associée aux émissions VUV du plasma NH_3 + H_2 qui peuvent créer des défauts à l'interface c-Si/SiO_x. L'ajout de SiH_4 dans le mélange de gaz permet de déposer du nitrure de silicium amorphe hydrogéné, et d'améliorer considérablement la durée de vie finale comme observé dans les Figures A3.12c et A3.12d. En particulier, cette amélioration a lieu pendant les premières minutes du dépôt, ce qui semble laisser une grande liberté sur le matériau déposé 5 minutes. Ainsi, une bi-couche a-SiN_x:H/a-SiN_xO_y:H pourrait être déposée sur le FPC, alliant bonne passivation, et une meilleure résistance au firing. En outre, l'ordre des étapes de dépôt doit être soigneusement choisi afin d'obtenir les meilleures propriétés de passivation possibles.

Jusqu'à présent, toutes les études d'optimisation et de MPL ont été réalisées sur des wafers Float-Zone (FZ) de haute qualité, et polis chimiquement sur les deux faces (DSP). Il est nécessaire de vérifier que le processus est transférable sur de grands wafers industriel.

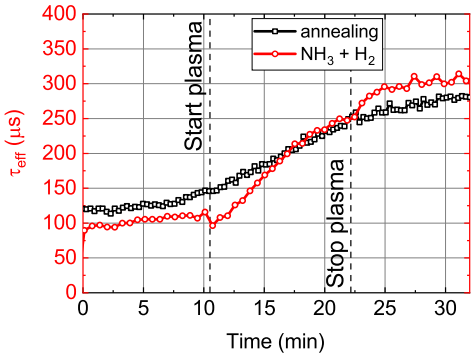

Figure A3.11: Évolution de la durée de vie des porteurs de charge d'un échantillon symétriquement passivé par un empilement SiO_x/(p) µc-Si:H (i) soit exposé à un plasma (NH_3 + H_2) à 350 °C (courbe noire), (ii) soit simplement mis dans la chambre de PECVD à 350 °C (en rouge).

Chapitre 5 : Vers des cellules FPC de grande taille

Dans ce chapitre, des FPC extracteurs de trou ont été intégrés sur des wafers industriel de type Cz et cast-mono, ce qui a permis d'atteindre des valeurs d'iV_{oc} équivalentes (autour de 655 mV). Ceci souligne l'intérêt d'intégrer des FPC sur des wafers cast-mono, qui sont à la fois moins chers et nécessitent moins d'énergie pour la fabrication des cellules. Cette étude permet de souligner que les propriétés de passivation prodiguées par les FPC sont très sensibles à la préparation de la surface: ils nécessite une couche de SiO_x conforme et de haute qualité afin de fournir de bonnes propriétés de passivation. Pour l'illustrer, les wafers utilisés précédemment sont polis afin de diminuer la rugosité de surface. Sur ces wafers de silicium polis des propriétés de passivation très encourageantes ont été obtenues. En particulier, une valeur d'iV_{oc} de 691 mV a été atteinte en intégrant un empilement FPC sur un wafer poli de type cast-mono, ce qui est proche des valeurs maximales obtenues sur des wafers FZ DSP. Un premier prototype de cellule solaire a été réalisé, avec une couche de (n) µc-SiO_x:H sur la face avant et une couche de (p) µc-SiO_x:H sur la face arrière. Un V_{oc} de 671 mV a été atteint, malgré d'importantes pertes résistives. Le processus de métallisation doit être optimisé et amélioré pour révéler tout le potentiel des FPC sur les cellules solaires en silicium.

Conclusion et Perspectives

Ce travail de doctorat s'est donc concentré sur l'étude d'un procédé simplifié pour la fabrication de contacts passivés avec recuit rapide, dits FPC. Ce procédé de fabrication de cellules solaires a l'avantage d'être simple (peu d'étapes) et de nécessiter un faible budget thermique, ce qui permet de réduire les coûts de production et l'intensité carbone de l'énergie photovoltaïque produite. Afin de mener à bien cette étude, différentes techniques de caractérisation ont été utilisées et optimisées, parmi lesquelles la photoluminescence modulée (MPL) *in situ* qui a permis de mesurer en temps réel la durée de vie des porteurs minoritaires dans les échantillons pendant une étape spécifique du processus de fabrication.

En résumé, nous avons montré que, dans les empilements complexes de couches que nous étudions, chaque étape de fabrication modifie les propriétés globales de l'échantillon :

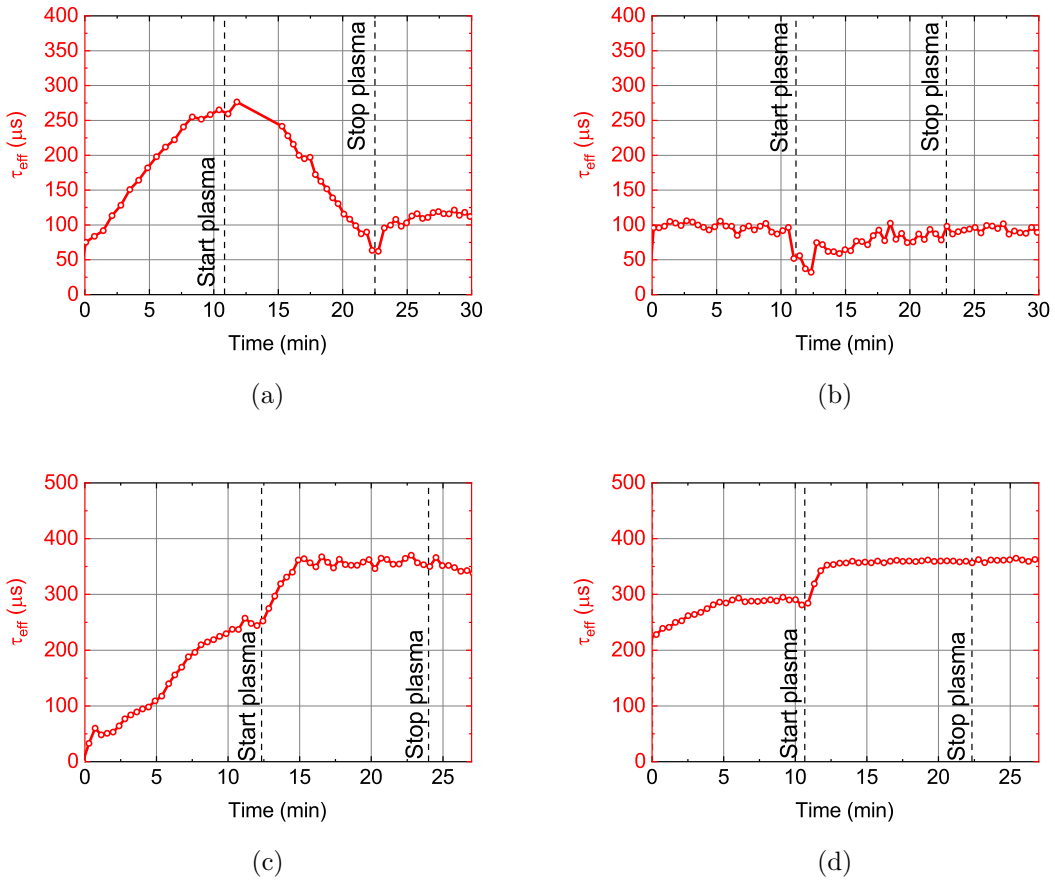

Figure A3.12: Évolution de la durée de vie des porteurs de charge d'un échantillon symétriquement passivé par un empilement SiO_x/(p) µc-SiO_x:H exposé à un plasma NH_3 + H_2 de 5W (a) sur la première face de l'échantillon puis (b) sur la deuxième face de l'échantillon, ou edposé à un plasma NH_3 + H_2 + SiH_4 de 5 W (dépôt de a-SiN_x:H) (c) sur la première face de l'échantillon puis (d) sur la deuxième face de l'échantillon.

les dépôts des différents films ont un impact sur les couches déposées précédemment (voir les mesures XPS et d'ellipsométrie). En raison du rôle critique des interfaces dans les performances de nos dispositifs, les techniques de caractérisation optique et chimique standard ne sont pas suffisantes, et des mesures électroniques sont nécessaires : un léger changement dans les conditions de dépôt des matériaux peut conduire à des propriétés électroniques complètement différentes (comme des charges fixes positives ou négatives dans les couches d'AlO_x en fonction du type de recuit appliqué). La caractérisation électrique sur les dispositifs finaux n'est pas suffisante pour comprendre les mécanismes physico-chimiques en jeu, ce qui a motivé l'utilisation de techniques de caractérisation *in situ*. Les mesures de MPL *in situ* peuvent aider à trouver la meilleure combinaison de matériaux pour maximiser à la fois la résistance au firing et les propriétés de passivation. Au regard des résultats obtenus, de nombreuses études pourraient être réalisées afin de pousser plus loin la compréhension et les améliorations qu'ont permis cette thèse.

Par la suite, des caractérisations supplémentaires doivent être réalisées pour mieux comprendre l'origine et la nature des charges fixes positives observées dans les couches d'AlO_x : des analyses XPS permettraient de connaître la configuration chimique de la couche d'AlO_x, la variation de la source lumineuse (distribution spectrale, flux de photons, ...) permettraient de mieux comprendre les mécanismes de formations de ces charges, et enfin il est nécessaire de vérifier la possibilité d'obtenir de l'AlO_x chargé positivement sur de plus grandes surfaces.

Une amélioration de la routine d'acquisition MPL et du traitement des données devrait être réalisée afin de mieux prendre en compte les variations de température. Le traitement doit être entièrement repensé pour les mesures à haute température (plus de 350 °C) si l'on veut visualiser uniquement les évolution de la passivation de surface et de volume. Toutefois, il est utile de rappeler qu'à température constante, les variations de la durée de vie mesurées représentent des variations réelles des propriétés de passivation.

Une étude plus approfondie de la couche supérieure du FPC devrait être menée pour de futures améliorations. L'augmentation de la durée de vie se produisant exclusivement pendant les premières minutes du dépôt de a-SiN_x:H, cela ouvre la voie au développement de nouveaux empilements : il peut être envisagé de faire un dépôt d'une couche de quelques nm d'un matériau riche en hydrogène qui pourrait augmenter la passivation de l'interface c-Si/SiO_x (comme du a-SiN_x:H) jusqu'à atteindre une durée de vie maximale, puis d'une couche qui pourrait augmenter la stabilité thermique de l'empilement de passivation lors du firing, comme le a-$SiN_xO_yC_z$:H. Ces bi-couches doivent être étudiées en utilisant la MPL *in situ* pendant leur dépôt afin d'optimiser la durée du procédé et d'obtenir une meilleure compréhension de l'impact des différentes espèces présentes dans le plasma.

Des recherches approfondies sur la métallisation et sur la température optimale de firing doivent être réalisées afin de permettre l'intégration des FPC sur des wafers de silicium de taille industrielle. De plus, il serait très intéressant d'étudier la stabilité à long terme et le vieillissement des cellules solaires FPC, et de les comparer à la durée de vie des cellules solaires à contacts passivés fabriquées par d'autres procédés de fabrication.

La recherche de procédés de fabrication de cellules solaires ayant un impact environnemental de plus en plus faible est d'une importance majeure pour adresser les problématiques d'acceptabilité du PV et justifier l'adoption à plus grande échelle de ces dispositifs (TW de capacité de production installée chaque année). Des recherches amont sur les procédés de fabrication devraient inciter l'industrie photovoltaïque à adopter des méthodes plus sobres afin de contribuer à un avenir plus durable.

ECOLE DOCTORALE

Titre: Developpement et caractérisation de contacts passivés avec recuit rapide (FPC) pour la fabrication de cellules solaires en silicium.

Mots clés: photovoltaïque, cellules solaires en silicium, contacts passivés, caractérisation *in situ*, photoluminescence modulée

Résumé: Etant appelée à jouer un rôle déterminant dans la transition énergétique, l'industrie photovoltaïque est mise au défi de réduire l'impact environnemental de la fabrication de panneaux solaires. Selon toute probabilité, les cellules solaires en silicium à contacts passivés (TOPCon) domineront le marché dans les prochaines années grâce à leurs excellentes performances électriques. Cependant, leur intégration est énergivore, d'où l'étude de nouveaux procédés de fabrication comme les contacts passivés avec recuit rapide (FPC).
Ce manuscrit présente l'optimisation des conditions de dépôts des différentes couches utilisées dans une cellule FPC, ainsi que des caractérisations poussées de ces couches. Des analyses de spectroscopie photoélectronique X ont permis de montrer que le dépôt d'une couche de (p) μc-Si:H par dépôt chimique en phase vapeur assisté par plasma (PECVD) modifie la composition chimique de l'oxyde tunnel enterré dans l'empilement passivant.
Des améliorations ont été apportées à un dispositif d'acquisition de Photoluminescence Modulée embarqué sur un réacteur de dépôt PECVD. Cette technique permet de mesurer en temps réel l'évolution de la durée de vie des porteurs de charge dans un échantillon durant une étape de fabrication. Cela a permis de montrer que l'action combinée de la température et de la lumière engendre l'activation de charges fixes positives stables dans des couches d'AlO_x, ce qui est très inhabituel.
Les mesures de passivation en temps réel d'échantillons FPC pendant une étape d'hydrogénation ont mis en évidence l'importance majeure de la température et de la durée du recuit pour atteindre les niveaux de passivation attendus. Cette technique a également été utilisée pendant le dépôt de couches de SiN_x:H. Elle a permis d'observer (i) les fortes dégradations liées aux plasmas directs de H_2 et NH_3 sur des couches de (p) μc-SiO_x et (ii) que pendant le dépôt de SiN_x:H, la majorité de l'amélioration de la passivation a lieu pendant les premières minutes de dépôt. L'intégration de contacts FPC a été réalisé sur de grands wafers industriels de type mono-cast, donnant des résultats prometteurs sur surfaces polies.

Title: Development and characterization of Fired Passivating Contacts for p-type silicon solar cells fabrication.

Keywords: photovoltaics, silicon solar cells, passivating contacts, *in situ* characterization, modulated photoluminescence

Abstract: Due to its expected role in the energy transition, the photovoltaic industry is being challenged to reduce the environmental impact of the manufacturing of solar panels. The silicon solar cells with Tunnel Oxide Passivated Contact (TOPCon) technology are likely to broadly hit the market within the next years due to their great electrical performances. Yet their integration is rather energy intensive, which is why novel manufacturing options such as the Fired Passivating Contact (FPC) cells are being investigated.
This dissertation presents the optimization of the deposition conditions of the various layers of a FPC cell, along with their thorough characterization. X-ray photoelectron spectroscopy analysis allowed to show that the deposition of a Plasma Enhanced Chemical Vapor Deposited (PECVD) (p) μc-Si:H layer modified the chemical composition of the buried tunnel oxide layer in the passivating stack.
Improvements were made on an *in situ* Modulated Photoluminescence acquisition setup mounted on a PECVD reactor. This technique allows to monitor in real time the evolution of the passivation properties of a sample during a given processing step. In a case study, this resulted to the demonstration that the combined action of light and temperature on AlO_x layers leads to the activation of stable positive fixed charges, which is highly unusual.
The real-time lifetime measurements of FPC samples during a hydrogenation step evidenced the importance of the temperature and duration of the annealing step in order to fully achieve high passivation properties. The technique was also used during the SiN_x:H deposition and allowed to show (i) the detrimental effect of direct H_2 and NH_3 plasma on FPC and especially on the ones based on (p) μc-SiO_x layers, and (ii) that during the SiN_x:H deposition, most of the improvement happens during the first minutes of deposition. The integration of FPC was carried out on large area mono-cast wafers with very promising results on polished surfaces.

Institut Polytechnique de Paris
91120 Palaiseau, France